PRECISION ENGINEERING CENTER

2008 ANNUAL REPORT
VOLUME XXVI
March 2009

Sponsors:	3M Corporation Lexmark International, Inc. Panasonic Boston Laboratory Vistakon, Johnson & Johnson Vision Care Inc. Lockheed Martin National Science Foundation B & W Y-12
Faculty:	Thomas Dow, Editor Jeffrey Eischen Ronald Scattergood
Graduate Students:	David Brehl Qunyi Chen Stephen Furst Timothy Kennedy Erik Zdanowicz Brandon Lane Meirong Shi
Staff:	Kenneth Garrard Alexander Sohn Paula Kelley
Consultants:	Karl Falter David Youden Amir Pirzadeh

Table of Contents

Summary i

Design

1. Design of a Fast Long Range Actuator - Flora II 1
   Erik Zdanowicz and Jeffrey Eischen
2. Polaris Mechanical Design and Alignment Procedures 21
   Alexander Sohn

Fabrication

3. Fast Long Range Actuator - Flora I 43
   Qunyi Chen, Thomas Dow, Kenneth Garrard and Alexander Sohn
4. Kinoform Lens Fabrication 69
   Alexander Sohn
5. Wear Analysis of Diamond Tools on AL-6061 and 1215 Steel 79
   Brandon Lane, Thomas Dow and Ronald Scattergood
6. Diamond Turning of Small Optics 99
   Alexander Sohn
7. 4-Axis Machining of Micro-features with the Ultramill 107
   Brandon Lane, Thomas Dow and Alexander Sohn

Metrology

8. Diamond Tool Wear Measurements by EBID 125
   Meirong Shi, Ronald Scattergood and Thomas Dow
9. Performance of Fresnel Optics 137
   Thomas Dow, Kenneth Garrard and Alexander Sohn

Control

10. Polaris 3D Operation and Control 149
    Kenneth Garrard and Amir Pirzadeh
11. Automatic Handling Technology for Precision Two-sided Parts 167
    Stephen Furst and Thomas Dow

Personnel 187

Graduates of the PEC 195

Academic Program 201

Publications 209

SUMMARY

The goals of the Precision Engineering Center are: 1) to develop new technology in the areas of precision metrology, actuation, manufacturing and assembly; and 2) to train a new generation of engineers and scientists with the background and experience to transfer this technology to industry. Because the problems related to precision engineering originate from a variety of sources, significant progress can only be achieved by applying a multidisciplinary approach; one in which the faculty, students, staff and sponsors work together to identify important research issues and find the optimum solutions. Such an environment has been created and nurtured at the PEC for over 25 years and the 100+ graduates attest to the quality of the results.

The 2008 Annual Report summarizes the progress over the past year by the faculty, students and staff in the Precision Engineering Center. During the past year, this group included 3 faculty, 7 graduate students, 2 full-time technical staff members and 1 administrative staff member. This diverse group of scientists and engineers provides a wealth of experience to address precision engineering problems. The format of this Annual Report separates the research effort into individual projects but there is significant interaction that occurs among the faculty, staff and students. Weekly seminars by the students and faculty provide information exchange and feedback as well as practice in technical presentations. Teamwork and group interactions are a hallmark of research at the PEC and this contributes to both the quality of the results as well as the education of the graduates.

The summaries of individual projects that follow are arranged in the same order as the body of the report, 1) design, 2) fabrication and 3) metrology and 4) control.

1) DESIGN

Projects with an emphasis on design range from design of optical systems to dynamic, mechanical systems to control systems. The current projects involve Fresnel lenses and fast tool servos.

Design of Long Range Fast Tool Servo – FLORA II

This paper discusses the design process for a new long range actuator that can be used to fabricate freeform optical surfaces with large sag (4 mm) at frequencies up to 20 Hz. FLORA II is smaller and lighter than its predecessor while achieving a high bearing stiffness coupled with smooth motion. This method proved that the FLORA II can improve upon the performance of the FLORA I in a smaller, lighter package.

Polaris Mechanical Design and Alignment
Polaris 3D is an evolution of the original Polaris concept to true three-dimensional measurement in a spherical coordinate system using a non-contacting probe. Design and assembly of this system is challenging because of the two pairs of stacked linear and rotary axes and the adjustments needed to align them into a single spherical coordinate system. The final design is presented with descriptions of the components, their functions and the alignment procedures needed to assemble the system.

2) FABRICATION
Fabrication of precision components is an emphasis area for the PEC. Current projects include machining of Fresnel lenses, freeform optics and micro devices.

Control and Performance of a Long Range Fast Tool Servo – FLORA I
FLORA I will soon give way to the second generation prototype. This prototype features a tool holder driven by a linear 3-phase motor, supported by an air bearing, measured by a high-resolution linear encoder and controlled by a high-speed Digital Signal Processor (DSP). Control algorithms and tool motion measurements are discussed. A freeform mirror with fiducial features was machined and procedures for this unique process are discussed.

Kinoform Lens Fabrication
Kinoform lenses represent a specific subset of Fresnel lenses that are designed to use both refractive and diffractive power to manipulate light. The objective of this exercise was to demonstrate that Kinoform lenses for use in the visible light spectrum, with their typically small groove spacings of 30 μm and less, can be fabricated. Adding a goniometer axis to the DMT, several test parts were cut and surface finish and groove fidelity were measured.

Wear Analysis of Diamond Tools
Orthogonal cutting experiments using 6061 Aluminum and 1215 Steel were conducted and wear of the diamond tool was closely observed using the electron beam induced deposition method. This method provides precise measurement of tool wear geometry, which was used to calculate tool stresses, volumetric wear loss, and wear rates. Comparisons are made between the modes of tool wear resulting from the two materials. These observations will be compared to results when the tool is vibrated at high-frequency during the cutting process.

Diamond Turning of Small Optics
Aspheric plastic optics are becoming increasingly prevalent and the demands for accuracy on those optics are increasing. Prototype lenses for testing are generally made by direct single point diamond turning and present some unique challenges. Compliance of most plastics, PMMA and

Polycarbonate being the most prevalent, can make diamond turning to high accuracy difficult but lenses were produced to figure error less than ±150 nm.

4-Axis Machining of Microfeatures

The Ultramill, an elliptical vibration assisted machining system, is currently mounted on a 4 axis diamond turning machine. It has 3 orthogonal linear axes and a controllable part spindle. Discussion of the alignment of these axis and techniques for programming the 4 axes are discussed. Example programs and sub-millimeter features are described including corner cube and circular features.

3) METROLOGY

Metrology is at the heart of precision engineering – from measuring fabricated parts to calibration artifacts to dynamic system characterization.

Measuring Diamond Tool Wear using EBID

Characterization of the tool wear condition is a critical step to revealing cutting mechanism in diamond turning. EBID (electron-beam-induced deposition) is used to measure the diamond tool edge geometry. Results show that EBID can be an effective way to measure tool edge radius and wear land, both in straight and round nose diamond tools. Wear mechanisms during the diamond cutting can be studied based on the measurement of the edge radius and wear land.

Performance of Fresnel Optics

This project involved design, fabrication and measurement of Fresnel focusing and scanning lenses. The predicted and measured spots (using a digital camera) for several commercial and custom fabricated lenses are discussed. The best performance came from an aspheric Fresnel lens fabricated at the PEC with spots sizes from 40 μm on-axis to 313 μm for a beam 45 mm off-axis beam. The commercial conical and fabricated kinoform lenses did not show the same performance with spot sizes that were twice as large.

4) CONTROL

Control of motion or a fabrication processes is a key ingredient in precision engineering.

Polaris 3D Operation and Control

An instrument for the metrology of high-aspect ratio surfaces has been constructed that allows a variety of convex and concave surfaces to be measured while keeping the optical probe nearly normal to the surface as it sweeps out a spiral path from the equator to the pole. Challenges in the operation of this instrument include reference generation, compensation for axes errors and building a control system that is both user friendly and fast enough to measure a part in less than two minutes.

Automatic Handling Technology for Precision Two-sided Parts

A complete part transfer and realignment system has been developed and demonstrated. The variation in radial separation between a part and a chuck can be maintained to less than 3 μm, and the axial position of the part with respect to the chuck can be controlled to within 5 μm. During the transfer demonstration, radial run-out was observed as expected and a part centering procedure was developed. This procedure succeeded in aligning a part to within 5 μm of the spindle centerline in less than 7 steps every time tested.

1 DESIGN OF A FAST LONG RANGE ACTUATOR – FLORA II

Erik Zdanowicz
Graduate Student
Jeffrey Eischen
Associate Professor
Department of Mechanical and Aerospace Engineering

Non-Rotationally Symmetric (NRS) optical surfaces are useful to optical designers because they provide additional degrees of freedom that can be used to improve optical performance and reduce system size. However, these benefits bring complications with regard to fabrication, assembly and metrology. This paper discusses the design process for a long range actuator that can be used to fabricate such surfaces with large sag (4 mm) at frequencies up to 20 Hz. The first generation Fast LOng Range Actuator (FLORA I) was created to operate at ± *2 mm and 20 Hz while creating a high-quality optical surface. While the FLORA I has carried out these tasks with reasonable success, it suffers from large physical size, large moving mass and unwanted vibrations. Therefore, a new system, FLORA II, has been designed to address these problems. Through the use of derived equivalent air bearing stiffness backed by static and dynamic experimental verification, the new system was modeled using Finite Element Analysis (FEA) software. FLORA II is smaller and lighter than its predecessor while achieving a high bearing stiffness coupled with smooth motion. This method proved that the FLORA II can improve upon the performance of the FLORA I in a small, light package.*

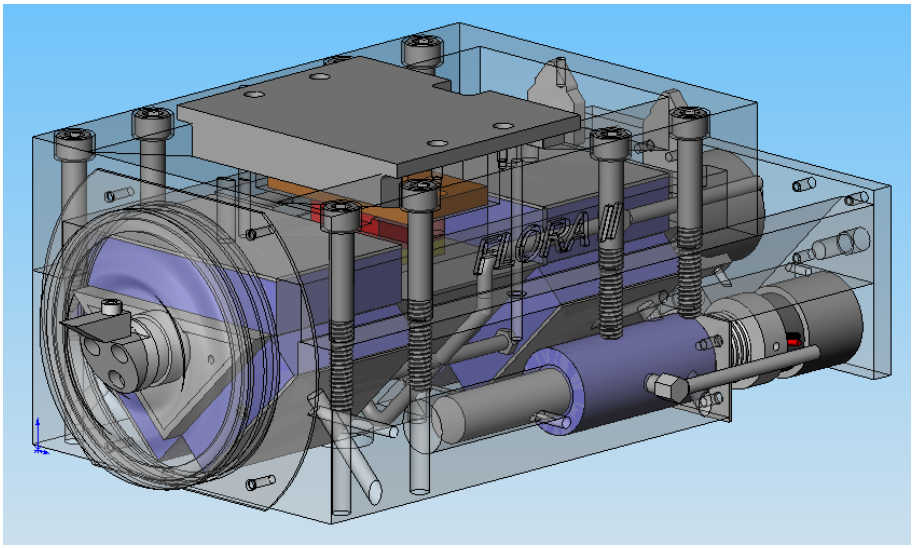

1.1 INTRODUCTION

The objective of this research is to develop a new way of machining Non-Rotationally Symmetric (NRS) surfaces. NRS optical surfaces have traditionally been machined using very slow spindle speeds and actuators with a range of hundreds of microns. This meant that a very long time was required in order to achieve a high quality NRS optical surface. A Fast LOng Range Actuator (FLORA I) was constructed with a goal of machining NRS surfaces with a sag of ± 2 mm at 20 Hz. The goal was to achieve the same quality as conventional diamond turning machines which means a form error of less than 150 nm and a surface finish of 2 nm RMS.

The FLORA I system consists of a triangular aluminum honeycomb piston supported by orifice type air bearings and driven by a linear motor. While machining with FLORA I has had success, the system is very large when compared with the size and path of the diamond tool. It was also seen that FLORA I has a 200 nm vertical vibration which has an impact when machining precision surfaces.

Therefore, the FLORA II has been designed to address the limitations of its predecessor. The FLORA II package will be smaller and lighter than FLORA I while maintaining bearing stiffness and improving system dynamics. This will be accomplished through theoretical derivation supplemented with experimental testing. The procedure described in this paper will allow the FLORA II to produce high quality NRS optical surfaces from a small, lightweight system.

1.2 DETAILS OF THE PROJECT

There were many factors that affected the design of FLORA II including the air bearings, piston geometry and material, housing, and counterbalance. Each of these factors not only individually affect the performance of the new design, but also interact with each other. For example, a large portion of the effort in this project was to model the air bearing stiffness coupled with the piston. If the piston had too much mass or the bearing stiffness was too soft then the mode frequencies of the system would decrease hampering performance. The thickness of the air film was another critical aspect of the new design which had to be accurate to within several microns. This air film is created through the expansion of the housing as well as the compression of piston. The influence of each component design on other components made this a challenging and deeply involved project

1.2.1 AIR BEARINGS

One of the main factors involved in the design of the FLORA II was the air bearings. FLORA I was designed with orifice type air bearings that consist of a number of small orifices along the

bearing surface that provide the pressurized air film. It is believed that these types of bearings are responsible for the 200 nm vertical vibration of FLORA I. For this reason, FLORA II was designed to use porous air bearings. Porous air bearings are constructed of an aluminum backing that acts like a manifold to distribute air through a porous carbon material. This porous carbon material has millions of small holes for air distribution which creates a very linear pressure distribution over the surface of the bearing. Orifice type bearings have a large pressure spike in the center of the bearing. A comparison of orifice and porous air bearings can be seen in Figure 1.

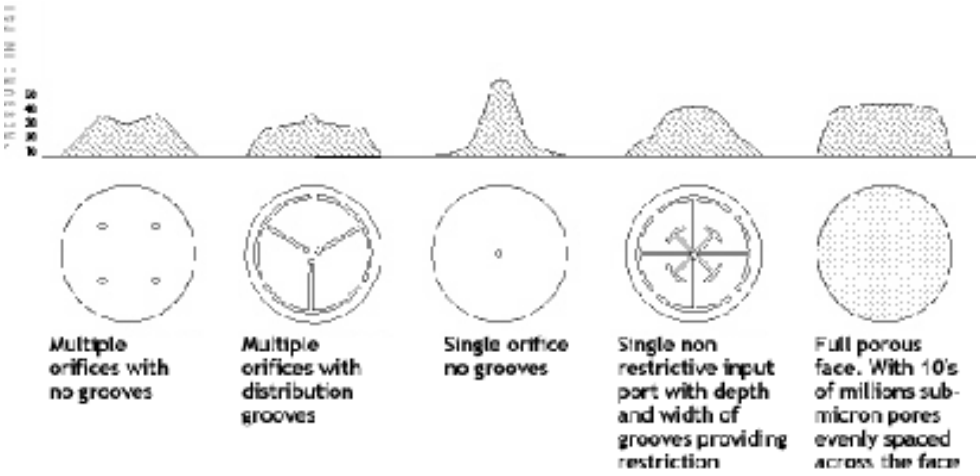

Figure 1. Orifice vs. porous air pressure distribution [1]**.**

Finite Element Analysis (FEA) software is a powerful design tool that, if used properly, can provide important results such as displacements and stresses over an entire body. The software ANSYS has an elastic foundation type of support with attaches a bed of springs from a part to the ground. It seemed as though this bed of springs foundation could be used to approximate the stiffness of the air bearing that the pressurized air film provides. The company that supplies the porous bearings, New Way, provides a stiffness for their bearings at a certain pressure. However, the stiffness that must be input into ANSYS is a stiffness per unit area. Therefore, an equivalent foundation stiffness for use in ANSYS had to be derived from the stiffness provided by New Way. In order to verify the derivation, a 25 mm diameter air bushing shown in Figure 2 was purchased. An air bushing is like a hollow tube with the bearings material on the inside in which a circular shaft could move in and out. A series of static and dynamic tests were run on the bushing.

Figure 2. New Way Air Bearings 25 mm diameter air bushing [1].

1.2.2 AIR BEARING EXPERIMENTAL SETUP

Static and dynamic experiments were run on the test bushing in order to verify theoretical derivations. The tests consisted of the 25 mm bushing, a 110 mm long stainless steel shaft, a flexure loading device, and a mounting block. It should be noted that the bushing has 4 rubber O-rings around its outside. When inserted into the mounting block, these O-rings have some compliance which acts like a set of springs. In order to eliminate this compliance, New Way recommended a static potting epoxy. This epoxy eliminated any effect the O-rings had on the bearing stiffness.

Test Setup for Static Characterization

The first static test was run in order to verify the radial stiffness of the bushing. This is the stiffness of vertical translation of the shaft inside the bushing. The experiment was run as shown below in Figure 3.

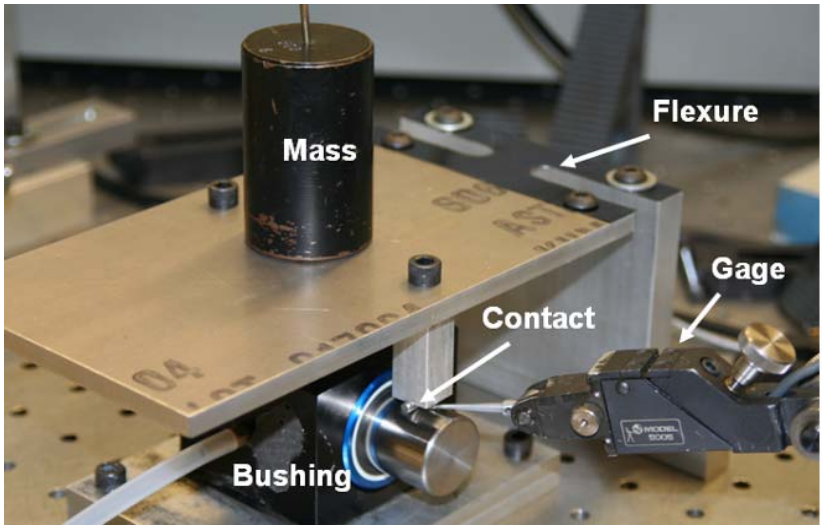

Figure 3. Experimental setup for radial stiffness.

It can be seen that a known mass was placed on the center of a load plate. This plate was hinged to a vertical support by a thin flexure. The flexure was ground down from the sides in order to allow the plate to twist so the contacts would apply equal loads. These two contacts were attached on either side of the bushing. The contacts had small cylinders glued to the bottoms to apply a point contact. A lever-type LVDT displacement measuring device was used to measure the displacement under the contact. Three different known masses were placed on the load plate 10 times each and the displacements were recorded.

Along with radial stiffness New Way also provides a pitch stiffness for the bushing. This is the stiffness of the shaft rotating in the bushing. Figure 4 shows the radial and pitch directions.

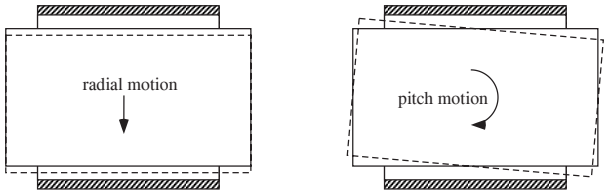

Figure 4. Shaft motion inside of air bushing.

To measure the pitch stiffness, the same equipment was used as in the radial test except one contact was removed to cause rotation. Also, because the flexure used in the radial test was ground to allow rotation, a new stiffer flexure with no cutouts was used. In this experiment two LVDT displacement measuring devices were used, one on each side of the bushing. This orientation allowed the rotation of the shaft to be calculated. Once again, three known masses were place over the remaining contact 10 times each and displacements were recorded. The setup is shown in Figure 5.

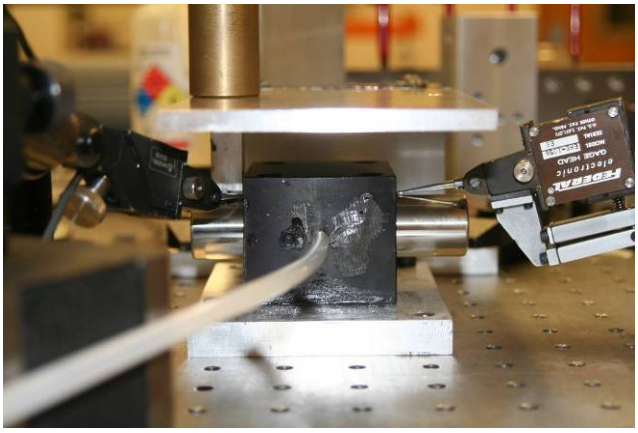

Figure 5. Experimental setup for pitch stiffness.

Test Setup for Dynamic Characterization

Characterization of the bushing's dynamic properties was an important aspect of the project since the FLORA I has unfavorable dynamics that can cause errors in the machined surface. The setup, which can be seen in Figure 6, used the same bushing, shaft, and mounting block as in the static experiments. The shaft was held in place by two rubber bands with low stiffness. An 'L' shaped bracket was then secured to the table near one end of the shaft. A capacitance gage was then attached to the bracket with a 'C' clamp. The cap gage could then be positioned to measure the motion of the shaft in different directions. Output from the cap gage was input into a Stanford Signal Analyzer where the frequency spectrum and time domain motion could be observed.

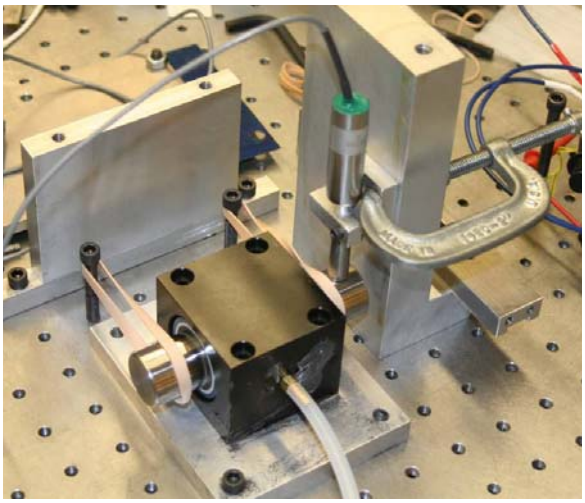

Figure 6. Setup to observe bushing dynamics.

1.2.3 ANALYTICAL APPROACH

In order to compare the results between the experiments with the bushing and ANSYS simulations, equivalent radial and pitch stiffness are needed. The approach for their derivation was a 'bed of springs' approximation where the air bushing acted like it had springs connected between it and the surface area of the shaft inside the bushing.

Equivalent Radial Stiffness

It is known that the equivalent radial stiffness is a function of the radial stiffness that New Way provides. The equivalent stiffness was derived using an end view of the shaft as shown in Figure 7 to visualize the deflection of the springs.

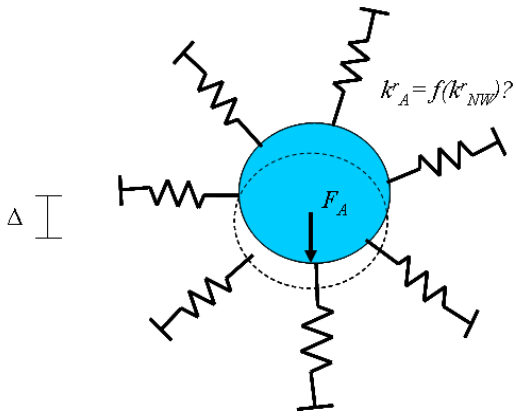

Figure 7. 'Bed of springs' approximation for radial stiffness.

Using this model, the deflection of the springs could be determined as a function of the applied force using Newton's Second Law. This resulted in

$$F_A = k^r{}_A L r \pi \Delta \tag{1}$$

where F_A is the applied force, L is the length of the shaft, r is the radius of the shaft and Δ is the vertical translation of the shaft. The symbol k^r_A is the equivalent radial stiffness that is input into ANSYS. It is known that

$$F_A = k^r{}_{NW} \Delta \tag{2}$$

where k^r_{NW} is the radial stiffness that is provided by New Way. Setting these two equations equal to each other and eliminating common terms

$$k^r{}_A = \frac{2k^r{}_{NW}}{A_s} \tag{3}$$

where A_s is the surface area of the shaft inside the bushing. Equation 3 is the formula for equivalent radial stiffness for ANSYS.

Equivalent Pitch Stiffness

As in the derivation of the equivalent radial stiffness, it was known that the equivalent pitch stiffness is a function of the pitch stiffness that New Way provides. Figure 8, a side view of the shaft, was used as a model to derive an equivalent pitch stiffness, which again must be done because the elastic foundation used in ANSYS is a stiffness per unit area.

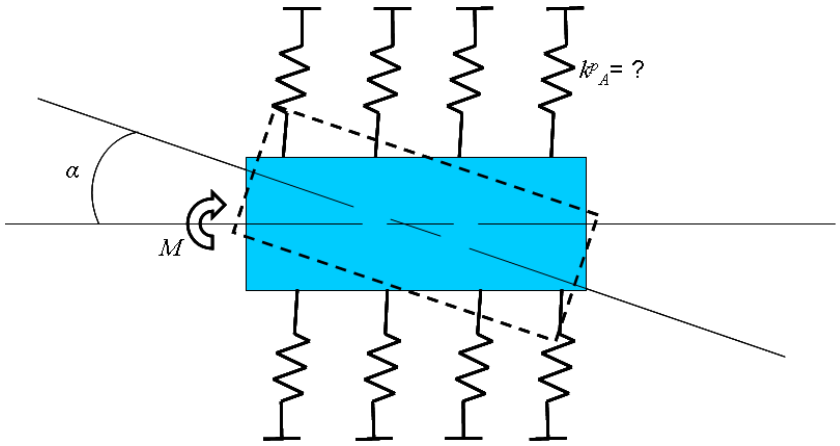

Figure 8. 'Bed of springs' approximation for pitch stiffness.

Once again, Newton's Second Law was used but instead to sum moments. This resulted in

$$M = \frac{k^p{}_A L^2 A_s}{24}\alpha \tag{4}$$

where M is the applied moment, $k^p{}_A$ is the equivalent pitch stiffness for ANSYS, and α is the pitch angle of the shaft. Also

$$M = k^p{}_{NW}\alpha \tag{5}$$

where $k^p{}_{NW}$ is the pitch stiffness New Way provides. Setting Equations 4 and 5 equal to each other and eliminating like terms, the following expression for the equivalent pitch stiffness is derived

$$k^p{}_A = \frac{24k^p{}_{NW}}{L^2 A_s} \tag{6}$$

1.2.4 AIR BEARING EXPERIMENTAL RESULTS

This section will describe the experimental results for the static (radial and pitch) as well as dynamic tests and compare these results with the results from the ANSYS simulations using the derived equivalent stiffnesses.

Static Experimental Results – Radial Stiffness

New Way Air Bearings report the bushing that was purchased has a radial stiffness of 34 N/um. However, the way that the experiment is setup will induce bending in the shaft as well. Therefore, the stiffness of the shaft was calculated and the total expected stiffness was for the shaft and bushing to act like springs in series. This expected experimental stiffness was 27.9 N/um. After the experiment was run and the data points were plotted (force vs. displacement), a line was fit through the data. The slope of this line is the stiffness.

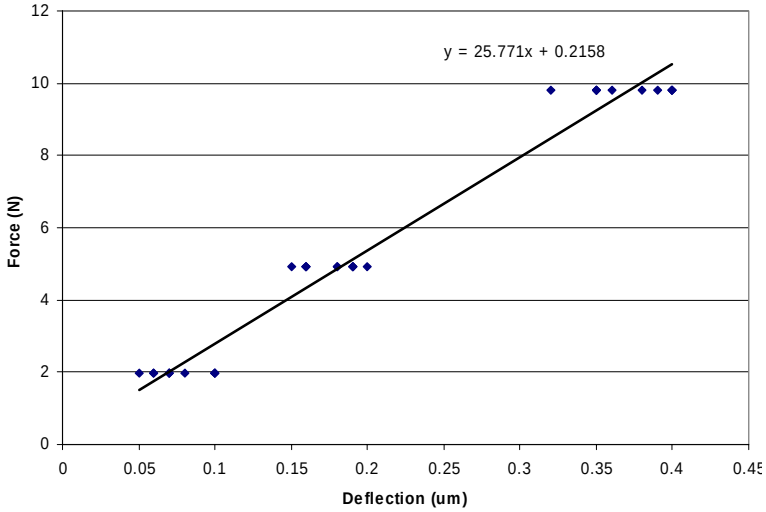

Figure 9. Radial stiffness experimental results.

From Figure 9 it can be seen that the measured stiffness was 25.8 N/um which is close to what was expected and verifies New Way's quote. Next, using Equation 3 with the New Way radial stiffness and shaft dimensions, an equivalent radial stiffness was calculated. This stiffness was input into ANSYS and a force of 10 N was applied vertically on the shaft. A deflection of 298 nm was observed. This was then compared with a simple Hooke's Law ($F = k\Delta$) calculation using a 10 N force and the stiffness New Way provides. The predicted deflection of 294 nm is almost identical to the ANSYS simulation. This proved that the derived equivalent radial stiffness was correct and a good approximation for the bushing.

Static Experimental Results – Pitch Stiffness

The procedure for pitch stiffness was carried out in a similar manner to the radial stiffness. First, the quoted stiffness from New Way was verified. Then, the equivalent stiffness was input into ANSYS and the simulation was checked against a predicted value. New Way quotes the bushing as having a pitch stiffness of 5.30 N-m/mil-rad. After the experiments with the bushings were

run, the displacements of each end of the shaft were converted into rotations. Then the rotation of the shaft was plotted against the applied moment. This gives the experimental pitch stiffness, shown below in Figure 10 as 5.53 N-m/mil-rad.

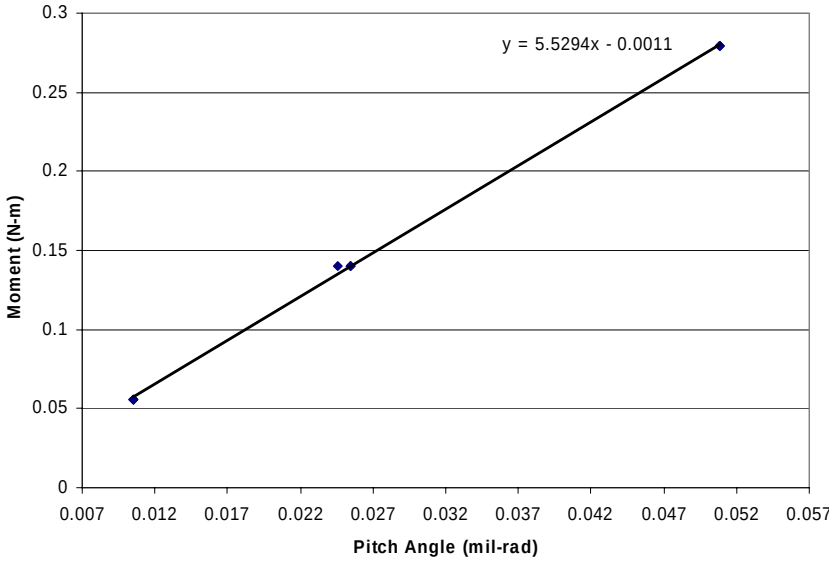

Figure 10. Pitch stiffness experimental results.

This verified the quote that New Way provided for pitch stiffness. Next, an equivalent pitch stiffness was calculated using New Way's pitch stiffness and the shaft dimensions. The equivalent pitch stiffness was input into ANSYS and a moment of 0.9 N-m was applied on the end. A rotation of 0.172 mil-rad was recorded. Hooke's Law ($M = k\alpha$) using the New Way pitch stiffness and a moment of 9 N-m resulted in a rotation of 0.170 mil-rad. These results prove that the experimental results agree with New Way's value and the equivalent pitch stiffness used in ANSYS accurately portrays the bushing.

An important characteristic these experiments revealed were that the equivalent stiffness for radial translation and pitch were different. There is only one value in ANSYS that can be input for the elastic foundation stiffness and the results show that there are two. Between the two, it was seen that the bushing is stiffer in the radial direction than pitch. To make sense of this phenomenon, note that the bushing stiffness actually comes from a pressurized air film and not springs. Therefore, the lower pitch stiffness could result from a drop in pressure due to an uneven gap when the shaft pitches. It was concluded that the lower pitch stiffness would be used for modeling since it is less stiff and will enforce a kind of safety factor when designing the system. While this method is not completely accurate, it is a good approximation without having to deal with non-linearity and the fluid dynamics of the bushing.

Dynamic Experimental Results

The two factors that influenced the study of the bushings dynamics were natural frequencies and noise. Natural frequencies are important in any dynamic system and the ability to predict these using ANSYS is a powerful tool. With the bushing setup as in Figure 6, the end of the shaft without the cap gage was gently tapped. The signal analyzer then output the natural frequencies of the shaft on the pressurized air film. The results are shown in Figure 11.

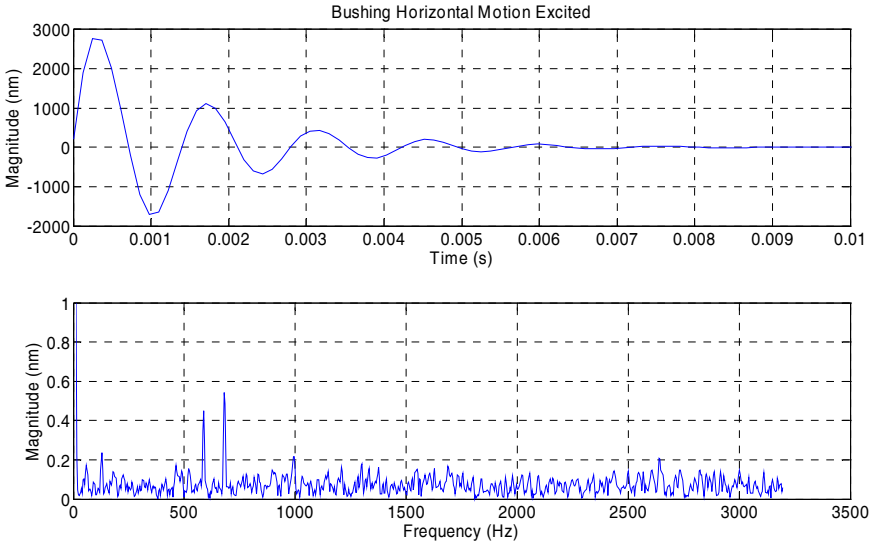

Figure 11. Dynamics of shaft in bushing after excitation.

From the time domain and frequency spectrum plots it can be seen that the first natural frequency of the bushing is at 680 Hz. Next, the ANSYS simulation is run with the equivalent pitch stiffness used to support the bearings to give a rigid body natural frequency of 700 Hz. This mode is a pitching mode which is the first mode that the cap gage would have detected also. These results support the use of the equivalent stiffness in ANSYS to predict natural frequencies.

The second reason for studying the dynamics of the bushing was to determine how much noise the porous type bearing induced compared to the current FLORA I. This experiment was the same as before except there was no tapping. A baseline recording of the shaft sitting in the bearing is shown in Figure 12.

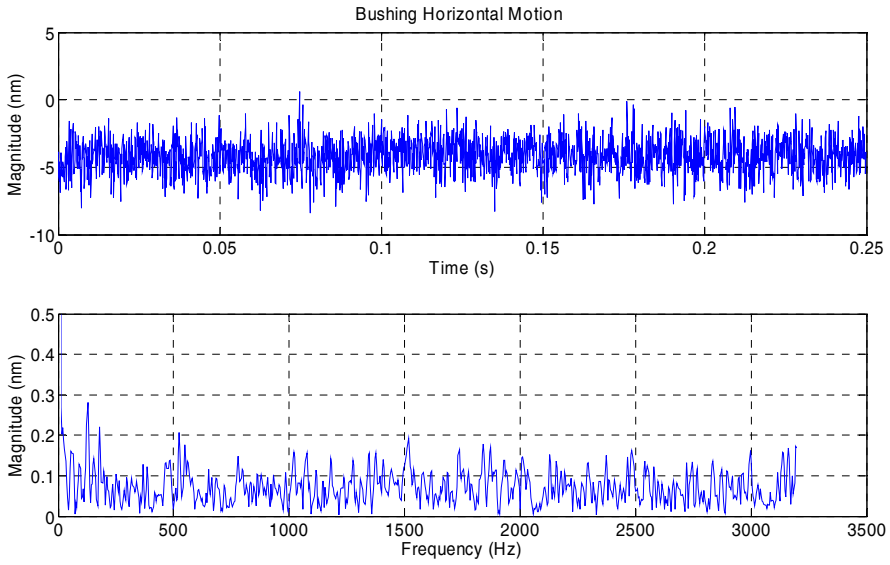

Figure 12. Busing noise with shaft at rest.

Figure 12 shows that the bushing has a total motion of 5 nm. This is most likely noise from the cap gage. FLORA I has a motion of ± 100nm which is significantly higher than the bushing. This finding reinforces the idea that porous air bearings are the right choice for use in FLORA II.

1.2.5 PISTON CROSS SECTION

After a method was derived for modeling the air bearings, the next task was to find a piston cross section. The cross section is important since it has an impact on the mass of the piston as well as its moment of inertia. A higher moment of inertia is desirable as to make the piston as stiff as possible. The cross section will also affect the bearing stiffness. Air bearings are stiffer as their projected area increases so a piston with more surface area has an opportunity for larger bearings and a higher stiffness.

After preliminary examination, three cross sections were chosen to compare. These cross sections were a box, triangle, and cross. Various simulations were run in ANSYS that were chosen to represent actual scenarios that the piston would encounter. All three cross sections were made into three pistons of equal length and mass to have as accurate a comparison as possible. After the simulations were run on all three pistons, was scored based on performance to help chose the superior cross section.

1.2.6 PISTON SIMULATION SCENARIOS

The first simulation that was run on the pistons was a static end load. This test simulates how much the piston would deform during cutting. A feature was modeled on the end face of each piston directly on the center of mass. This is where the 10 lb vertical load was applied on each. The elastic foundation was also applied to the piston, it was not cantilevered. Figure 13 shows the pistons in a deformed shape from this test.

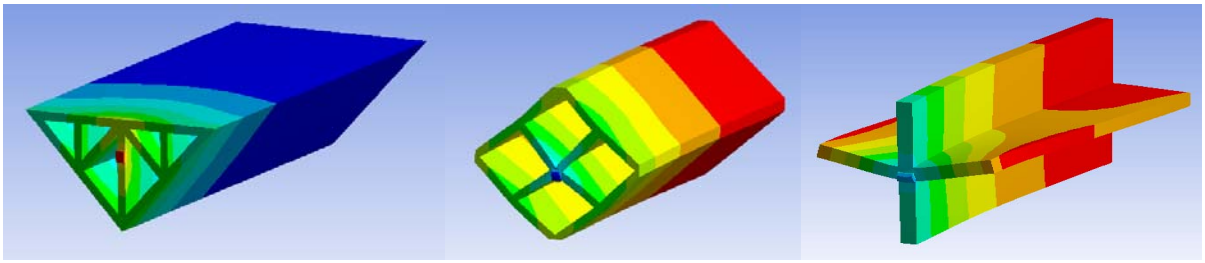

Figure 13. Deformed pistons after end load simulation.

The next test simulated the pressure that the air bearings apply to the piston. New Way states that the pressure that bearings apply on the piston will generally be half of the supply pressure. Since the bearings for FLORA II will be run at 80 psi, a pressure of 40 psi was applied to the bearing surfaces of the pistons. The amount and shape the pistons deflected determined scoring in this category.

The dynamics of the piston in the bearing are a significant part of the design. Therefore, the next two tests determined the first bending mode of each piston and the first rigid body mode of the piston on the elastic foundation. Bending modes were found by simply running a free-free modal analysis in ANSYS. Rigid body modes were found by applying an elastic foundation and running a modal analysis, just as with the bushing simulation.

Ease of assembly is an important factor to consider when designing any system. There were three major issues that had to be thought about for each piston. First was how many bearing faces had to be machined. To have a viable, precise system, each bearing face would have to be machined accurately relative to other bearing faces. The higher the number of bearings, the more difficult this would be. The second aspect was how to make the piston. Could the shape be extruded or would separate pieces have to be glued together? Finally, mounting the linear scale that determines the piston's position was considered. The scale is 20 mm wide and must be attached directly to one of the piston's outside surfaces with no overhang. These factors determined the score for the assembly category.

1.2.7 PISTON SELECTION RESULTS

Below, Table 1 shows the scoring results for each cross section. A score of 3 was given to the piston that had the best performance while a 1 was given to the worst.

Table 1. Results from Cross Section Simulations

Scenario	Triangle	Box	Cross
End Load	3	1	2
Pressure	1	2	3
Bending Mode	2	3	1
Rigid Body Mode	2	2	1
Assembly	3	2	1
Total	**11**	**10**	**8**

It can be seen from Table 1 that the triangular cross section is the most attractive. The box and the triangle had similar performance, but what separated the triangle was the assembly category. The triangle has one less surface to machine and the linear scale can be easily attached to the top surface. For these reasons the triangular cross section was chosen for FLORA II's piston. The current design for the piston calls for 70 mm length across the top of the piston and a depth of 150 mm.

1.2.8 PISTON MATERIAL

Choosing a material for the FLORA II's new piston influences its mass and stiffness. Steel is a very stiff material but it is too dense (more density, more mass) for the application. A stiff, lightweight material is optimal. Aluminum was also considered which is very lightweight but has only a fraction of the stiffness of steel. Aluminum is a good option, but to in order to get a high ratio of stiffness to density, composites were examined. After this study, one material that stood out was silicon carbide ceramic. Table 2 shows a comparison between steel, aluminum, and silicon carbide.

Table 2. Piston Material Comparison

Material	Modulus (GPa)	Density (kg/m^3)	Modulus/Density
Aluminum	70	2700	0.026
Steel	200	7900	0.025
Silicone Carbide	410	3150	0.132

It is clear that silicon carbide has a superior stiffness to mass ratio (5 times that of aluminum and steel) and that is why this material has been chosen for the FLORA II's piston.

1.2.9 FINAL PISTON DESIGN

As stated earlier a pressure of 40 psi can be expected on the portion of the piston surface on which the air bearings operate. This pressure will cause the piston to deform and the amount of deformation is a critical factor in the piston design. The first iteration of the triangular piston's cross section resembled a roof truss. This can be seen in Figure 14.

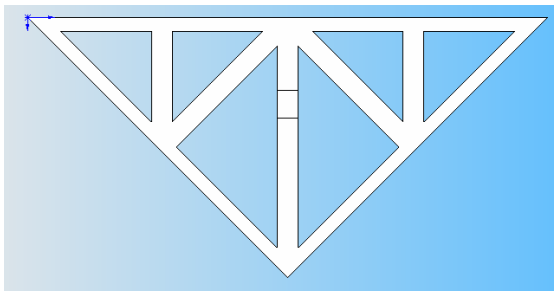

Figure 14. Cross section of original triangular piston.

The cross section shown in Figure 14 was extremely stiff in all directions under every loading scenario. It was concluded that this piston was overly stiff and some material could be removed to reduce weight. After consulting with Coors Tek, a manufacturer of silicon carbide parts, three orientations that could be manufactured while retaining the stiffing ribs were suggested. These three cross sections can be seen in Figure 15.

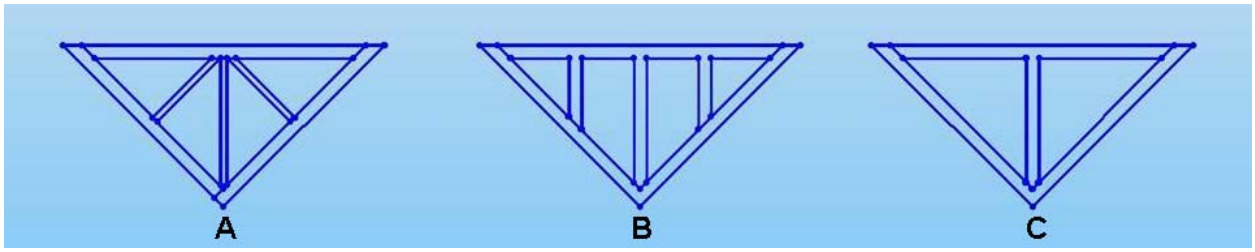

Figure 15. Possible cross section designs for FLORA II piston.

These cross sections were analyzed as pistons with a 150 mm length and material properties of silicone carbide. All pistons had a similar mass with piston A weighing 333 grams, piston B weighing 320 grams, and piston C weighing 317 grams. The difference between the lightest and heaviest piston is only 16 grams so weight is not an issue between the 3 arrangements. ANSYS

simulations showed that all three piston designs exhibit high stiffness when a vertical end load is applied. What separated the different arrangements was the application of the bearing pressure on the piston surfaces. Pistons B and C resisted deformation from the top well enough but the side loads proved to be too much and large deformations resulted. Piston A on the other hand resisted the bearing pressure well in all directions (see Figure 16). Cross section A was selected for the FLORA II piston. Figure 16 depicts the deformation of the piston under the 40 psi bearing pressure.

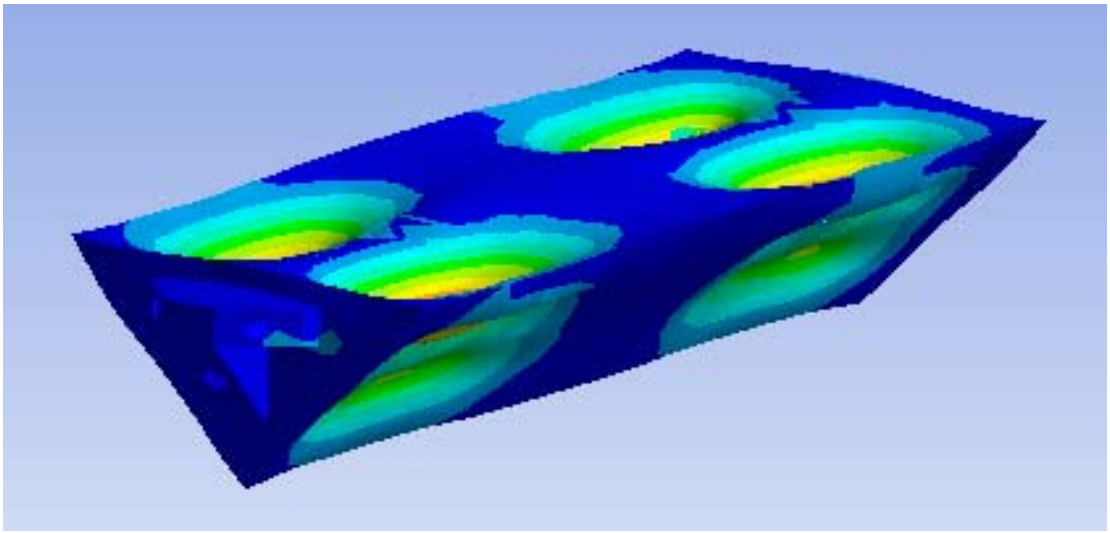

Figure 16. Deflection of piston with cross section 'A' under bearing pressure.

Since the piston will be assembled in pieces, the thickness of the individual pieces was optimized to provide a high stiffness while maintaining as light a structure as possible. Using ANSYS to perform this optimization yielded a top piece that was 3 mm thick, side pieces of 2 mm thickness, and support ribs 1.5 mm thick. The maximum displacement on the top horizontal is 0.5 μm halfway between the edge and the center support. This can be expected since this is the point furthest away from support. The sides experience a maximum displacement of 0.3 μm halfway between the edge and the side support for the same reason. These displacements must be taken into account when the housing is designed since the deflection of the piston, housing expansion, and glue shrinkage will all contribute to the air gap. Coors Tek then assembled the piston using a high modulus epoxy. An exploded image of these pieces can be seen in Figure 17 and the assembled piston is Figure 18.

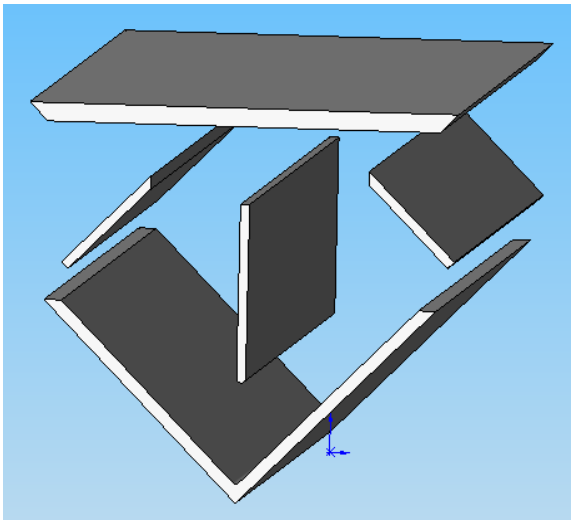

Figure 17. FLORA II piston pieces in exploded view.

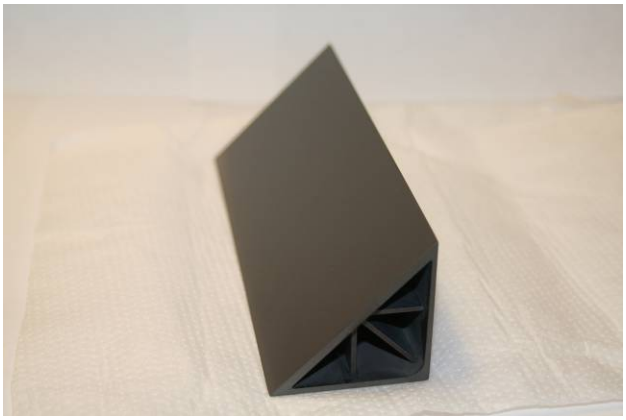

Figure 18. Actual FLORA II piston constructed by Coors Tek.

1.2.10 HOUSING DESIGN

The design of the FLORA II housing was a complex task that depended on many different effects. First of all, the housing must deform properly when the pressurized air is supplied to the bearings to allow the correct space for the air film. The housing must allow a clear path for plumbing to reach the air bearings. These tasks were completed while keeping the housing as compact as possible.

1.2.11 HOUSING EXPANSION

The design procedure of the FLORA II housing was different than the design of the FLORA I housing. The gap for the pressurized air film was machined out of the FLORA I housing before

the air pressure was supplied. This meant when the air pressure was turned on the piston had lift-off but the housing experienced minimal forces due to the bearings. It was discovered after conversations with New Way Air Bearings that this method results in a less stiff system. They suggested using the pressure from the air bearings on the piston to create the gap for the air film which would increase stiffness. The first model, seen in Figure 19, assumed that the two halves of the housing would be bonded together.

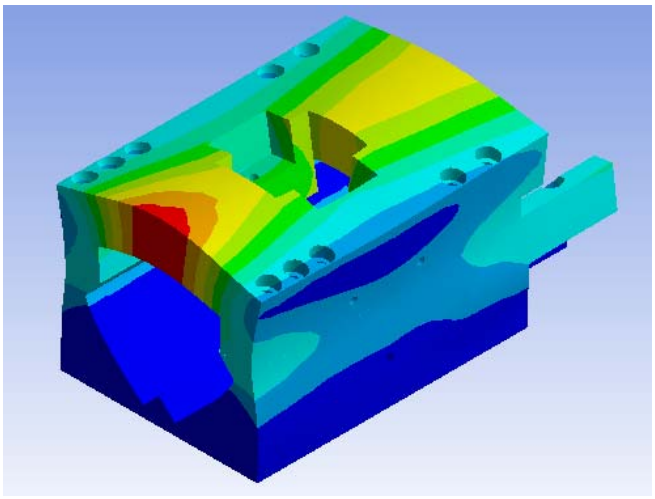

Figure 19. Original model of bonded housing deforming under bearing pressure.

It can be seen in Figure 19 that there is significant deformation in the housing with the maximum deflection being 5 µm on the center of the housing front. The deformation was not constant down the length of the housing which could cause unwanted motion or system failure. To correct for this material was removed from the top of the housing at an angle which allowed a uniform deformation along the housing's length. The altered housing top is seen in Figure 20.

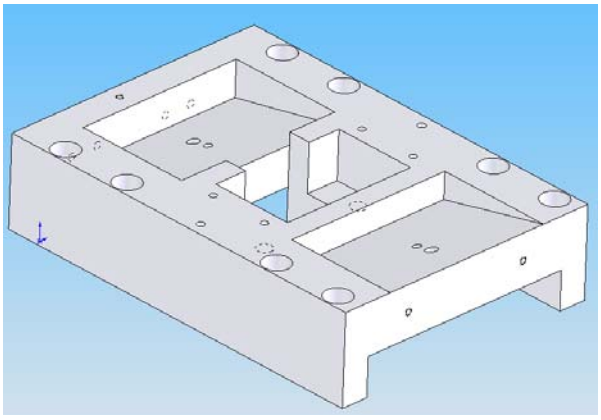

Figure 20. Housing top with removed material for uniform deformation along length.

The model previously described was not completely accurate because the housing top and bottom will be bolted instead of bonded. With the area of connection going from the entire interface between the housing top and bottom to just the bolts the new bolted model, Figure 21, was less stiff.

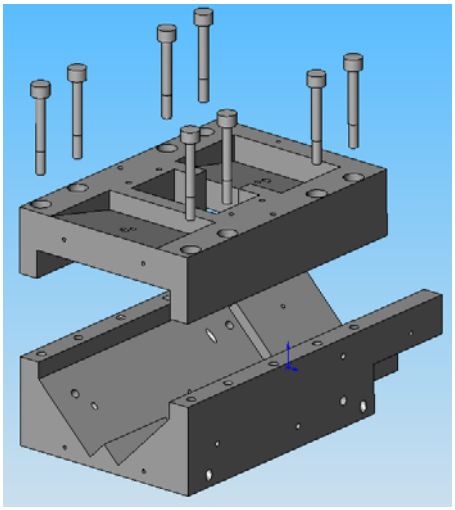

Figure 21. Complete model of FLORA II housing with bolts used to determine expansion.

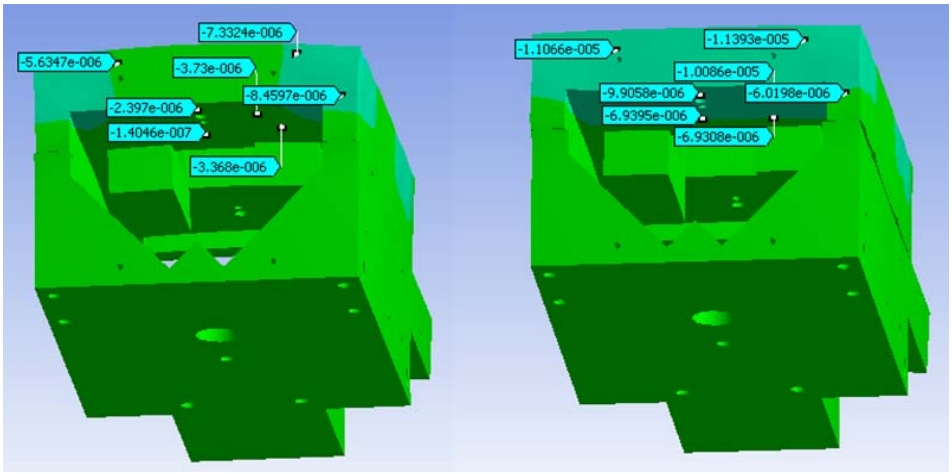

Figure 22. Housing with pretension bolts and applied pressure (left) and housing with only pretension bolts (right).

The bolted model, however, ignored a key feature that would significantly impact the actual behavior of the housing. When the housing is bolted together, the bolts will have a pretension based on the tightening torque. ANSYS FEA software has a bolt pretension load type which was used to simulate the tightened bolts. The simulation was run once again with appropriate contact surfaces and types specified. Figure 22 shows the results (in meters) for both the deflection of

the housing with just the pretension and with the pretension and the 40 psi pressure. The difference between the two cases is the expected deformation.

A pretension of 7220 N was found to be a common force for the specific bolt torque. Taking the difference between the center values from both housings in Figure 22 yields a deflection of 7.5 μm. As stated previously the piston will deform 0.5 μm and the glue used to pot the air bearings will shrink 2 μm making the entire deflection 10 μm. This total deflection is sufficient to sustain an optimum pressurized air film.

1.3 CONCLUSIONS

Machining NRS surfaces has traditionally required a long machining time due to slow spindle speeds. The FLORA II is a fast tool servo that is designed to operate at a stroke of ± 2 mm and 20 Hz vastly improving production of free form optics. This paper has described using finite element analysis software to simulate the performance of a new design. It has been proven through experimental verification that the equivalent foundation stiffnesses derived properly mimic the physical air bearings. The amount of noise in porous air bearings has also been shown to be much less than in the orifice type air bearings found on the FLORA I. A triangular cross section has been chosen for the piston based on a series of simulated tests. The material for the piston, silicon carbide, ensures that the piston will be very stiff while achieving a low mass. The deformation of the piston coupled with the expansion of the housing and shrinkage of glue will allow a proper thickness for the pressurized air film. These findings have led into a new design for the FLORA II that will produce optical quality NRS surfaces while reducing the size and mass of the FLORA I significantly.

ACKNOWLEDGEMENT

This project was supported by NSF contract CMMI-0556209 monitored by George Hazelrigg.

REFERENCES

1. New Way Air Bearings. Aston, Pennsylvania, http://www.newwayairbearings.com/

2 POLARIS MECHANICAL DESIGN AND ALIGNMENT PROCEDURES

Alex Sohn
Precision Engineering Center Staff

Polaris 3D is an evolution of the original two-dimensional polar profilometer Polaris. The expansion to true three-dimensional measurement in a spherical coordinate system using a non-contacting probe presents a number of design challenges. Foremost of these challenges is the mounting of two additional stacked axes and provisions for adjusting these axes relative to the existing ones. Additionally, the inclusion of an air-actuated collet chuck means the modification of a standard air-bearing table to accept a rotary non-influencing coupling. The final design is presented with descriptions of the components, their functions and the alignment procedures needed to assemble the system.

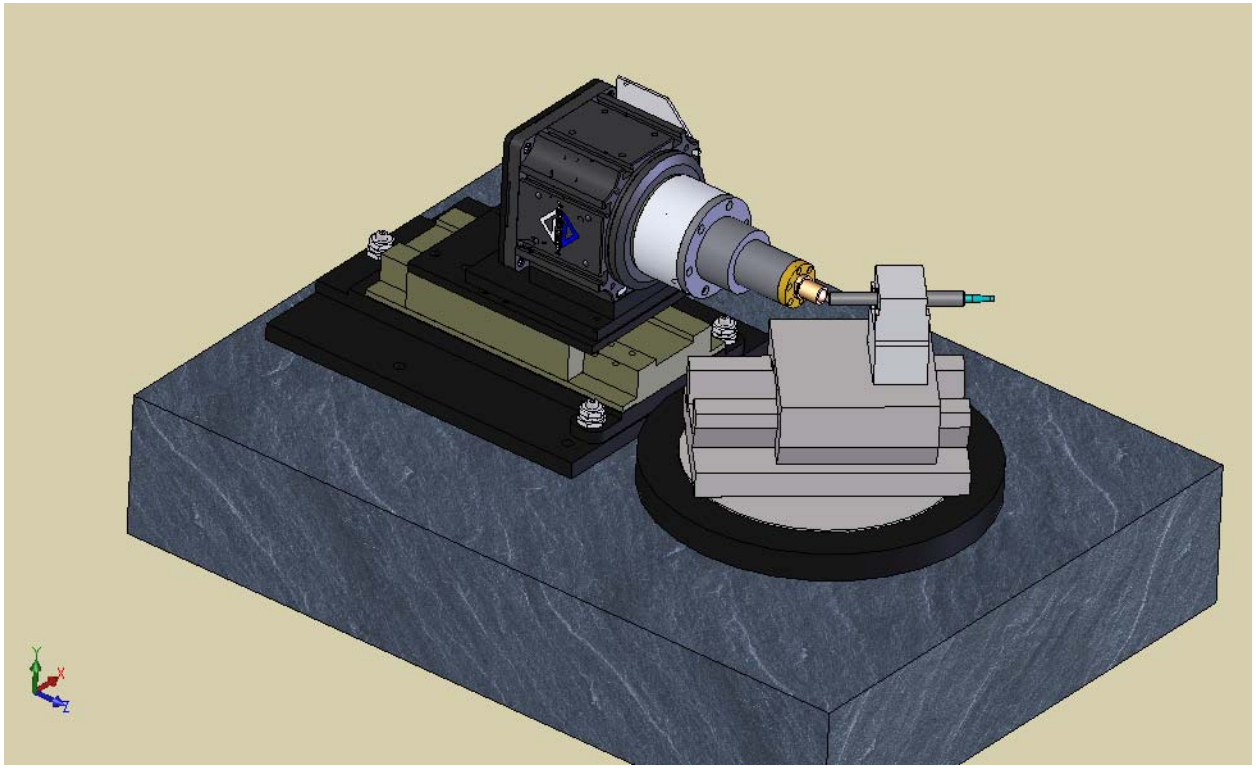

2.1 INTRODUCTION

The capabilities of the polar profilometer (Polaris) [1] are being extended by the addition of an optical probe and more axes to allow non-contact 3D measurement of highly aspheric and non-rotationally symmetric surfaces. The spherical coordinate-based measurement environment is produced by a unique arrangement of axes as shown in Figure 1. The R, θ and ϕ axes form the spherical coordinate axes while the Z-axis positions the part at the appropriate location to allow the probe to measure the surface with a minimum of angular deviation from normal incidence. With this arrangement, surfaces with very large sags including hemispheres can be measured. Critical to accurate measurement, however, is alignment of the axes relative to each other to form an arrangement as close as possible to an ideal spherical coordinate system.

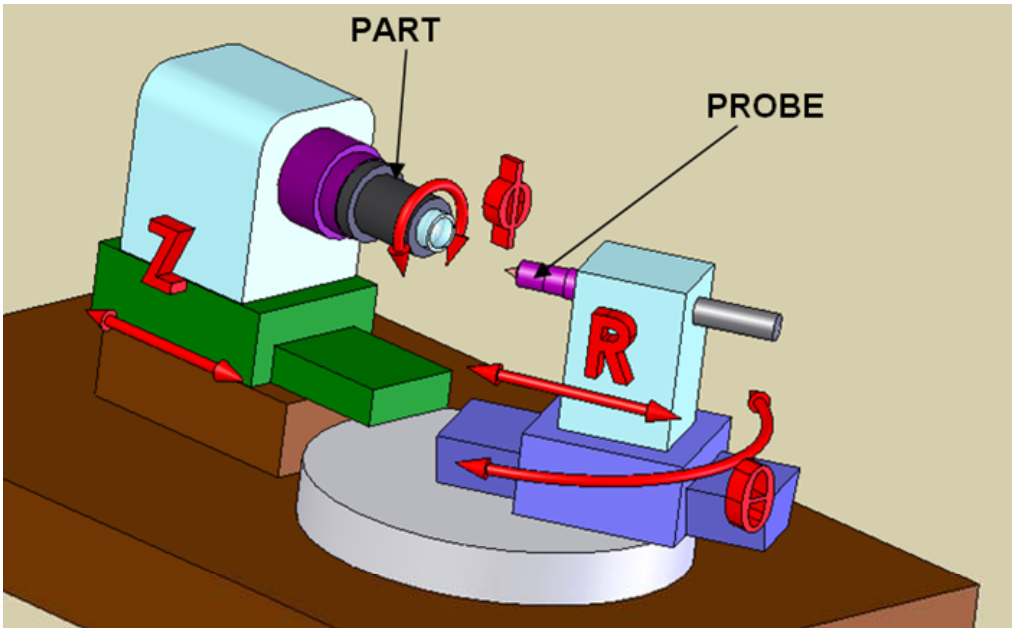

Figure 1. Schematic Layout of machine axes

2.2 OPTICAL PROBE

The optical probe used in the 3D Polaris works on the principle of chromatic aberration for distance measurement. Chromatic aberration is normally an undesirable defect in optical systems that causes light of different wavelengths to be focused a different distance from the lens as shown in Figure 2. The reason for this effect is that dispersion rates in most materials vary somewhat with wavelength - longer wavelengths are refracted less than shorter wavelengths. As shown in Figure 2, the probe focuses white light into a spot. The reflected light s then collected by the probe and sent to a spectrometer. The distance at which the light is focused depends upon wavelength or color since the lens is designed to display a certain degree of chromatic aberration.

The spectrometer thus sees a peak in reflectance at a wavelength that varies as a function of distance.

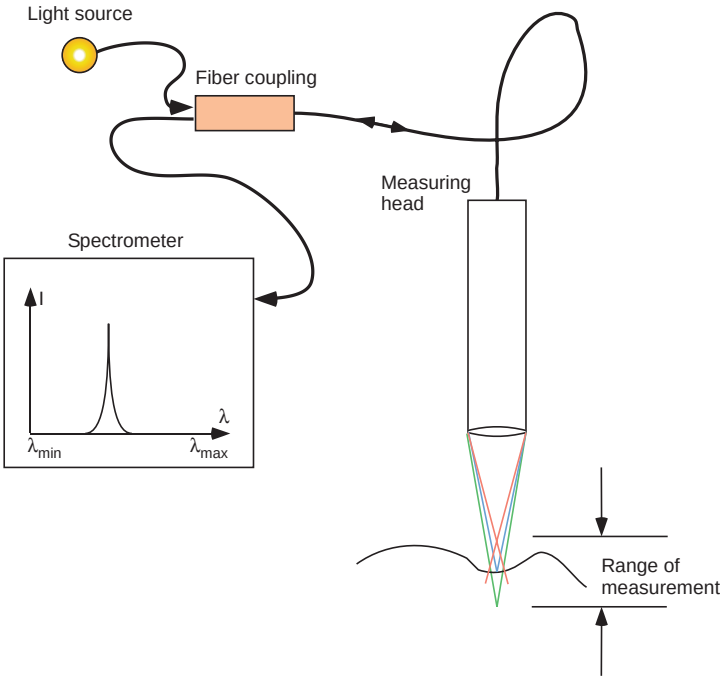

Figure 2. Light of different wavelengths has varying focal lengths when chromatic aberration is present [3].

One significant advantage of the chromatic aberration probe is that the frequency component of the reflected light changes very little as a function of angle of incidence. This allows the probe to operate even when it is not normal to the surface being measured. Given the aforementioned characteristics and the capability to operate at 1 kHz, a CA probe manufactured by Stil S.A. has been obtained by the PEC and will be tested on the Polaris system. The model chosen has a 300 µm displacement range and ±25º angular range. Spot size is on the order of 7 µm, so lateral resolution is somewhat limited, though substantially better than most interferometers used for figure measurement.

2.3 MACHINE DESIGN

The Polaris 2D had a polar coordinate system with a stationary part and a probe mounted on a linear axis that is supported by a rotary axis. The linear axis (R) was specially designed by Precitech with a dovetail slide having a range of 70 mm, a linear motor and an encoder with 20 nm resolution. The rotary slide (θ) is a standard 270 mm diameter air-bearing from Precitech driven by an Aerotech brushless direct drive motor and a high-resolution (1.8 µrad) Heidenhain optical encoder. Two additional measurement axes are added to extend operation to three dimensions. As shown in Figure 3, the θ and R axes used in the 2D version of polaris are to be

supplemented with a φ and Z axis. Both axes are air-bearing brushless motor driven axes with high-resolution encoder feedback. The models chosen are manufactured by Aerotech with the Z-axis having a linear range of 100 mm with 20 nm position resolution and the φ axis having a resolution of 0.026 arcsec. The Z-axis is not considered a measurement axis since it is to remain stationary during measurement, but its straightness is considered critical to maintain the correct relationship between the measurement axes, φ, θ and R. This may change; however, as experience with these axes is gained because moving Z during the measurement can be used to keep the optical probe within its angular range.

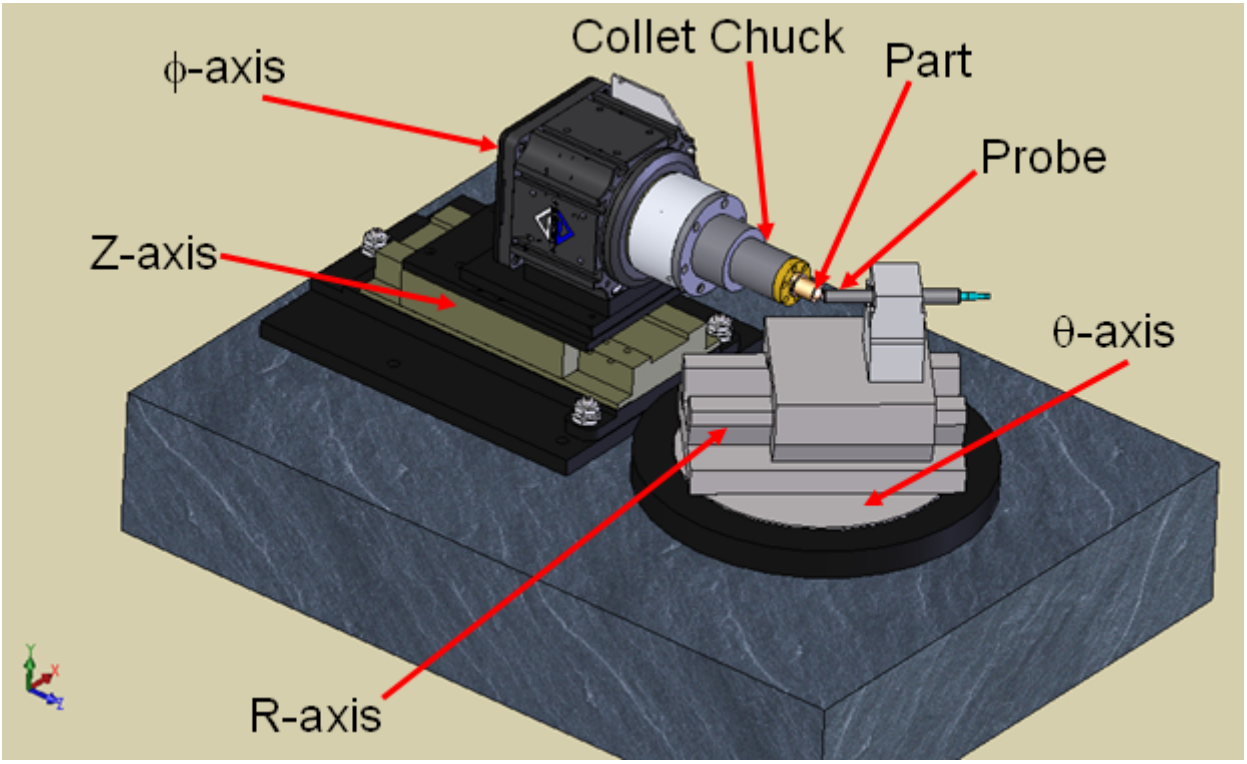

Figure 3. Axis Layout of final polaris version showing new φ and Z axes and location of optical probe.

2.3.1 AXIS SELECTION AND MOUNTING

The new machine axes have been chosen and mountings designed to meet several requirements. The linear Z-axis was mainly chosen for its travel (100 mm) and load capacity. The combination of the rotary φ axis, mounting plates and part chuck have a combined mass of 10 kg, well within the stated 15 kg load capacity of the Aerotech ABL-1000 air-bearing stage. The φ axis is mounted horizontally so the load requirements for this axis are based on a moment due to the cantilevered load of the part chuck and part. Given a mass of 1.8 kg for the part chuck, and a distance of 113 mm from the spindle air bearing center to the chuck center of mass, the moment is approximately 2 N-m, well below the specified 3.5 N-m tilt load limit of the Aerotech ABRT-

150 unit selected. In addition to load requirements, straightness, angular errors and roundness specifications were also important.

The mounting plates are designed to place the φ-axis spindle at the height of the probe focus with the axis adjusters halfway through their adjustment range. The mounting plates also locate the spindle correctly in the Z-direction to allow use of the full measurement range and also locate a typical part surface over the θ-axis center of rotation with the Z-axis at the center of its range of motion .

2.3.2 AXIS ALIGNMENT ADJUSTERS

For proper operation, optimal alignment of the Z- and ϕ-axes to each other and to the other axes of the machine is of the utmost importance. To facilitate this alignment, six screw adjusters,

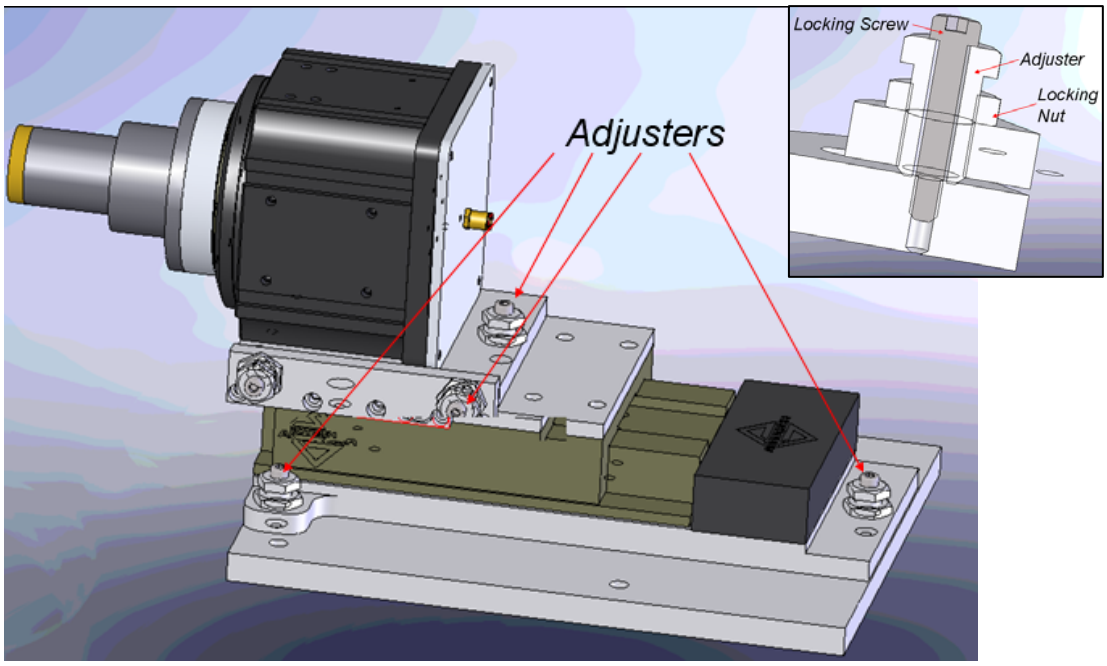

Figure 4. ϕ/Z sub-assembly with axis adjusters. Inset shows locking mechanism for adjuster bolts which are threaded for 0.794 mm/turn adjustment.

shown in Figure 4 are employed. These adjusters allow the Z- and ϕ-axes to be translated and rotated in the relevant directions to allow proper alignment as described in Section 2.4. The adjusters consist of:

1. a 5/8”-32 TPI adjuster screw which allows fine adjustments of 0.794 mm per turn,
2. a locking screw that preloads the adjuster screw against the stationary base and
3. a locking nut that preloads the threads of the adjuster screw against the moving plate to take up play in the screw threads and prevent movement if loads change.

2.3.3 PART HOLDING

All parts to be measured on Polaris 3D are to be held on the ϕ-axis spindle using a 12.7 mm mounting stud. An air-actuated ER collet chuck both locates the stud radially and pulls the part against the diamond-turned face of the chuck to ensure good alignment. Two challenges exist in this design: first, air must be brought to the rear of the collet chuck without influencing the air bearing spindle of the ϕ-axis and, second, the chuck face must rotate normal to the spindle axis. Complicating the former is that air from the spindles air bearings is exhausted through the hollow center of the spindle. In order not to disturb this air exhaust, a nylon pressure tube is held at either end of the rotating portion of the spindle with the a central hole in the chuck adapter and a mounting flange with exhaust holes to vent bearing air as shown in Figure 5. The rotating pressure tube is positioned to within 25 µm of the stationary rear cover by the initial placement

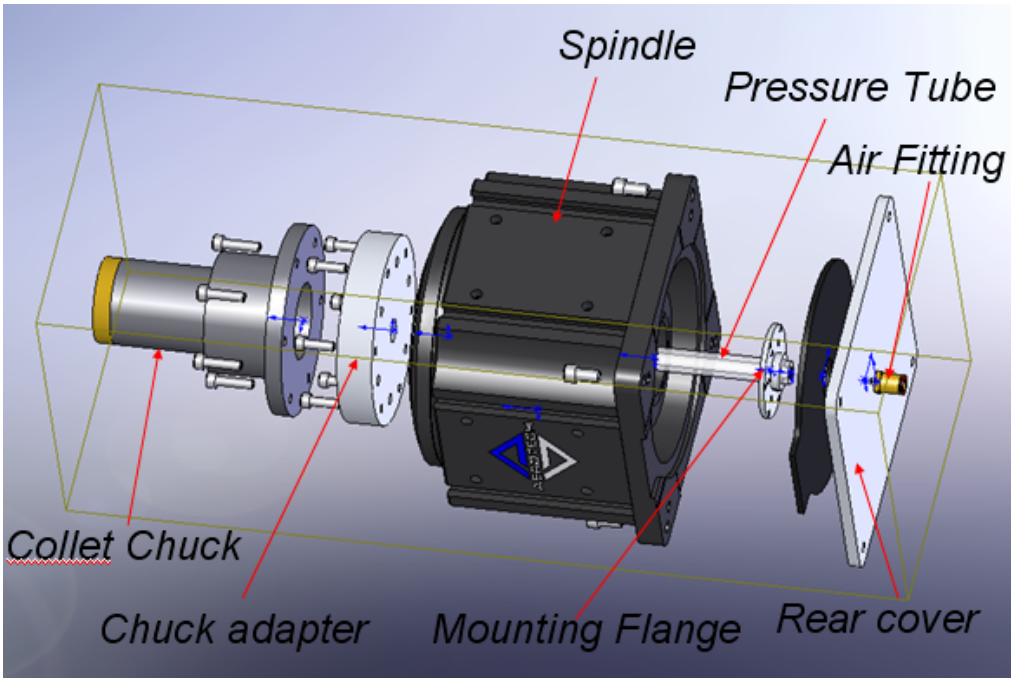

Figure 5. Exploded view of φ-axis assembly with air-actuated collet chuck. The nylon pressure tube has a 25 µm clearance to the rear cover to allow for a non-influencing air coupling with minimal loss of pressure.

of a shim between the two when the cover plate is attached. This positions the air tube, which can then be locked in place with a set screw after the cover is removed to eliminate the shim. An adequate clearance is thus set to where the coupling provides enough clearance for air bearing exhaust yet allows actuation of the collet chuck. Parallelism of the face of the chuck is maintained by diamond turning both the chuck adapter and the face of the chuck on the ASG 2500 diamond turning machine.

2.4 MACHINE ASSEMBLY

Components were assembled with special attention to the flatness of support plates attached to the Z-axis to prevent distorting the air-bearing. Screw torques were set to 8 N-m (6 lb-ft) for 1/4"-20 screws and 5.5 N-m (4 lb-ft) for M5 screws. These torques were chosen to minimize distortion yet still provide more than adequate holding force. The stainless steel adjuster bolts and nuts were lubricated to prevent galling. Adjustments for aligning the axes are performed in a specific sequence:

1. ρ-alignment of probe to θ-axis origin
2. τ- alignment of probe to θ-axis origin
3. R/Z parallelism in y and x
4. ϕ/θ-alignment (in the x-direction)
5. ϕ /Z-parallelism in the x- and y-directions
6. ϕ-axis origin to probe y- alignment
7. R/ρ parallelism in y and θ

The alignment sequence is designed such that adjustment of one misalignment has a minimal impact on other misalignments. However, the entire procedure should be repeated to assure alignment errors are within acceptable limits.

2.4.1 ρ-ALIGNMENT OF PROBE TO θ-AXIS ORIGIN

Before any measurements are made, the origin of the machine's measurement axes (R and θ) must be aligned with the probe. The primary criterion for this alignment is that the probe output be constant $\rho = 0$ (set at probe output of 5V, midrange) for all positions of θ. This means that the probe should have a constant output of 0 μm (5V) for all positions of θ if the focus is positioned with its center at $\rho = 0$.

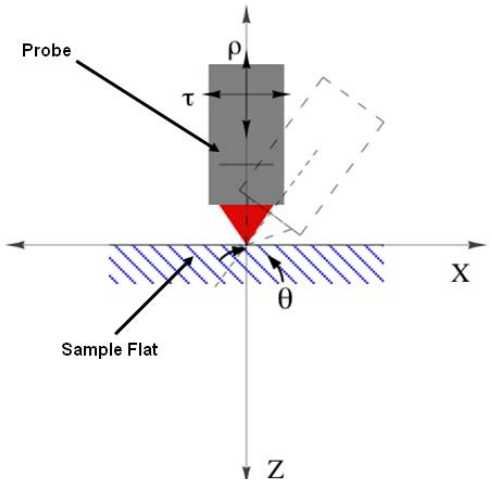

Figure 6. When the focus of the optical probe coincides with the θ-axis origin, the output remains constant as it rotates

Measurement

One means of achieving this is by placing a flat plate at zero as shown in Figure 6. If the probe is truly centered, the probe output will not change as θ is traversed from –20° to 20°. If, however, there is an offset in either the ρ or τ- directions, the probe output will change in a characteristic way for each direction.

For an offset of ρ_0 in the ρ-direction, the output of the LVDT will change as a function of the rotary axis position θ as shown in Figure 7 and by Equation (1):

$$\rho = \rho_0\left(\frac{1}{\cos\theta} - 1\right). \quad (1)$$

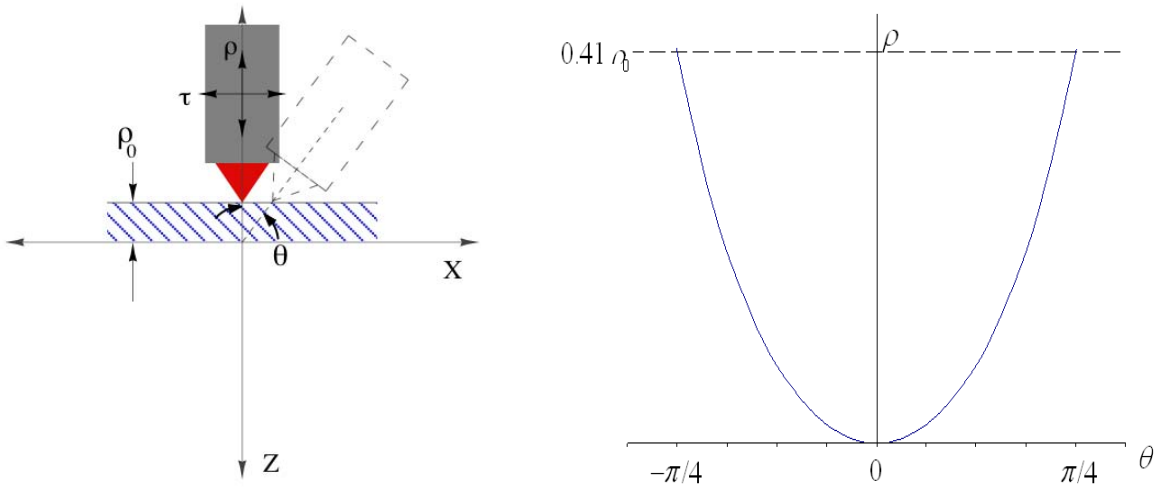

Figure 7. Schematic representation when probe focus is not rotating about the θ-axis origin and the resultant error produced by an offset in the ρ-direction (ρ_0)

Adjustment

When an origin measurement is made and the ρ-offset is measured, the *R*-axis zero can be reset to eliminate the offset.

2.4.2 τ- ALIGNMENT OF PROBE TO θ-AXIS ORIGIN

In addition to ρ-offsets, there can be an offset in the τ-direction. This offset produces a different response when measured using the flat method. As shown in Figure 8, the response of the LVDT as a function of θ that can be written:

$$\rho = \tau_0(\tan\theta). \quad (2)$$

Measurement

Currently, the probe alignment process for both ρ-offsets and τ-offset is performed via an automated routine. A diamond-turned flat is then placed on the ϕ-axis chuck and Z is jogged toward the probe with probe following engaged until the R-axis follows Z. The Z-axis is then

moved to position the probe at the first guess for the origin. The calibration routine then moves the probe to θ=20º, 0º and -20º, each time collecting position data when it arrives at its position. These three points are then fit to Equations (1) and (2) and values for ρ_0 and τ_0 are calculated.

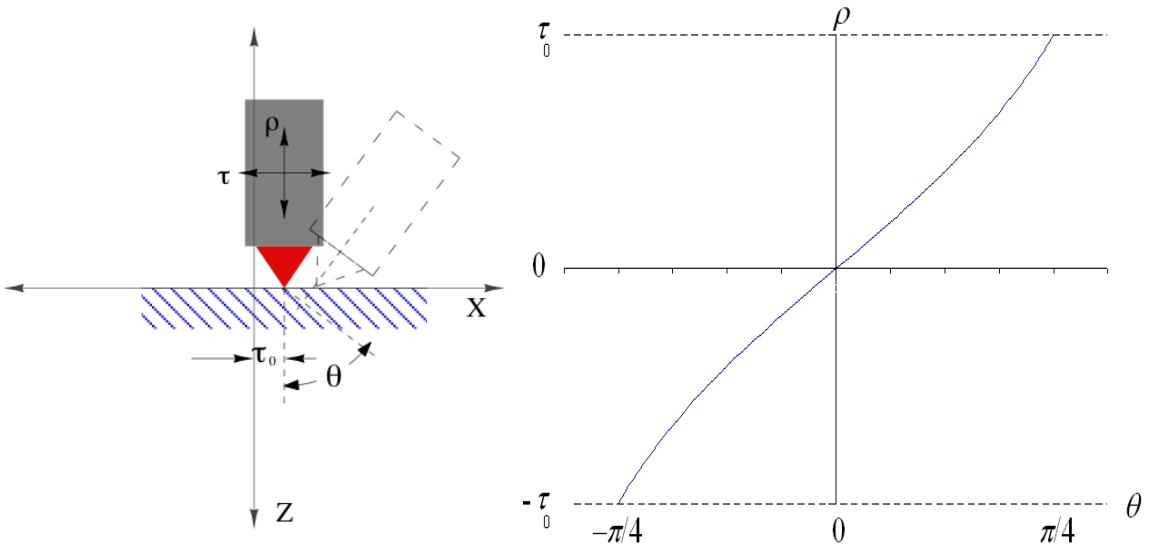

Figure 8. Schematic representation when probe focus is not rotating about the θ-axis origin and the resultant error produced by an offset in the τ-direction (τ_0)

Adjustment

To adjust τ_0 a fine-pitch adjuster screw is rotated on the right side of the probe mount. It is useful to place an electronic indicator against the mount to measure the exact amount that the probe is moved.

2.4.3 R/Z PARALLELISM IN Y AND X

Alignment between the R and Z axes is critical because a lack of parallelism would essentially make the above ρ- and τ-alignments invalid everywhere except for the R and Z-positions where they were measured. It is therefore important that these alignments be properly performed.

R/Z parallelism in the y direction

Figure 9 illustrates R/Z parallelism in the y-direction while Figure 10 shows the measurement of this error using a Zerodur bar in the R axis with capacitance gages on the Z axis. Correction is made with the adjustment screw at the back of the Z axis mount.

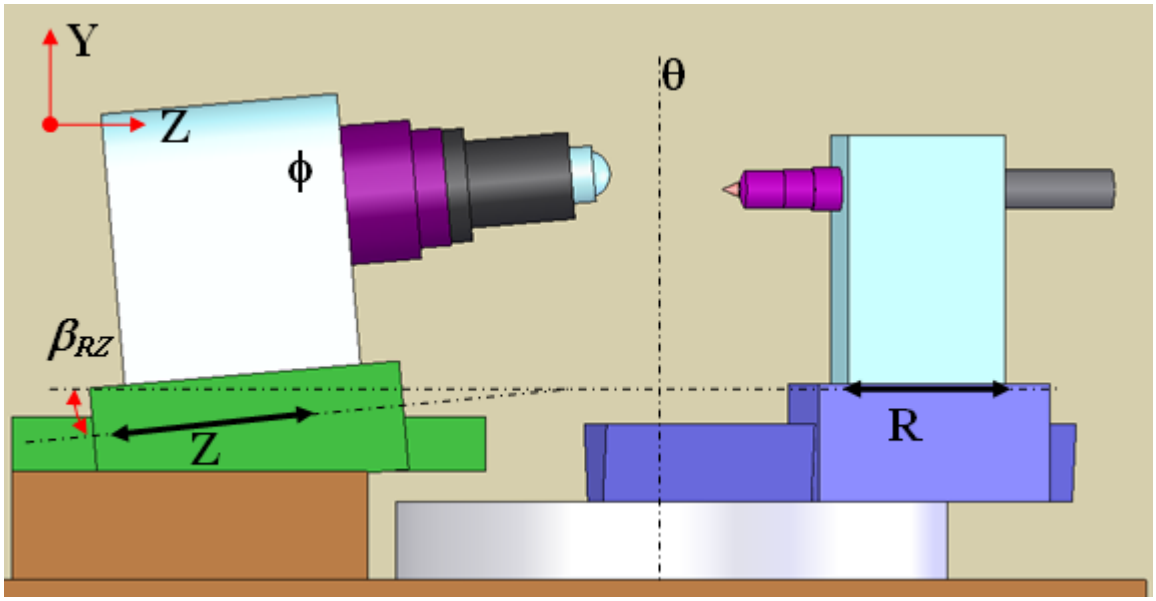

Figure 9. Illustration of R/Z parallelism in the y-direction. As the two axes move, the vertical distance between them changes as a function of the angle between them.

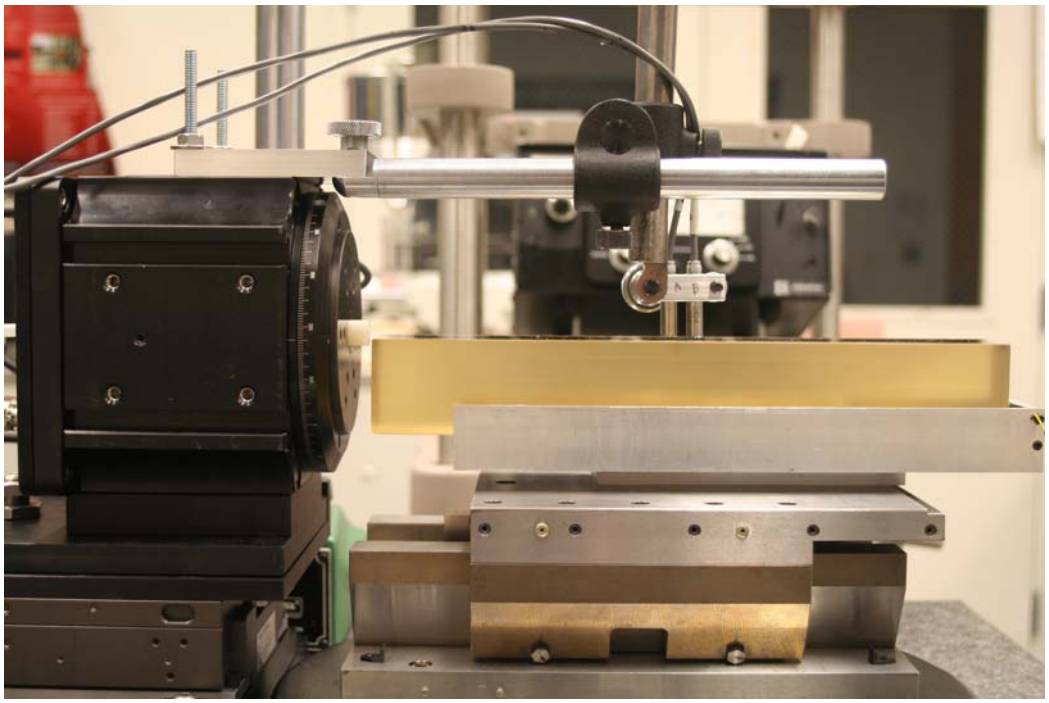

Figure 10. Measurement of R/Z parallelism in the y-direction. This error is eliminated by tilting the Z axis around the x axis to make it parallel to the R axis motion.

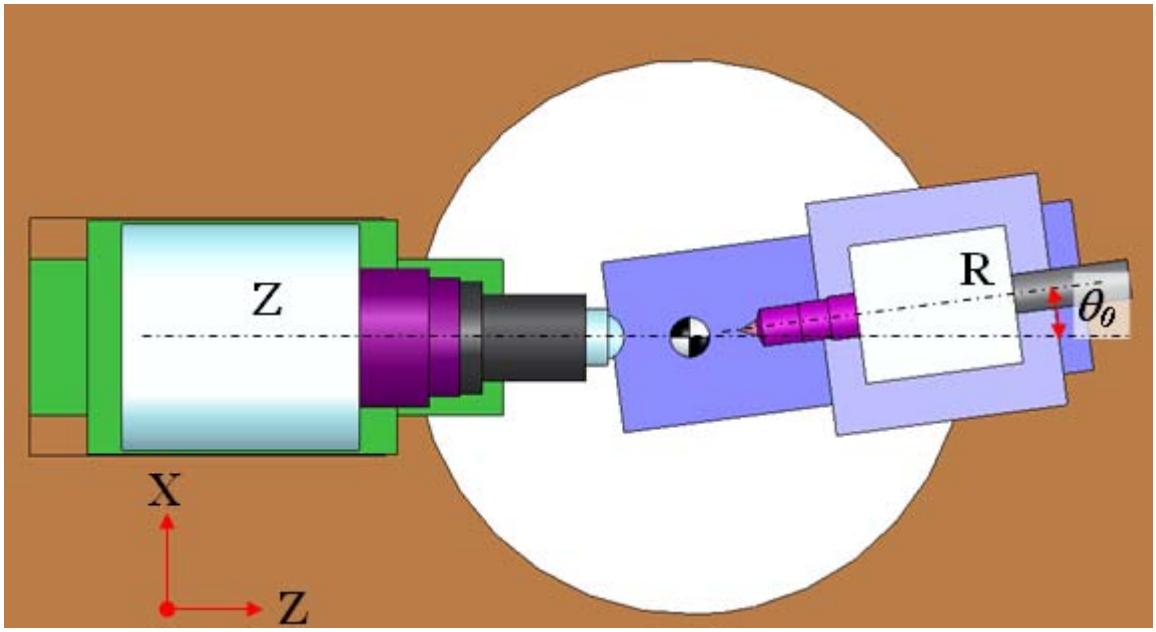

Figure 11. Illustration of R/Z parallelism in the x-direction. As the two axes move, the horizontal distance between them changes as a function of the angle (θ_0) between them.

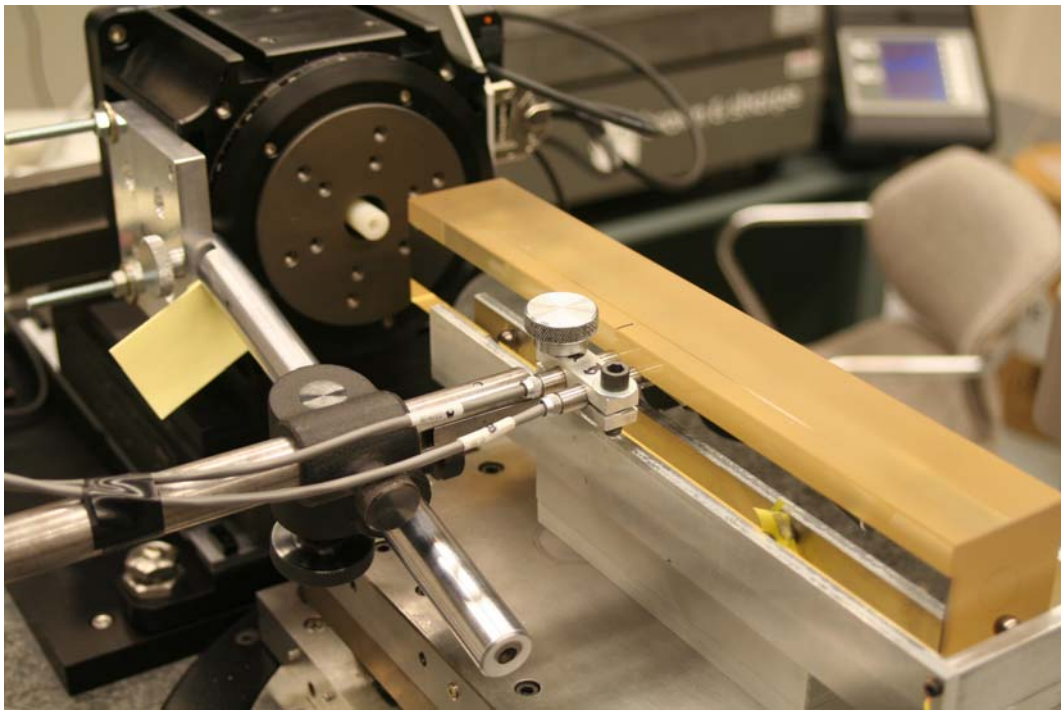

Figure 12. Measurement of R/Z parallelism in the x-direction. The cap probe is mounted to the Z slide with the reference bar on the R slide. When they are parallel, the θ_0 is set to zero.

Adjustment

Adjustment of R/Z parallelism in the y-direction is performed via the adjuster at the rear of the Z-axis base as shown in Figure 13. Since the offset between the adjuster and the pivot at the front adjusters is 325 mm, each turn of the adjuster screw represents about 0.14º or 1.5 milliradians. After each adjustment, the parallelism should be re-measured and repeated until the error is minimized.

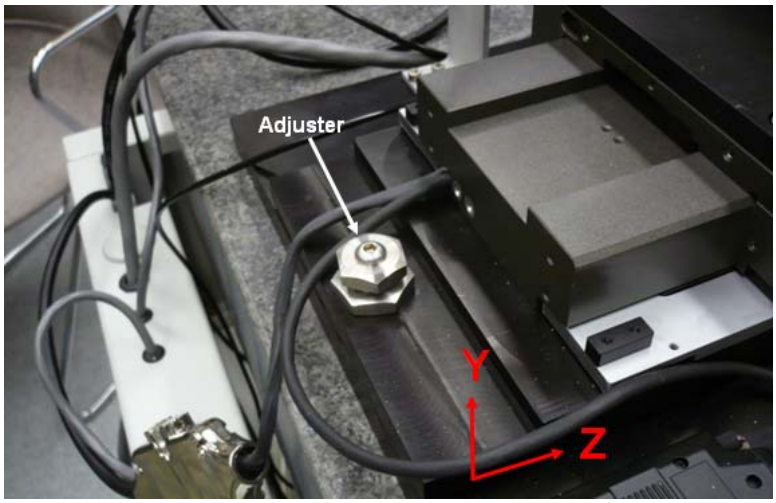

Figure 13. Adjustment of R/Z parallelism in the y-direction is performed via the single adjuster at the rear of the Z-axis base plate.

Adjustment of R/Z parallelism in the x-direction simply requires re-setting the θ_0 position in the controller, though when adjustment is complete, the zero point must be saved to the controller configuration so that this new zero point will be used again when the machine is re-started.

2.4.4 ϕ/θ-ALIGNMENT (IN THE X-DIRECTION)

Once the R/Z parallelism is set, the spindles must be aligned so that their axes intersect. When they do not intersect, an error $e_{x\phi}$ is generated as shown in Figure 14.

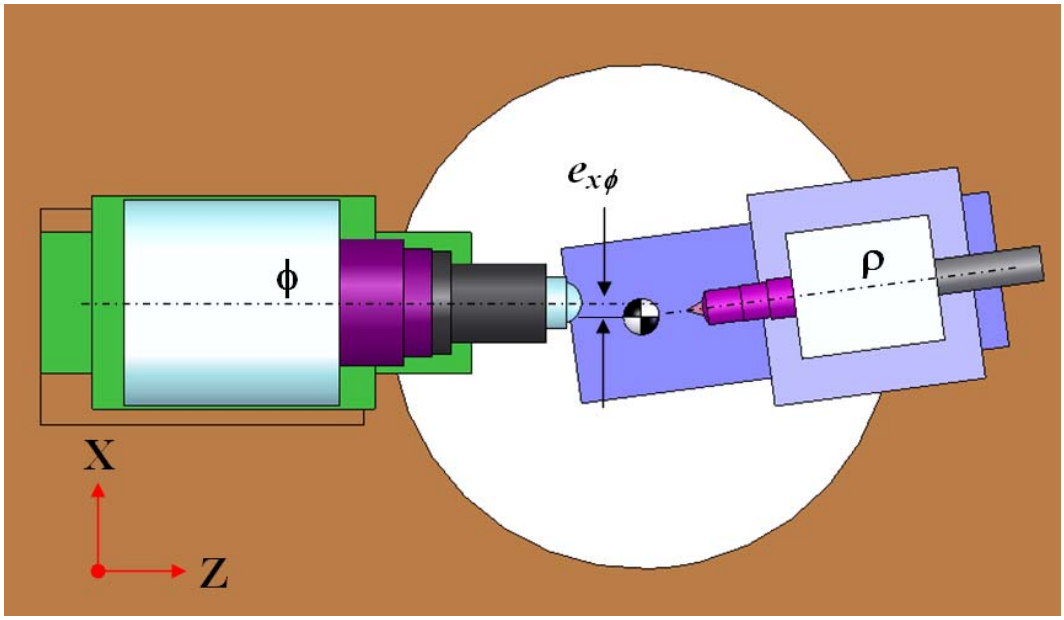

Figure 14. Illustration of alignment error $e_{x\phi}$ between the ϕ-axis and the θ-axis.

Measurement

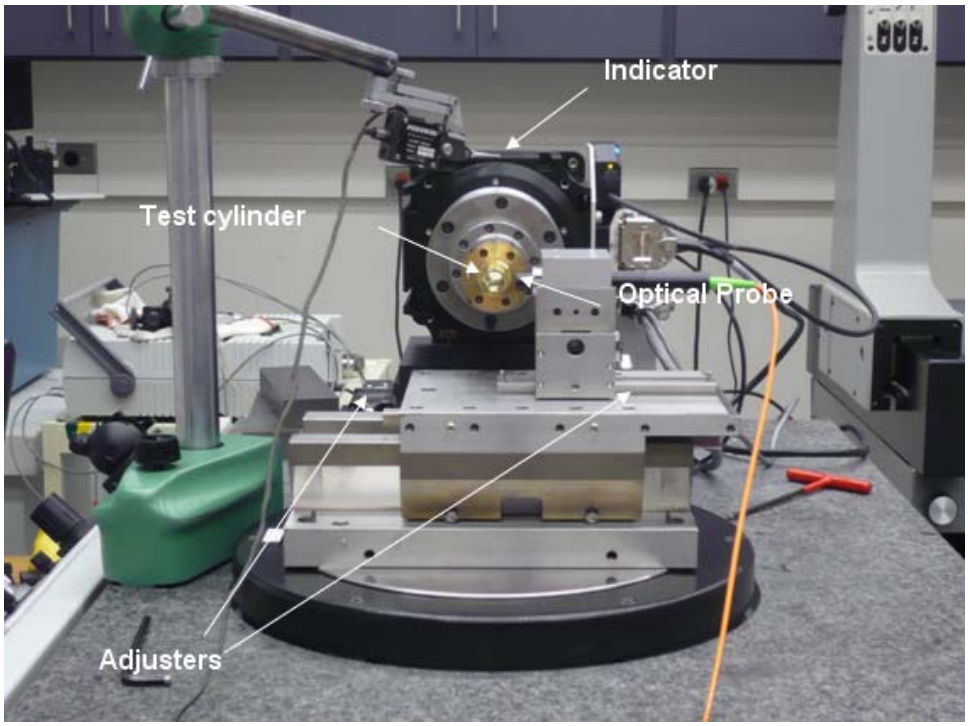

Figure 15. Illustration of the ϕ/θ-alignment error adjustment. Indicator is placed at center top of ϕ-axis spindle to ensure that the two indicated adjusters produce only motion in the x-direction.

Measurement of ϕ/θ-alignment can be carried out in conjunction with ϕ /Z-parallelism in the x-direction and is described in section 2.3.5.

Adjustment

Adjustment of the ϕ/θ-alignment requires moving the ϕ-spindle in the x-direction. This is best achieved by differential adjustment of the two front adjusters on the Z-axis base plate as shown in Figure 15. To be certain that the differential adjustment produces only x-direction displacement, an electronic indicator is place at the center top of the ϕ-spindle in line with the adjusters. Before beginning adjustment, the indicator is zeroed and at the end of adjustment brought back to zero with the adjusters. Displacement in the x-direction is measured with the optical probe.

Impact on sphere measurement

Any ϕ/θ-misalignment produces an ogive error but no real radius error. The base radius of the measured hemisphere, however, will be increased or reduced by the magnitude of the alignment error. Also, there will be a disparity between the +θ and -θ measurement. Each measurement produces a positive and negative ogive error as shown in Figure 16.

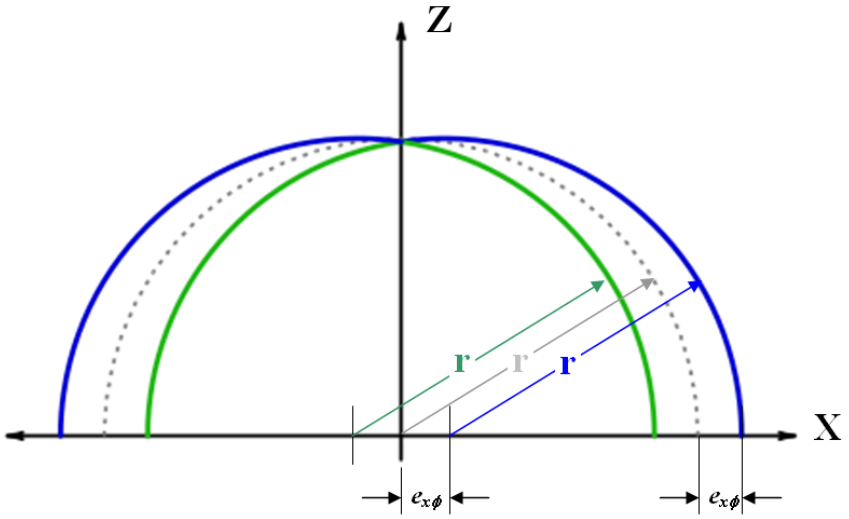

Figure 16. Example of a sphere measured with ϕ/θ-alignment error. Note that measuring on the negative x-side produces one ogive error and measurement on the positive side produces the opposite ogive error.

2.4.5 ϕ /Z-PARALLELISM IN THE X- AND Y-DIRECTIONS

ϕ /Z-parallelism in the x and y-direction will cause both ϕ/θ-alignment and ϕ/probe-alignment to change depending on where the part is mounted on the spindle i.e. a long part would see a larger

error than a short part. Both errors are illustrated in Figures 17 and 18.

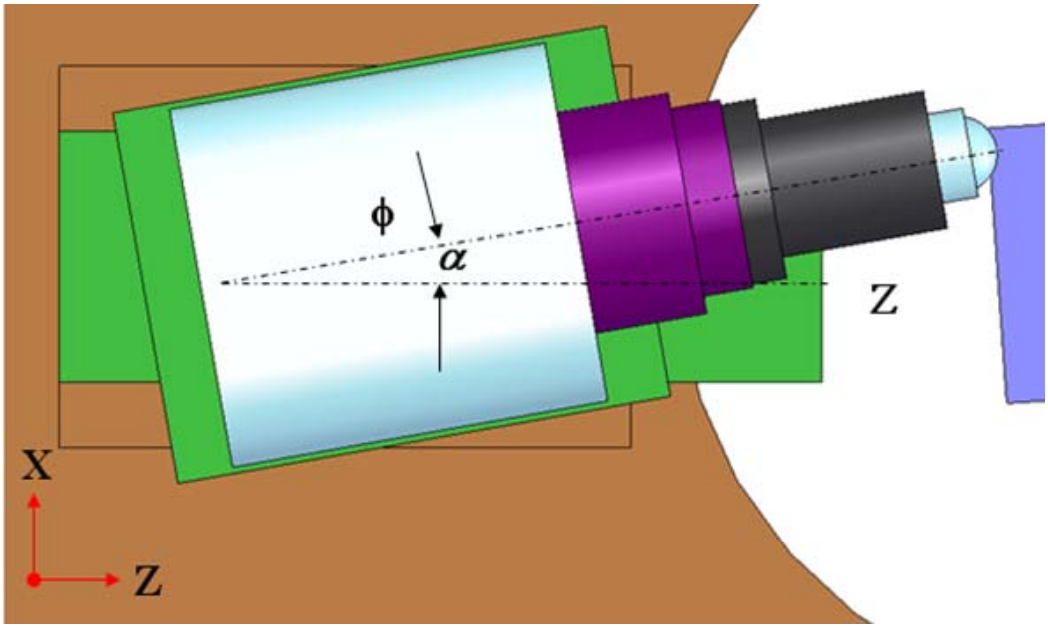

Figure 17. Illustration of alignment error α between the ϕ-axis and the Z-axis in the x-direction.

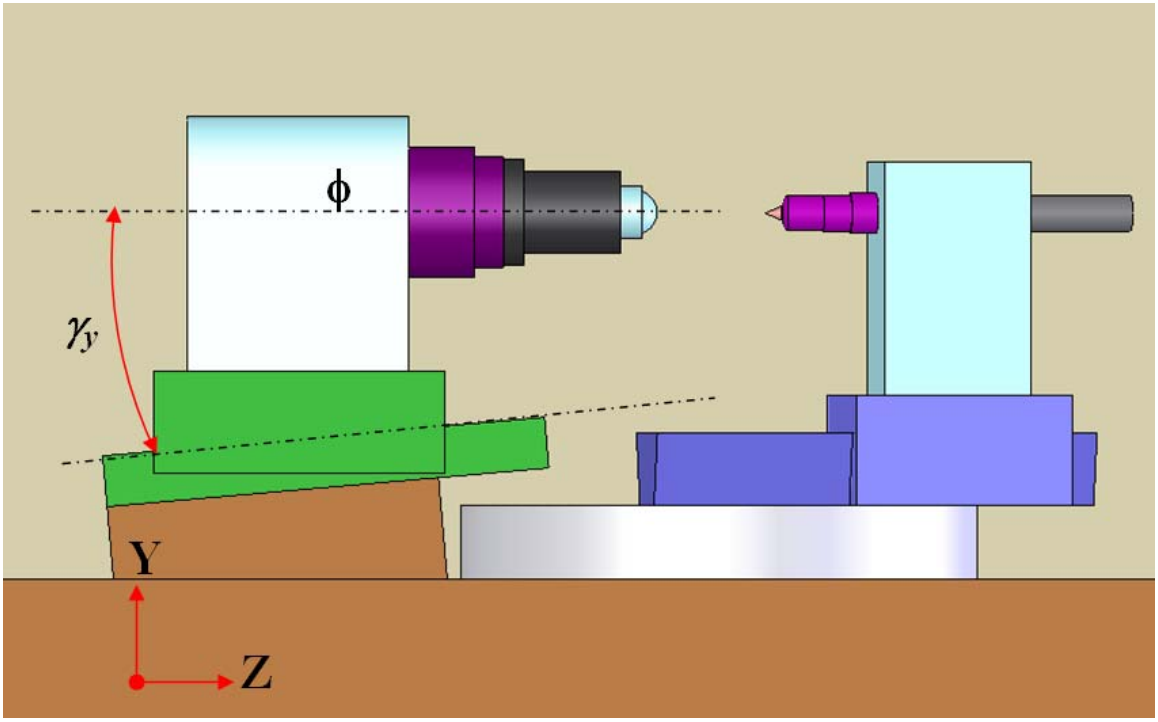

Figure 18. Illustration of alignment error γ_y between the ϕ-axis and the Z-axis in the y-direction.

Measurement

Measurement of the alignment error α between the ϕ-axis and the Z-axis is performed together with measurement of the ϕ/θ-axis intersection error as shown in Figure 19. Four points on a diamond-turned cylinder as shown in Figure 20 are measured using the probe in the positions A, B, C, and D indicated. In between measurements A, B and C, D, both the ϕ and θ-axes are rotated to provide a reversal of the artifact and make the measurement independent of errors in the part. With all of the measurements complete, the ϕ/θ-axis intersection error $e_{x\phi}$ and the ϕ/Z alignment error angle α can be calculated from the measurements.

$$\arctan(\alpha) = \frac{C - B - D + A}{2\Delta Z} \tag{3}$$

where ΔZ is the displacement of the Z-axis between measurements. The intersection angle

$$e_{x\varphi=} \frac{C - B + D - A}{2} \tag{4}$$

represents the error at a Z-position halfway between the two sets of measurement points.

The alignment error γ_y between the ϕ-axis and the Z-axis in the y-direction can be measured using the same cylinder used in the x-measurements. This time, however, an electronic indicator is set up to measure two points along the top of the cylinder, then the cylinder is rotated 180º and the same two points are measured on the bottom of the cylinder. Again, using Equation (3), the relative angle between the Z-and ϕ-axis can be calculated.

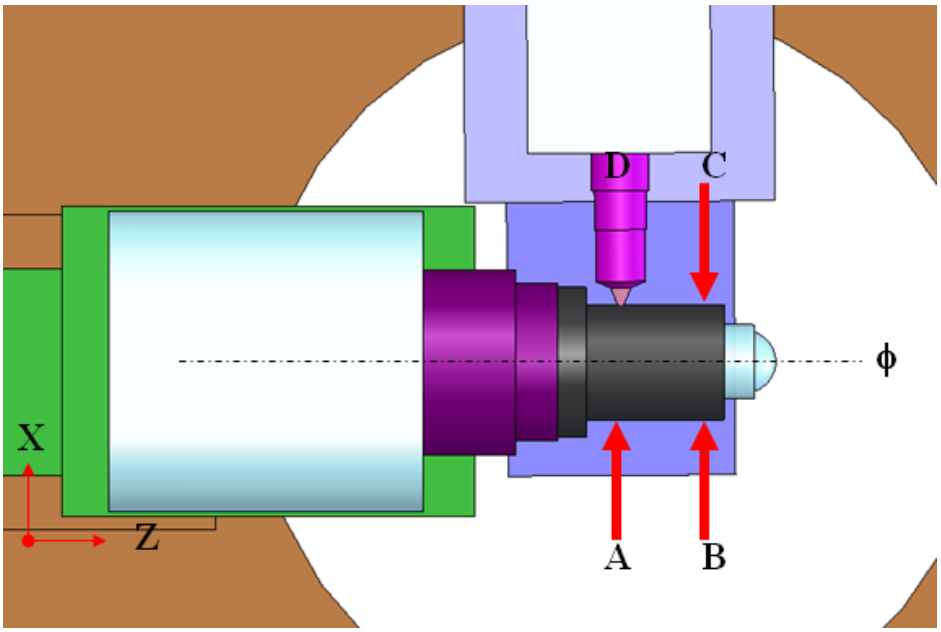

Figure 19. Combined measurement of the ϕ /Z alignment error and the ϕ/θ-axis intersection error is performed with measurements of a cylinder in the four locations shown.

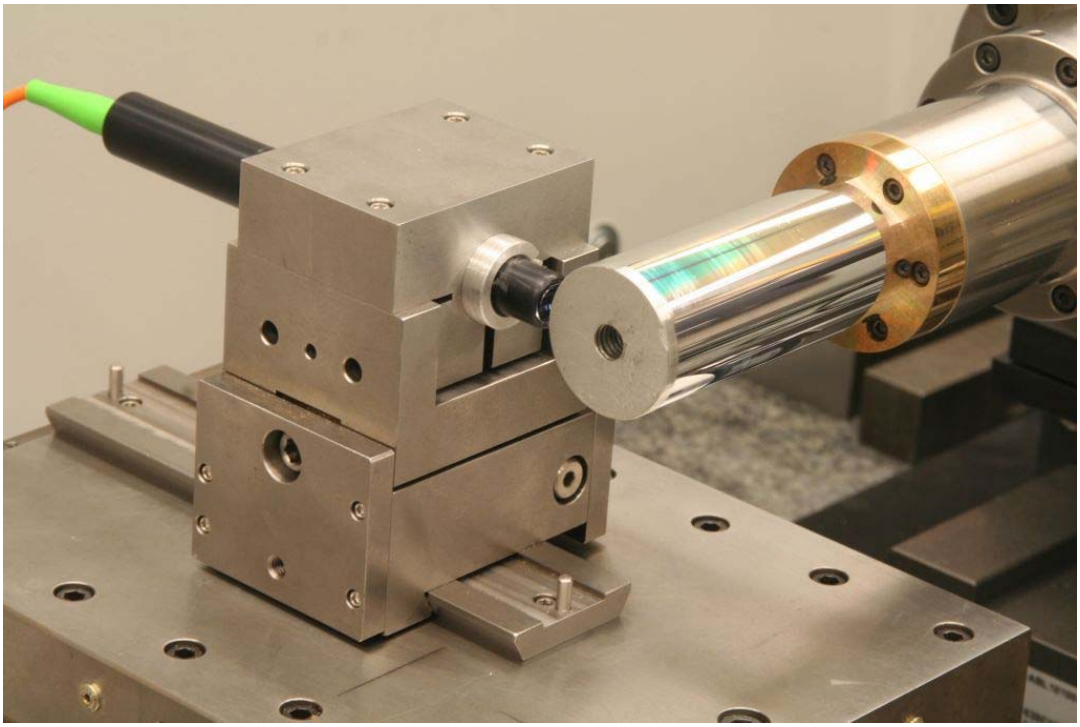

Figure 20. Measurement of the ϕ /Z alignment error and the ϕ/θ-axis intersection being performed on a diamond-turned cylinder. Shown is position B from Figure 19.

Adjustment

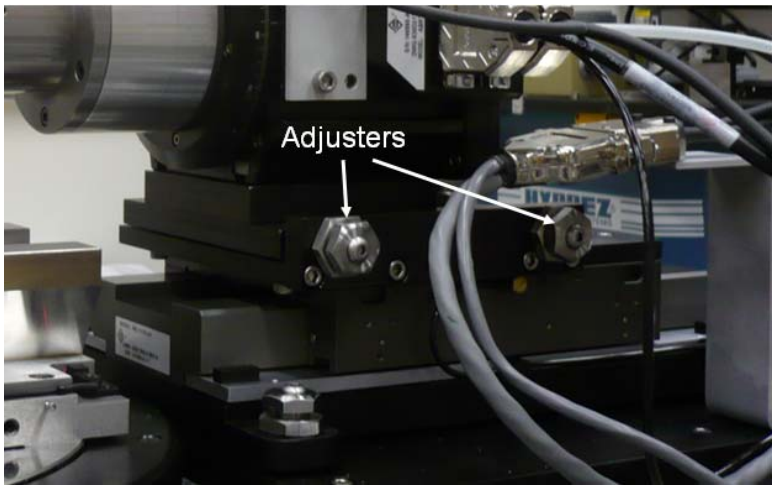

Figure 21. Adjustment of the ϕ /Z alignment error in the x-direction is performed with the indicated adjusters.

The x-direction ϕ /Z alignment error is adjusted using the two adjusters on the side of the spindle base as shown in Figure 21. Again, this adjustment is performed in conjunction with the

adjustment of the ϕ/θ-alignment. This is important, since relatively small differential displacement of the spindle horizontal adjusters producs a small angle, but a significant x-displacement at the part location. This x-displacement can then be brought back to it's correct vaclue by performing the ϕ/θ-adjustment as described in section 2.3.4.

2.4.6 ϕ-AXIS ORIGIN TO PROBE Y- ALIGNMENT ($e_{y\phi}$)

Vertical alignment of the ϕ-axis to the measurement probe is illustrated in Figure 22. This error produces a y-offset of the probe. Impact on most measurements is minimal, but depends on part shape.

Error measurement

Measurement of the ϕ-axis to probe vertical alignment error can be done with a tilted flat as shown in Figure 23. If the tilt angle and tilt axis relative to a fiducial are measured on a coordinate measuring machine (CMM), the Y-component of the tilt and the X-component can be separated. The tilted flat was made by attaching a diamond turned aluminum flat with epoxy adhesive and a spacer onto a brass substrate mold plug. This was measured on the Brown & Sharpe CMM for both tilt angle and orientation. The tilt angle was measured to be 7.451º (0.130 rad), with the axis through the high and low spots rotated with respect to the fiducial flats on the side of the part by 13.899 º (0.2426).

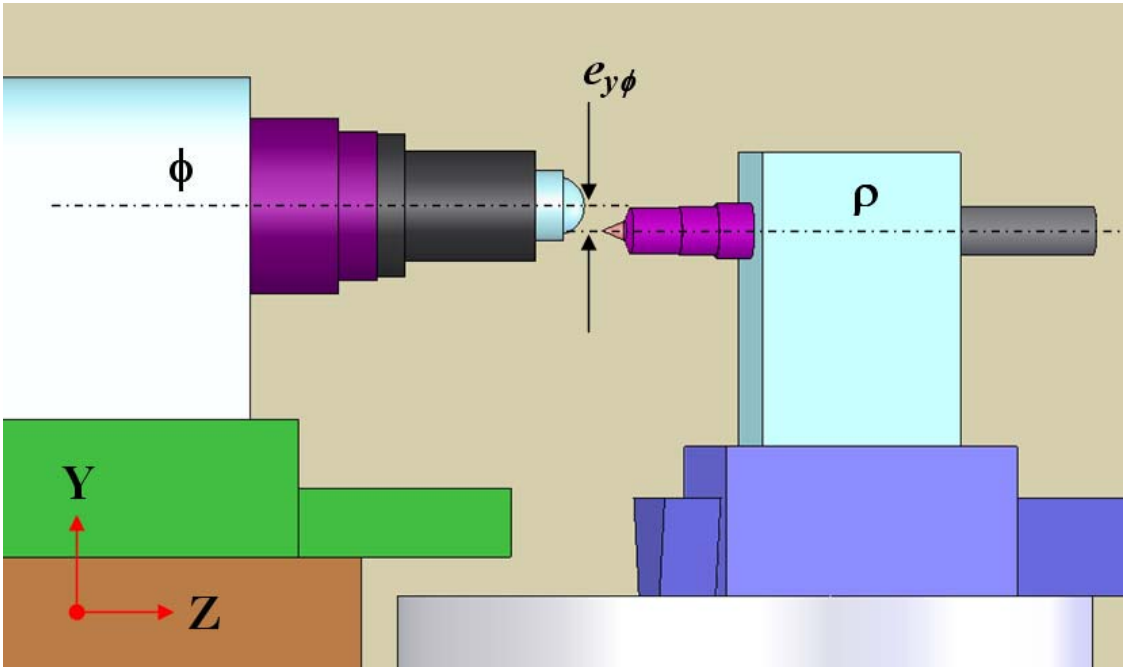

Figure 22. ϕ-axis to the probe alignment error in the y-direction

Figure 23. Tilted flat used for measuring ϕ-axis to probe vertical alignment error

The tilted flat is then mounted on the ϕ-axis indexed relative to the flat on its base via a machinist's square placed on the R-axis table while the ϕ-axis is set to zero. With θ=0 and R=0, the ϕ-axis is then rotated and data collected.

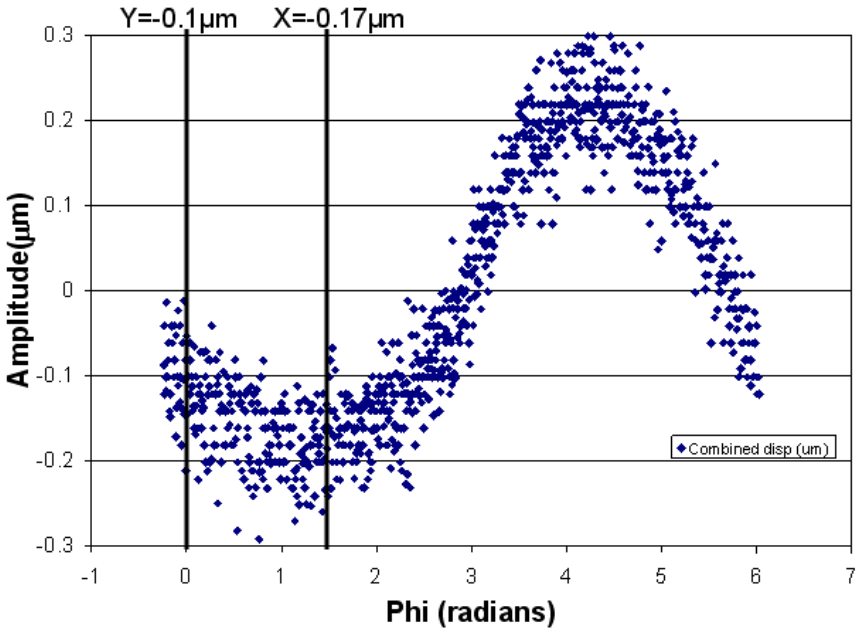

Figure 24. Plot of ϕ-axis vertical alignment error measurement using a tilted flat resulting in a y-error of -0.77 µm and an x-error of -1.5 µm when combined with the tilt angle of the flat.

The result of one such measurement is shown in Figure 24 where R axis position + probe motion are plotted as a function of ϕ. While the ideal signal when the probe and ϕ-axis are aligned in

both X and Y would be a constant, the measured signal shows a value of 0.1 μm for the y-component. This value can be converted to a total alignment error in the y-direction of 0.77 μm by dividing by the tanα. The tilt of the flat in this case is 7.451º.

Impact on the measurement of a sphere

The measurement produces a radius error (no figure error) with

$$e_r = r - \sqrt{r^2 - e_{y\phi}^2} \tag{5}$$

where r is the true radius of the sphere and $e_{y\phi}$ is the y-alignment error. Measuring through +θ or -θ produces no disparity in the measurement; for example given a 25μm alignment error and the 1" diameter sphere, the radius error will be 25 nm.

Adjustment

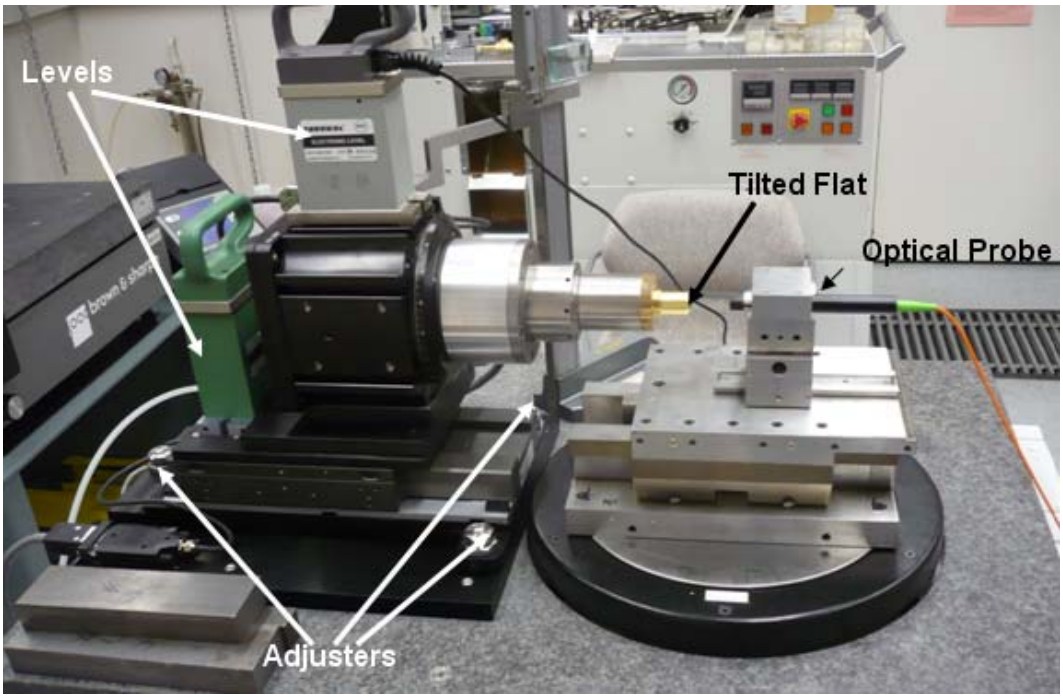

Figure 25. Adjustment of ϕ-axis to probe alignment is performed by adjusting all three Z-axis base adjusters. Levels are used to ensure uniform height adjustment.

Adjustment of the ϕ-axis in the y-direction is carried out via adjustment of all three of the adjusters on the Z-axis base by the same amount. Ideally, turning each adjuster screw the same amount will produce purely vertical motion, but variance in torques and threads require an independent means of maintaining axis level to prevent losing R/Z parallelism. This is achieved, as illustrated in Figure 25 , by placing a pair of electronic levels orthogonally on the ϕ- and Z-

axes. Before any adjustment is carried out, the air table of the machine is fixed via holding brackets and the level readings are noted. The adjusters are then moved the required amount one at a time to prevent shifting the axes in the x- and z-directions. The adjusters are then fine tuned to return the levels to their original values and the adjustment is complete, with the measurement ready to be repeated until the misalignment value is within an acceptable range.

2.4.7 R/ρ PARALLELISM IN Y AND θ

Since the optical probe is used as a null probe and displacements during measurement are seldom greater than 20 μm and the 1-cos nature of the measurement error, the impact of this error is minimal. Even if the entire 200 μm range of the probe is used, an angular misalignment as large as 1° would only produce a measurement error of 30 nm. Since mechanical tolerances can be expected to be much better than this, this error can safely be ignored.

2.5 CONCLUSIONS

With the completed assembly and continued refinement of alignment and error measurement on Polaris 3D, the machine edges ever closer to the 100 nm measurement accuracy goal established for it. Sophisticated alignment procedures and rigorous testing will complete this goal. With continued development, it will be shown that Polaris 3D can be used in a broad range of applications such as DVD lenses, opthalmics, prosthetic joints, diesel engine lifter cups and many more.

REFERENCES

1. A. Sohn, K. P. Garrard, T. A. Dow, *The Polar Profilometer Polaris*, Proceedings of ASPE 2001 Annual Conference
2. A. Sohn, K. P. Garrard, T. A. Dow, *US Pat No 6895682: Polar coordinate-based profilometer and methods*, Nov. 2002.
3. http://www.stilsa.com/

3 FAST LONG RANGE ACTUATOR (FLORA I)

Qunyi Chen
Graduate Student
Thomas A. Dow
Dean F. Duncan Distinguished Professor
Department of Mechanical and Aerospace Engineering
Kenneth Garrard and Alex Sohn
Precision Engineering Center Staff

The goal of this project is to develop a Fast Long Range Actuator (FLORA) to produce optical quality freeform surfaces. The target range of motion of ±2 mm at 20 Hz creates a challenging problem and required innovation in design, fabrication and control. The prototype features a tool holder driven by a linear 3-phase motor, supported by an air bearing, measured by a high-resolution linear encoder and controlled by a high-speed Digital Signal Processor (DSP). Feedback and feedforward control strategies are discussed along experimental results of motion control and machining tests. A technique for creating optical feature and fiducial feature for assembly purpose in one machining setup is also described.

3.1 INTRODUCTION

The development of a Fast LOng Range Actuator (FLORA) is driven by the need to create Non-Rotationally Symmetric (NRS) optical surface with millimeters of sag at high production rates, since the existing technology on tool positioning with the PZT FTS is limited by stroke or the slow slide servo is limited by speed. The FLORA piston is supported by an air bearing, driven by a linear motor, measured by a high-resolution linear encoder and controlled by a high-speed DSP based controller. To retain the surface quality of existing diamond turning machines (less than 5 nm RMS surface finish, less than 150 nm form error), the real-time tool motion control must position the tool within ±20 nm of desired location while moving the tool over a range of 4 mm at a frequency of 20 Hz in the machining process. The requirements on the motion range (4 mm), speed (250 mm/s) and positioning error (40 nm) make the control of tool motion very demanding. The key parameters that set this application apart are the ratio of range to position error (100,000) and the position error to speed (120 ns).

3.2 SYSTEM DEVELOPMENT AND CONSIDERATIONS

A prototype FLORA was built in 2004 and has been upgraded over the last three years with support from NSF. A photograph of the actuator is shown in Figure 1. The FLORA consists of a light-weight, aluminum-honeycomb triangular piston, an orifice air bearing, an ironless three-phase linear motor, a linear amplifier and a laser linear encoder. This physical construction of actuator is free of major nonlinearities such as hysteresis, backlash and friction commonly seen in other motion systems. When integrated with high-speed (20 kHz sampling rate) and high-bandwidth real time closed-loop control, the FLORA exhibited good tool motion control and machining performance.

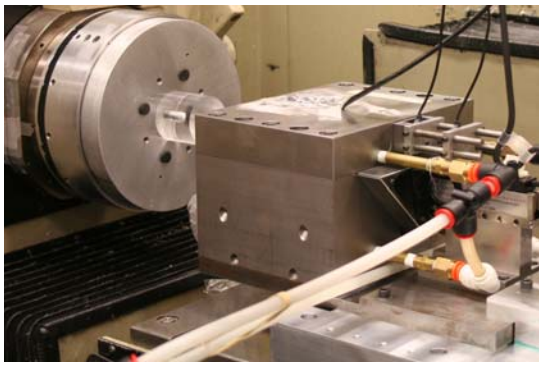

Figure 1. Photograph of the FLORA system mounted on the ASG 2500 DTM.

Comparing with a stationary tool post, the FLORA adds significant capability but, at the same time, has the potential to add unwanted motion to the tool. Since the FLORA is oriented normal to the Z axis, the additional error in Z direction can be written as:

$$Z = A_z \sin(\omega_z t) \tag{1}$$

where A_z is the error magnitude at the frequency of ω_z. At the cross-feed rate of f and the spindle rotation frequency of Ω, the radial position of the tool is

$$X = \Omega f t \tag{2}$$

The model of the surface finish has been developed [1] by removing the time variable in the Equations 1 and 2

$$Z = A_z \sin\left(\frac{\omega_z X}{\Omega f}\right) \tag{3}$$

It can be seen that the synchronous motion in the Z error component increases the form error in Figure (a) and asynchronous motion increases surface roughness in Figure 2(b).

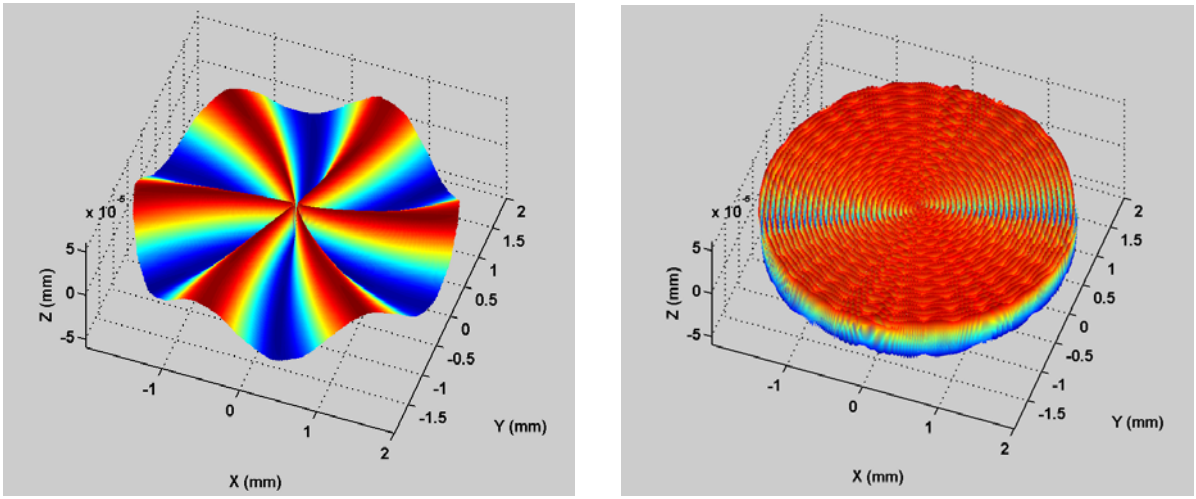

(a) Synchronous motion (b) Asynchronous motion

Figure 2 Simulation of the impact of Z motion error on the surface formation

It has been verified with a fixed tool post that the surface finish on a machined part can be better than the vibration level in the Z direction. The reason is the averaging effect from the round-nose tool: at low cross-feed rate where some of cutting passes are absent in the surface formation process. As a result only those passes with the peak motion into the workpiece will leave the final cusps on the surface.

The additional errors in the radial direction (X and Y) are caused by side motion of the piston in the air bearing, flexibility of the toolholder and deflection of the support structures (piston and height adjuster). The oscillation of the tool tip in X and Y direction was measured with a capacitance gage (Lion C2-B) and the results are shown in Figure 3 when the piston was actively held in position by the motor.

$$X = \Omega f t + A_X \sin(\omega_X t) \tag{4}$$

$$Y = A_Y \sin(\omega_Y t); \qquad \theta = 2\pi\Omega t + Y / X \tag{5}$$

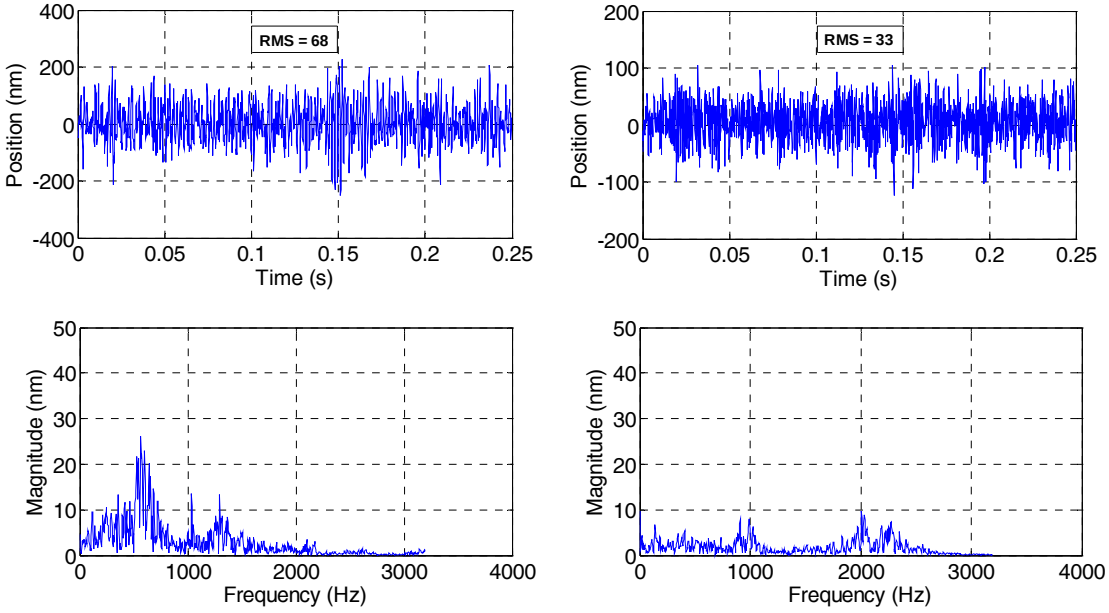

(a) horizontal direction X (b) vertical direction -Y

Figure 3. Measured oscillation at the tool tip. Top is plot of position vs. time and bottom is the frequency spectrum

Since the optical surface typically has slopes in both radial and circumferential direction, the positioning error in X, Y and Z direction can be converted into the error components in the radial, tangential and normal directions. It is easy to qualitatively understand that the error in normal direction affects both form and surface finish and the error in radial (cross-feed) direction mainly affect surface finish. Furthermore, because the cross-feed rate during the finish pass is only a few micrometers per revolution which is much smaller than tool radius value. As a result, for round nose tool, the surface finish is determined by the error in the surface normal direction. Due to wide variation of surface geometry, it is not feasible to provide a generic equation on how the positioning errors in X, Y and Z direction affect surface finish even by statistical method (linear regression) from experimental results. Nevertheless, to retain the surface quality of existing diamond turning: form error of 200 nm and surface finish of 5 nm RMS, it is desirable to achieve 5 nm RMS values for all three error components in X, Y and Z direction.

3.3 METROLOGY

To create a freeform surface, the position of the tool is synchronized to the position of the DTM axes by generating its motion command ($\boldsymbol{Z_t}$) as a function of the spindle angular position ($\boldsymbol{\theta}$), z-slide position ($\boldsymbol{Z_s}$) and cross-feed slide position ($\boldsymbol{X_s}$) in Equation (6).

$$Z_t = \mathbf{f}(X_s, Z_s, \theta) \tag{6}$$

It is desirable to have any measurement induced tool positioning error within a few nanometers. Laser interferometers installed on the ASG-2500 have measurement resolution of 2 nm for z- and x-slide positions. However, there are measurement errors in the spindle and FLORA axes.

3.3.1 SPINDLE ANGULAR POSITION MEASUREMENT

A 20,000 count/rev encoder (Heidenhain ERO1324) is used for spindle angular position measurement. The encoder alignment was found to contribute to the errors in the tool motion trajectory. The runout in the encoder disk will appear as a non-uniform pitch of the angular steps when read by the stationary read head as shown in Figure 4.

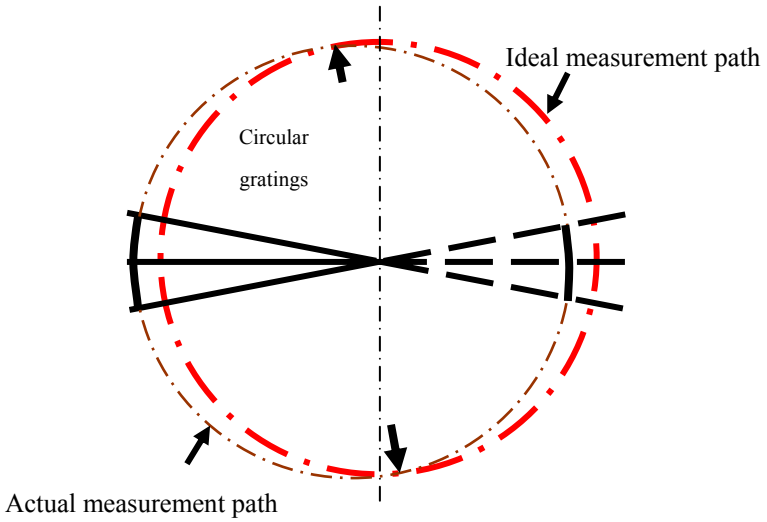

Figure 4. Non-uniform pitch caused by rotary encoder disk runout

Because the rotary error repeats each revolution and the spindle speed is constant over that short interval, this measurement error can be calibrated and compensated at the servo sampling rate. Figure 5 shows how this error can be calibrated and compensated. Figure 5 (a) and (b) show the encoder counts readings at the start and the end for one full revolution of encoder sampling at 20 kHz for the spindle speed of 630 rpm. The difference between the actual reading and ideal reading (the linear line fitting between the first and last data point) produces the error in counts shown in Figure 5 (c). Removing the sinusoidal component of error due to the encoder disk runout in Equation (7), the residual error within one encoder count (Figure 5 (d)) due to the limited resolution issue is smoothed out by the filtering technique [3]. The effectiveness of these techniques was experimentally verified using a tilted flat as illustrated in Section 3.6.2.

$$\tilde{\theta} = 5.045\cos\left(\Omega t + 84.754^{\circ}\right) \tag{7}$$

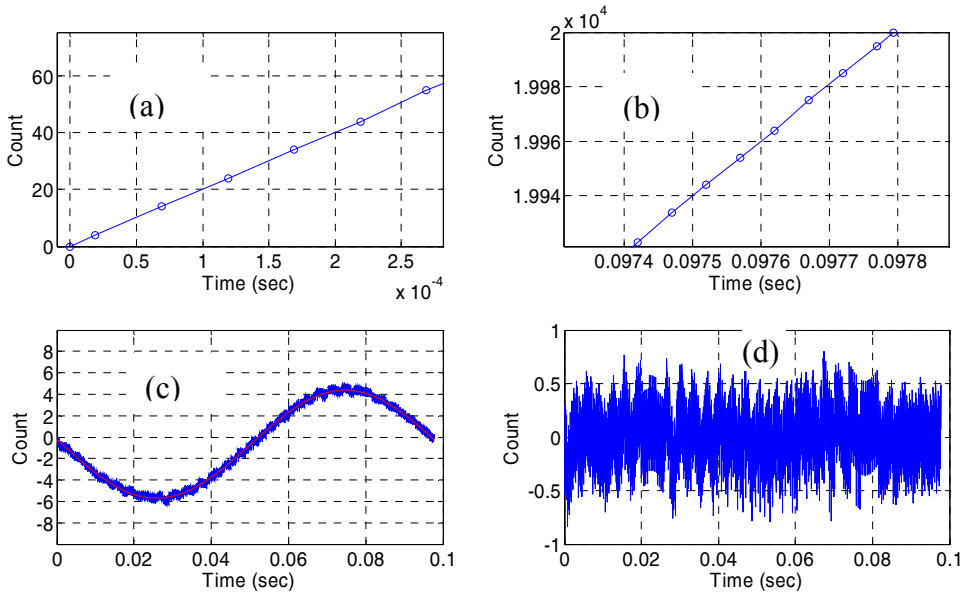

Figure 5. Calibration and compensation (a) Start of encoder reading for one revolution of encoder, (b) End of encoder reading for one revolution of encoder, (c) The encoder reading error due to disk runout, (d) The residual error after the compensation of disk runout error.

3.3.2 TOOL POSITION MEASUREMENT

The tool position is measured by a linear encoder (Sony BH25) with 0.25 μm signal wave length. It is one of the best reflective type linear encoders available. Once integrated with PMDi interpolator, the position measurement shows 3 nm of noise when the air bearing is turned off and the piston maintains static position. However, the position measurement resolution degrades to 125 nm [1] when the sin/cos encoder signals entering the interpolator reach its frequency limit of 325 kHz. Figure 8(a) shows the error that occurs when the encoder frequency exceeds the interpolator limit. The interpolator ceases to operate and the encoder resolution increases to zero crossing of the sine wave of 125 nm (half the scale period of 250 nm). To addresses this problem, collaborative efforts with PMDi were taken to increase the frequency limit of interpolation process above 1 MHz. This is the sine wave frequency for the peak speed of the ± 2 mm, 20 Hz sine wave or 250 mm/sec. The steps were:

(1) Remove signal filtering and compensation in interpolation process,
(2) Synchronize the analog interpolation and digital zero-crossings counting paths ,
(3) Make 4x interpolation of 10 MHz ADC at 40 MHz clock cycle.

Figure 8(b) shows the position error for 2 mm 20 Hz sine wave tracking with a PID controller and an acceleration feedforward controller, the improvement on the motion control quality is obvious by comparing the plots in Figure 6.

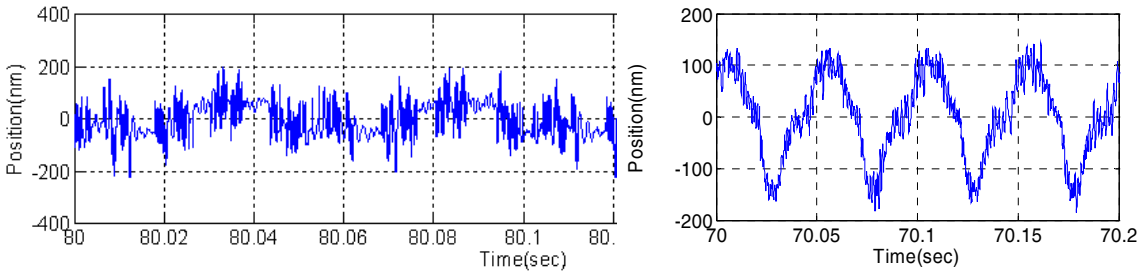

Figure 6. 2 mm 20 Hz sinusoidal tracking test. Left, error when the sine wave frequency exceeds the interpolator speed and right, tracking error with high-speed interpolator

3.4 ANALYSIS OF TOOL SERVO DYNAMICS

Cutting and actuation forces are transmitted through the lightly-damped FLORA and into the whole DTM structure represented by the component masses, damper and springs. While the effects of this transmitted vibration are negligible for most applications, they can be significant at the nanometer scale. The modes of vibration of the honeycomb piston and the motor/piston connectin were studied by Buescher [5]. In the longitudinal direction, the direct drive with a linear motor significantly increases the stiffness in the mechanical power transmission, the structure holding the tool can be taken as a rigid body. There are other potential vibration modes at lower frequencies due to the bending of motor forcer mount, in the pitching of the air bearing support and motion of the encoder read head mount. These modes can introduce parasite motion in the tool feed direction at the tool tip (the encoder scale), or introduce measurement errors in the tool position feedback.

Measurements of the piston motion were made to evaluate the magnitude of these disturbances. Observations were made with the piston held in place by a rubber band without energizing the motor and measuring the motion with a capacitance gage perpendicular to the piston motion. The frequency spectrum from 100 Hz to 10 kHz for piston motion in this tool feed direction is shown in Figure 7. Those peaks at 900 Hz and 1500 Hz are attributed to the air bearing pitching motion and the peaks at 2000 Hz and 2300 Hz are attributed to the structural bending [5]. The existence of these resonance peaks is also verified in the open-loop system frequency response test in Figure 7(b).

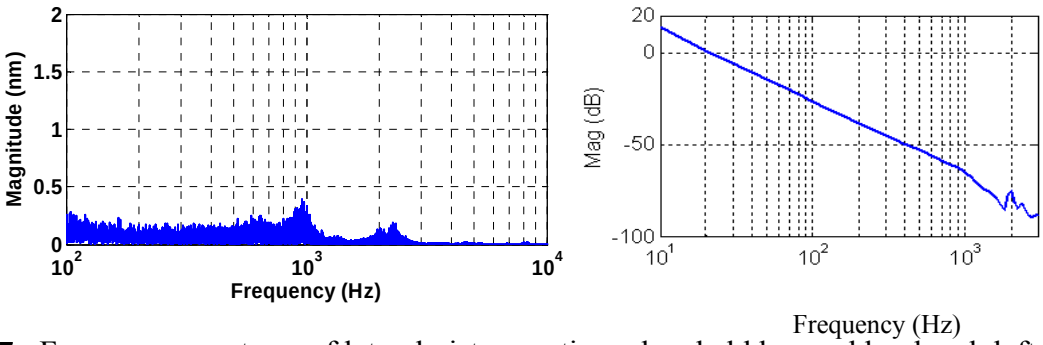

Figure 7. Frequency spectrum of lateral piston motion when held by a rubber band, left, and the magnitude of the frequency response of the open loop system, right.

These high frequency modes limit the achievable performance of closed loop tool servo control. The solution is to push these modes up to a higher level, i.e. above 3 kHz, and also reduce their peak levels. It can be accomplished by increasing the stiffness of the piston and the mount coupling the piston and the motor, reduce amount of misalignment of actuation force to the gravity center of moving mass and increasing the stiffness of the air bearing. .

3.5 CONTROL SYSTEM DESIGN

The functional requirement for the FLORA is to follow the tool motion profile as closely as possible while minimizing the effects of measurement errors and disturbances. The disturbance force to the tool motion could be from the errors in motor actuation force generation process or from the tool-workpiece interaction process.

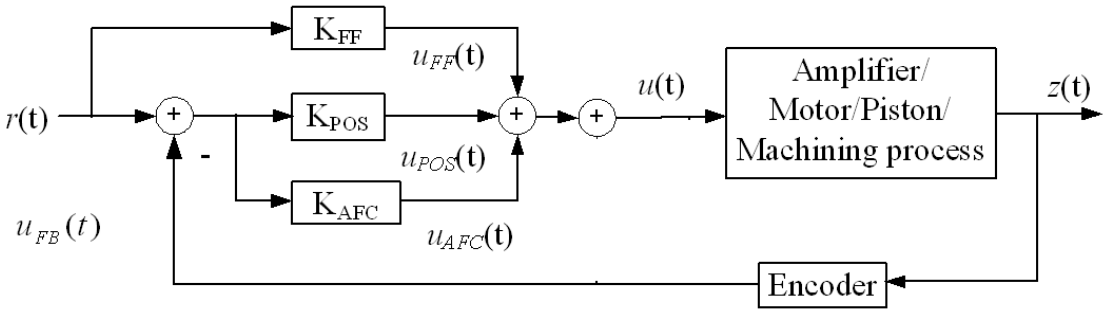

Figure 8. Schematic diagram of the proposed controller structure

Figure 8 shows a block diagram of the proposed composite controller structure to achieve control task. A position feedback controller (K_{POS}) is designed based on the dominant linear model to establish the basic closed-loop control system. A feedforward controller (K_{FF}) is applied to compensate the phase lag in profile tracking. An adaptive feedforward controller (K_{AFC}) is designed to further improve trajectory tracking and reject disturbances at selected frequencies.

3.5.1 CLASSICAL LOOP-SHAPING DESIGN FOR POSITION FEEDBACK CONTROLLER

Controller Design

The closed-loop block diagram is shown in Figure 9, where *C* contains the dynamics of actuator and position feedback controller together, and *P* contains the dynamics of the tool holder. *N*(s) is the encoder position feedback error or noise, *R*(s) is the position command for the tool motion, *D*(s) is the disturbance, and *Z*(s) is the resulted tool position.

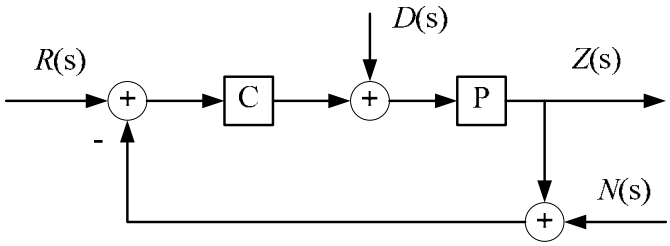

Figure **9**. FLORA control system diagram

The true tool positioning error *E*(s) is the difference of *R*(s) and *Z*(s), and can be expressed as a function of all closed loop system inputs and dynamics

$$E(s) = \underbrace{\frac{1}{1+C(s)P(s)}}_{S(s)} \cdot R(s) - \underbrace{\frac{P(s)}{1+C(s)P(s)}}_{M(s)} D(s) + \underbrace{\frac{C(s)P(s)}{1+C(s)P(s)}}_{T(s)} \cdot N(s) \qquad (8)$$

where the first term is the sensitivity function, *S*(s), second is the disturbance sensitivity function *M(s)* and the third is the complementary sensitivity function, *T*(s). The process of designing feedback controllers is to make proper compromises among different factors based on these three functions. To this end, design specifications are translated into following frequency response characteristics:

- High loop-gain (magnitude) in the low frequency range for desirable performance on tracking and disturbance rejection.
- Adequate loop-gain crossover frequency for high speed-of-response.
- A slope of -20 dB/decade for the loop-gain at the crossover frequency, and a minimum of 30° phase margin for stability.
- Low loop-gain (magnitude) in the high frequency range to have sufficient gain margin for modeling uncertainty, reduce the effect of the noise (or error) in the position command and measurement, and avoid actuation saturation.

A graphic representation of these requirements is given in Figure 10. A high-gain controller (at low frequencies) is very important to achieve good performance with respect to tracking and disturbance rejection. It can be done by pushing the loop-gain crossover frequency to a higher value and by increasing the slope of loop-gain. However, the crossover frequency is normally limited by high frequency modes in the amplifier current dynamics and mechanical resonances. When a set of components are driven faster than their natural mode frequencies, the system will saturate.

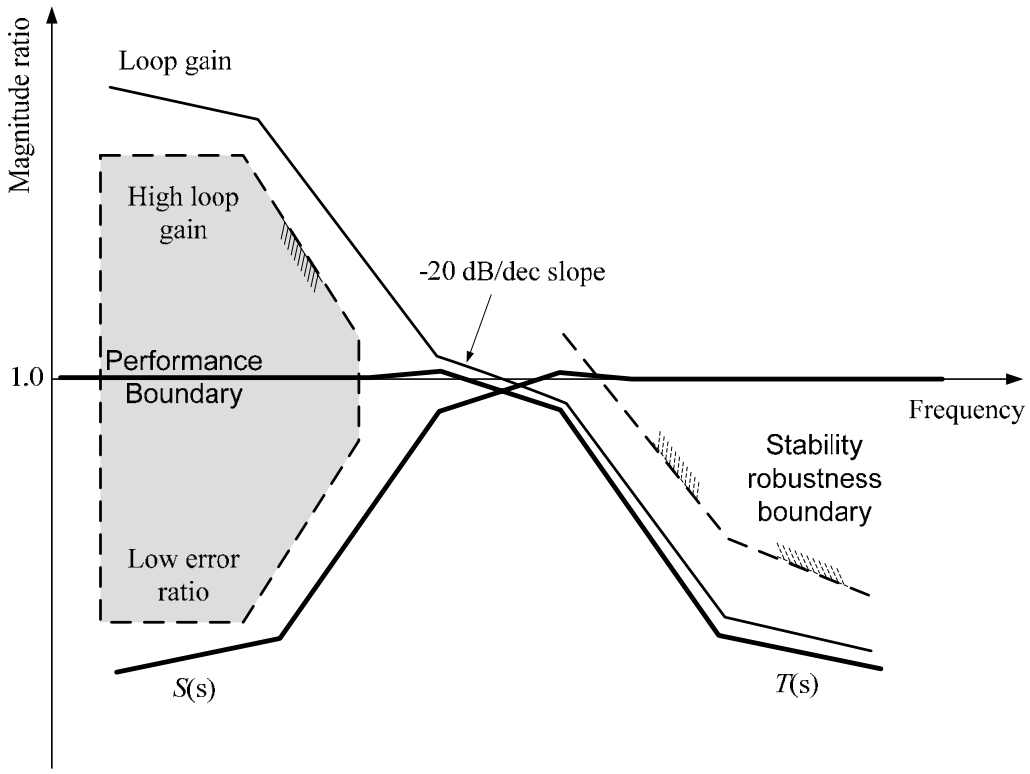

Figure 10. Loop shaping design criteria

Based on the measured open loop system frequency response characteristic in Figure **7**(b), three different position feedback controllers [3] were designed with different loop gain crossover frequencies of 100Hz, 600Hz, and 1000Hz. The controller parameters for each are:

(1) PID controller: (600 Hz) K_P =120; K_I = 42560; K_D = 0.160;

(2) Lag-lead compensator: (100 Hz) α=6; $\omega_c = 2\pi \cdot 20$; $\omega_{lead} = 2\pi \cdot 100$; $\omega_{lag} = 2\pi \cdot 20$

(3) Lag-lead compensator: (1 kHZ) α=15; $\omega_c = 2\pi \cdot 1000$; $\omega_{lead} = 2\pi \cdot 1000$; $\omega_{lag} = 2\pi \cdot 100$

The corresponding algorithms in discrete time *Z*-domain in the same order are:

$$K_{PID}(z) = \frac{3321z^2 - 6519z + 3200}{z^2 - z} \tag{9}$$

$$K_{LL1}(z) = \frac{233z^3 - 692z^2 + 685z - 226}{2z^3 - 5.7037z^2 + 5.4184z - 1.7147} \tag{10}$$

$$K_{LL2}(z) = \frac{20407z^3 - 57411z^2 + 53822z - 16815}{2z^3 - 3.1848z^2 + 1.3602z - 0.1755} \tag{11}$$

These three controllers behave similarly in the frequency domain; that is, they increase loop gains at low frequency, add phase lead to obtain phase margin at the crossover frequency and lower the gain at high frequency. A comparison of the theoretical closed-loop system frequency response is shown in Figure 11 based on the nominal open loop system dynamics in Equation (12).

$$G_{n1}(s) = \frac{51806782\,(s + 13448)}{s^2 \cdot (s^2 + 5717s + 37424559)} \tag{12}$$

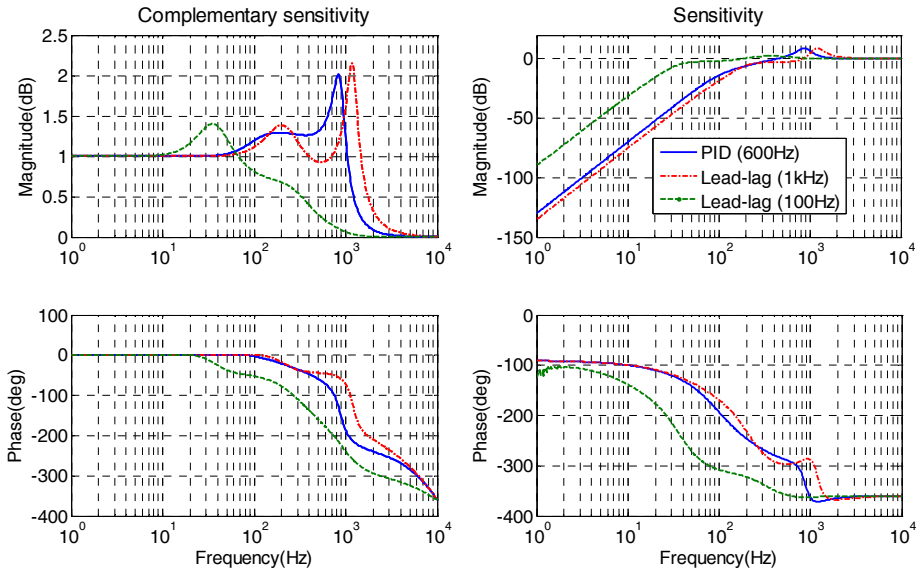

Figure 11. Closed loop simulations controllers with three different crossover frequencies; complementary sensitivity function at the left and sensitivity function at the right.

By placing the loop-gain crossover frequency much lower than the first mode in the open loop system around 900 Hz (combined contributions from current dynamics and mechanical resonance), K_{LL1} makes obvious difference from the other two controllers. It has the lowest peak magnitude and the highest stability margin, but it also has the lowest speed of response and stiffness for the servo control. K_{PID} and K_{LL2} place their loop-gain crossover frequencies close to the first mode, so they both produce much larger peak magnitudes. However, there are still some differences between these two controllers. The lead-lag system with 1 KHz crossover frequency has the highest servo stiffness, but its gain margin is the lowest, it causes the saturation of the amplifier during the tracking task.

Servo Control Test

In a position holding test without cutting, the dominant error source is from the disturbance due to electrical noise. Figure 12 shows the positioning error when the FLORA was mounted on the ASG-2500 x-slide stage. Before cutting a flat, the position is held at 17.1 mm where the piston is at the mid travel range of the air bearing. Positioning error for the Lead-lag controller (K_{LL1}) is 12.0 nm RMS, 16.0 nm RMS for the PID controller (K_{PID}), and 13.5 nm RMS for the Lead-lag controller (K_{LL2}). It is clear from Figure 12 that the magnitudes are the smallest for frequencies less than 1 KHz in the case of K_{LL2} but that controller also has the highest magnitudes for frequencies higher than 900 Hz. The system with 100 Hz crossover frequency (K_{LL1}) has the lowest stiffness in the lower frequency range so the magnitudes below 500 Hz are the highest.

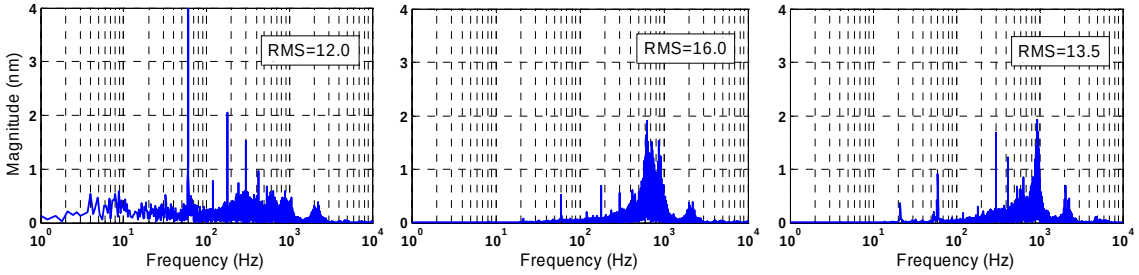

(a) (b) (c)

Figure 12. Frequency spectrum of positioning error when holding position at 17.1 mm (a) Lead-lag with 100 Hz crossover frequency (b) PID (c) Lead-lag with 1 kHz crossover frequency.

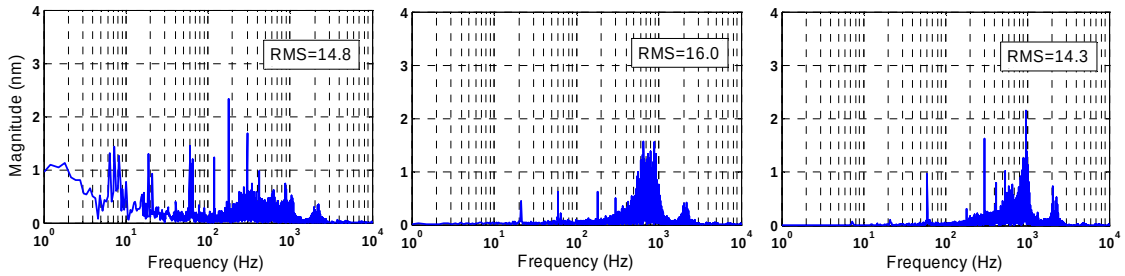

(a) (b) (c)

Figure 13. Frequency spectrum of positioning error during flat cutting when holding position (a) Lead-lag with 100 Hz crossover frequency (b) PID (c) Lead-lag with 1 kHz crossover frequency.

Position data were captured when plated copper flats were machined with 0.53 mm radius tool, at a 2 μm depth of cut, 2 mm/min cross-feed rate, and 500 rpm spindle speed. In addition, the tool is held at the position of 17.1 mm. The frequency spectra and corresponding RMS positioning errors are shown in Figure 13. A comparison of spectra with Figure 12 indicates that

the tool-material interaction forces (cutting force and thrusting force) in the finish cutting process of plated copper flat have minor impact on the tool position holding for the K_{PID} and K_{LL2}. But for the K_{LL1}, there is significant amount of amplitude increase in the low frequency range due to its low stiffness, as a result, the RMS error increases by 2.8 nm. To this end, the approach is not to lower the crossover frequency of servo system by manipulating controller design but to remove (or lower) the modes peak around 900 Hz in the open-loop physical system. It may be done by a new design of air bearing/piston or possibly the selection of a new linear amplifier.

Figure 14 shows the improvement on position holding from the notch filter. The frequency spectra of position data is only displayed in the range from 1500 Hz to 3000 Hz, Figure 14(a) is for the case that the piston is held in place by a rubber band without any control action, Figure 14(b) is for the case that the piston is actively held in place with the PID controller, Figure 14(c) is for the case that the piston is actively held in place with a combination of the PID controller and the notch filter. It can be seen that, the closed-loop system with the PID controller amplifies the peak around 2000 Hz and 2300 Hz. But a notch filter significantly reduces the controller gain around the notch frequency, so that the corresponding peak level is not increased due to the active control. The performance gain achieved by implementing a notch filter in this system is not significant, but it will be more important when the bandwidth of current dynamics increases to a level much higher than 2000 Hz.

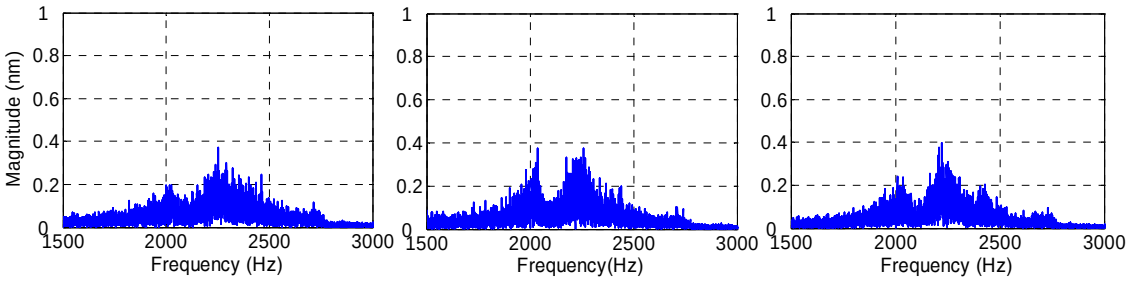

(a) (b) (c)

Figure 14. Frequency spectrum of position data when holding position by (a) A rubber band (b) PID (c) PID and notch filter

In summary, the classical position feedback controller (PID or lad-lead) improves the robustness, profile tracking and disturbance rejection of the servo control system, and provides a firm ground for other control components to be added. However, due to the inherent limitation of wide-band position feedback control approach, it is impossible to obtain ideal response across all frequencies while maintaining the stability of the closed-loop system. The capability of tracking and disturbance rejection is further enhanced by controllers in following sections.

3.5.2 FEEDFORWARD CONTROLLER

In tracking control, feedforward control can achieve faster response because it does not act based on the measured positioning error, but it is never a replacement of feedback controller. Most feedforward controller designs can be classified as a form of command shaping. By processing the desired output by a feedforward controller which acts as an inverse of the open/closed loop system as shown in Figure 15, the effective bandwidth of the overall system can be improved compared with feedback alone. Functionally, two schemes in Figure 15 are equivalent and have the same tracking sensitivity in Equation (13).

$$S(s) = \frac{1 - K_{FF}(s)G(s)}{1 + K_{POS}(s)G(s)} \tag{13}$$

The implementation format in Figure 15(b) is typically called as command shaping since the reference is pre-shaped by the feedforward controller before it is used as the command for the feedback control loop. The design of this controller depends on the feedback controller, so it is less flexible than the format in Figure 15(a).

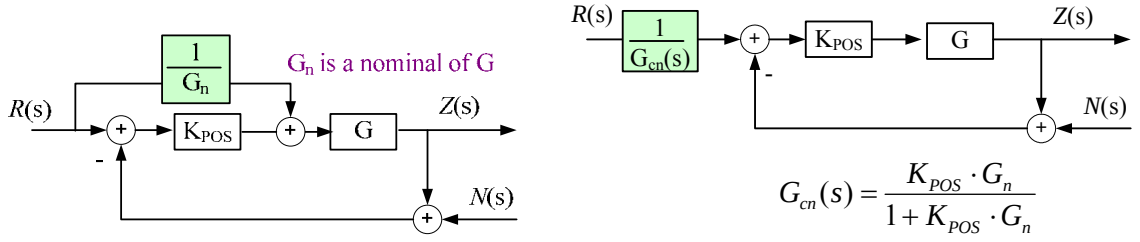

(a) (b)

Figure 15. Implementation structure of feedforward controller (a) from open loop system dynamics (b) from the closed-loop system dynamics

The simplest design of feedforward control law is an acceleration feedforward controller as described in [1]. A simulation of sensitivity functions in Figure 11 shows the enhancement for trajectory tracking. The solid-line in the figure shows this acceleration feedforward controller reduces the sensitivity of closed-loop system with PID position controller in low frequency range, about 33 dB (44.7 times) for frequencies below 100 Hz in the simulation. The zero-crossing frequency also increases from 430 Hz to 610 Hz. The amount of improvement from acceleration feedforward controller is limited by the first mode of high-frequency dynamics (i.e. 900 Hz resonance peak). Figure 6(b) shows the positioning error of ±170 nm in a test of sinusoidal profile tracking at the amplitude of 2 mm and the frequency of 20 Hz. A combination of PID and acceleration feedforward controller is first used. With PID control only, the error magnitude at 20 Hz is about ±5 μm for the same tracking test, so the acceleration feedforward control improve the tracking performance by 30 times. A further improvement of tracking performance

over acceleration feedforward control was not achieved by implementing the inverse of higher order model for the open loop dynamics, i.e. Equation (16).

3.6 CUTTING PERFORMANCE

3.6.1 FLAT

Flat surfaces on plated copper were machined to test the ability of the FLORA piston to hold position while being excited by the machining forces. The flats were machined with a 0.53 mm radius diamond tool at 500 rpm with a 2 mm/min feedrate (4 μm/rev) and 2 μm depth of cut on the finish pass. Table 1 compares the RMS of flat surface finish when the tool is locked or positioned by the control system. For the locked case, the air bearing was locked down by removing the air from the lower sides of the triangular piston.

(1) Comparing to the case of the locked tool, the three controllers added surface roughness. This is due to the fact that the later cases add tool positioning error in X, Y and Z direction.

(2) The active closed-loop control adds 3.7 nm RMS surface finish error for the 100 Hz lag-lead controller, 7.7 nm for PID controller, 6.8 nm for 1 kHz lead-lag controller. There is wider variation of surface finish than the difference of RMS tool positioning errors in the feed-direction due to these positioning errors have quite different frequency spectrum as shown in Figure 17. To further improve the surface finish, it is desirable to reduce the magnitude level above 500 Hz in the tool positioning error.

(3) The achievable surface finish is much lower than the corresponding motion error. This is consistent with the analysis of surface formation process for low cross-feed rate when some cutting passes do not leave any cusps on the surface.

Table 1. Comparison of RMS error with a locked and position controlled tool holder

Unit (nm)	Tool holding method			
	Piston Locked	**Lead-lag (100 Hz)**	**PID (600 Hz)**	**Lead-lag (1 kHz)**
RMS Piston motion error	1	14.4	16.0	14.3
RMS Surface finish	3.7	7.4	11.4	10.5

The tool height adjustment on FLORA I is accomplished by bending the base plate with a single or pair of bolts under the front of the base. The surface finish results in Table 1 were obtained when the tool height adjustment was done by two bolts (one for each side of the FLORA base). The same machining test was done when the FLORA is supported by a single bolt in the middle of the front and the measured surface finish was 9.8 nm RMS for 100 Hz lead-lag controller.

This increase of surface roughness may be caused by additional torsional vibration from the single support.

3.6.2 TILTED FLAT

A tilted flat was machined to evaluate the ability of the servo to create non-rotationally symmetric optical surfaces. The tilted flat requires a sine wave motion of the tool with the amplitude changing linearly with the radial position [3]. Only a combination of acceleration feedforward controller and PID controller is used for the tool motion control in tilted flat machining. Acrylic tilted flats with 50.8 mm diameter and 4 mm sag were created at three different spindle speed, 300 rpm, 600 rpm and 1200 rpm.

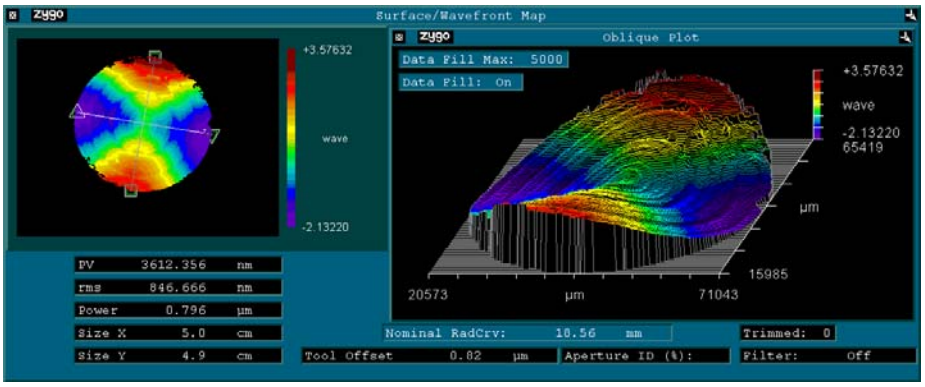

(a) With spindle encoder measurement error

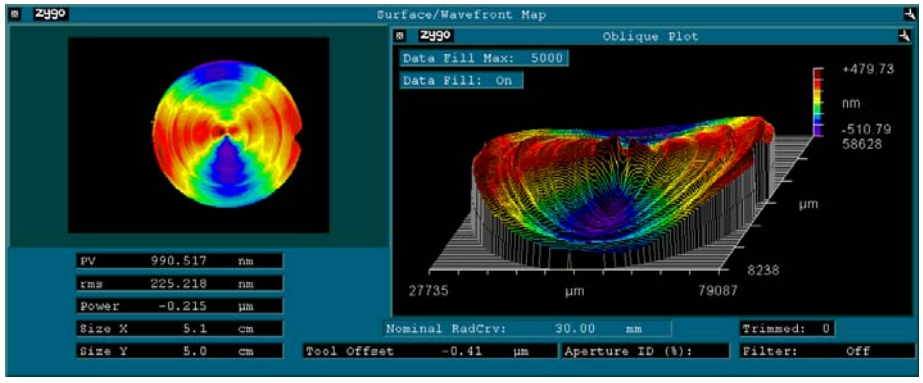

(b) With the corrected spindle encoder reading

Figure 16. Measured flatness error of the 50 mm diameter tilted flat using laser interferometer

The measurement of flatness by the Zygo GPI laser interferometer for the tilting surface shows consistent pattern as in Figure 16(a) for the case of 600 rpm. The plot shows the surface residual error with the best-fit tilted flat removed. The flatness of the machined plastic part was 3.6 µm PP. Note that the surface has astigmatism (two highs and two lows on the surface) and the high spot of this astigmatism has about 80° lead to the high spot of the tilted flat. The 3.6 µm (PV)

flatness error is mainly caused by the spindle rotary encoder feedback error due to the rotor runout as discussed in Section 1.3. This error introduces twice-per-spindle-revolution error in tool motion trajectory which increases in amplitude when the tool cutting depth increases. Since this error is repeatable, it was measured and removed in the motion trajectory. The effectiveness of this solution is validated in another machining test at 630 rpm, in which the flatness is reduced to less than 1 μm (PV) in Figure 16(b). The measured average RMS surface finish is 17 nm (RMS) for the two bolt height adjuster and 22 nm (RMS) for one bolt height adjuster.

For the purpose of comparison, an acrylic flat with 50.8 mm diameter was also cut when the piston was actively held in position with the two bolt height adjuster, the resulted flatness error is 0.244 μm (PV), the RMS surface finish is 11.5 nm. When the machining moves from flat to non-rotationally symmetric tilted flat, the flatness error increases by 0.756 μm (PV) potentially due to the lack of counter-balance for linear actuation in the machining process.

3.6.3 BICONIC MIRROR WITH FIDUCIAL FEATURES FOR KEVIN COUPLING

The Optical Feature and the Fiducial Feature

The IRMOS mirror M4 is an off-axis biconic toroidal surface [6] designed by NASA for a space-based spectrometer. The surface is a blending of two oblate ellipses with different curvature and eccentricity in the XZ and YZ planes. As such it has no axis of rotational symmetry. Figure 17 shows a section of the biconic surface as a wire frame and the aperture of the mirror blank as a solid. This optic was machined in 2002 using a piezoelectric actuator with 400 μm range. The limited range required the optical blank to be machine off-axis and tilted 35.3° with respect to the fabricating axis. The actuator was also tilted with respect to the spindle axis. These two changes allowed the surface to be machined with this actuator even though the Non-Rotationally Symmetric (NRS) sag of the surface is about 545 μm.

With the extended range of the FLORA, it is feasible to machine M4 surface on axis. Figure 17(a) shows the on-axis M4 surface with aperture size of ∅98 mm, the surface is translated in Y direction by -227.41 mm and rotated at an angle of -35.3° around X axis. The total excursion of the on-axis surface is 4.054 mm, but after removing the best sphere of ∅304.881 mm, the excursion of NRS component is 0.545 mm. After considering the tool radius compensation, the best fit sphere has a diameter of 303.919 mm, but the excursion of NRS component has no change.

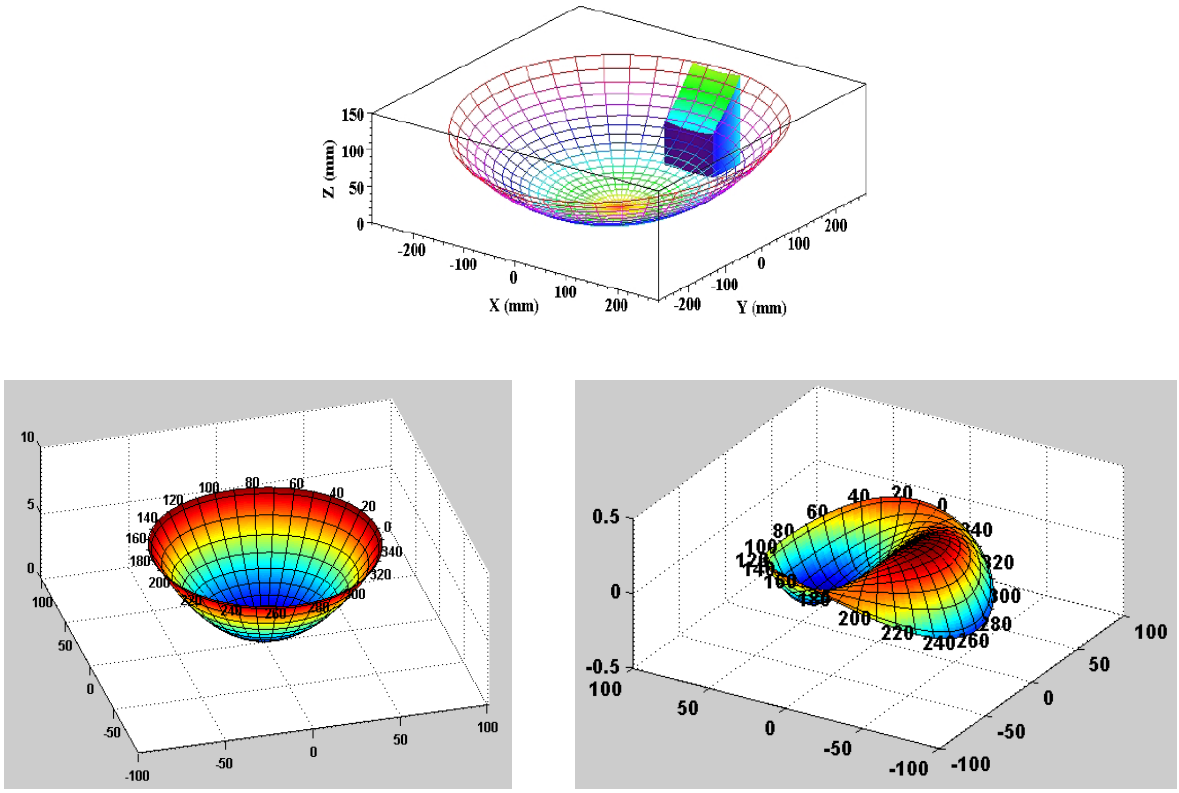

(a) (b)

Figure 17. Biconic optic M4 (a) On-axis M4 surface (b) NRS component [6]

The ability to machine large-amplitude (> 1 mm) features also makes it possible to create fiducial locating features for assembly purpose in the same setup as the functional optical surface so that the geometric relationship of optical and fiducial features can be preserved within the tolerance of the DTM. To design the fiducial feature on the kinematic coupling, there are two main concerns:

(1) The stress at the contact should not exceed the yield stress of the material
(2) The slope of contact surfaces should be sufficient to overcome friction at the interface.

Figure 18 shows detailed shape of this feature design, it has constant width is 4 mm in radial direction, and the full sinusoidal wave in the circumferential direction has a constant wave length of 8 mm. The mid point of width center in the radial direction is at the position of 61.5 mm. At this radial position, the sinusoidal wave has the maximum amplitude of 0.6 mm, but the amplitude (A) changes as a parabolic function of radial position (r)

$$A = 0.6 - \frac{(r - 61.5)^2}{100} \tag{14}$$

The two designated contact points are shown in the Figure at the radial position 61.5 mm, and 60° wave phase away from the peak point (or 0.3 mm lower in height), so two points are 8/3 mm

arc-length apart in circumferential direction. The slope at the contact point is 22°, but the maximum slope reaches 25.22° on the feature, so a customized diamond tool is used with large clearance angle of 27°. The slope was selected to be larger than the critical angle for a pair of mating aluminum surfaces. This was measured to be 9° or a friction coefficient of 0.16.

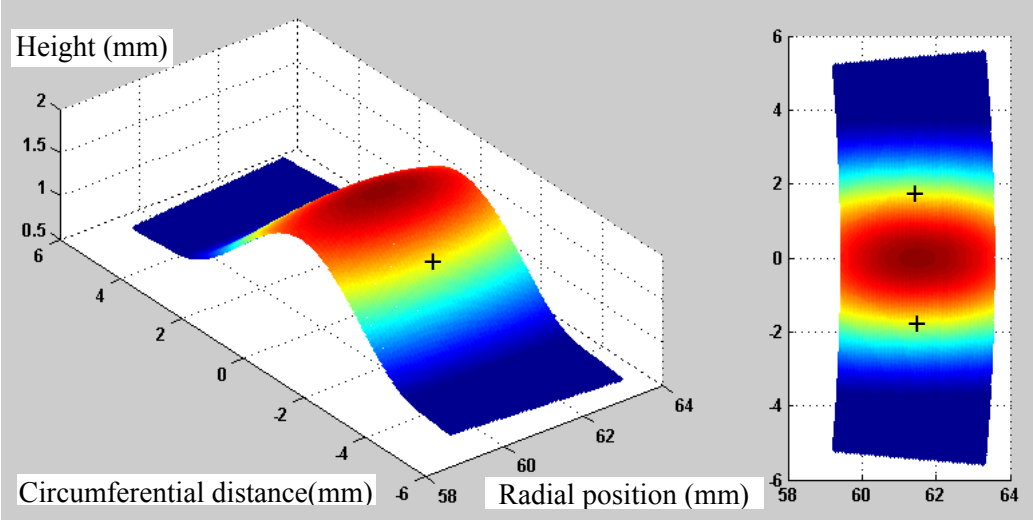

Figure 18. Details of the fiducial feature. The theoretical contact points with the v-groove is indicated by the crosses.

Figure 19(a) shows a photograph of the machined M4 mirror with the fiducial features. Figure 19(b) shows three fiducial features distributed 120° apart rotationally to form a kinematic coupling. The mid point for one of the features in the circumferential direction is selected as the zero degree rotationally which is coincident with the zero rotational degree of the M4 surface. As a result, the rotational relationship between the optical feature and fiducial features is established. The height relationship is established from the flat reference surface between the optical feature and the fiducial feature, the spindle rotational center point on the M4 surface shall be 4.139 mm lower than the flat reference surface the peak point of fiducial surface shall be 1.9 mm from the reference.

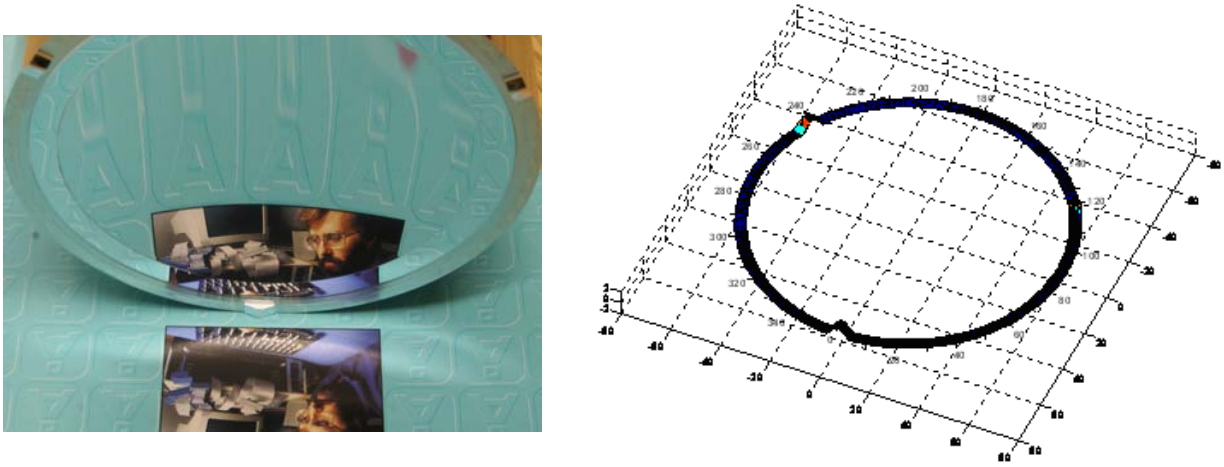

(a) (b)

Figure 19. (a) Machined mirror with fiducials and 3D model of the three fiducial features for kinematic coupling

Toolpath Generation and Test

The surface of the optical feature and the fiducial feature can only be represented by point cloud after correction for the tool nose radius. For the M4 surface shown above, the uniform polar mesh grid of 50×361 (mm or radial feed x degrees) is created only for NRS component, then the bilinear interpolation algorithm [6] is applied in real-time to generate NRS position command and acceleration command. The final position command for M4 mirror machining consists of three elements including circular path from the equation, NRS position command and residual error correction. Figure 20 (a) shows a test of tool motion at the spindle speed of 500 rpm and cross-feed rate of 200 mm/min when the radial position changes from 49 mm to zero, the tool positioning error in Figure 20(c) is within the ±100 nm. Figure 20 (b)and (d) provides close-up view of the tool motion and error magnitude for two revolution of spindle. The dominant motion amplitude is at the second harmonic of spindle speed because of the biconic surface.

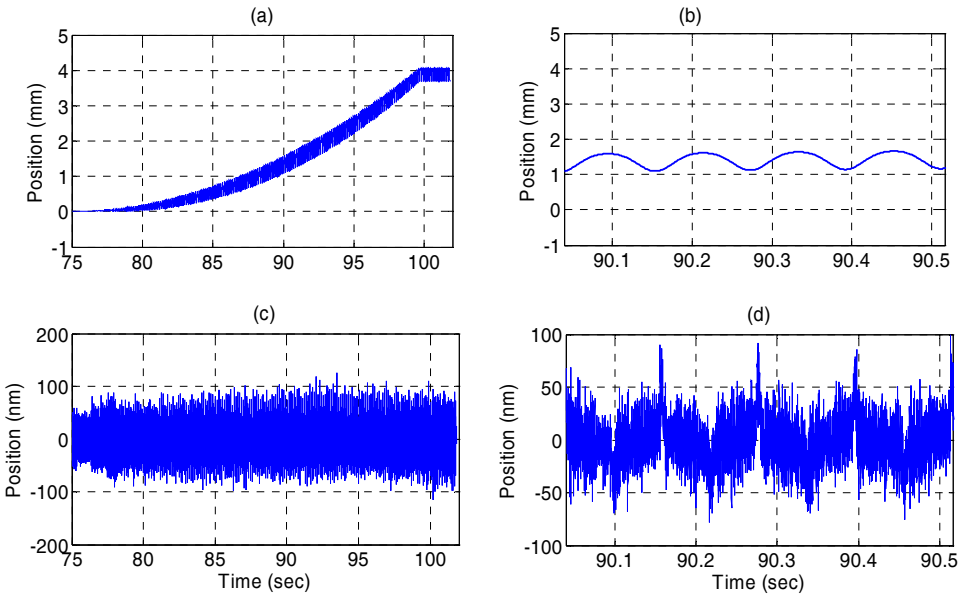

Figure 20. Motion test for the toolpath of M4 surface (a) The full toolpath (b) Close-up view for toolpath around 90 sec for two revolution of spindle (c) The tool servo positioning error in full toolpath (d) Close-up view for position error around 90 sec for two revolution of spindle

For the case of the fiducial feature, the dominant position command (Equation (15)) and acceleration command can be easily generated from sinusoidal function. The polar mesh grid is only created for the tool radius compensation part of surface profile as shown in Figure 21. Since the fiducial feature only has 8 mm wavelength in the circumferential direction and repeats itself every 120°, the grid covers an area a little larger than the size of the feature, i.e. radial range from 58.5 mm to 64.5 mm with grid spacing of 0.1 mm, the angle range within ±5° with grid spacing of 0.05°. The final position command is a combination of two elements including sinusoidal position command and additional position correction from tool radius compensation. In addition, there are two more considerations for the tool path generation:

(1) Since the dominant motion frequency of tool used to create the fiducial surface is 46~50 times of spindle rotational frequency, the spindle speed was reduced to 21 rpm to minimize the difference of dominant frequency level in the toolpath for both optical feature and fiducial feature. Changes in frequency of operation can introduce phase lag and the orientation of the fiducial surface with the optical surface.

(2) As shown in Figure 22, at the start and end of sinusoidal tracking, there are much bigger position errors. This is due to the fact that, the motion frequency changes along the radial direction which indicates the acceleration feedforward controller is as effective as the case of constant frequency. To reduce this error, three continuous cosine waves are used in the toolpath, but only the middle wave machines the surface. The position error is less than ±500 nm.

$$Z_{F1} = A\left(1 + \cos\left(\frac{\theta r}{8}\right)\right) \tag{15}$$

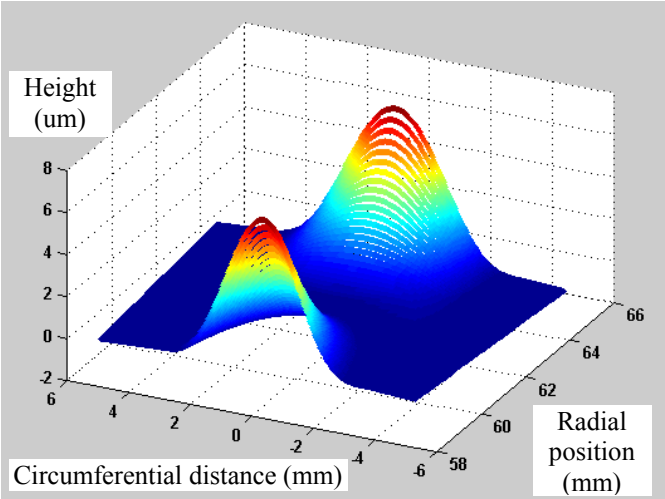

Figure 21. Tool radius compensation position profile for the fiducial feature

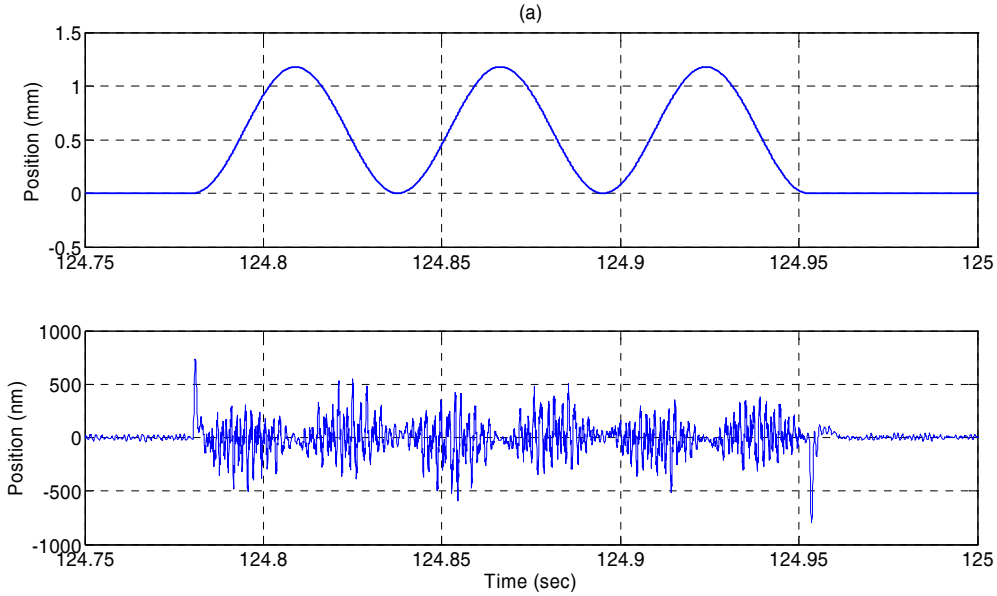

Figure 22. Toolpath for fiducial feature

Machining Process

Due to the requirement of using one setup to create three surfaces, there are large amount of materials need to be removed by one tool, tool wear will be significant over long cutting length for the diamond tool with 27° clearance angle. As a result, tradeoff has been taken among the

depth of cut and cross-feed rate vs. cutting length. . The tool wear will be measured using the technique discussed in Section 8. There are three major procedures to cut this NRS optic:

Rough Machining Use conventional machining process to cut a blank out of 6061-T651 Aluminum as shown in Figure 23. The thickness of the blank is large to avoid any distortion due to vacuum chuck attachment.

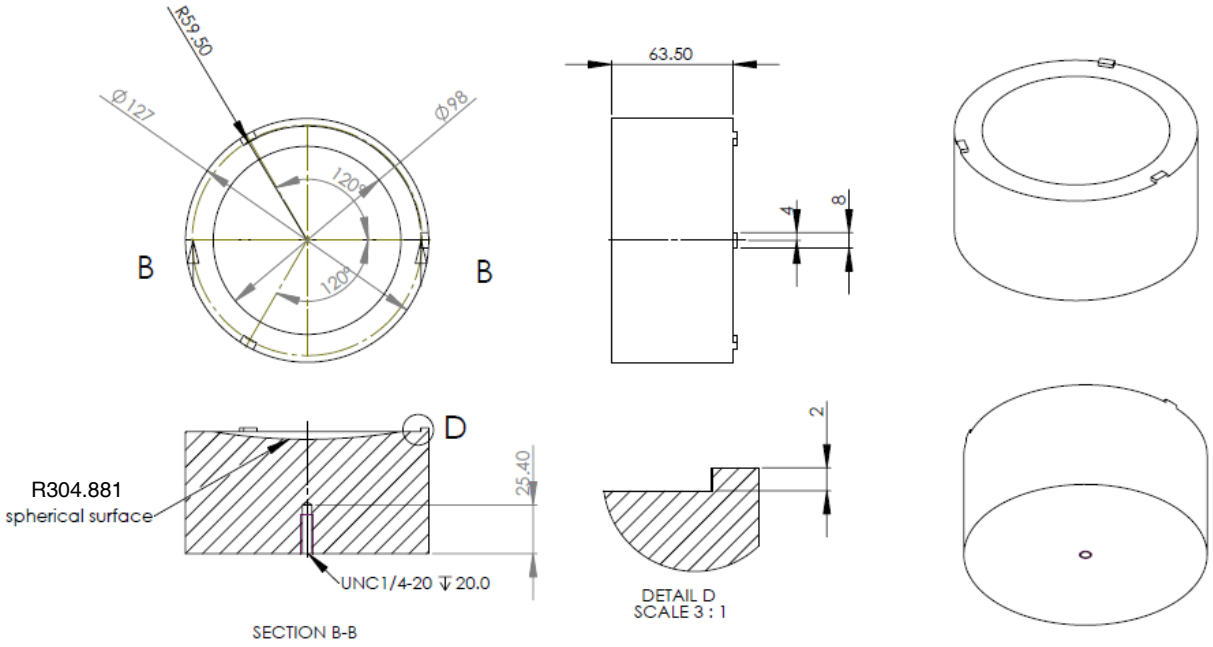

Figure 23. Optical blank used for the mirror and fiducial fabrication.

Preparation Machining of RS Surfaces Use a diamond tool with regular clearance angle and tool radius of 1 mm to cut three surfaces with following specifications

(1) Cut the flat between the radial position 57 mm and 49 mm
(2) Cut the spherical concave surface with a radius of 304.881 mm, the depth of spherical apex shall be 3.943 mm below the reference flat surface.
(3) Remove the material on the fiducial features till its top flat surface is 1.9 mm above the reference flat surface.

Detailed steps of Final Machining Use the customized tool with 27° clearance angle:

(1) Install the part with the θ=0° at the center of the selected fiducial feature.
(2) Set FLORA position at neutral value = 17.100 mm by active control
(3) Machine the flat reference surface (500 rpm spindle speed)
(4) Touch off on flat surface and remove 10 μm of material
(5) Shift the ASG-2500 DTM relative z position by -3.943+0.010 mm (*setz d -3.933*). This will set the desired position of the bottom of the sphere but the tool slightly above the surface.

This sphere has already been machined so the relative position of the flat and bottom of sphere should be correct.

(6) Move the ASG to the relative (x,z) position to (0,5)

(7) Machine the sphere (500 rpm spindle speed)

(8) Close FLORA control and restart with the sphere program in which the FLORA position depends on the radial position.

(9) Run ASG machining motion cycle[1] as (0,5)→(50,5)→(50,0)→(0,0)→(0,5), remove 10 µm of material to put the base of the sphere in the correct relationship with the flat (3.943). Depth of cut shall be 8 µm and feed rate 30 µm/rev for rough pass, depth of cut shall be 2 µm and feed rate 20 µm/rev for finish pass.

(10) Take off the part and measure the spherical surface, Figure 24 shows the spherical error of 225 nm.

(11) Put the part back to the chuck, Shift the ASG relative z position by 0.329 mm (*setz d 0.329*).

(12) Machine the M4 surface (500 rpm spindle speed)

(13) Close FLORA control, and reprogram and launch the FLORA control for the M4 biconic surface

(14) Run ASG machining motion cycle as (0,5)→(50,5)→(50,0)→(0,0)→(0,5), remove 0.329+0.216 = 0.545 mm of material. Depth of cut shall be 21 µm and feed rate 50 µm/rev for rough pass, depth of cut shall be 2 µm and feed rate 20 µm/rev for finish pass.

(15) The distance of the rotational center of M4 surface to the flat surface is 3.943+0.216-0.020 = 4.139 mm

(16) Shift the ASG relative z position by 1.9+3.943+0.216 mm (*setz d 6.059*).

(17) Move the ASG to the relative (x,z) position to (64, 5)

(18) Machine the fiducial surfaces (21 rpm spindle speed))

(19) Close FLORA control, and reprogram and launch the FLORA control for the fiducial surface

(20) Run ASG machining motion cycle as (59,5)→(64,5)→(64,0)→(59,0)→(59,5), remove 1.2 mm of material. Depth of cut shall be 20 µm and feed rate 50 µm/rev for rough pass, depth of cut shall be 2 µm and feed rate 20 µm/rev for finish pass.

[1] The command is (x,z) location in mm for machining the surface and return for the subsequent pass.

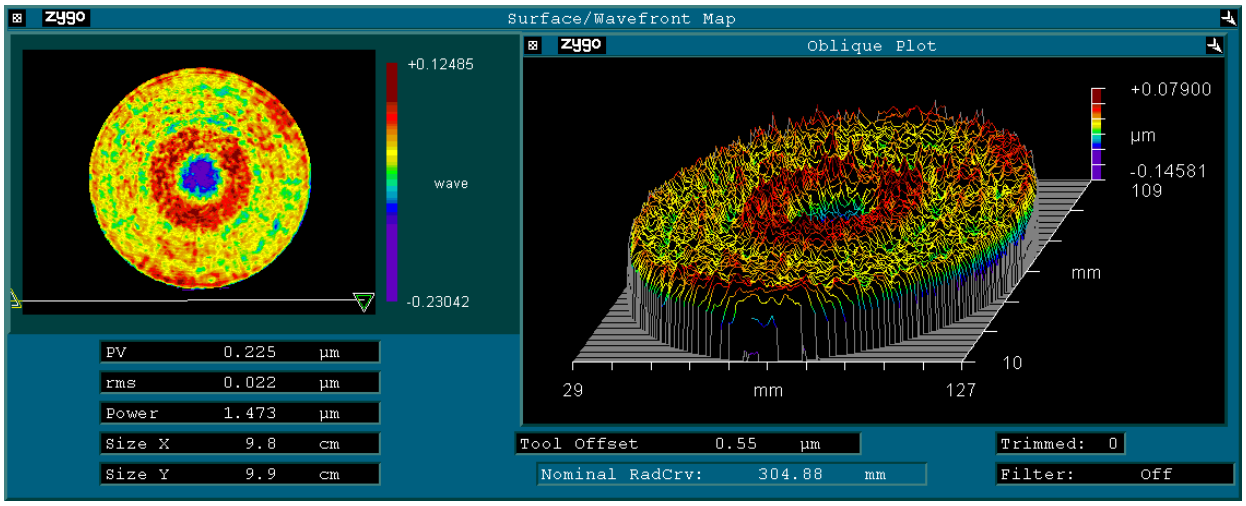

Figure 24. Measured spherical error of the 98 mm diameter sphere using laser interferometer

3.7 CONCLUSIONS

The FLORA has been successfully integrated to the ASG 2500 DTM to produce freeform optical surfaces with accompanying fiducial surfaces for assembly. It has been proven through machining tests that the tool servo control (from encoder scale to read-head) is a critical factor that determines the achievable surface quality. The smaller the positioning error, the smaller the surface form error and roughness. To achieve 100000 to 1 tool positioning precision (20 nm for 2 mm command) at a frequency of 20 Hz, a systematic approach is required to study the performance of each component and properly integrate them through high-speed, high-bandwidth real time control. The results achieved so far in the motion control and machining tests establish the base-line performance of the existing design and the new control system of FLORA but do not yet meet the figure and surface roughness goals for the project.

ACKNOWLEDGEMENT

This work is supported by NSF Grant CMMI-0556209 monitored by G. Hazelrigg.

REFERENCES

1. Lamonds, Lucas, Garrard, Kenneth and Sohn, Alex Erik's, "*Modeling of vibration and dithering in SPDT*", PEC Annual report, Volume XXIV, p59-95, 2006
2. Zdannovic, Erik, Eischen, Jeff and Dow, Thomas A, "*FLORA II*", PEC Annual report, Volume, p, 2008
3. Chen, Qunyi, Dow, Thomas A., Garrard, Kenneth and Sohn, Alex, *Fast long range actuator – FLORA*, PEC Annual Report, Volume XXV, p35-54, 2007.
4. Messner, W. and Bodson, M., "*Design of Adapative Feedwardard Algorithms using Internal Model Equivalence*", International Journal of Adaptive Control and Signal Processing, Vol 9, pg 199-212m 1995.
5. N. Buescher, "*Live Axis Turning*", MS Thesis, Dept. Mech Eng., North Carolina State Univ., Raleigh, NC, 2005
6. Garrard, Ken and Sohn, Alex, "*Off-axis biconic mirror fabrication*", PEC Annual Report, 2002.

4 KINOFORM LENS FABRICATION

Alex Sohn
Precision Engineering Center Staff

Kinoform lenses represent a specific subset of Fresnel lenses that are designed to use both refractive and diffractive power to manipulate light. The objective of this exercise was to demonstrate that Kinoform lenses for use in the visible light spectrum, with their typically small groove spacings of 30 µm and less, can be fabricated. Through the use of a specially adapted goniometer axis mounted on the PEC's Nanoform 600 diamond turning machine, several test parts were cut with the final part being a 5 mm annular segment of a 55 mm diameter aperture lens. Surface finish and groove fidelity were measured with good results.

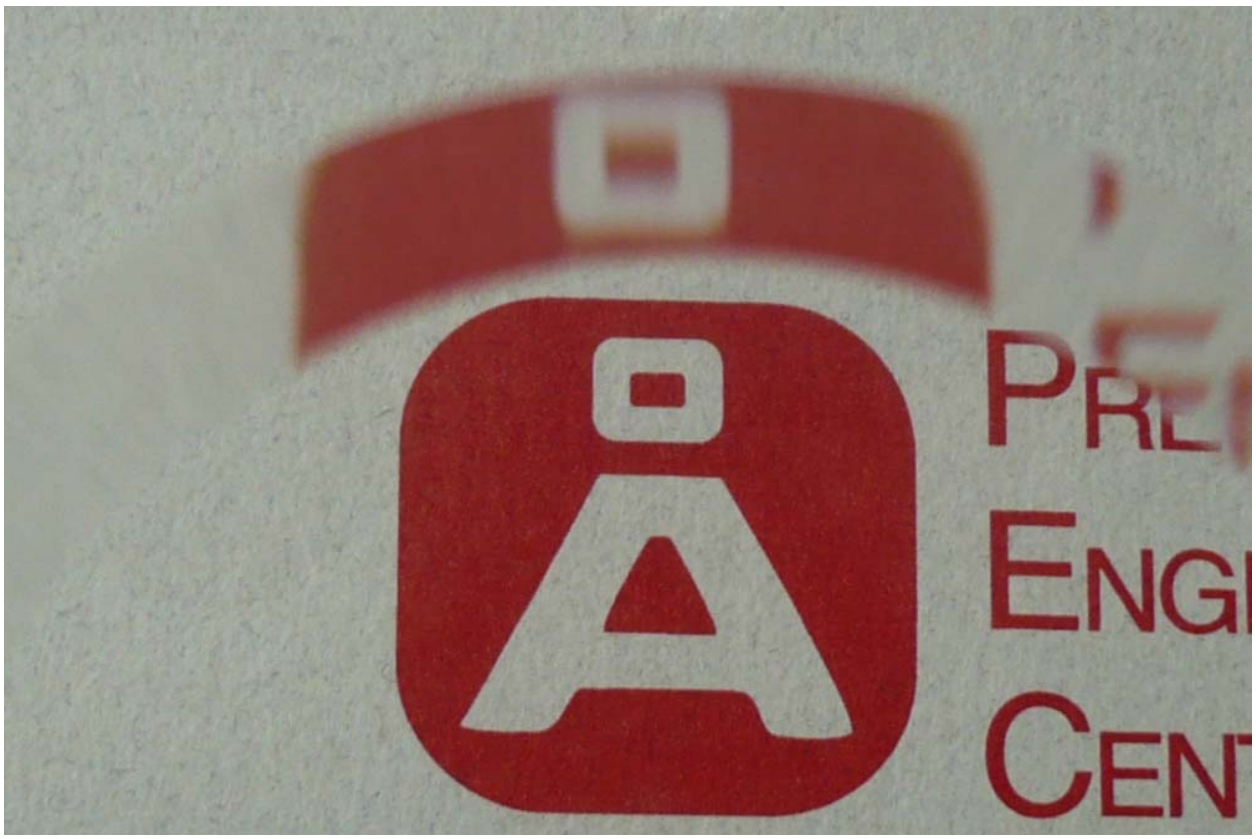

4.1 INTRODUCTION

In the course of a project to develop Fresnel lenses for scanning systems, it has been discovered that the discontinuities inherent in a Fresnel lens lead to diffraction. This diffraction can have undesirable results by redirecting light away from the focused spot and into other spots. Diffraction does not, however, have to be detrimental. The concept of a Kinoform lens is to tailor the diffraction to enhance the focusing ability of the lens instead of disturb it. With grooves spaced at precise intervals, it is therefore theoretically possible to achieve a spot size as good or better than without diffraction. In the real world, however, manufactuiring such lenses requires some compromises and challenges to available fabrication capabilities.

4.2 MACHINING

4.2.1 PRELIMIARY GROOVE CUTTING TESTS

The spacing and angle of the facets on the Kinoform lens determine the location of the refractive and diffractive beams. For a phase match order of M = 1 [1], the groove spacing must be very small at larger apertures and the lens becomes difficult to fabricate; for example, 6 μm spacing for a 200 mm f/l. lens at r = 11.5 mm. Even when the phase match order is increased to M = 5, the groove spacing is still very small. The lens cannot be contoured with a radius tool as is done for aspheric lenses, but rather must be machined as a series of plunge cuts as shown in Figure 2. The side of the dead sharp tool forms the flat refractive portion of the lens and must be rotated at each plunge to change the angle as the groove radius is changed.

Since kinoform lens grooves with the fine spacing required (5-50 μm) had not previously been fabricated at the PEC by turning, several test cuts were made in PMMA (PolyMethylMethAcrylate) to determine the best cutting conditions and procedures. Of primary interest was whether there was any appreciable influence of the cutting direction on the final parts. Figure 1 shows the diamond turning setup where an annular ring of grooves is cut with the dead sharp tool tilted at an angle.

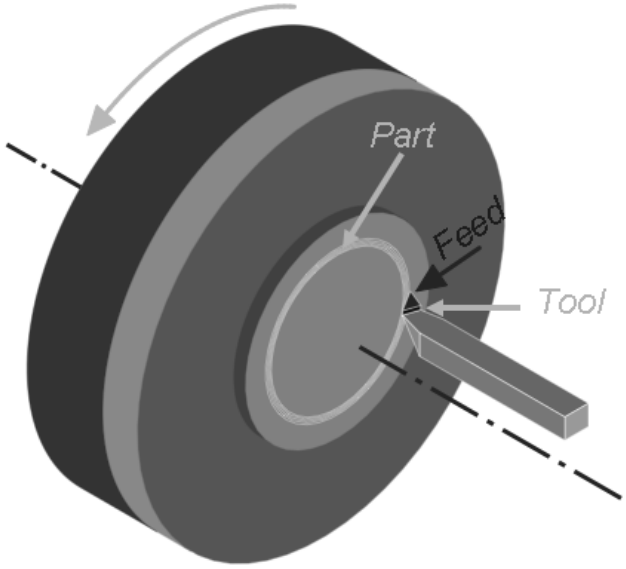

Figure 1. Setup for preliminary groove cutting tests.

The grooves were cut with the tool at a fixed angle in a stationary toolpost to ensure that compliance in a new, moveable tool holder would not influence results. To test the impact of cutting direction, plunge cuts were performed both from the inside to the outside of the part and vise versa as shown in Figure 2. This change in cutting direction produces a significantly different chip, as shown if Figure 3 though the overall amount of material removed in the same. This is thought to have a significant impact on the cutting mechanics and the final result of the cut. The SEM micrographs in Figure 4 show a distinct difference between the surfaces as a result of the two different cutting directions. It appears that while the outside-to-inside cut produced grooves that are relatively free of burring, the inside-to-outside cuts produced large "curtain" like burrs that were firmly attached to the tips of the grooves. This is believed to be caused by the chip remaining attached at the tip of the groove because the tip of the previously cut groove is now unsupported and can easily deform around the cutting edge of the tool.

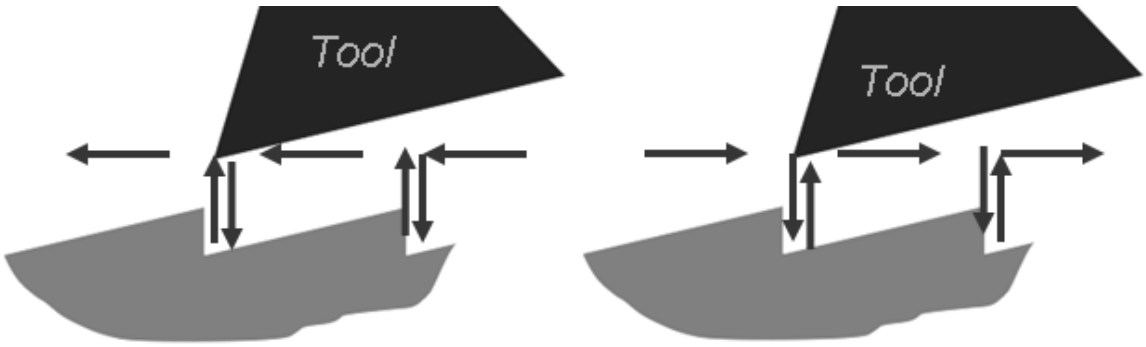

(a) (b)

Figure 2. Preliminary cutting tests shown with different cutting direction a)outside to inside and b) inside to outside.

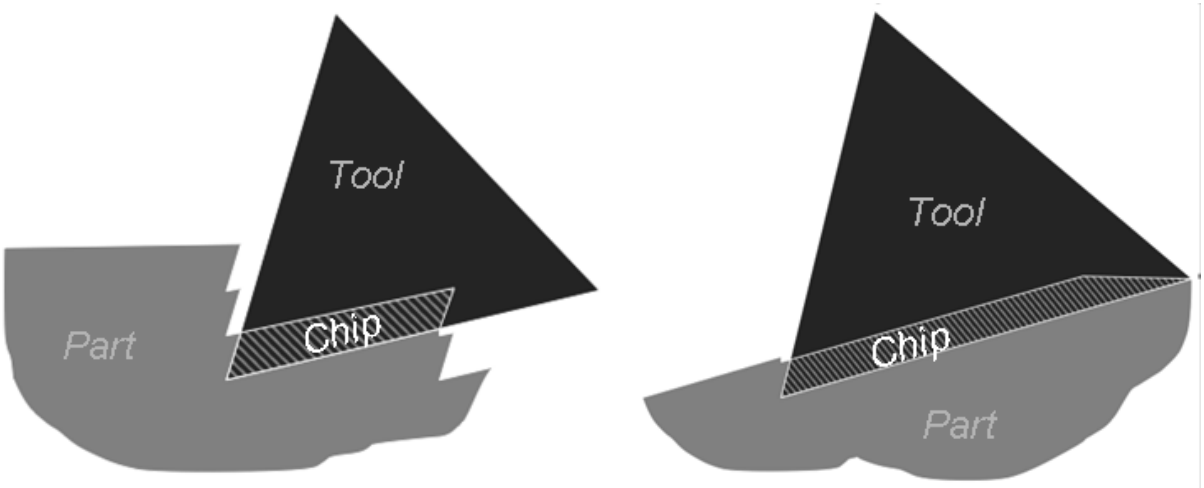

(a) (b)

Figure 3. The chip cross section differs significantly for a) outside to inside and b) inside to outside cutting.

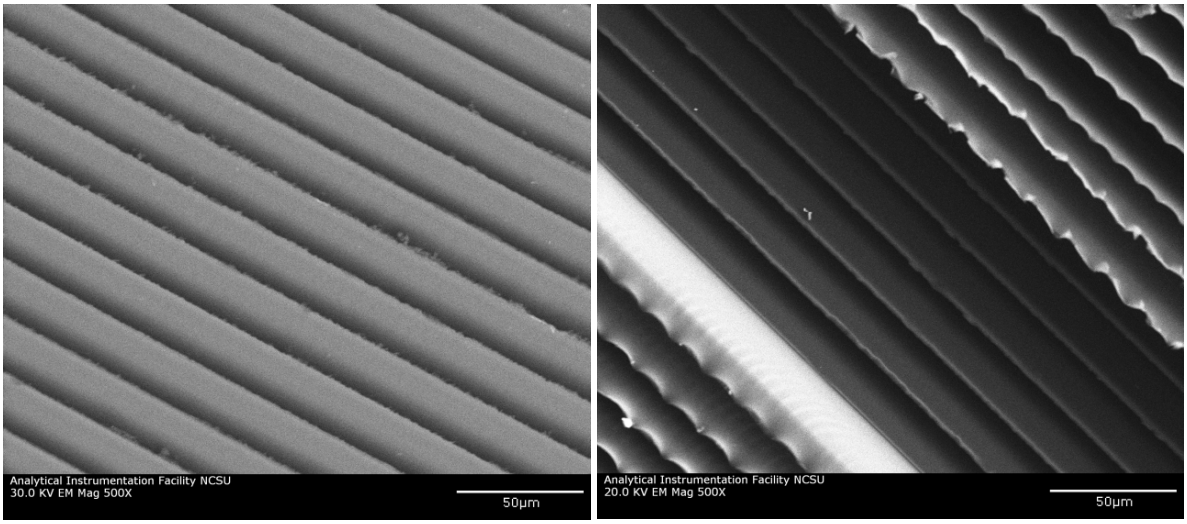

Figure 4. The chip cross section differs significantly for a) outside to inside and b) inside to outside cutting.

Based on these results, all subsequent cuts were made in the outside-to-inside direction. An additional set of tests was performed using different coolants. These tests showed little difference between the use of ionized air, mineral spirits or cutting oil. Given that the coolant did not matter, ionized air was used for all tests since lenses cut in this way are much easier to clean.

4.2.2 FLEXURE-BASED TOOL HOLDER

Ideally, a rotary axis (oriented perpendicular to the X-and Z- axes of the diamond turning machine) would be used to rotate the tool. Unfortunately, neither of the diamond turning machines at the PEC has such a rotary axis, so a temporary solution was devised to machine small segments of Kinoform lenses. This tool rotation device was based on a flexure mechanism that is mounted on the cross-feed axis of the DTM and a linear stepper motor that is used to push on the actuation point to rotate the tool as shown in Figure 5.

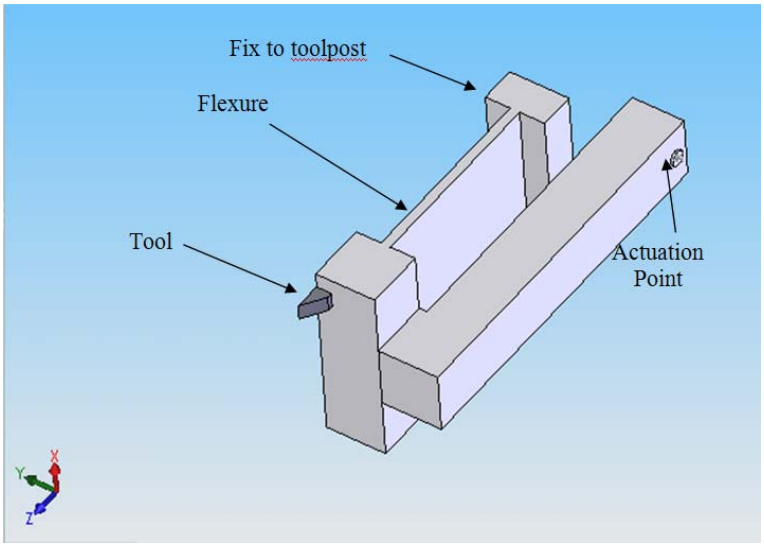

Figure 5. Flexure based tool rotation mechanism. A flexure that is very stiff in the vertical direction allows the tool to rotate in the Y-Z plane.

The force at the actuation point produces a force and a moment at the tool. The moment rotates the tool and the force moves it in the y-direction creating a small motion in the z-direction (depth of cut). The flexure was designed to allow actuation at reasonable forces without exceeding the yield strength of the aluminum flexure. A finite element model was used to evaluate the stress vs. deflection for different flexure designs. The results indicated that the flexure could tilt the tool up to 2 degrees while staying within 20 % the yield stress of 6061-T6 aluminum.

The flexure bends predictably and causes deflections of the tool that can be modeled. Parameters of interest are 1) position at the actuation point 2) deflection angle 3) position of the tool tip. After modeling, the same parameters were measured on the mechanism and a linear relationship (close to the calculated one) between the tool position and angle was developed. Larger tilt displacement is possible by extending the load arm.

4.2.3 TOOL HOLDER USING BALL-BEARING GONIOMETER

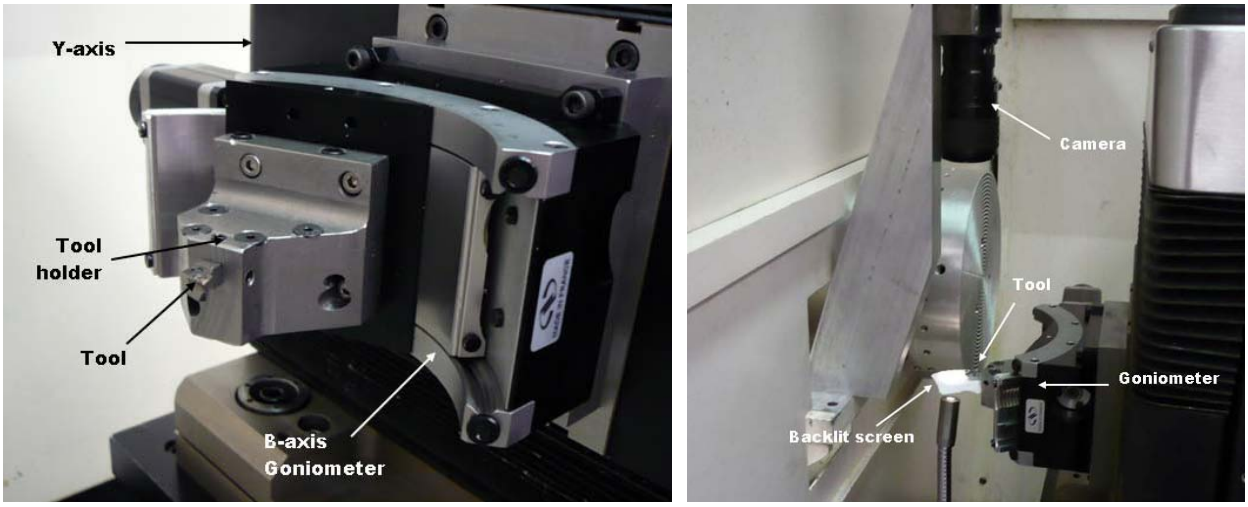

(a) (b)

Figure 6. Newport Goniometer mounted on y-axis of diamond turning machine with a) showing a closeup of the axis and b) showing the placement on the DTM with camera looking down.

Mounting and Control of the B-Axis

Equipment funding from NC State University became available near the end of the project and a ball-bearing goniometer B-axis was purchased to fabricate a larger range of angles than are possible with the flexure design. The B-axis is mounted to the Nanoform 600's Y-axis and the tool is held securely via a non-adjustable tool holder as shown in Figure 6. The control integration of the goniometer axis is performed using an external dSPACE DSP controller. The dSPACE system reads axis data from the Nanoform 600's Zygo ZMI 501 laser system quadrature output. This axis position data is then used to find a corresponding B-axis coordinate position in a lookup table generated off-line. The B-axis coordinate is then converted to step/direction signals and sent to the stepper driver via the dSPACE digital I/O interface. The digital I/O also interfaces to the B-axis' limit and home position flags. This allows the axis to be homed at the zero (centroid) position and provides an absolute reference.

Tool Centering

Centering the tip of the dead-sharp tool mounted on the B-axis is performed using correcting motions of the X and Z-axes of the DTM instead of actually repositioning the tool. To calculate the necessary motions of the X and Z-axes, the tool offset must first be measured. To measure tool position, a CCD camera with 100X magnification optics and crosshair reticule is mounted above the tool as shown on the right in Figure 6.

Figure 7. Image from video camera used to find the errors in tool edge positioning as a function of the angle of rotation of the ball-bearing goniometer

With the tool in focus, the machine axes are moved to make the tip of the tool coincident with the crosshairs. A monitor shows the tool relative to the crosshairs in Figure 7.

The procedure for B-axis centering of the tool is as follows:

1. Zero the X and Z axes at B=0. Measure X and Z-positions as a function of B. A minimum of three positions is required. More points will yield a more robust fit that sees less influence from individual measurement errors, particularly since the maximum included angle of points is 90º.

B	X	Z
B_1	X_1	Z_1
B_2	X_2	Z_2
.	.	.
B_n	X_n	Z_n

2. Fit X, Z data to obtain R, X_c and Z_c. Use circfit in Matlab. Also, obtain the initial angle

$$B_0 = \arctan\left(\frac{Z_c}{X_c}\right) \tag{1}$$

which is the angular offset to the center of the circle.

3. Now, any point's corrected X and Z position can be calculated from the B-axis position:

$$\begin{aligned} X' &= X_c + R\sin(B - B_0) \\ Z' &= Z_c + R\cos(B - B_0) \end{aligned} \tag{2}$$

where the addition of the circle center coordinates offsets the tool to allow programming relative to B=0, which can then be used to touch off on the part.

4. The corrected positions X' and Z' can then be added to the programmed positions as a function of B in any part program.

4.2.4 CONTROL

The coordinates and angles of the grooves are calculated using the diffraction modeling software developed by Garrard [1]. The form of these coordinates is X and Z at the bottom of each groove and a slope for each facet. These points are read into Excel, where a spreadsheet adds the X and Z axis corrections and appends the G-code components to allow the PMAC-NC controller to run the part program. Also added are the rest of the points required to make the series of plunge cuts and a dwell command for at least one spindle rotation at the bottom of each groove. The spreadsheet is saved as plain text to avoid conflicts with the controller which often result from Unicode text (default excel text format). The coordinates and angles are also processed into a set of corrected X and angle (B-axis) values that are saved as a plain text lookup table for the D-space program. The dSPACE controller is programmed in Simulink and has a Control Desk user interface.

4.3 METROLOGY

The surface finish and flatness of the kinoform lens facets is excellent. Figure 8 shows the surface finish of one facet of the lens. It is about 28 µm wide and is flat to 19 nm over this width; that is, about one part in a thousand. The surface finish is also exceptional - 2.7 nm RMS. Some of the facets had high frequency features from the plastic shearing during machining, but in general, the surface illustrated in Figure 8 reflects the quality of the machined features.

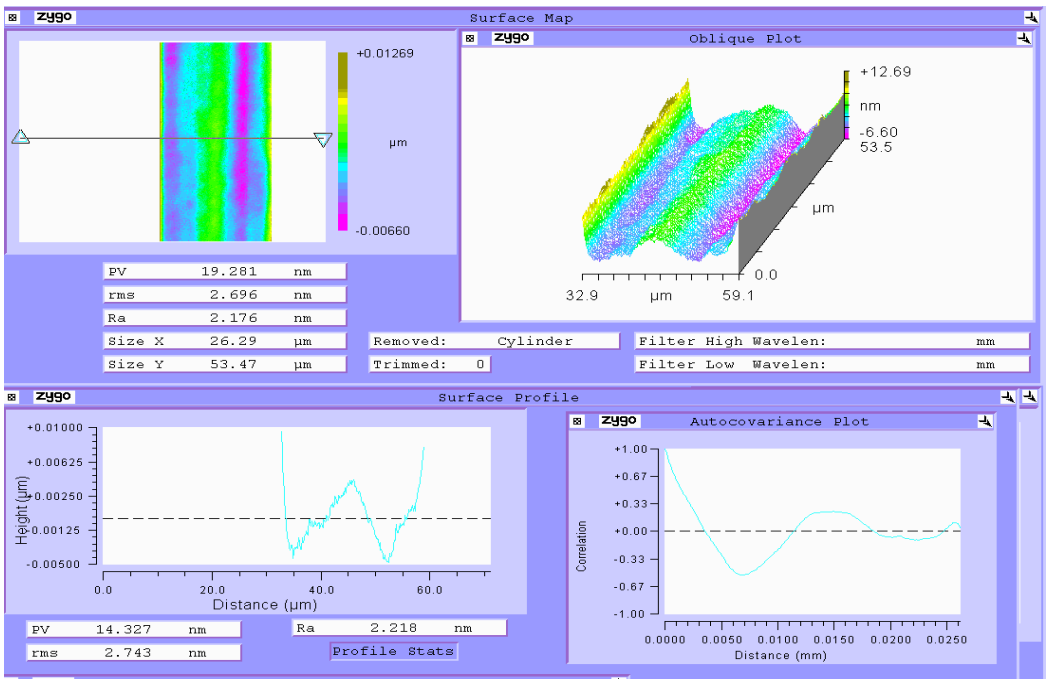

Figure 8. Surface finish of a facet of the kinoform focusing lens. The face of the facet is flat to 19 nm over a width of 28 µm and the surface finish is 2.7 nm RMS.

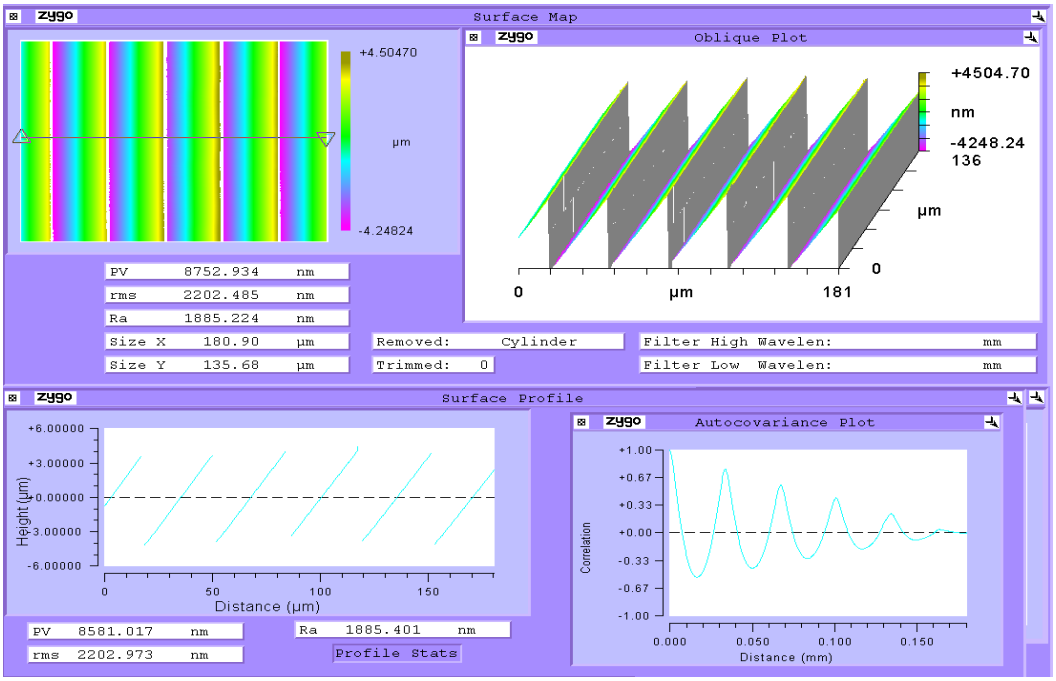

Figure 9. Shape of selected kinoform facets machined on the DTM. Note the variation in the height of the grooves (approximately 1 µm) in the lower left-hand section of this figure.

Figure 9 shows a white-light interferometer (Zygo NewView) image of a number of grooves over a surface area which 180 µm long and 136 µm wide. The depth of the grooves in this section of the lens is approximately 9 µm deep with a spacing of 33 µm and a tilt angle near 14 degrees. One feature of the grooves which is a concern is the variation of the depth of adjacent facets as illustrated in the lower left cross section of Figure 9. While this single cross section does not definitively identify a problem, it indicates that variations in the depth of cut caused by goniometer repeatability or non-synchronous spindle errors may be a factor in the performance of the lens.

The kinoform lens was designed to have the path length from adjacent facets to the focus to be exact increments of 7 times the wavelength, or 5.55 µm. This factor (called the phase match order M in the derivation earlier in this report) matches the phase of the refracted light so that the location of the constructive interference can be controlled. However, to achieve this design, the tolerance on the facet tilt and location must be carefully controlled. The variation illustrated in Figure 9 may be an indication of a fabrication problem.

4.4 CONCLUSIONS

While the machining process for the kinoform lens still requires some refinement, the results of the first cut are encouraging. In order to achieve higher tolerances on groove spacing, it is likely that a more sophisticated tool tilting mechanism will have to be employed. Apart from this, the surface quality results of the lens were excellent, showing that the plunging process is feasible for generating the stepped conical features of a Kinoform lens.

REFERENCES

1. K.P. Garrard, *Fresnel Design Software*, 2008 PEC Annual Report, pp1-23.

5 WEAR ANALYSIS OF DIAMOND TOOL ON AL6061 AND 1215 STEEL

Brandon Lane
Graduate Student
Thomas Dow
Professor, Department of Mechanical and Aerospace Engineering
Ronald Scattergood
Professor, Department of Materials Science and Engineering

Studies have shown the benefits of applying micrometer scale vibration motion of a diamond tool during precision diamond turning (DT). Reported benefits include a decrease in machining forces and consequent wear of the diamond tool. The particular causes for decrease in force and wear while utilizing vibration assisted machining (VAM) are not well understood, nor is there great understanding in the wear mechanics of a normal diamond turning operation for many materials. Orthogonal cutting experiments using 6061 Aluminum and 1215 Steel were conducted, and wear of the diamond tool was closely observed using the electron beam induced deposition method. This method provides precise measurement of tool wear geometry, which is in turn used to calculate tool stresses, volumetric wear loss, and wear rates. Comparisons are made between the modes of tool wear resulting from the two materials. These observations will later be used in comparison with data collected during similar experiments utilizing VAM. Noted benefits of VAM will then be verified and quantified, and a greater understanding of the diamond tool wear process will be achieved.

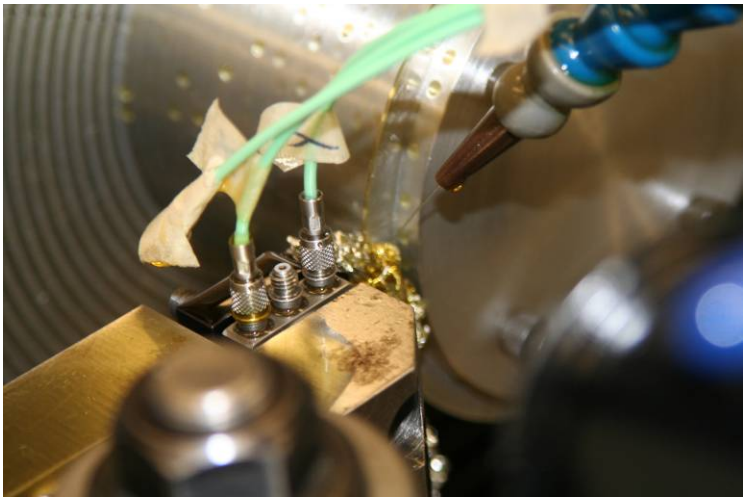

5.1 INTRODUCTION

Diamond turning (DT) has revolutionized the fabrication of optics and precision devices since its inception in the early 1970s. Some materials, however, have proven to be difficult if not impossible to machine with a single crystal diamond by standard turning methods. This difficulty is due to either the brittle nature of the material or excessive wear on the diamond tool. Vibration assisted machining (VAM) was introduced into the DT process to alleviate these issues by allowing the diamond tool to separate from the workpiece and return to contact in cycles occurring 1000s of times per second. VAM has been proven through many studies to decrease tool forces and tool wear while sustaining optical quality surface finish on precision turned parts [1]. Of particular interest is a variation of VAM called elliptical vibration assisted machining (EVAM). An EVAM device created at the Precision Engineering Center (PEC) at North Carolina State University called the Ultramill enables the tool vibration frequency to be altered from 1-4kHz along with the size and shape of the elliptical tool path. This enables the EVAM process to be studied while varying the cutting parameters. A comprehensive study is underway to determine the principles behind the improvements encountered with EVAM, and quantitatively explain processes such as material flow, heat generation, tool wear, and tool forces.

Before experiments are conducted using EVAM, baseline studies on standard DT processes must be conducted as a means for comparison. Aluminum and steel alloys are common engineering materials that pose challenges to standard DT due to tool wear, but are more machineable when VAM is utilized. Al6061 is a standard aluminum alloy that contains hard alloying microstructures that cause tool wear after extended cutting. The method of wear is presumed to be abrasive in nature due to these included microstructures. Steel alloys have proven to be even more of a challenge than Al6061. Wear rates of diamond on steel are exceedingly high, and have been found to be on the order of one carbon atom lost from the tool for every five atoms of clean metal passing over the diamond [2]. Wear due to steel and other ferrous alloys occur from chemical interactions between the diamond and cutting material. These reactions are exacerbated by high cutting temperatures. 1215 steel was chosen for this experiment due to its similar hardness properties to Al6061, and the promised effect of high wear rates.

The cutting process is complicated in nature combining interactions such as high stresses accompanying plastic material flow, strain-rate temperature effects, friction forces and heating, and chemical interactions. This process is simplified as much as possible by proceeding with orthogonal cutting conditions during experimentation. This allows cutting interactions to occur at approximately the same rate along the length of the tool edge. By creating a workpiece that is smaller than the width of the diamond edge, the process is simplified more by having a specific

location on the tool where the cutting process will occur. This also creates a section of diamond that can be worn by the workpiece material while maintaining and unworn region for direct comparison.

In previous studies at the PEC [3,4], a method for measuring tool wear was developed that is capable of resolutions of less than 10nm. Utilizing electron beam induced deposition (EBID) encountered during use of a scanning electron microscope (SEM), a stripe is created perpendicular to the tool edge. This stripe creates a traceable contrast on the SEM image that follows the edge of the diamond tool and can be used to accurately measure the worn profile of the diamond tool. To date, no reports on the use of the contamination stripe method to measure tools worn after VAM or EVAM cutting have been found. The EBID method is used extensively in this paper for the analysis of diamond tool wear.

This paper presents comparisons of tool wear encountered when orthogonally cutting Al6061 and St1215 with a diamond tool. Cutting force measurements coupled with EBID imaging allow for an in depth view of the cutting process. Comparisons can be made between the effects of predominantly abrasive wearing materials and chemical wearing materials. These comparisons can then provide a basis of understanding and comparison for future experiments utilizing EVAM.

5.2 EXPERIMENTAL SETUP

5.2.1 WORKPIECE MATERIAL

Two workpiece material holders were fabricated. Previous studies on the wear of diamond on Al6061 required cutting distances on the order of kilometers before measureable wear could be observed [3,4]. This requires a workpiece holder that can incorporate multiple, replaceable aluminum disks. The fabricated holder for this experiment consists of a thick aluminum base and cover plate that fastens the workpiece disks with four cap screws. The thick base and cover plate prevents deformation caused by the vacuum chuck, and limit plate waviness and runout in the spindle axis direction. Axial runout of the disks was measured prior to DT using a Federal gauge, and resulted in magnitudes of less than 15μm.

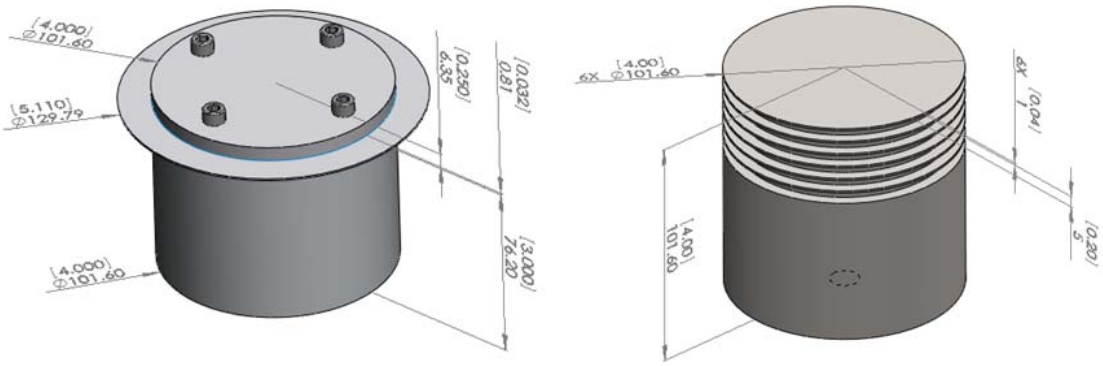

Figure 1: (*left*) Holder for replaceable Al6061 disks. (*right*) Fins created directly in 1215 steel material.

A sheet metal form of 1215 steel could not be purchased; therefore it was decided to fabricate turned surfaces and holder out of one piece. Fins were machined on a 4in diameter rod of 1215 steel that could be diamond turned in the same manner as the aluminum. Previous attempts at turning 1010 steel provided excessive forces and wear after 34m cutting distance, therefore large amounts of cutting material was deemed unnecessary for the 1215 steel. The length of the 1215 steel fins was also made short to reduce axial runout. Axial runout of the leading fin was found to be less than 10µm. Figure 1 shows dimensions of the aluminum disk holder, and the steel fin workpiece.

5.2.2 FORCE MEASUREMENT

Cutting forces contribute to the degree of wear of diamond tools, therefore a force measurement system was incorporated into the tool post shown in Figure 2. The post allows cutting forces to be freely resolved into the load cell axes while maintaining the high required preload. A Kistler 9271A three-axis load cell was used.

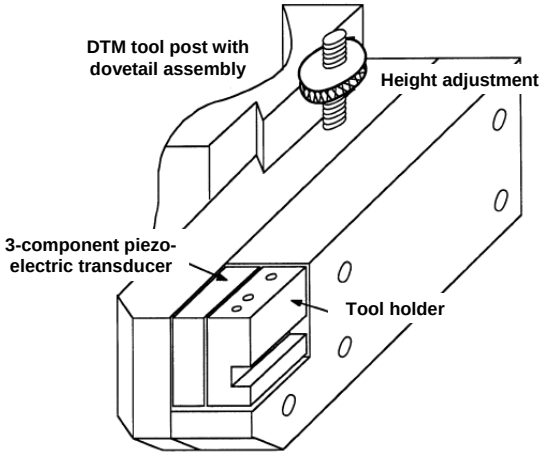

Figure 2: Diamond tool post incorporating 3-axis piezoelectric load cell.

Load cell charge signal was directed into a Kistler 3504 three-channel charge amplifier, and into a National Instruments SCB-88 data acquisition board. A NI Labview virtual instrument was programmed that allowed data acquisition of 1000 samples/s and forces to be monitored on a virtual oscilloscope display.

5.2.3 CUTTING PARAMETERS

A previous study at the PEC was conducted that attempted several depths of cut (DoC) during orthogonal cutting of Al6061 [5]. Cutting parameters for the experiments expressed in this report were chosen based on experience from these previous experiments, and are given in Table 1. Larger DoC's created chips that clustered on the tool, even while using oil and an air stream in an attempt to blow them free. Large buildup of chips on the diamond tool may obscure accurate force measurement and interfere with application of coolant. A depth of cut of 2µm was found to be an appropriate DoC that allowed chips to be cleared from the diamond tool. A separate study observed the tool forces while cutting 1010 steel disks at a DoC of 2µm. Cutting forces were very high (>10 N) when compared to those when cutting aluminum (~1-3N) and large vibration occurred (1:1 signal to noise ratio). Reducing the DoC to 1µm allowed for reduced forces, yet large vibrations persisted on the 1010 steel. 1215 steel was attempted as replacement material due to its greater stated machinability and similar hardness to Al6061. The DoC of 1µm was maintained to reduce cutting forces.

Table 1. Cutting parameters and material properties for two materials used in the experiment.

	Al6061 Disk	**St1215**
Cutting Distance, d_s	10 km (4 x 2.5 km)	40 m (4 x 10m)
Cutting Velocity	3.40 - 2.66 m/s†	2.13 m/s
Depth of Cut	2 µm	1 µm
Material Width, w	0.813 mm	1.20 mm
Material Hardness, H	1185 MPa*	1716 MPa**
Young's Modulus, E	70 GPa**	200 GPa**
† Cutting velocity is reduced as disk diameter is reduced * Determined from Vicker's microhardness test ** Determined from Matweb.com		

The tool used to turn the Al6061 disk was a flat edge natural diamond tool with 2.045mm wide cutting edge, 0° rake, and 6° clearance angle. The tool used to turn St1215 fins was a round nose natural diamond with a nose radius of 5.409mm (2.082mm wide), 0° rake, and 12° clearance angle at the center of the tool.

The Al6061 and 1215 steel were turned using an ASG 2500 diamond turning machine. Prior to cutting, the aluminum disk or steel fin was approximately aligned with the center of the straight edge tool. Machine axis coordinates were stored in memory so that the tool center location could be relocated with consecutive cuts. Material was initially turned with a carbide tool to reduce runout of the disk and fin perimeters. This ensured reduced vibrations in force measurements during initial contact with material, and maintained a more accurate measure of cutting distances. All cutting was conducted with an oil stream and compressed air directed at the cutting region.

Four cuts were made each for the Al6061 and St1215 at 2.5km and 10m cutting respectively for a total of 8 cuts. After each cut, the diamond tool was removed for wear analysis. The tool was put in a batch sonicator with de-ionized water and mild detergent for 5 minutes to remove any machine oil. The tool was rinsed again with water and dried with compressed air. A small drop of 5wt% sodium hydroxide solution was placed on the tool after cutting aluminum, or a 5wt% nitric acid solution was used for the steel tool to remove any material buildup deposited during cutting. The sodium hydroxide or nitric acid solutions were allowed to sit on the tool for 5 minutes. The tools were once again rinsed with de-ionized water, dried with compressed air, and carefully brushed with an optical wipe saturated with isopropyl alcohol. After cleaning, the tools were examined with the SEM before being returned for another of the consecutive cuts.

5.2.4 DIAMOND TOOL WEAR MEASUREMENT

EBID Method

A method for directly observing and measuring the wear of diamond tools was discovered by PEC personnel in the early 90's. The electron beam induced deposition (EBID) method utilizes the effect of focusing a low voltage electron beam within a SEM chamber to grow hydrocarbon contamination on the diamond surface. A deposition stripe creates a contrast along the tool edge, which in turn can be measured; SEM images without this contrast only allow subjective observation, and the tool edge profile cannot be distinguished. The deposition stripe and tool edge is tilted at a known angle on the SEM stage, and images taken with this orientation can then be stretched in a manner that recovers the true dimensions of the deposition stripe and tool cross section. Measurements can then be taken of the stretched images that provide accurate analysis of tool wear. Figure 3 shows examples of EBID-SEM images that were taken of the same diamond tool on the unworn and worn region. These images are vertically stretched to replicate the cutting edge cross section geometry. Details of the EBID process are described in section 8 Diamond Tool Edge and Tool Wear Measurement by EBID.

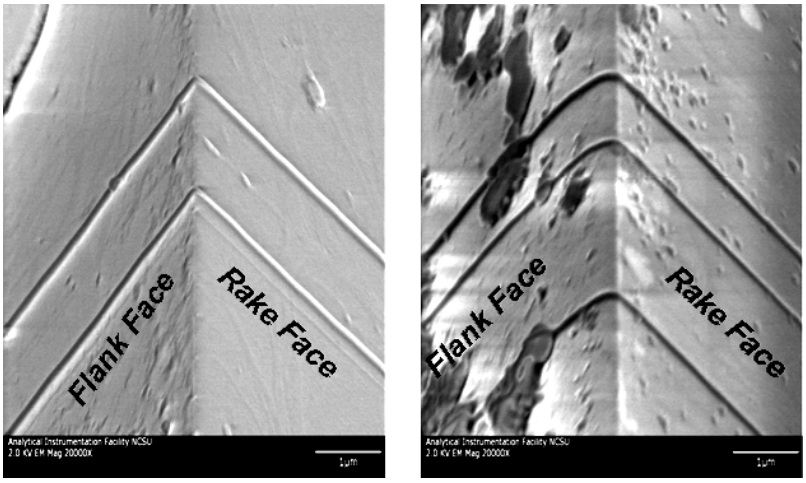

Figure 3: Example of vertically stretched SEM images of diamond tool edge worn after cutting 5km of Al6061 and contamination stripes used to measure wear. *(left)* Unworn region of diamond tool. *(right)* Worn region in center of tool shows rounding of tool edge.

Image Analysis

While the contamination stripe method allows for an accurate means of measuring tool wear, subjectivity errors may still occur during image analysis. A Matlab program was created to address these issues, and create an environment that allows for accurate and objective measurement of the SEM images. Digitize09 utilizes script that allows for individual pixels to be selected from an SEM image and have their respective X-Y coordinates stored. Geometric calculations can then be conducted using these selected pixel coordinates.

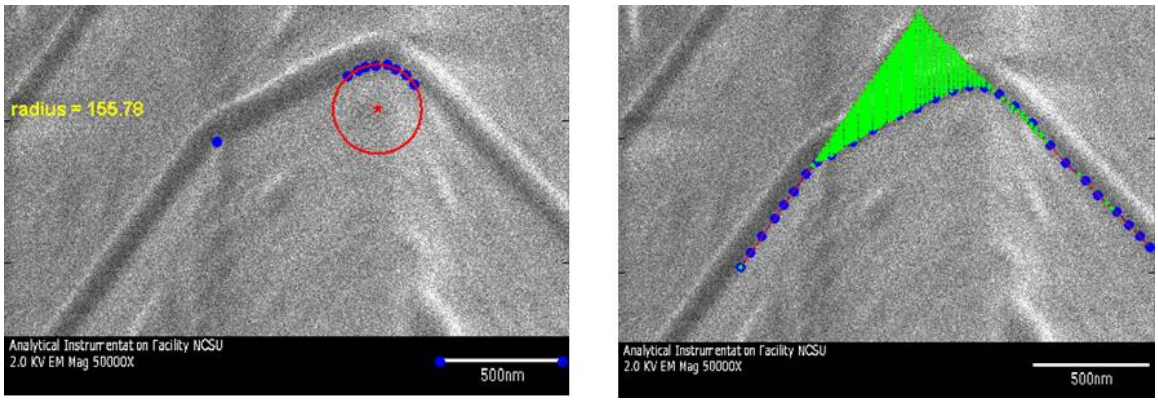

Figure 4: Tool edge measurements taken via Digitize09 of tool worn after cutting 10m of St1215. *(left)* Tool edge radius measured from circle-fitting algorithm along with wear land, and measurebar. *(right)* Worn area and tool edge angle are measured.

Subroutines were created for Digitize09 that calculate radii of curvature, worn areas, and tool edge angles. A least squares circle-fitting algorithm was used to approximate radius of curvature of a selected group of pixels which is used to approximate worn tool edge radius. An example of this least squares fit circle is given in Figure 4, left. The worn-area subroutine utilizes coordinates of pixels selected along the entire tool-edge/contamination stripe (blue dots in Figure 4, right). A line fitting algorithm is used for pixel selections that occur along the rake and flank faces of the tool image. These lines correspond to the unworn tool edges, and are used to determine the tool edge angle. This angle can be compared to tool manufacturer specifications, and verify that the SEM image accurately depicts a cross-section of the tool edge.

By locating the point of intersection of flank and rake lines, a polygon can be formed with a perimeter that consists of worn and unworn edges. The green shaded region of Figure 4, right shows an example polygon resulting from the selected pixels along the rake and flank face, and the point of intersection. If the vertices of polygon are known, a numerical form of Green's theorem can be utilized to calculate the area enclosed by the polygon. Green's theorem relates a closed path integral to the area bounded by that path. Fortunately, the Polyarea function is supplied in the Matlab function library which applies Green's theorem to set of polygon vertices, and is used to calculate the worn area of the diamond tool.

5.2.5 Analytical Analysis of Forces and Wear

Wear Parameters

Typical wear on a diamond tool that has undergone extensive orthogonal cutting can be described by a flattened region called the wear land, and a rounding of the cutting edge called the nose radius. Figure 5 depicts the locations of these wear parameters with respect to the cutting direction and material flow under the tool. While wear does occur on the rake face of tools, the majority of volume loss occurs from the formation of a these two features.

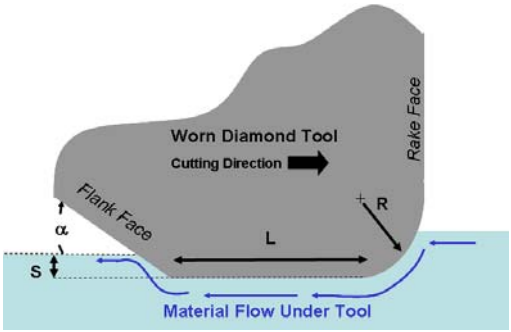

Figure 5: Side view schematic of wear parameters used in force and wear calculations. Material flow along rake face not depicted.

In the scenario of purely abrasive wear, the wear land will occur parallel to the cutting direction and material flow under the tool. This can be assumed, since any hypothetical portion of the tool that protrudes further into the cutting material will experience higher forces, therefore will be worn at a higher rate until the wear area is again parallel to the flow of abrasive material. For this reason, if the wear land does not occur parallel to the material flow, abrasive wear cannot be the dominant wear mechanism.

If the wear land occurs parallel to the cutting direction, and cutting occurs with zero degree rake angle (rake face is perpendicular to cutting direction), the worn area can be calculated from simplified wear geometry. The wear area illustrated in Figure 6 can be described by the nose radius, r, the wear land length, L, and the clearance angle, α, in the following formulation.

$$A_w = r^2\left(1-\frac{\pi}{4}\right)+\frac{1}{2}\left(L+r\right)^2\tan\alpha \tag{1}$$

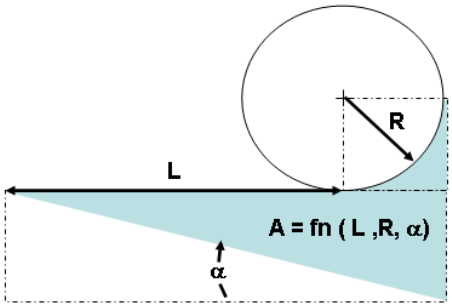

Figure 6: Schematic of parameters used to calculate worn area in the case of zero rake angle and wear land parallel to material flow.

Wear areas calculated by the abrasive wear assumption can be compared to those found by integration methods, such as those used in Digitize09 (see Figure 4, right on page on p.85) While agreement between results from both methods does not verify any particular wear mechanism, it simplifies the problem of describing wear and tool forces using the same parameters.

Tool Force Model and Archard Wear

Forces on the diamond tool are one factor known to contribute to the wear of the tool. A model for the tool forces was created by Arcona at the PEC that has proven abilities in predicting tool forces during the diamond turning process [4], and has also been incorporated into tool force models for VAM [6]. Concluded from experiments observing the cross-section of the formation of chips, the model incorporates a force balance on a section of the chip that includes the assumptions of uniaxial material flow stress acting normal to the shear zone, and a VonMeses

failure criterion for pure shear acting in the direction of the shear zone. In addition to the chip section force balance, models for sliding friction forces and thrust forces associated with material springback, *s* were made (see Figure 5 on p.86). Based on previous research into material springback during indention hardness tests, Arcona hypothesized that the ratio of the springback to the tool nose radius, *r*, was proportional to the ratio of the material hardness to the elastic modulus.

$$\frac{s}{r} = k\frac{H}{E} \tag{2}$$

Arcona also created an empirical model for the average flank stress, σ_f, based on observations made during experiments incorporating the sliding of worn diamond tools along different materials. Constants of proportionality were found to be 43 and 0.62 for the springback and average flank stress models, respectively.

$$\sigma_f = kH\sqrt{\frac{s}{r}} \tag{3}$$

$$\sigma_f = 0.62H\sqrt{43\frac{H}{E}} \tag{4}$$

The flank area in contact with the workpiece material can be derived from tool profile parameters shown in Figure 5.

$$A_f = w\left(r + l + \frac{s}{\tan\alpha}\right) \tag{5}$$

While it is assumed that there exists a stagnation point somewhere on the nose radius that locates the separation of upward and downward flowing material, tool edge measurements have shown that the size of the radius is relatively small compared to the wear land (*r* is approximately 7 to 15% of *L*, see Figure 8 on p.90 and Figure 13 on p.93). Therefore, *r* is used in eq. (5) rather than using a smaller length associated with the stagnation point.

In calculating (5), *s* can be determined from eq. (1), and α is determined from EBID images, or supplied by the tool manufacturer. This supplies A_f as a function of measured wear parameters and tool geometry. Eqs. (4) and (5) can be used to acquire the flank force, F_f. Cross section wear area, A_w, can be determined from eq. (1) or integration methods described in section 5.2.4 Diamond Tool Wear Measurement. The worn region of the diamond tool is assumed to be the same width as the turned material. The wear area combined with the wear width can determine

the worn volume. This worn volume can also be described by the Archard Wear Law for abrasive wear, in which the worn volume is proportional to the applied force times the sliding distance.

$$V = A_w \cdot w \tag{6}$$

$$V = k \cdot F_f \cdot d_s \tag{7}$$

In some references, Archard's wear equation includes an inverse proportionality to the hardness of the worn material [9,10]. The scope of this paper only observes the wear of diamond, and the hardness value of diamond would be used for the Archard wear equations for diamond worn by aluminum and diamond worn by steel. Since both equations would use the same hardness value, the form of Archard's wear equation that omits reference to hardness is used, which is expressed in eq. (7).

5.3 EXPERIMENTAL RESULTS

5.3.1 ALUMINUM

Measurements taken using the contamination stripe images with the Digitize09 program yielded interesting results. Figure 7 shows the trend in wear geometry changes as sliding distance increases. The wear land grew linearly with increase in cutting distance while the rate of growth of the edge radius appeared to decline with distance.

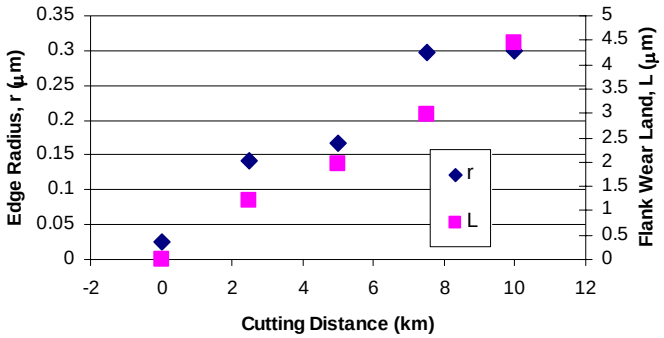

Figure 7: Diamond wear parameters measured after cutting Al6061

Figure 8 shows the relationship between edge radius and wear land. Since the Arcona tool force model is used to predict average flank stress, it is prudent to compare results from the current experiment with those Arcona used in the formation of his force model. Arcona described the relationship of the wear land and the nose radius as a second order polynomial, and wear geometry results from the recent experiment agree well with those encountered by Arcona.

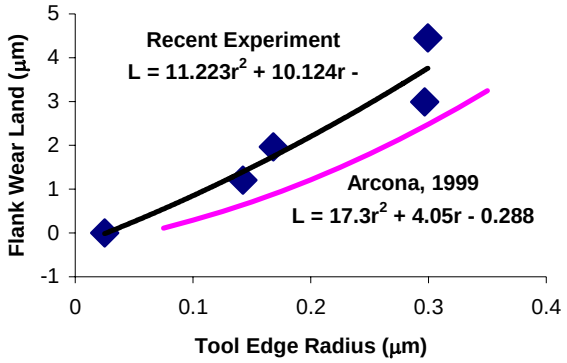

Figure 8: Wear parameters of a diamond tool on Al6061 agree with past studies conducted for the derivation of the Arcona tool force model.

Wear areas were found using Digitize09 and compared to calculated areas utilizing (1). These numbers agreed well with one another, therefore results from (1) were used as the definitive worn area for the Al6061 worn tool. These areas were used in (7) to determine to total wear volume. The increase in wear volume with cutting distance is given in Figure 9. The trend of volumetric wear for the diamond worn by Al6061 can be compared with wear progression types defined in [9].

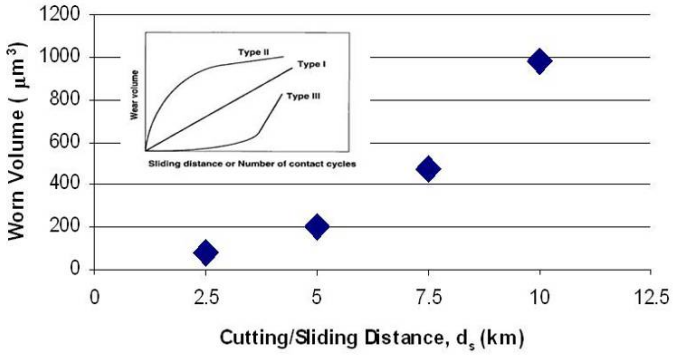

Figure 9: Worn volume of diamond tool on Al6061 exhibits Type 3 wear mechanism [9].

Wear geometry was used to calculate the worn volume, and the same geometry with material properties were used to calculate average flank force using eq. (4) and eq. (5). In Arcona's model, the total thrust force (that acting perpendicular to material flow under the tool) had components arising from average flank force and sliding friction on the rake face. While the coefficient of friction for diamond on Al6061 is not known, previous research has found that this value for diamond on other metals at forces and speeds typically encountered in diamond turning ranges from 0.1-0.3 [7]. Neglecting this sliding friction, the flank force ought to be less than the total measured thrust force on the tool. When comparing the calculated flank force to the measured thrust force, this doesn't always occur (Figure 10). Nevertheless, these related values

agree in general magnitude, and verify the Arcona model as a functional tool for prediction forces.

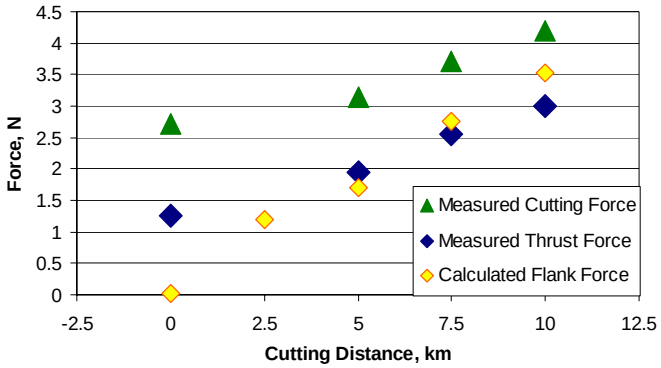

Figure 10: Measured and calculated tool forces while cutting Al6061. Measured data for 2.5km cutting distance is omitted due to chip buildup on the tool disturbing force measurements.

One should also note the difference between the measured thrust force and calculated flank force values at 0km cutting distance. The flank force was calculated by assuming no wear land so that the only contribution to the flank contact area was due to nose radius and material springback. While this resulted in minimal calculated flank force the measured thrust force was found to be significantly higher (Figure 10). This may be due to a rapid wear during initial cutting, such that the nose radius and wear land are formed soon after initial penetration of the tool into the workpiece material. While this hypothesis agrees with the general trend shown in Figure 7, wear geometries would need to be measured soon after initial cutting to observe initial wear rates.

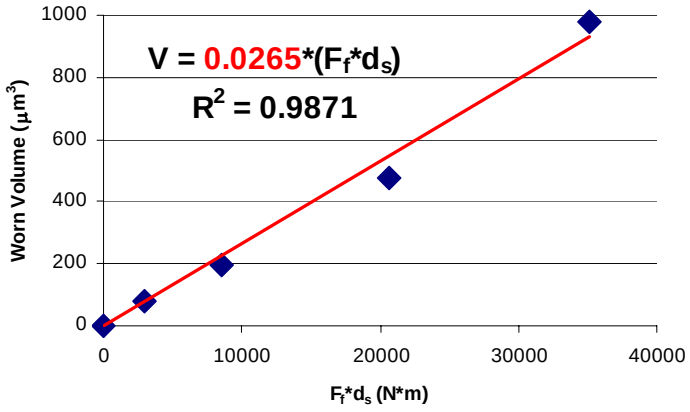

Figure 11: Archard wear constant for diamond on Al6061 determined to be 0.0265 $\mu m^3/N*m$.

Since calculated flank forces and measured thrust forces agree, the calculated flank force can be used in analyzing wear on the diamond tool. This enables the Archard wear constant for

diamond on Al6061 to be determined entirely from 5 parameters; edge radius, wear land length, clearance angle, workpiece material hardness, and Young's modulus.

As stated by the Archard wear law, the worn volume is a linear function of the normal force (average flank force) multiplied by the sliding distance (cutting distance). Calculated flank forces in Figure 10 were used to find the Archard wear constant, and Figure 11 shows the linearity exhibited by recent wear experiments of diamond on Al6061.

5.3.2 STEEL

As expected, wear of the diamond tool on the St1215 was significant after only 10 meters of cutting. Figure 12 shows the trend of wear geometry with cutting distance for the steel-worn tool, and can be compared with Figure 7 for the aluminum-worn tool. While both wear land and edge radius increased with cutting distance, the general trend was much different than that for the Al6061 disks. For the wear on steel, the edge radius tended to increase linearly, while the rate of increase of the wear land tended to decrease.

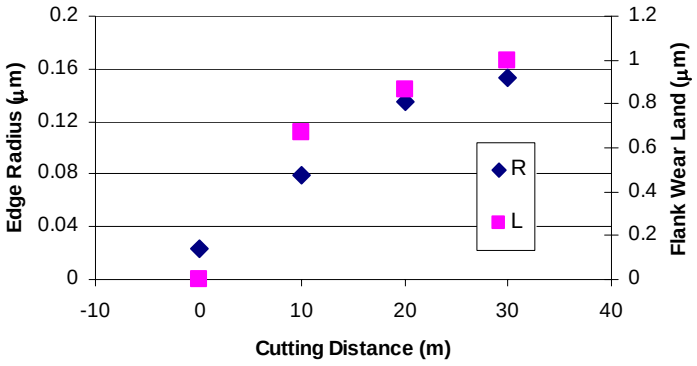

Figure 12: Wear parameters of a diamond tool on Al6061 agree with past studies conducted for the derivation of the Arcona tool force model.

Contamination stripe images after 40 m of cutting yielded wear areas less than that for images taken after 20 m and 30 m. This is counterintuitive, since the wear should always increase with further machining; therefore 40 m data is omitted.

As with aluminum, the relationship of the wear land to the edge radius was observed (Figure 13). The ratio of the change in wear land length to the change in edge radius for the steel-worn tool decreased with cutting distance (dL/dr decreased), while the opposite occurred for the aluminum-worn tool. While values are in the same range as those found by Arcona, the general trend is much different.

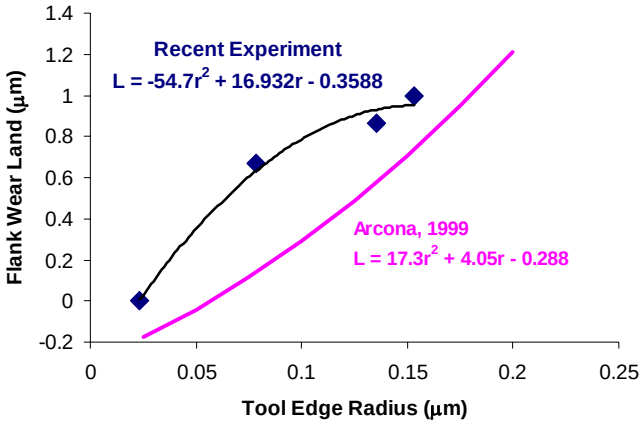

Figure 13: Wear parameters of a diamond tool on St1215 resemble past studies in magnitude, but differ in general trend.

While observing contamination stripes made on the tool worn by steel, it was evident that the tool cross-section of the steel-worn diamond was much different than that of the aluminum-worn diamond. Apart from a substantially greater wear rate, the wear land formed at an angle that was not parallel to the material flow under the tool. Although this angle is apparent when comparing images of aluminum and steel-worn tools side by side, it was measured by tracing a line along EBID images that coincided with the worn tool cross section. These cross sections were then rotated until the rake face edge was at 0° so the wear land angle could be observed as shown in Figure 14.

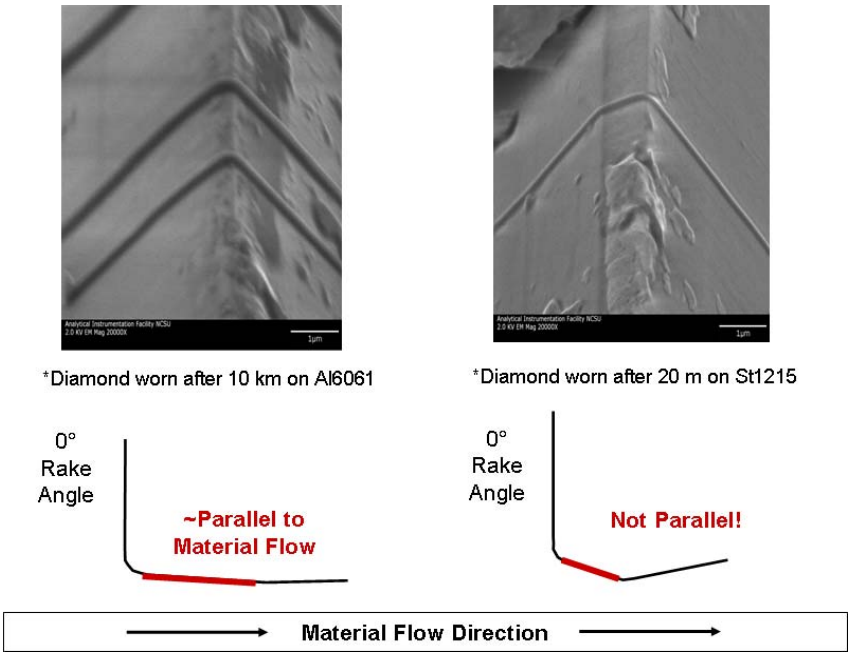

Figure 14: Tool edge profiles for diamond worn on Al6061 *(left)* and St1215 *(right)* at 20 kX.

The change in wear land angle does not allow wear calculations to be made in the same manner as for the Al6061 experiment. Since the wear land is not parallel to the material flow direction, Equation (1) cannot be used to calculate the worn area, nor can eq. (5) be used to calculate flank contact area. However, the worn area was still calculated with Digitize09 (Figure 4), and multiplied by the material width to give the worn volume (Figure 15).

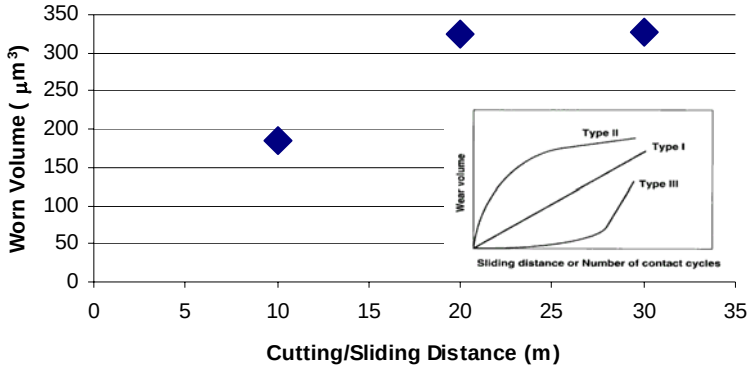

Figure 15: Worn volume of diamond tool on St1215 exhibits Type 2 wear [9].

Tool forces measured while cutting steel were significantly higher than for aluminum as expected. Forces varied little with subsequent cuts, and steady state forces are achieved within the first meter of cutting distance (Figure 16). Thrust forces remained at approximately 4.5N and aluminum at 6.5N.

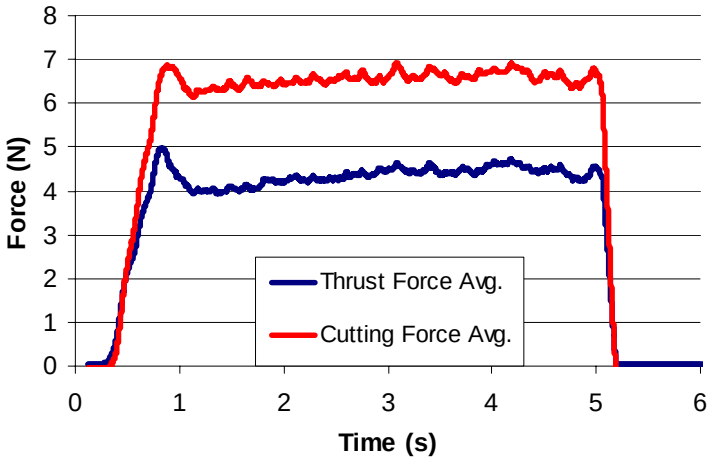

Figure 16: Example of force data taken when cutting St1215 form 0 to 10m. Data is taken at 1000 kS/s and plotted with a 100-point running average. Forces varied little with subsequent cuts.

5.4 CONCLUSIONS

1. Orthogonal cutting of Al6061 disks was conducted with intermittent observations of tool wear made with the EBID method.
    - EBID technique proved to be a valuable tool in measuring and studying wear geometry on diamond tools.
    - Two techniques were attempted to calculate worn area; integration used in Digitize09 and calculations from simplified wear geometry. Agreement of values found by both methods allows the worn area to be determined from edge radius, wear land, and clearance angle.
    - Forces determined by the Arcona tool force model agreed with measured values. Combined wear volume and force calculations fit Archard's wear equation well. The Archard wear coefficient for diamond on Al6061 was determined to be 0.0265 $\mu m^3 N^{-1} m^{-1}$.

2. Similar cutting and observation was performed on St1215 fins.
    - Tool forces and wear rates were significantly higher for the St1215 than for Al6061. Comparable wear on the diamond tool from steel was encountered at cutting distances 1000 times less than for the aluminum.
    - Wear geometry was significantly different than that observed after wearing via aluminum. Wear geometry trends differed than that for aluminum, likely due to a differing wear mechanism.
    - The wear land on the steel-worn tool was not parallel to material flow, therefore Arcona tool force model did not accurately predict tool forces. This also disallowed worn area to be calculated with the same wear parameters used in the Arcona tool force model.
    - The un-parallel wear land may be attributed to higher rates of chemical wear near the high temperature cutting zone. This feature may provide signature of chemical wear, but further experiments are needed to verify.

5.5 FUTURE WORK

The intended purpose of this particular experiment is to form a basis of understanding of the different wear mechanisms that may occur on a diamond tool while turning different material. Similar experiments will be conducted on other materials that are known to exhibit abrasive wear, chemical wear, or combinations thereof when diamond turned. Candidate materials include pure iron, silicon, other steel alloys, and titanium alloys.

Results from this experiment will be compared with similar experiments conducted using EVAM. Initial tests will repeat use of Al6061 and St1215 as workpiece materials for direct comparison with results stated in this paper. Future EVAM tests will also consider the other candidate materials mentioned above. The EBID method has not been employed on tools that have been used in EVAM, therefore will give great insight to the wear characteristics encountered. Improvements in surface quality and tool wear when utilizing VAM will be quantified. These tasks will eventually define best working conditions for the VAM process, and elucidate the means by which VAM is able to reduce forces and wear, and increase surface finish in precision machined materials.

ACKNOWLEDGEMENTS

Primary funding for this work was by National Science Foundation Grant CMMI-0800560 monitored by G. Hazelrigg. Chuck Mooney of the Analytical Instrumentation Facility at North Carolina State University provided training for the contamination stripe growth method, the AIF granted use of the SEM, and Meirong Shi provided stripe growth and SEM image analysis. Ken Gerrard of the PEC provided conceptualization of Digitize09 and incorporation pixel selection and circle-fitting algorithms. Chardon Tools supplied the diamond tools used in the machining experiments.

REFERENCES

1. Brehl, D.E., Dow, T.A., *Review of Vibration-Assisted Machining,* Precision Engineering, vol. 32, pp. 153-172 (2008)
2. Thornton, C., Wilks, J., *Clean Surface Reactions Between Diamond and Steel,* Nature, vol. 274, pp. 792-793, (1978)
3. Drescher, J.D. *Tool Force, Tool Edge, and Surface Finish Relationships in Diamond Turning.* PhD. Dissertation, North Carolina State University (1991)
4. Arcona, C. *Tool Force, Chip Formation, and Surface Finish in Diamond Turning.* PhD. Dissertation, North Carolina State University (1996)
5. Lane, B., Dow, T.A., Scattergood, R. *Orthogonal Cutting for Observing Tool Force and Wear.* PEC Interim Report, pp. 17-24 (2008).
6. Broccato, B.C., *Micromachining Using Elliptical Vibration Assisted Machining (EVAM).* PhD. Dissertation, North Carolina State University (2005)
7. Wilks, J., Wilks, E. *Properties and Applications of Diamond.* Butterworth-Heinmen Ltd., pp. 307 (1991)

8. Crompton D., Hirst, W., Howse, M. G. W., *The Wear of Diamond.* Proceedings of the Royal Society of London. Series A, Mathematical and Physical Sciences, Vol. 333, No. 1595 pp. 435-454 (1973)
9. Kato, K., Adachi, K. EIC Bhushan, B. *The Modern Tribology Handbook* CRC Press., pp. 273-299 (2001)
10. Tylczak, J.H., *Abrasive Wear*. ASM Handbook, Vol. 18, pp. 184-190 (1992)
11. Alden, K.L., *Friction and Wear of Cutting Tools and Cutting Tool Materials*. ASM Handbook, Vol. 18, pp. 610-620 (1992)

6 DIAMOND TURNING OF SMALL OPTICS

Alex Sohn
Precision Engineering Center Staff

Plastic optics have penetrated a wide array of applications and markets from consumer electronics to opthalmics. While most of these applications still use spherical optics, aspheric optics are becoming increasingly prevalent and the demands for accuracy on those optics are increasing. While most of these lenses are molded, prototype lenses for testing are generally made by direct single point diamond turning and present some unique challenges to that technique. Specifically, the compliance of the most plastics, PMMA and Polycarbonate being the most prevalent, can make diamond turning to high accuracy difficult. Described here are some techniques for surmounting these challenges, including mounting and error compensation, and producing small aspheric lenses to ±150 nm.

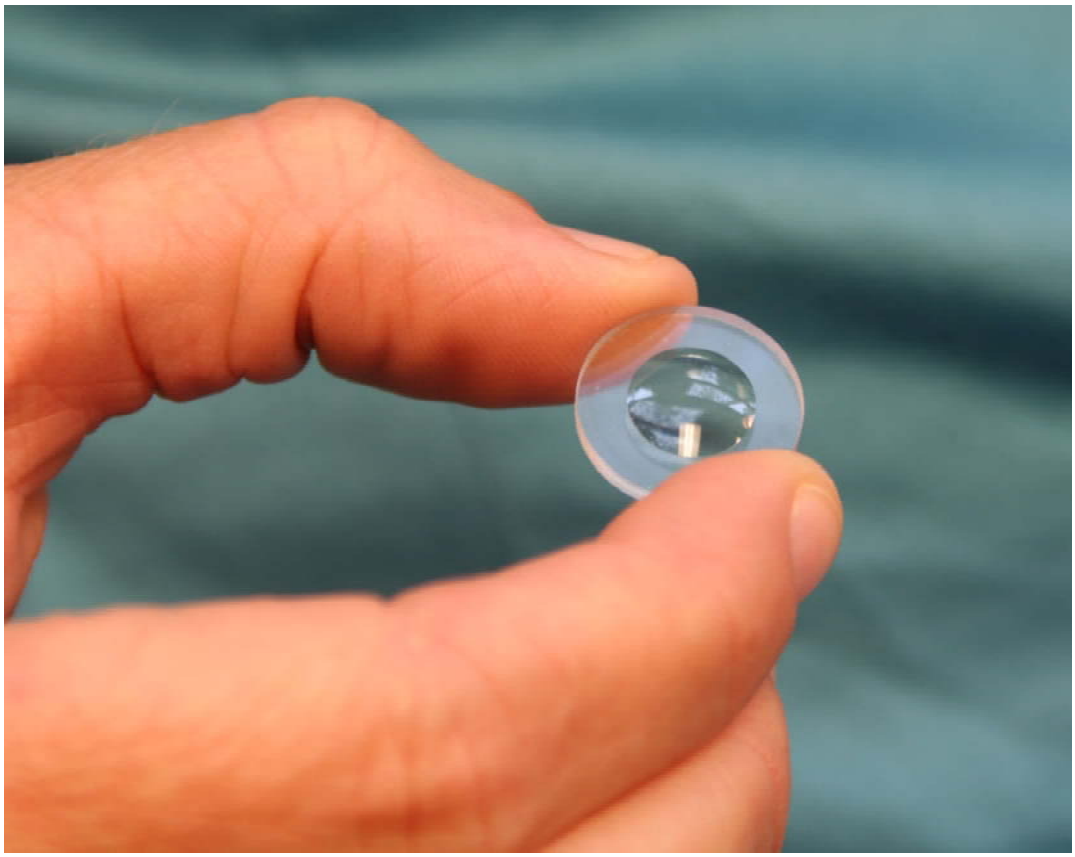

6.1 INTRODUCTION

Diamond turning of PMMA (Polymethyl-methacrylate) has been of importance to a number of industries and presents some unique challenges. While PMMA (also known by the trade names Plexiglas® and Lucite® as well as the generic term "acrylic") has low shear strength, creating low cutting forces and, hence, long tool life, certain quasi-brittle behavior can cause surface finish issues. While this "tearout" or "zippering" phenomenon has been encountered before [1, 2], typically it can be avoided by using low feedrates and depths of cut. Achieving good surface figure also presents a unique challenge due to the low modulus of PMMA (2-3 Gpa) makes stress-free mounting difficult, particularly since blanks are not initially flat. The chief advantage of aspheric lenses is their ability to eliminate spherical aberration with a single surface whereas spherical lenses require multiple surfaces (usually three or more) to achieve the same result. This is of particular significance in instances where space or cost limits the application of doublet or triplet lenses such as CD/DVD lenses, cell phone camera lenses and opthalmics. While most of these applications end up with molded lenses in the final product, prototype lenses for testing and development are typically machined directly from polymers such as PMMA. The objective of this project was to fabricate a set of aspheric lenses with an aperture diameter of 6 mm and overall sag of up to 1 mm. A photograph of the lens is shown in the title figure.

6.2 ASPHERIC LENS DESIGN AND TOOLPATH GENERATION

6.2.1 CALCULATING THE SHAPE

The aspheric shape of a lens is generally described by the general optics equation:

$$z = \frac{cr^2}{1+\sqrt{1-c^2(\kappa+1)r^2}} + dr^4 + er^6 + fr^8 + gr^{10}\cdots \qquad (1)$$

Where z is the surface displacement, r is the radial coordinate along a meridian of the lens, c is the curvature of the lens, κ is the conic constant and $d, e, f\ldots$ are the higher-order aspheric terms. From this equation, data points along the lens's surface can be generated at an arbitrary interval. In order to maintain a good surface finish, the spacing of the data points must be chosen so that, with the lens's general curvature, the sag between each data point is less than the best achievable P-V surface finish. In this case, a value of 1 nm was chosen. With a general curvature c of $1/R$ where R=11.45 mm, the parabolic approximation can be used to estimate the points spacing d is

$$d = \sqrt{PV \cdot 8R} \qquad (2)$$

Or in this case, the spacing shall be 9.57 µm. Since the lenses being fabricated have an aperture radius of 3 mm, this produces 300 data points total along the toolpath, not an unreasonable number. The data points were generated in Microsoft Excel and appended with code and feedrate information to allow interpretation by the PEC's ASG 2500 Diamond Turning Machine.

6.2.2 TOOL RADIUS COMPENSATION

Tool radius compensation must be performed to maintain the proper form of the part. There are two methods for perfoming tool radius compensation: 1) analytically derive an offset path one tool radius away from the original path or 2) find surface normals at given points along the toolpath and find new points offset by one tool radius in the normal direction. The latter was chosen because the generated toolpath points are close together and the slope change between each set of surface points is small enough that the local slope can be approximated from neighboring points. Again, this action is simple and it was performed in Microsoft Excel. In this case, a 98 µm radius tool was used.

6.3 FABRICATION

With the toolpath generated, several fabrication issues loomed, the most significant being part mounting.

6.3.1 PART MOUNTING

For part mounting, three distinct possibilities exist: 1) Mechanical restraint, 2) Vacuum mounting and 3) Adhesive mounting. The significant problem with PMMA and other polymers is that they have relatively low elastic moduli and are easily distorted even with small applied stresses. Because these parts are only 1-2 mm thick and the blanks do not start out flat it is difficult to securely mount the parts without distorting them. Both mechanical methods and vacuum were immediately dismissed for these reasons. With vacuum, the non-flat mounting face of the part is distorted into a flat shape so that if the part is faced off, it remains flat only while it is held with vacuum.

The distortion left bonding as the only viable mounting method. Bonding is, however not without its own problems, as adhesive can distort the part, damage the mounting surface or leave residue that is difficult to remove. Optical mounting wax was tried since it conforms well to irregular surfaces and applies little stress. The relatively low melt temperature of the wax, 50ºC, minimizes thermal stress. However, in tests it was found that the process still induces too much thermal stress in PMMA to be useful, likely due to its high CTE. This is illustrated in Figure 1 with a measurement of residual error before and after mounting. While the part was flat before release from the wax, after release, the part exhibited a sag of 1.743 µm. This is a significant

error for any optical component and greatly exceeds the tolerance of ±150 nm for the asphere parts. Similar tests performed with double-adhesive film tape revealed no residual stress and this method was thus chosen for mounting all samples.

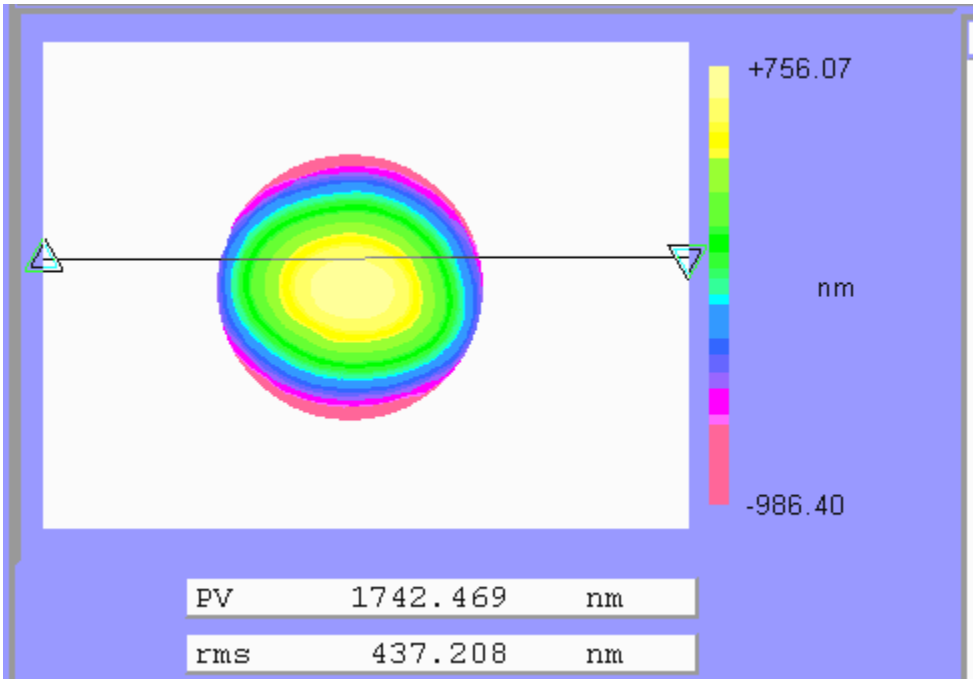

Figure 1. Residual error in plastic flat bonded to substrate with mounting wax after releasing.

6.3.2 TEST PART

Machining Test Sphere

Since the metrology of aspheres presents significant challenges, a spherical test part was chosen as a good independent indicator of the figure error that could be achieved in turning one of these parts. The radius of curvature was chosen to be the same as the base curvature of the aspheres to be machined, so that the only change between the test spheres and the final aspheres would be the conic constant. This would not only allow testing of the figure error with the Zygo GPI interferometer, but also the basis for compensation for systematic errors in the machining such as residual ogive, tool waviness and axis errors.

Error correction

The test sphere was measured using the Form Talysurf Profilometer as well as the Zygo GPI XP interferometer. The resulting errors come close to the tolerance of ±150 nm and, hence must be

corrected. Shown in Figure 2, a polynomial is fit to the data points. This error, likely caused by tool waviness, is then subtracted from the tool path.

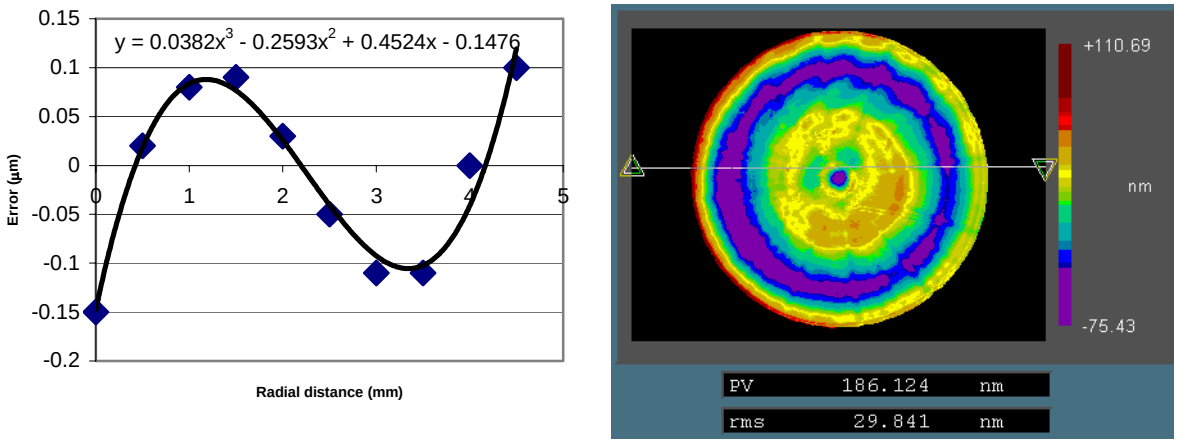

Figure 2. Polynomial fit to error data on a spherical test part (left) and the resultant interferometry results after using the polynomial correction (right).

6.3.3 MACHINING

With error correction applied, the aspheric lenses were machined using a cross-feed of 2.5 mm/min on the finish pass with a depth of cut of 2 µm. Cuts were performed dry with ionized air used to remove chips. The ionization prevents static discharge which is potentially damaging to the tool and static attraction of the chip to the part. All parts were faced on one side to achieve a flat back surface and then re-mounted using the double-stick adhesive tape to contour the aspheric face.

6.4 METROLOGY

6.4.1 SURFACE FINISH

Given a theoretical surface finish of 1 nm RMS, the actual surface finish of between 5 and 6 nm RMS measured on all samples was quite satisfactory. Shown in Figure 3 is the result of one such measurement performed with a Zygo New View 5000 Scanning white-light interferometric microscope. This surface finish is typical of the best finishes that have been achieved in PMMA on the ASG 2500 [1] and appears to be mainly limited by the material as evidenced by the irregular tooling marks on the surface.

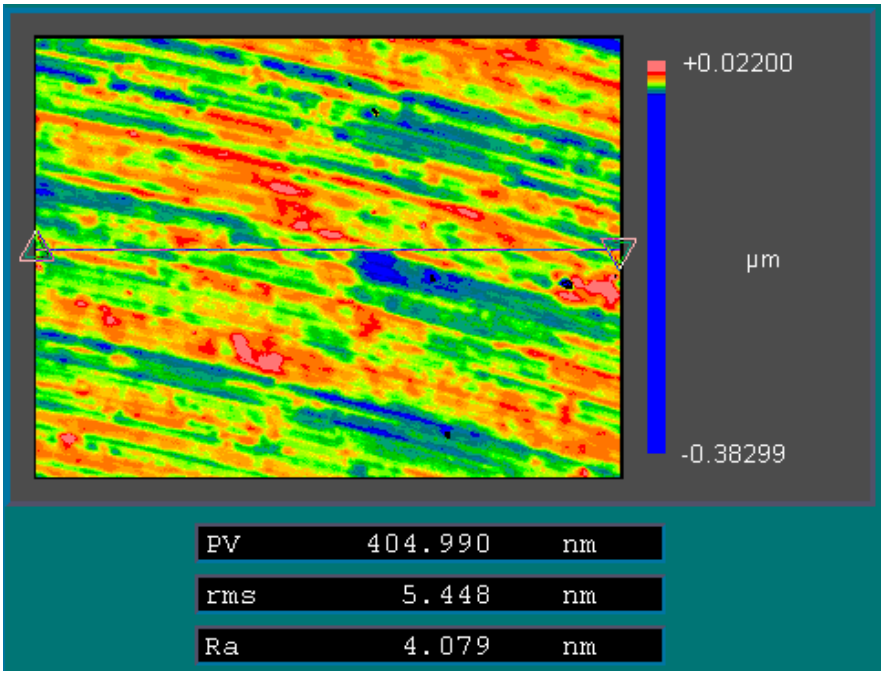

Figure 3. Typical surface finish measurement for one of the aspheric PMMA lenses.

6.4.2 FIGURE MEASUREMENT

Final figure measurements could not be performed with an interferometer due to the aspheric nature of the lenses, so the PEC's Form Talysurf was used for measurement and analysis. The stylus profilometer was used to measure one meridonal trace for each lens. The aspheres are conic sections with no higher order polynomial terms. They were all ellipsoidal with conic constants ranging from +0.52 to -0.13. This allows the Talysurf's fitting routine for ellipses and hyperbolae could be used. The result of these fits produce an output of major and minor axis dimensions *a* and *b*. From the values of *a* and *b*, the conic constant, k and radius can be calculated.

$$\kappa = \frac{b^2 - a^2}{a^2}, \qquad R = b(\kappa + 1) \tag{3}$$

Residual errors were below the target uncertainty of ±150 nm. Figure 4 shows that the residual error is well within the specified limit and is typical of the types of error measured on all of the PMMA lenses.

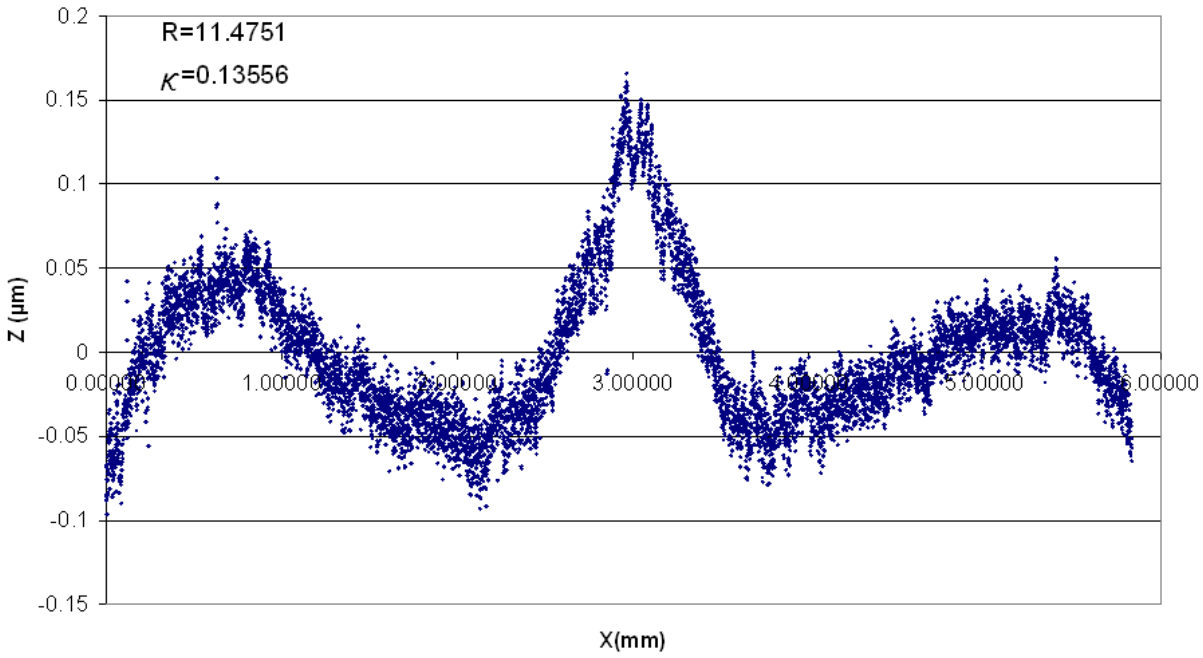

Figure 4. Figure error measurement for an aspheric lens. Peak-to-Valley error was measured at 265 nm with the best-fit ellipse removed from the data.

6.5 CONCLUSIONS

This work represents a practical look at machining aspheric surfaces in PMMA. In general, the lessons learned apply to all instances where easily deformed parts must be securely mounted and where distortion can play a significant role. In this case, the traditional vacuum mounting techniques do not work well and are replaced by the use of adhesive that applies substantially less stress to the part. It has also been demonstrated that systematic, repeatable machining errors such as tool waviness, axis errors, etc. can be removed from the process without regard to their source. In the end, high-tolerance PMMA lenses can be directly machined for prototype work.

REFERENCES

1. A. Sohn, K.P. Garrard, and T.A. Dow, *Fabrication of Non-Imaging Optical Surfaces.* PEC Annual Report 1998, pp 207, (1998).
2. A. Kobayashi, Machining of Plastics, Robert E Krieger, New York pp 59ff, (1981).

7. 4-AXIS MACHINING OF MICRO-FEATURES WITH THE ULTRAMILL

Brandon Lane
Graduate Student

Thomas Dow
Dean F. Duncan Distinguished University Professor in Mechanical Engineering

Alex Sohn
Precision Engineering Center Staff

The capability of the Ultramill to machine micro-features with optical quality has been improved. Alignment of the Y axis with respect to the Nanoform 600 X and Z axes is critical to form fidelity of micro-machined parts. This alignment was done roughly when the Y axis was added to the machine a few years ago, but more careful squareness measurement and adjustment was made. The spindle axis of the Diamond Turning Machine (DTM) has been enhanced to become a positioning axis with a new motor and high-resolution encoder. Now there are 4 positioning axes: three orthogonal linear axes and a rotary axis. Programming these axes to move in coordinated motion was a significant outcome of the project. G-code programs to make straight, curved and off-center curved features were developed. Finally, several features were fabricated to demonstrate the accuracy of the machine to place the tool in the correct position to fabricate high-fidelity features.

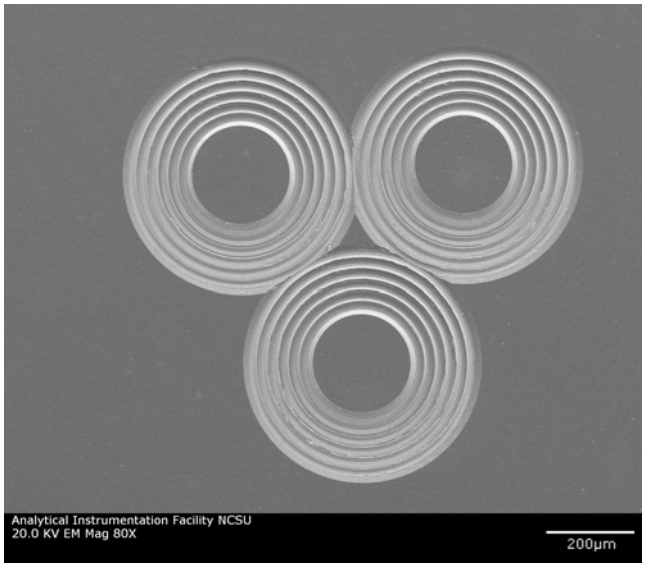

7.1 INTRODUCTION

The ability to program the 4 axes of the Nanoform 600 DTM enables complex tool paths to be generated when machining with the Ultramill. The layout of the machine and a photograph are shown in Figure 1. The Ultramill is mounted on the Y-axis of the DTM with its cutting direction in the negative X-direction (feeding X in the negative direction causes "upfeed" of the Ultramill). For rotational direction changes, a C-axis, holding the part to be machined, is aligned with the Z-axis. Motion of all the axes must be coordinated to maintain positive motion of the Ultramill in the cutting direction along the tool path.

For the following discussions, part coordinates will be designated as lower case such as (x, y, z, etc.) while machine axis positions will be designated as uppercase (X, Y, Z, C). Linear motion will be in units of mm and rotary motion in degrees.

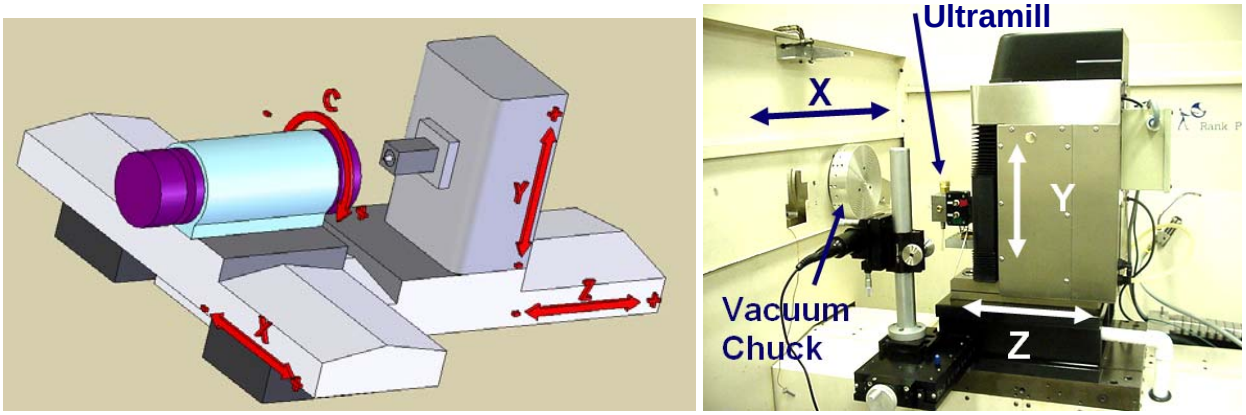

Figure 1. Layout of the Nanoform 600 DTM showing the 3 linear axes (X, Y, Z), rotary axis C and the Ultramill mounted on the face of the Y axis.

7.2 MEASURING AND ADJUSTING SQUARENESS OF DTM AXES

During early machining tests using the Ultramill, spherical features were machined and measured in the laser interferometer. This experiment determined the capability of the Ultramill to create precise, sub-millimeter sized features. During these tests however, it was discovered that a lack of squareness between the Y axis that supports the Ultramill and the X and Z axes produced a significant figure error even for small spheres on the order of 1 mm.

7.2.1 SQUARENESS MEASUREMENT

Measurement of squareness of the axes was performed with a Zerodur square (8.75x13x2 inch) and an electronic indicator as shown in Figure 2. Reversal was performed to remove the angular

error in the square but it was found to be 0.006 arcsec. This value is small enough to be ignored in all subsequent measurements [1]. The Nanoform Y-axis has adjustable feet to allow tip and tilt adjustment of the axis. The objective was to use the Zerodur square as a reference and adjust the squareness of the Y-axis to both the X-and Z-axes to better than 10 arcsec.

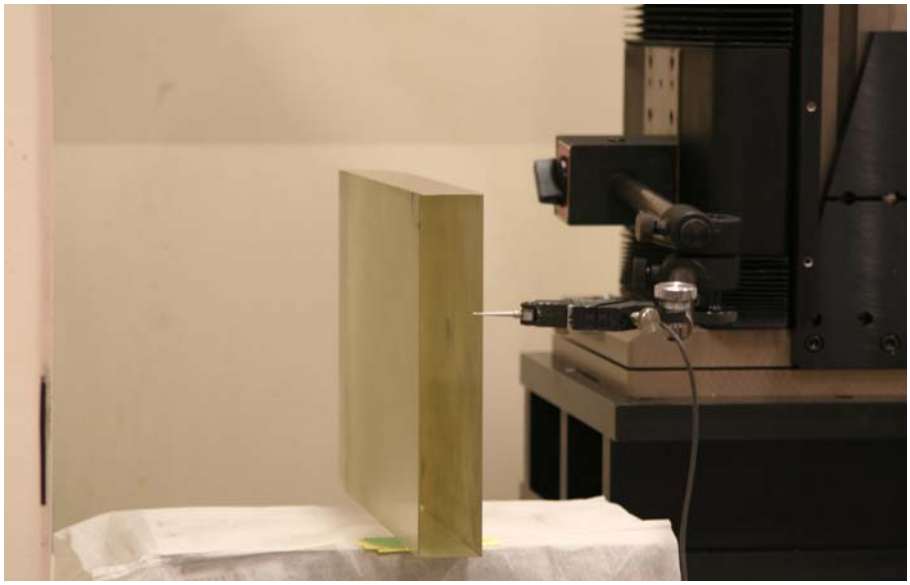

Figure 2. Zerodur square being measured in the Y-direction for X/Y squareness.

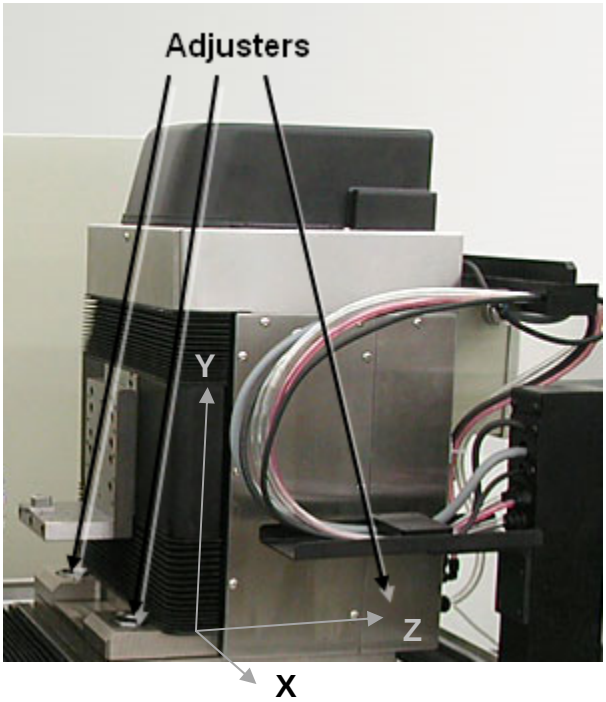

Figure 3. Adjustment of Y axis angular errors

7.2.2 ADJUSTMENT

The orthogonality of the Y-axis with respect to the X and Z axes was changed using the three adjusters shown in Figure 3 (one hidden at the rear of the axis). The procedure is to first adjust the X/Y squareness using the front two adjusters. This will rotate the Y axis around the Z axis to make Y perpendicular to the X axis. The front and rear adjusters were then used to rotate the Y axis around the X axis to make Y and Z perpendicular. These two adjustments can influence each other unless care is taken to move the front two adjusters the same amount in the opposite directions to avoid changing the Y/Z alignment.

For both squareness adjustments, the square was first leveled with respect to the X and Z-axes respectively with shims and then probed along the Y-axis. The slope measurement of the Y-direction was added to the residual X- and Z-slopes to determine squareness error. To provide feedback as the adjustment screws were moved, an electronic indicator was placed on the Y-axis at a known vertical distance from the adjusting screws. Based on the tilt angle error, the adjustor was moved until the calculated displacement based on the residual squareness error was observed. This process was repeated several times until the following values were obtained.

	Initial		Final	
Squareness	Degrees	Arc Sec	Degrees	Arc Sec
X/Y	0.09591	345	0.0031	11
Z/Y	0.05	180	0.0011	4

7.3 LINEAR INTERPOLATION

Once the axes were aligned, techniques for programming the PMAC controller to create complex shapes were developed. For standard machining of straight paths in a plane with the Ultramill, the C-axis is rotated to the required angle for aligning the path with the X-axis of travel. The starting point of the path then becomes the point at the positive end of the line.

Given a linear path defined by endpoints (x_1, y_1) and (x_2, y_2) then the C-axis position is

$$\mathrm{C} = \tan^{-1}\left(\frac{y_2 - y_1}{x_2 - x_1}\right) \tag{1}$$

And the X and Y axis positions are generally given by

$$\begin{bmatrix} X_n \\ Y_n \end{bmatrix} = \begin{bmatrix} \cos C & \sin C \\ -\sin C & \cos C \end{bmatrix} \begin{bmatrix} x_n \\ y_n \end{bmatrix} \tag{2}$$

Or, for (x_1, y_1),

$$\begin{aligned} X_1 &= x_1 \cos C + y_1 \sin C \\ Y_1 &= -x_1 \sin C + y_1 \cos C \end{aligned} \tag{3}$$

The points are then filtered to select the more positive point in X as the starting point.

7.3.1 EXAMPLE: LINEAR TOOLPATH

Given a linear path with endpoints (3.60, -8.32) and (10.45, 5.80), the points will be:

C =64.12070198

X_1= 9.779532025

X_2= -5.914317089

Y_1=Y_2= -6.870462384

Assuming the depth of cut is set at Z=0 and the tool is withdrawn to Z=5 after the cut, the resulting G-code program is:

```
(header)
G00 C64.12070198 X9.779532025 Y-6.870462384
Z0.1 (move to within 0.1 mm of the part)
G01 Z0 F1 (plunge @ 1 mm/min)
G01 X-5.914317089 F10 (feed @ 10 mm/min)
G01 Z5 F25 (retract @ 25 mm/min)
```

7.4 ON-AXIS CIRCULAR INTERPOLATION

For circular interpolation, a circular path whose center coincides with the C-axis centerline is straightforward. X=0, Y=r where r is the radius of the circular path and C starts at 0 and ends at 360. With the PMAC controller in the Nanoform DTM, however, the command must include several points along the C-axis path that represent less than 180º of arc since the controller will always select the shortest distance between two points. Hence, a complete circle will require at least four points in C. For example, C=0 (start), C=170, C=340 and C=360. Note that all of the paths represent less than 180º.

7.4.1 EXAMPLE: ON-AXIS CIRCULAR TOOLPATH

Given a circular path with a radius of 8 mm that coincides with the C-axis centerline, the X- and Y-axis would be positioned at (0, -8). Assuming the depth of cut is set at Z=0 and the tool is withdrawn to Z=5 after the cut, the resulting G-code program is:

```
(header)
G00 C0 X0 Y-8
Z0.1 (move to within 0.1 mm of the part)
G01 Z0 F1 (plunge @ 1 mm/min)
G01 C170 F72 (C-axis feed of 72 deg/min feed corresponds to
10 mm/min @ an 8 mm radius)
C340
C360
G01 Z5 F25 (retract @ 25 mm/min)
```

7.5 OFF-AXIS CIRCULAR INTERPOLATION

For machining a circle whose center is not coincident with the C-axis, the X-and Y-axes must move in a coordinated fashion with the rotation of the C-axis. For a circle of radius r with its center at (x_c, y_c), the C-axis will rotate through 360 º. The X-and Y-axes will interpolate a circle of radius shown in Equation 4.

$$r_{xy} = \sqrt{x_c^2 + y_c^2} \text{ centered at } Y = -\frac{r + r_{xy}}{2} \tag{4}$$

While the X-and Y-axes are interpolating a circle, all other machine axes will perform linear interpolation to arrive at their specified point at the same time as long as circular interpolation is set to the XY plane by the G17 command. The C-axis can therefore be commanded to perform its rotation at the same time as the XY interpolation. In addition, the XY circular interpolation must always be in the clockwise (G02) direction for C-axis positive rotation. The Ultramill will be setup below the center of rotation of the spindle as a matter of convention. Figure 4 shows a circular path being cut while the spindle rotates about its center of rotation as the Ultramill traces out a circular path using the X and Y axes.

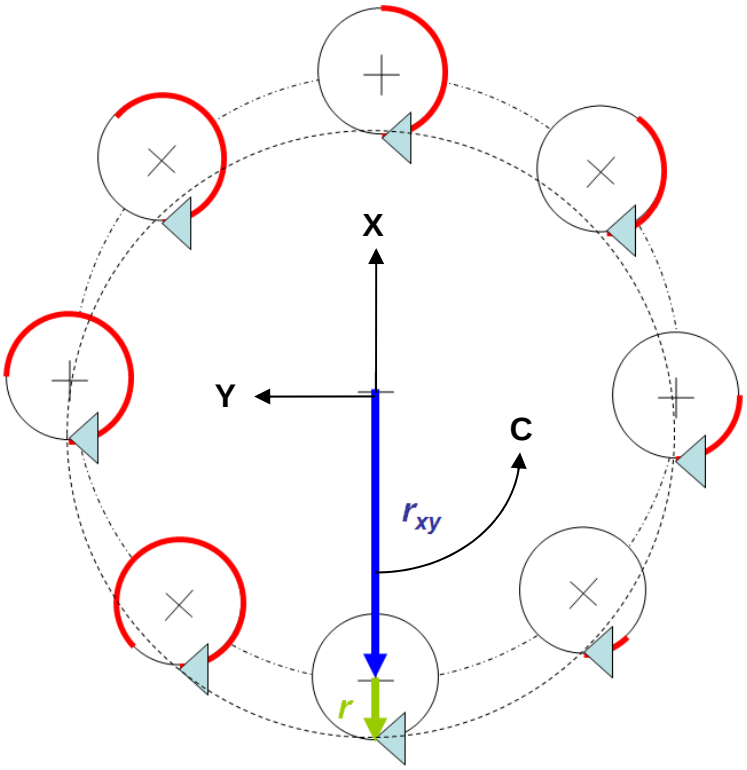

Figure 4. Illustration of the motion of two linear and one rotary axis to produce an off-center circle with the Ultramill. A full circle is cut after one revolution of the spindle.

An additional complication arises from the issue of C-axis rotations of more than 180º mentioned in the circular interpolation section. The off-axis circle must therefore be broken up into three segments of less than 180º. The most convenient way to do this is to place the waypoints at 120º intervals. Hence, for any circle with its center point not on axis:

$$\begin{aligned} X_2 &= X_1 - r_{xy}\cos 30^0 \\ Y_2 &= Y_1 + r_{xy}\sin 30^0 \\ C_2 &= 120^0 \\ X_3 &= X_1 + r_{xy}\cos 30^0 \\ Y_3 &= Y_2 \\ C_3 &= 240^0 \end{aligned} \tag{5}$$

7.5.1 EXAMPLE: OFF-AXIS CIRCULAR TOOLPATH

Given a circular path with a radius of 8 mm with its center located at (3.6, -9.5), $r_{xy} = 10.16$ and therefore:

$$
\begin{aligned}
R &= 10.1595 \\
X_1 &= 3.60 \\
Y_1 &= -17.5 \\
X_2 &= -4.67145 \\
Y_2 &= 6.22818 \\
C_2 &= 120^0 \\
X_3 &= 11.87145 \\
Y_3 &= 6.22818 \\
C_3 &= 240^0
\end{aligned} \tag{6}
$$

Assuming the depth of cut is set at Z=0 and the tool is withdrawn to Z=5 after the cut, the resulting G-code program is:

```
(header)
G17 G00 X3.6 Y-17.5 C0
Z0.1 (move to within 0.1 mm of the part)
G01 Z0 F1 (plunge @ 1 mm/min)
G02 X-4.671453577 Y6.228179997 R10.1595 C120 F10 (Feedrate
of 10 mm/min along circularly interpolated path)
X11.87145358 Y6.228179997 R10.1595 C240
X3.6 Y-17.5 R10.1595 C360
G01 Z5 F25 (retract @ 25 mm/min)
```

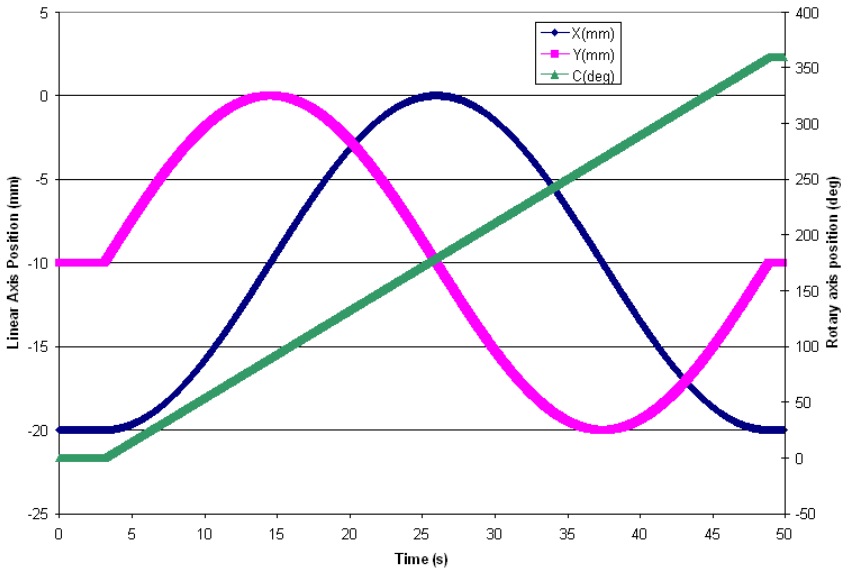

Figure 5. Motion of the axes to make a 10 mm radius circle centered at (0, -10).

This program was used to command the axes of the Nanoform 600 to move in the prescribed path to form a closed circular arc. Figure 5 shows the motion of the axes for a 10 mm radius circle center at (0,-10).

7.5.2 OFF-AXIS CIRCULAR ARC INTERPOLATION

For a circle of radius r with its center at (x_c, y_c) and endpoints (x_1, y_1) and (x_2, y_2), the relationship between the coordinates is

$$r = \sqrt{\left(x_n - x_c\right)^2 + \left(y_n - y_c\right)^2} \tag{7}$$

Again, the X-and Y-axes will interpolate an arc of radius r_{xy} centered at Y as calculated using Equation 4.

As in the case of the full circle, G02 and G17 are used; however, if the cutting direction (-X direction) and plane (XY) are changed, this will have to be modified accordingly. Also, this method of circular interpolation assumes that only circular arcs of less than 180° are being machined. Those arcs of larger included angle will have to be subdivided into smaller segments as was done in the case of the full circle. If, however, the above conditions are met, then the axis positions and interpolated radius for the arc segment can be calculated in Equation 8.

$$\begin{aligned}
\mathrm{X}_1 &= x_1 \cos \mathrm{C}_1 + y_1 \sin \mathrm{C}_1 \\
\mathrm{Y}_1 &= -x_1 \sin \mathrm{C}_1 + y_1 \cos \mathrm{C}_1 \\
C_1 &= a \tan\left(\frac{y_1 - y_c}{x_1 - x_c}\right) + 90^0 \\
\mathrm{X}_2 &= x_2 \cos \mathrm{C}_2 + y_2 \sin \mathrm{C}_2 \\
\mathrm{Y}_2 &= -x_2 \sin \mathrm{C}_2 + y_2 \cos \mathrm{C}_2 \\
C_2 &= a \tan\left(\frac{y_2 - y_c}{x_2 - x_c}\right) + 90^0 \\
R &= r_{xy}
\end{aligned} \tag{8}$$

7.5.3 EXAMPLE: OFF-AXIS CIRCULAR ARC TOOLPATH

Given a circular path with a radius of 15.56205 mm with endpoints at (-4.47327, -15.18431) and (4.0473, -26.49367) its center at (10.85295, -12.48536), $r_{xy} = 16.54299665$ and therefore:

$$
\begin{aligned}
X_1 &= \text{-}14.178399 \\
Y_1 &= 7.038920 \\
X_2 &= \text{-}15.217825 \\
Y_2 &= 22.061573 \\
C_1 &= 99.98739626^0 \\
C_2 &= 154.0881518^0 \\
R &= 16.54299665
\end{aligned}
\tag{9}
$$

The corresponding G-code is:

```
(header)
G54 G17 G00 X-14.178399 Y7.038920 C99.98739626
Z0.1 (move to within 0.1 mm of the part)
G01 Z0 F1 (plunge @ 1 mm/min)
G02  X-15.217825  Y22.061573  R16.54299665  C154.0881518  F10
(Feedrate of 10 mm/min along circularly interpolated path)
G01 Z5 F25 (retract @ 25 mm/min)
```

7.6 MACHINING TESTS

7.6.1 CORNER CUBE WITH MANUAL SPINDLE

With the addition of the C axis as a controlled axis, several experiments were conducted to evaluate the ability of the machine to create complex features. Before the spindle was modified to become a controlled axis, features were made using a sharp tool to cut corner cubes for a plastic mold. The spindle was rotated by hand with holes in the OD of the spindle and pins in the base to hold it at three 60° locations. Figure 6 shows the steps in the fabrication process. A series of five parallel grooves are machined with the tool cutting in the -X direction and the center of the cut was at (0, R). The spindle was rotated to 60°, the X and Y axes were moved to center the features at (-0.866R, 0.5R). A second set of five grooves was cut with the cutter moving in the -X direction. The final cut involved another 60° rotation, and X and Y moves to (-0.866R, -0.5R).

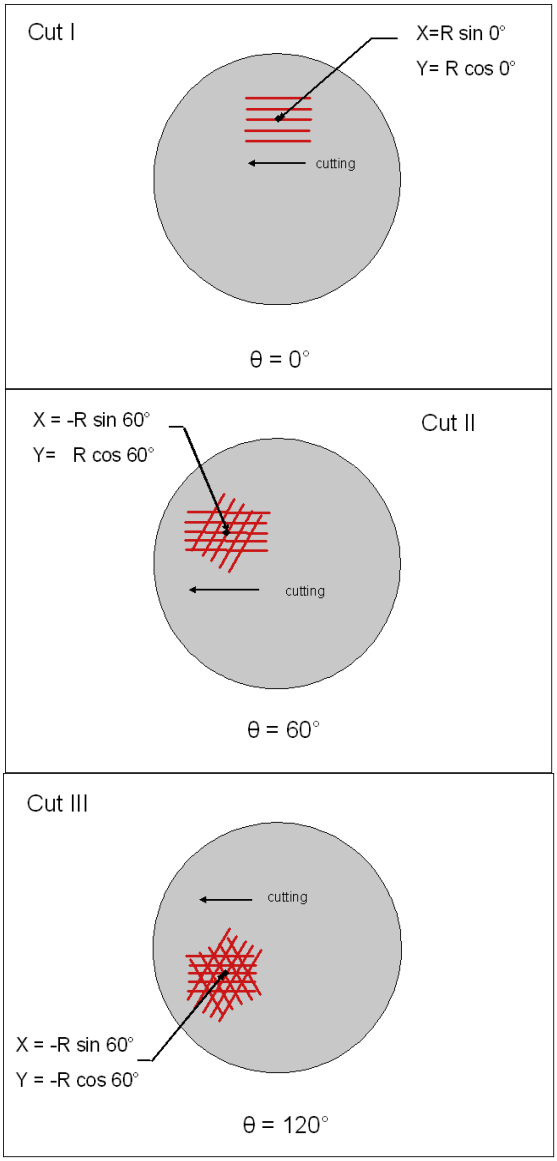

Figure 6. A corner cube can be created by intersecting 60° grooves with a dead sharp tool having an included angle of 70.53°. The result is a trihedron with a dihedral angle of 90°.

The resulting features are shown in the SEM image in Figure 7. Note that the three cuts do not intersect at a point as desired but rather create a smaller corner cube with a size of about 20 µm. The material for this fabrication is a hard plated copper that produces excellent fidelity in the shape and surface finish of the groove.

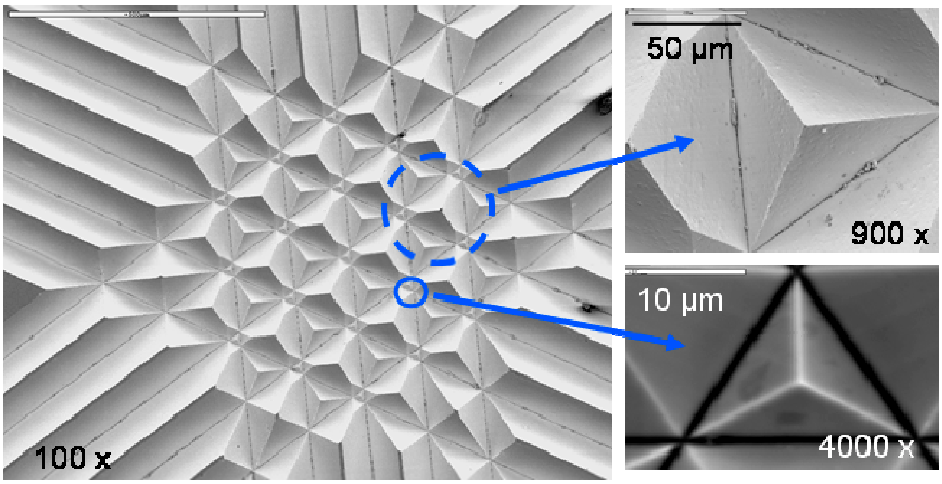

Figure 7. SEM images of trihedron array machined in hard-plated copper. Small interstitial features have a width of 20 µm are were caused by tool location errors.

7.6.2 CORNER CUBES WITH CONTROLLED SPINDLE

A similar experiment was conducted with the spindle controlled by the PMAC controller. The spindle has a high-torque motor and a circular encoder with $1.5x10^6$ pulses per revolution. The same tool, algorithm and material were used to reproduce the results shown in Figure 7. Figure 8 is the result of this experiment. Note that the depth of the grooves in the right hand figure are not exactly the same depth but the bottom of the three lines seem to intersect at a point.

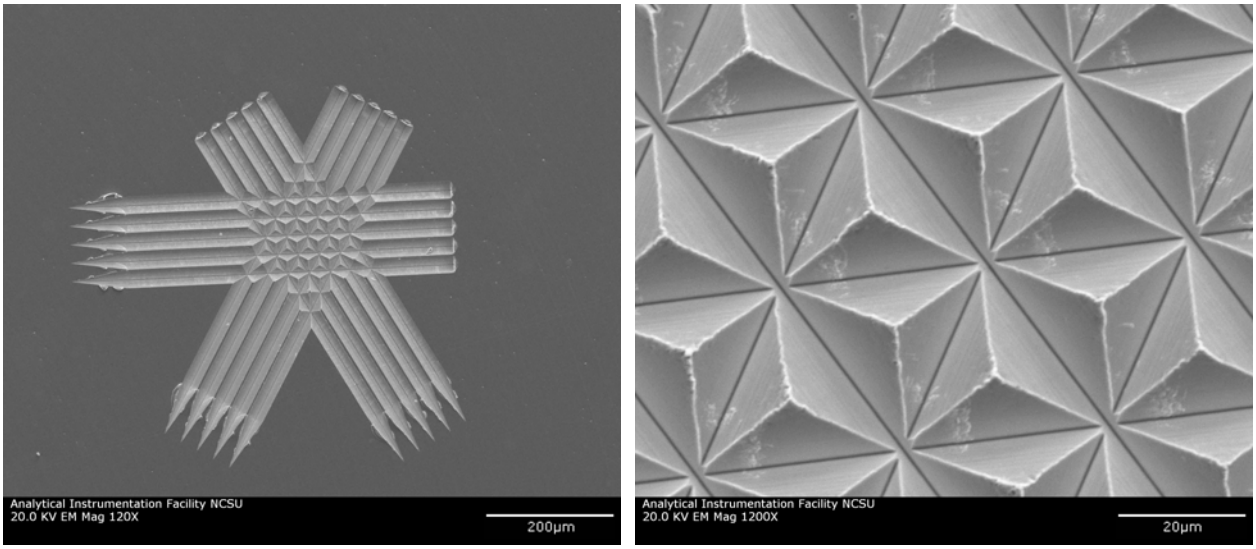

Figure 8. Machining corner cubes with dead sharp tool. Low magnification image at left shows the overlapping features and the corner cubes and the right image is at 10x magnification.

To create a more quantitative evaluation of the image, a higher magnification (~7 times) image of the intersection is shown in Figure 9. Here thin red lines are drawn through the center of each groove and the size of the error is estimated. Based on the marker at the lower right, the side of the intersection error is 200 nm. This error is 100 times smaller than with the manual rotary spindle.

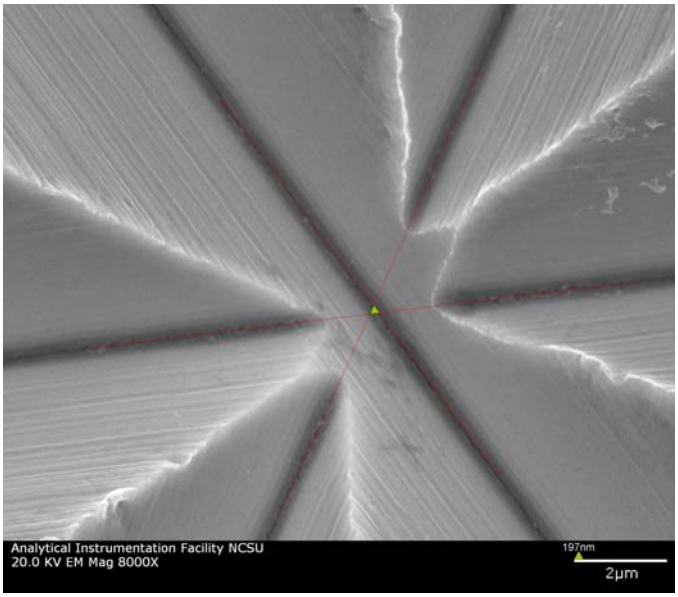

Figure 9. Higher magnification of intersection of the three 60° grooves. Error in the intersection of the grooves is 200 nm.

7.6.3 CIRCULAR FEATURES

The next demonstration part is shown in Figure 10. This part showed how a non-centered circular groove could be machined using the X, Y and C axes.

The microfeature consists of three circle sets, each with concentric ring grooves. The outer radius of each set is 250 µm while the inner is 100 µm. Each groove is 25 µm wide for a total of 6 grooves per circle set. The circle sets are configured in an equilateral triangle such that the outer edge of each set touches the outer edge of the two others. Figure 11 shows the planned geometry of the microfeatures as they appear on the workpiece. The circle sets are numbered 1-3, with the center of set one located at $(x_{c1}, y_{c1}) = (1,0)$ measured from the center of rotation of the C-axis. Set 2 and 3 centers are located at $(x_{c2}, y_{c2}) = (1.5, 0)$ and $(x_{c3}, y_{c3}) = (1.25, 0.4330127)$, respectively, in part coordinates. The 25µm wide grooves cut with a 70.53° included angle tool must have the final groove depths on each ring of each circle 17.661µm deep, as shown on the bottom of Figure 11.

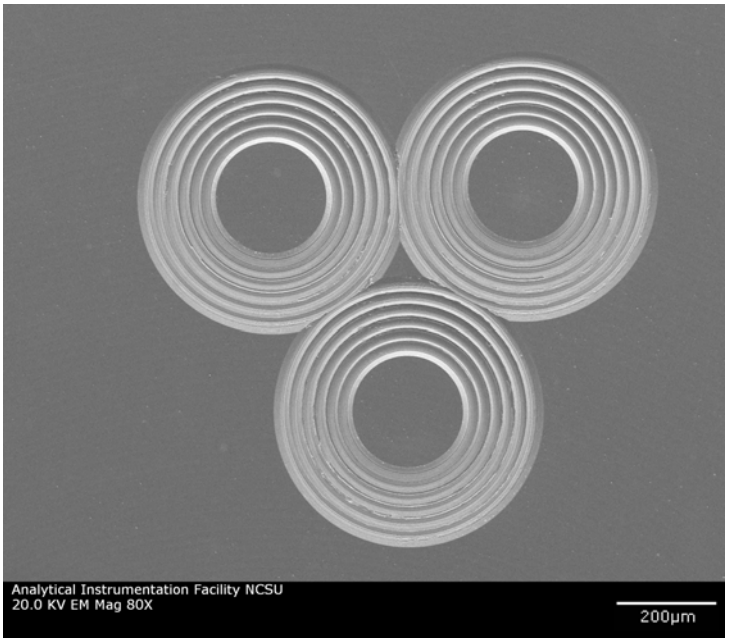

Figure 10. Circular features cut in the plated copper. Diameter of largest groove is 0.5 mm.

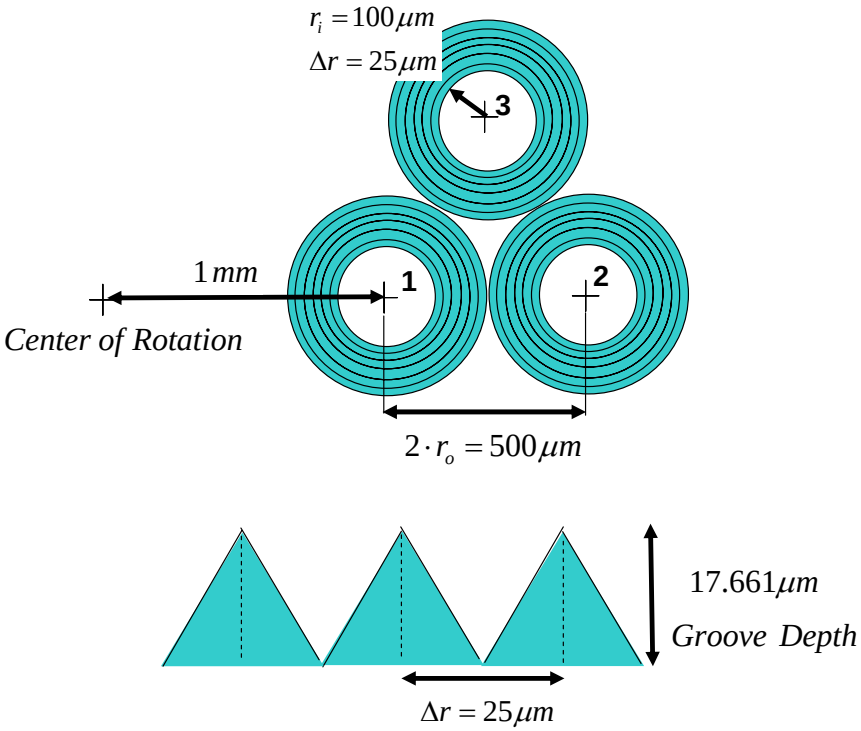

Figure 11. Schematics of circle sets (top, not to scale) and groove geometry (bottom).

A Matlab program was created to take user-defined geometry inputs and create the G-code to cut a circle set. The user defines the initial circle set center position (X_c,Y_c), ring radii, depth of cut, and circumferential feed rates. The program calculates the tool positions at spindle rotations of 120°, 240°, and 360°, and generates the necessary G-code for the required off-axis circular interpolation. Figure 12 shows the data calculated for circle set 1. Each red asterisk is a waypoint in machine coordinates through which the Ultramill tool must pass to complete one ring during circular interpolation. Red triangles connecting the waypoints are used to ensure that the calculated waypoints form equilateral triangles, but do not represent tool trajectories. The small blue circles represent each ring that is intended to be cut as it will appear when the C-axis is rotated at 120°, 240°, and 360°. The large blue circle represents the trajectory of the circle set center as the workpiece is rotated.

The generated G-code has the Ultramill tool start at the center of the outermost ring ($r_o - \Delta r/2$) of one circle set. The tool starts with a C-axis angle value of 0°, then performs an off axis circular interpolation through waypoints at C-axis value of 120°, 240°, and 360° to complete the outer ring. It then moves to the second-to-largest ring, ($r_o - 3\Delta r/2$) and performs a complete circular interpolation again. This is repeated for each ring until the innermost ring is cut ($r_i + \Delta r/2$).

G-codes were generated for 3 circle sets with 3 depths of cut each for a total of 9 programs. Circumferential feed rates were set at 4mm/min with Ultramill operating at 1 kHz. The first set was cut with successive depths of 10 µm, 17 µm, and a finishing pass at 17.661 µm. Circumferential feed rates were set at 4 mm/min with Ultramill operating at 1 kHz. Circle set 2, and then circle set 3 were cut in the same manner.

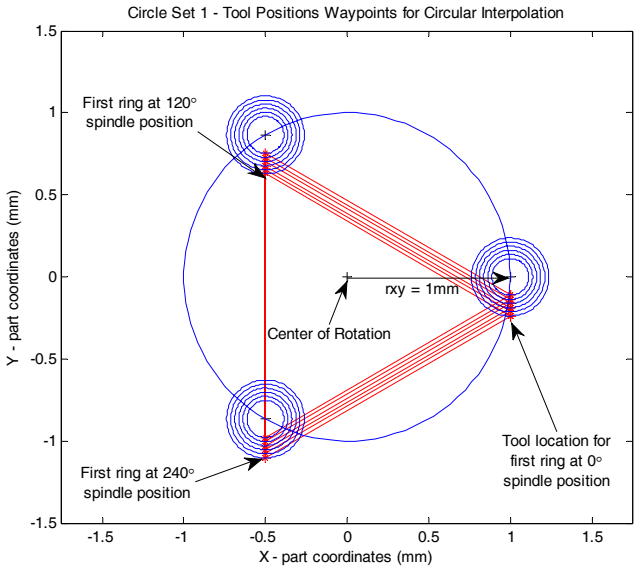

Figure 12. Plot generated in Matlab for all tool positions required to cut circle set 1.

7.6.4 DIFFRACTION GRATING

A diffraction grating with four different rectangular zones as shown in Figure 13 including an off-center circular arc segment, a vertical linear grating, a horizontal linear grating and another off-center circular arc segment was also planned. Each rectangular segment was to be a 1 mm X 0.5 mm with a grating pitch of 0.01 mm. With this number of grooves, code generation must be automated. This is fairly simple with the straight sections, though a little more challenging with the curved segments.

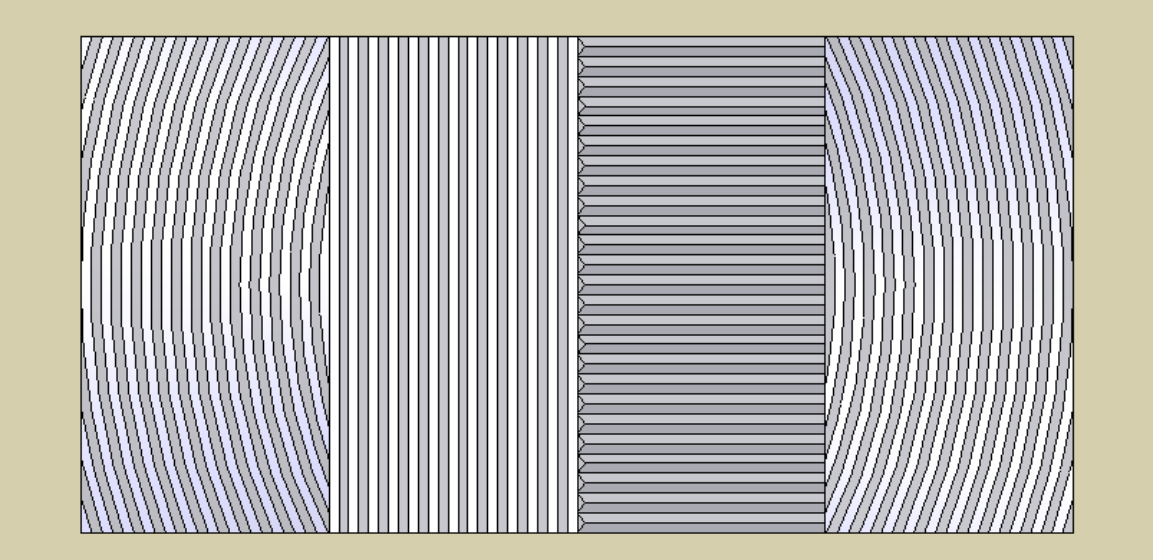

Figure 13. Plan view of a demonstration grating that could be machined. Each of the four segments is 1 mm high by 0.5 mm wide

To machine this grating, the endpoints of the arcs must be calculated and the centerpoint and then converted to the machine coordinates to process the G-code programming. To calculate the intersection of the arcs with their boundaries, the equation of a circle is simply evaluated at any given x- or y- value that represents the bounding line for the arc.

$$r = \sqrt{\left(x_n - x_c\right)^2 + \left(y_n - y_c\right)^2} \tag{10}$$

where x_n is the n^{th} intersection of the n^{th} radius at a certain y_n (in this case ±0.5) with all of the arcs centered at x_c =±0.5 and y_c =0. Once all the intersections are found, they must be sorted according to their order in the toolpath and translated into arc segment paths for the machine X, Y, and C axes. Figure 14 shows a schematic illustration of one such arc being machined.

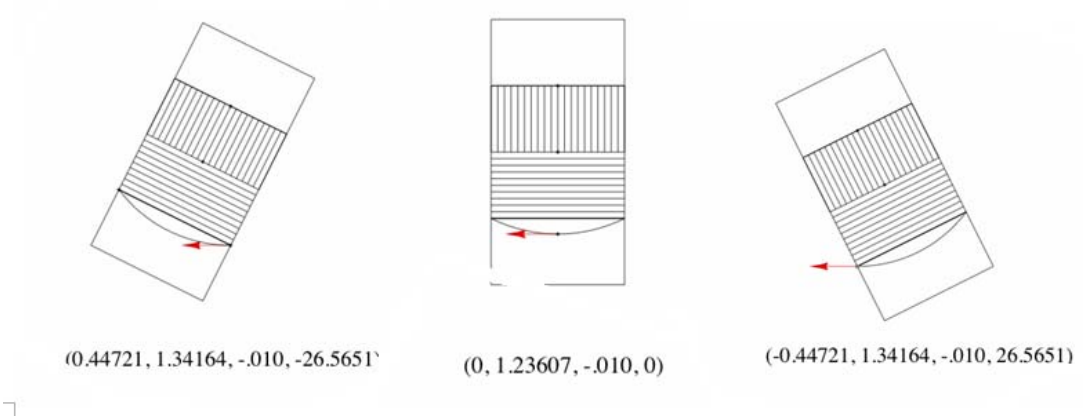

(a) (b) (c)

Figure 14. Schematic of planned diffraction grating showing one arc segment being machined in it (a) starting position, (b) midpoint and (c) ending position. The machine coordinates are shown in parentheses as (X, Y, Z, C).

7.7 CONCLUSIONS

Improvements in the machining capability of the Nanoform/Ultramill have been significant as a result of making the spindle axis a positioning axis and adjusting the squareness of the Y axis. When the spindle was manually positioned, the intersection of three 60° lines could be controlled to 20 µm and that was improved to 200 nm or 100x better. In addition, techniques to machine features that require coordinated moves of all of the axes have been developed. Demonstrations of straight lines, circles and circular arcs have all been completed.

REFERENCES

1. Collins, B, “Slide Motion Errors of a 3-Axis Ultraprecision Diamond Turning Machine”, MS Project Report, Mechanical Engineering Department, North Carolina State University, 2008.

8 DIAMOND TOOL WEAR MEASUREMENT BY EBID

Meirong Shi
Graduate Student
Ronald Scattergood
Professor, Department of Materials Science and Engineering
Thomas Dow
Dean F. Duncan Distinguished Professor in Mechanical Engineering
Department of Mechanical and Aerospace Engineering

Elliptical vibration assisted machining (EVAM) is thought to be a good alternative for diamond turning (DT) when machining some ferrous materials due to the observed decrease in force and wear and the improved surface finish. However, the inherent tool wear mechanisms are still not clear. In order to investigate the wear process for DT and EVAM cutting, it is necessary to perform a systematic investigation of the materials, tool condition, and machining parameters. Characterization of the tool wear condition will be critical to reveal the cutting mechanism. The experiments are designed to measure diamond tool wear in conventional diamond cutting, which is the basis for further EVAM experiments. EBID (electron-beam-induced deposition) is used to measure the diamond tool edge geometry. Results show that EBID can be an effective way to measure tool edge radius and wear land, both in straight and round nose diamond tools. Wear mechanisms during the diamond cutting can be studied based on the measurement of the edge radius and wear land.

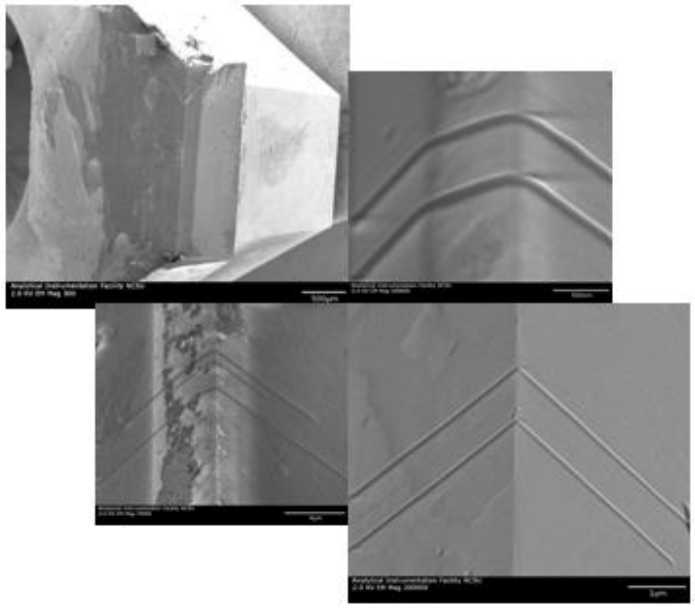

8.1 INTRODUCTION

Although conventional diamond turning (DT) has many advantages in precision machining, it cannot be applied to some materials, such as ferrous metals, due to tool wear. Elliptical vibration assisted machining (EVAM) is an alternative to decrease the force and wear [1, 2]. However, the inherent tool wear mechanism in both methods is still not clear [3]. Since the edge shape and sharpness of the worn tool are vital to the cutting performance during DT and EVAM machining, it is necessary to characterize the tool wear condition.

Tool wear during cutting is referred to as the gradual loss of tool material. Edge radius and flank wear land (especially the edge radius) are thought to be the main factors to describe the tool wear. In the past few years, numerous attempts have been reported to describe the diamond tool condition. However, the diamond tool edge radius is on the order of a few tens to hundreds of nanometers and the diamond itself is nonconductive. These features limit the use of conventional metrology methods.

Researchers have developed several methods to measure the cutting edge radius [4-7], such as atomic force microscopy (AFM) combined with nanoindentation, and scanning electron microscopy (SEM) using two detectors. The results were found to vary from one technique to another, which may be caused by the limitations of the measuring methods. Previous work at the PEC developed a better and simpler SEM method using electron-beam-induced deposition (EBID), to measure the diamond tool edge contour [8, 9].

EBID is an observed effect in the SEM environment. It can happen because the SEM vacuum chamber contains hydrocarbon contaminants from the vacuum pumps. Under appropriate operating conditions, the high voltage electron beam can deposit hydrogenated amorphous carbon onto the diamond tool surface. In conventional SEM measurements, one tries to limit the EBID phenomenon. Recently, EBID was exploited to be used for making nanostructures, acting as masks and locally attaching carbon nanotubes onto the AFM tips for mechanical tests [10, 11]. In our experiments, EBID was adopted to measure the diamond cutting tool edge radius and edge geometry.

By setting the diamond tool edge perpendicular to the electron beam, the high voltage electron beam can be used to induce hydrogenated carbon deposition on a selected area. If the electron scan is controlled to be a line trace, an electron beam induced deposition line will appear across the rake and flank face. This is called a contamination line. The length of the line can vary from several hundreds of nanometers to several micrometers according to different deposit times and magnification. The shape of contamination line can be used for analyzing the tool wear condition.

8.2 DETAILS OF THE PROJECT

8.2.1 EXPERIMENTAL SETUP

To set the diamond tool edge exactly perpendicular to the electron beam, a 45º tilted sample holder was used to fix the diamond tool. Figure 1a is the side view of the diamond tool on a 45º tilted sample holder, while Figure 1b gives the top-down view of the tool edge in the SEM chamber. All measurements of the diamond tool edge by EBID were done on a JEOL 6400 field emission SEM, which is designed to operate at lower voltage and has the capability of high resolution imaging. Studies have shown that many factors can affect the EBID rate, such as the electron beam energy, the beam current, the contamination source and the sample condition [10]. On the other hand, diamond is nonconductive and the surface will be charged under high-energy electron beam, which will result in distortion of the image. In light of these factors, and with many variations in operating conditions, 2kV was found to be the most suitable accelerating voltage. To get a suitable amount of electron emission, the condenser lens and objective aperture were set at 6 and 4, respectively. The working distance was approximately 13 mm.

After the SEM electron gun and apertures were aligned and the astigmatism was removed, scan rotation was selected to bring the cutting edge vertical on the SEM CRT screen. Then, the center area of the tool edge was located and the scanning mode was switched to line scan. After several minutes, a hydrocarbon contamination line was found to be deposited on the surface. To get the profile of the contamination line on the edge, the diamond tool edge was tilted 45º backward. A curved line across the rake and flank face can be seen. Finally, SEM images of the tool edge with the contamination line on it were collected at different magnifications. However, due to the charging effect, the highest magnification image at 2kV that can be obtained is 50kX. During the measurement process, the sample was tilted only once (45º backward to see the edge profile). Compared to former work at the PEC, mechanical rotation of the sample stage was replaced by changing the direction of the scan of the electron beam. Since errors in the mechanical sample stage may bring about measurement errors, tilting the diamond tool only once will result in more precise measurement.

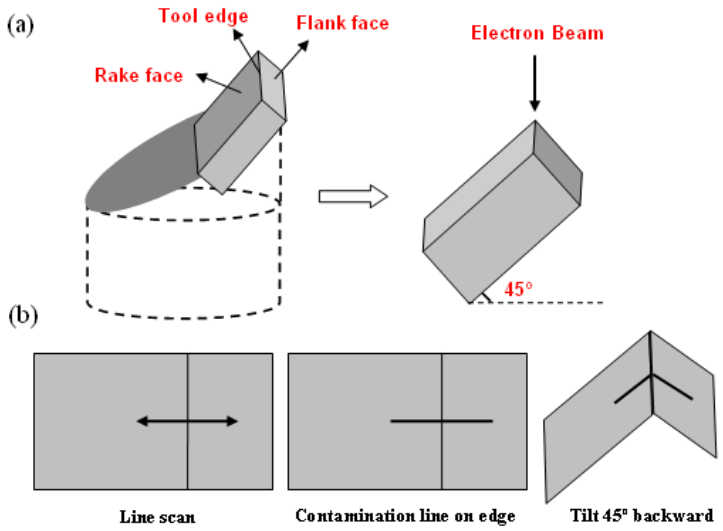

Figure 1. Diamond tool position in SEM chamber (a: side view of the diamond tool fixed on a 45° sample holder; b: top-down view of the diamond tool edge in the SEM chamber).

8.2.2 SEM IMAGES OF DIAMOND TOOL EDGE

Figures2-5 are SEM images showing the edge of the unworn and worn tools. Figure 2 is an image of the cutting edge image of a new diamond tool with a straight cutting nose (Tool 1), while Figure 4 is the image of a new diamond tool with a round cutting nose (Tool 2). Figure 3 and Figure 5 are the worn tool edge images of tool 1 and tool 2 after cutting 7.5km with 6061 Al and 30m with 1215 steel, respectively. In each figure, lower magnification images (10kx) are at the left and the highest magnification images (50kx) that can be obtained are at the right. The deposited contamination lines across the tool edge can be seen clearly. In the low magnification images, the length of the contamination line is about 7 μm on each side, which could reflect the whole profile of interested area. In the higher magnification images, the edge sharpness can be observed in a better view. By comparing worn and unworn tool edge images, it can be found that the unworn tool edge profile is much sharper than that of the worn tool. For the worn tool edge images, the wear pattern of the tool edge for cutting different materials is quite different.

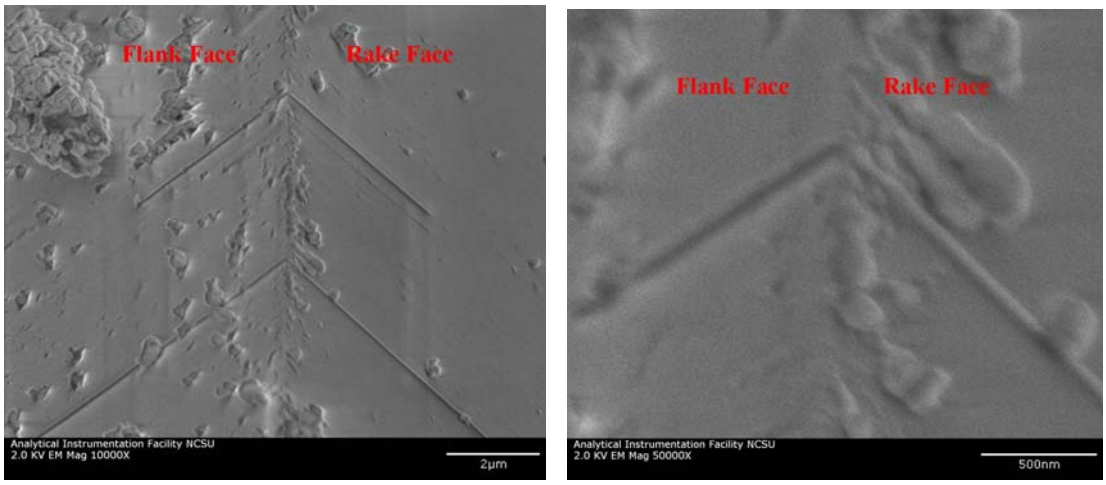

Figure 2. Cutting edge of new diamond tool with straight nose. In each image the flank face is on the left and the rake face is on the right.

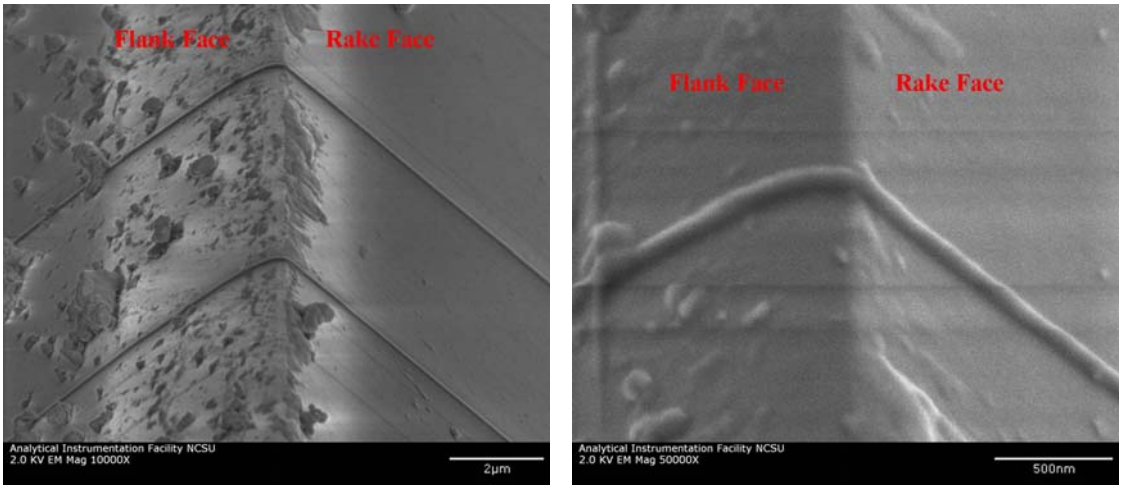

Figure 3. Cutting edge of worn diamond tool with straight nose for 6061 Al. In each image the flank face is on the left and the rake face is on the right.

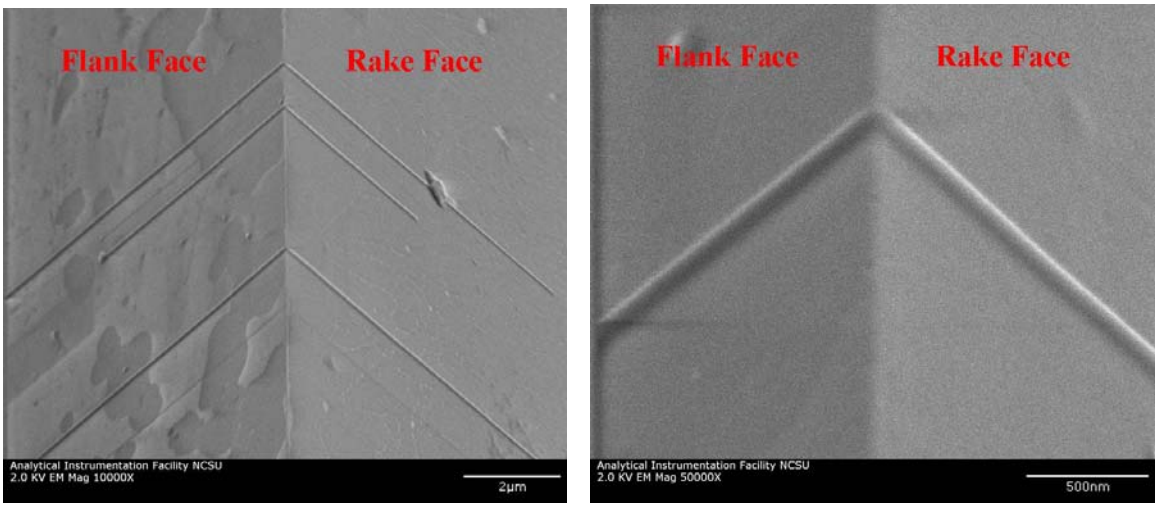

Figure 4. Cutting edge of new diamond tool with round nose. In each image the flank face is on the left and the rake face is on the right.

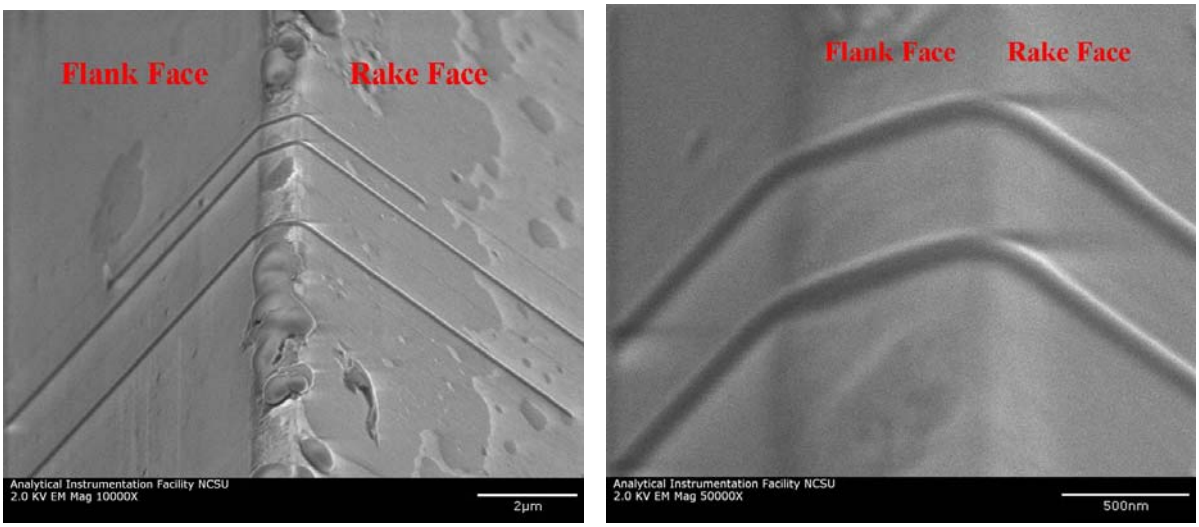

Figure 5. Cutting edge of worn diamond tool with round nose for 1215 steel. In each image the flank face is on the left and the rake face is on the right.

8.2.3 SEM IMAGES ANALYSIS

During the EBID measurement process in the SEM, the diamond tool edge has been tilted 45º backward, so the tool edge in the initial SEM images has the same tilted angle. To get the real edge geometry, every image used for analysis should be stretched 141% (1/cos45º) in the vertical

direction to compensate for the 45º tilt. Figure 6 shows the high magnification SEM images stretched from Figures 4 and 5.

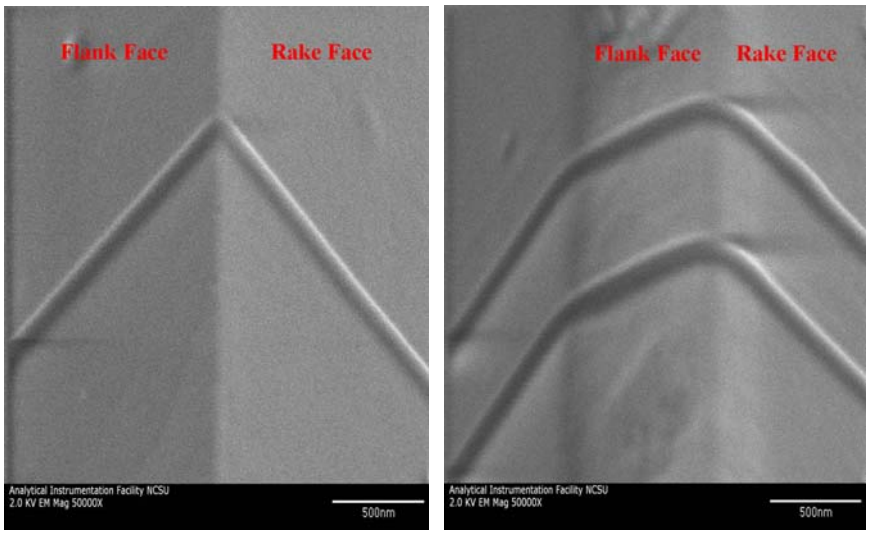

Figure 6. SEM image stretched from figure 4, 5 (Left: new diamond tool with round nose; Right: worn diamond tool with round nose).

To quantitatively analyze the edge radius, a Matlab program was developed to process the digital images. After drawing a set of points along the tip area of the edge, a circle based on a least squares method is used to describe the tool edge radius. The program reports the circle radius in pixel units. By comparing the pixel value with that of the scale bar below the images, the actual value of the edge radius can be obtained. While the circle fitting process is subjective, gradually drawing points very close to the tip area of the cutting edge can allow for a best-fit circle be found. Figure 7 demonstrates the process to find the edge radius of the new tool before cutting. First, the highest magnification (50kV) image was used and stretched (Figure 7a). Then, two lines were drawn close to the contamination trace to see the tool edge clearly (Figure 7b). The image was expanded to better view the tool tip and points were selected that correspond to the tool edge radius. Note that the edge radius ought to be tangent to the rake face and flank face trace lines, and not overlap as shown in Figure 7c, which will give an erroneous edge radius. Remove some points far away from the tip and repeat the fitting circle process until a best fit circle is found (Figure 7d).

The wear pattern for a worn tool is quite different for the two workpiece materials. For the diamond tool cutting 1215 steel, the wear land can be seen clearly and measured directly. Figure 8a-8c shows the fitting process for a worn tool cutting 1215 steel. For 6061 Al, the wear land is not very obvious, so the initial line on the new tool image is needed to make a comparison. Figure 9a-9c illustrates the fitting process for a worn tool cutting 6061 Al. First, the initial edge

geometry formed by two straight lines in the unworn tool image is obtained as the base line (Figure 9a). Then, the base line is transferred to the worn tool image (Figure 9b). The deviation from the base line then describes the flank wear land and a circle is fit to best describe the edge radius (Figure 9c).

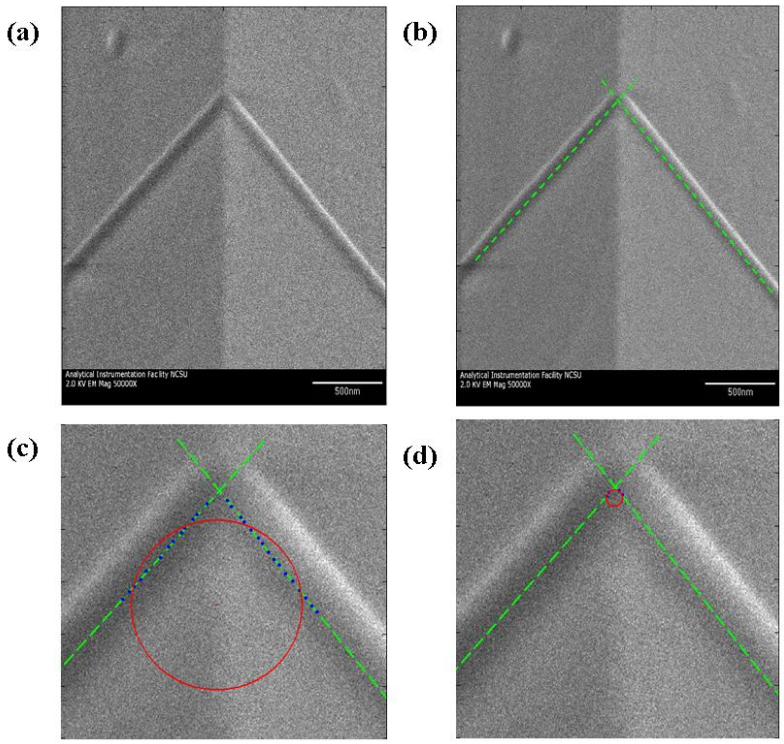

Figure 7. Matlab program fitting process for a new tool.

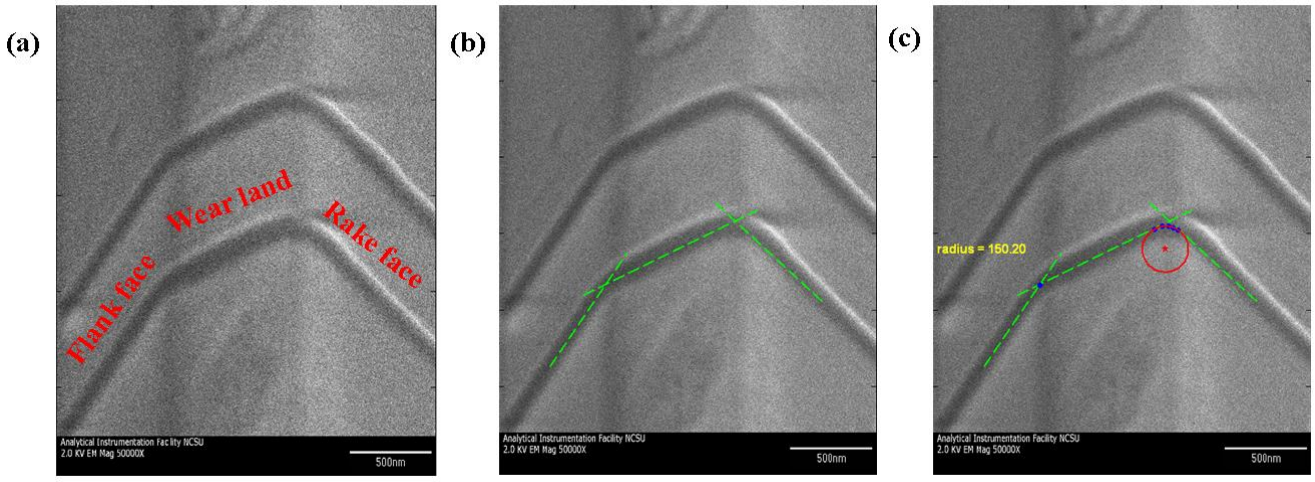

Figure 8. Matlab program fitting process for a worn tool cutting 1215 Steel.

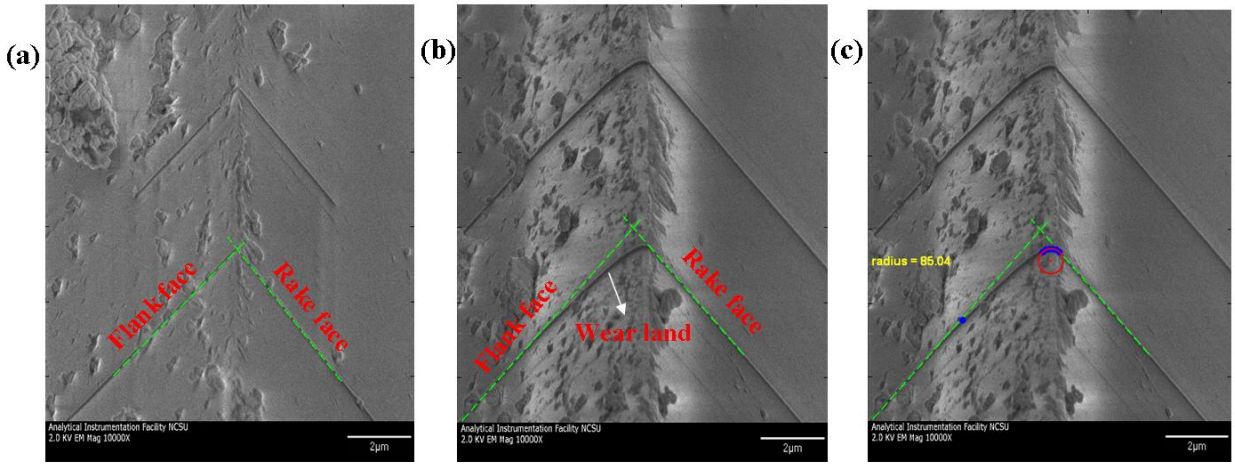

Figure 9. Matlab program fitting process for a worn tool cutting 6061 Al.

8.2.4 WEAR RESULTS OF DIAMOND TOOL FOR CUTTING 6061 AL AND 1215 STEEL

To demonstrate the EBID measurement method for diamond tool wear, two cutting experiments were discussed. Two workpiece materials and two different shape diamond tools were used. One is a straight nose tool with 6º clearance angle; the other is a round nose tool with 12º clearance angle. The diamond tools were supplied by Chardon Tool and Supply Company. Orthogonal cutting was performed using the ASG2500 Diamond Turning Machine. Four 6061 Al disks with a total of 10 km cutting distance were prepared to study the gradual edge retraction of the diamond tool. The diamond tool was measured using the EBID method after each test. In the case of 1215 steel, a total cutting distance of 30m was used and the tool was measured after each 10 m of cut. Cutting parameters and diamond tool conditions in the two experiments are shown in Table 1.

Table 1. Orthogonal cutting experiment parameters and tool conditions.

	Experiment 1	Experiment 2
Workpiece	6061 Al alloy disk Thickness: 0.8128 mm	1215 steel disk Thickness: 1.20 mm
Depth of cut	2 μm	1 μm
Cutting distance	0, 2.5 km, 5 km, 7.5 km, 10 km	0 m, 10 m, 20m, 30 m
Oil and gas	Yes	Yes
Diamond tool	Straight nose Top rake: 0º Clearance angle: 6º Cutting edge length: 2 mm	Round nose Clearance angle: 12º

Table 2 shows the tool wear conditions corresponding to Table 1. The edge radius and wear land length increased with the cutting distance. The edge radius of the new diamond tool is around 20 nm, which is the same as the value reported by Asai [4] and smaller than the value reported by Li [6].

Table 2. Wear conditions of diamond tool for cutting 6061 Al and 1215 steel.

		Edge radius (nm)	Wear land (μm)
Experiment 1	**Al_0km**	25.06	0
	Al_2.5km	142.32	1.201
	Al_5km	168.13	1.961
	Al_7.5km	296.77	2.990
	Al_10km	299.34	4.453
Experiment 2	**Steel_0m**	23.55	0
	Steel_10m	78.61	0.667
	Steel_20m	135.70	0.863
	Steel_30m	152.99	0.997

8.3 CONCLUSION

The EBID method can be used to measure the diamond tool edge geometry. The experimental results show that it is a direct and effective way to obtain diamond tool edge radius and wear land both in straight and round nose diamond tools. The measured edge radius for new commercial diamond tools is around 20 nm, somewhat smaller than values previously reported. Because of the higher magnification of the diamond tool edge images, this method is considered

to be the most accurate measurement to date. Based on the measurement results of the edge radius and wear land, the wear volume can be estimated and wear models can be developed. In future work, the EBID method can be further refined to get higher magnification images for improved data fitting.

ACKNOWLEDGEMENT

Primary funding for this project is being supplied by NSF under contract CMMI-0800560 monitored by George Hazelrigg.

REFERENCES

1. Moriwaki, T., Shamoto, E., *Ultraprecision diamond turning of stainless steel by applying ultrasonic vibration*. Ann. CIRP, 40, pp 559, (1991).
2. Moriwaki, T., Shamoto, E., *Ultraprecision diamond cutting of hardened steel by applying elliptical vibration cutting*. Ann. CIRP, 48, pp 441, (1999).
3. Paul, E., Evans, C. J., et al., *Chemical aspects of tool wear in single point diamond turning.* Precision Engineering, 18, pp 4, (1996).
4. Asai, S., Taguchi, Y., Horio, K., et al., *Measuring the very small cutting-edge radius for a diamond tool using a new kind of SEM having two detectors*. Ann. CIRP, 39, pp 85, (1990).
5. Lucca, D. A., Seo, Y. W., *Effect of tool edge geometry on energy dissipation in ultra-precision machining.* Ann. CIRP, 42, pp 83, (1997).
6. Li, X. P., Rahman, M., Liu, K., et al., *Nano-precision measurement of diamond tool edge radius for wafer fabrication.* J. Mat. Pro.Tech., 140, pp 358, (2003).
7. Brinksmeier, E., Glabe, R., *Advances in precision machining of steel.*, Ann. CIRP, 50, pp 385, (2001).
8. Drescher, J. D., *Tool force, tool edge, and surface finish relationships in diamond turning*. PhD Dissertation, North Carolina Sate University. (1991).
9. Drescher, J. D., *Scanning electron microscopic technique for image a diamond tool edge*. Precision Engineering, 15, pp 112, (1993).
10. Ding, W., Dikin, D. A., Chen, X., *Mechanics of hydrogenated amorphous carbon deposits from electron-beam-induced deposition of a paraffin precursor*. J. Appl. Phys., 98, pp 014905, (2005).
11. Wei, X. L., Liu, Y., Chen, Q., et al., *Controlling electron-beam-induced carbon deposition on carbon nanotubes by Joule heating*. Nanotechnology, 19, pp 355304, (2008).

9 PERFORMANCE OF FRESNEL OPTICS

Thomas Dow
Dean F. Duncan Distinguished University Professor in Mechanical Engineering

Kenneth Garrard
Alexander Sohn
Precision Engineering Center Staff

The objective of this project was to develop Fresnel focusing and scanning lenses. A technique for measuring spot sizes was developed during the project beginning with a color digital camera and evolving to a monochrome array. The measured and predicted spots for several commercial and custom fabricated lenses are discussed. The best performance came from an aspheric Fresnel lens fabricated at the PEC. Spots sizes measured ranged from 40 µm on-axis to 313 µm for a beam 45 mm off-axis beam. The commercial conical and kinoform lenses did not show the same performance with spot sizes that were twice as large. A theoretical and experimental foundation has been created for understanding the operation of Fresnel lenses including refraction and diffraction. The discontinuous nature of the Fresnel-type surfaces presents unique design and fabrication challenges. This activity will add to the understanding of Fresnel design and how this type of lens might fit into a lens designer's tool box.

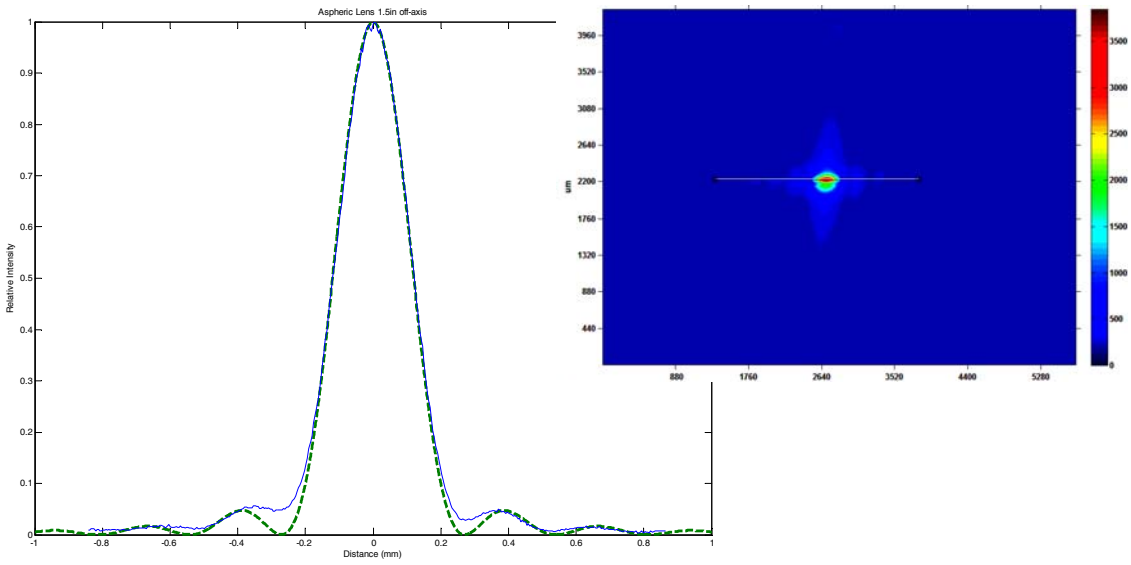

9.1 INTRODUCTION

Fresnel lenses are a type of lens that eliminates the bulk of a conventional lens by collapsing the lens thickness while retaining surface slopes necessary for focusing. Figure 1 shows the Fresnel lens equivalent of a conventional lens. For a rotationally symmetric lens, the discontinuities or grooves formed when collapsing the lens are annular. This produces a much thinner lens, particularly for large apertures.

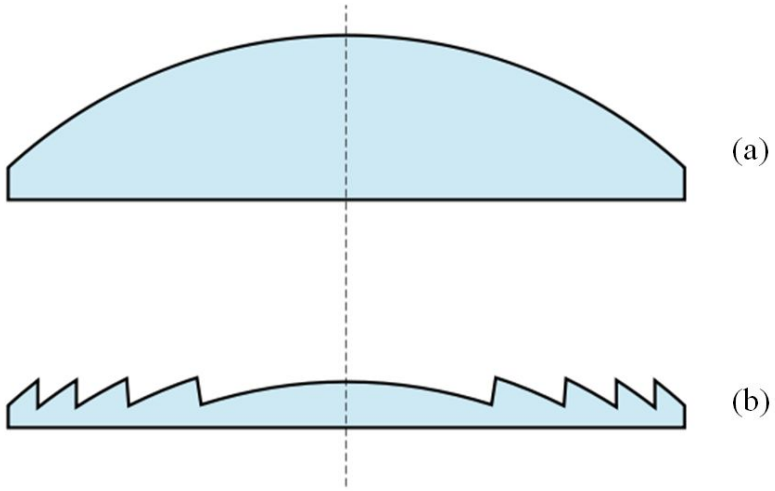

Figure 1. A Fresnel lens (b) is basically a collapsed version of a conventional lens (a).

The advantages of a Fresnel lens are that more light is transmitted due to less absorption and dispersion in the material and with more uniform thickness a Fresnel lens is typically easier to replicate by molding. The latter of these two reasons is why Fresnel lenses are being considered for improving scanning systems in this project. Cost is a driving factor in scanning systems for laser printers, so a switch to an easily moldable Fresnel lens could provide a significant advantage. Fresnel lenses are intended as purely refractive lenses. A common misnomer is to refer to a diffractive lens as a Fresnel lens. Properly, this is called a Fresnel zone plate. Separate and distinct from a Fresnel lens, a zone plate focuses light using diffraction from a series of annular rings. A Kinoform lens combines refractive and diffractive properties of Fresnel lenses and zone plates to produce a more efficient diffractive lens that can also cancel chromatic aberration.

Fresnel lenses have found their way into a number of applications including infrared motion detectors, overhead projectors, solar collectors, theatrical lighting and many more. Typically, Fresnel lenses are used for non-imaging applications where the effects of scatter and multiple internal reflections are not critical problems. While it also qualifies as non-imaging, the application of focusing a rapidly scanning beam to a small spot size is, however, challenging.

9.2 DIGITAL CAMERA

The technique for measuring spot sizes has evolved with the project. The initial sensor was a Canon EOS Rebel XT SLR with an 8 Mpixel color array but this proved unsatisfactory due to the method the camera uses to process the intensity and color of the incoming light. A monochrome Cohu 7700 camera was borrowed but it did not have the sensitivity needed for the measurements. Finally a monochrome Epix 5M10 camera with the proper sensitivity and resolution was purchased. This camera is much easier to use than the Canon camera because it has video capability so the exposure can be set and intensity viewed prior to saving the spot measurement.

This camera has 2592 x 1944 array of photocells spaced 2.2µm apart. The overall size of the array is 5.7 mm wide by 4.28 mm high. It has a sensitivity of 1.4 V/lux-sec at 550 nm illumination. The camera uses a pair of A/D converters to send the data from each sensor to the video board in a PC. One row uses the first A/D and the next row uses the other converter. Unfortunately, each of these converters has a slightly different gain and as a result adjacent pixels have an offset value. After much discussion with the manufacturer, it was decided to average adjacent pixels and the resulting horizontal and vertical resolution is 4.4µm.

A collimated laser source was provided by Lexmark for the experiments. This solid state laser has a wavelength of 650 nm and a 4 mm beam diameter.

9.3 DIFFRACTION FROM A NARROW SLIT

A pair of razor blades were glued to an aluminum block with a spacing on the order of 100 µm to test the spot size measurement. The laser light illuminated the slit and the resulting diffraction pattern can be measured with the camera in both spacing and intensity. This pattern can then be compared to that expected for the light wavelength, the slit gap and the slit to camera spacing.

The camera setup is shown in Figure 2. The Epix camera has a RJ45 cable to connect it to the video board on the computer. It has no lens. The camera is mounted on a xyz stage and the laser is attached to an optical rail along with the slit. The right side of Figure 2 shows the 88 µm width of the slit as measured in a light microscope.

The diffracted intensity pattern in Figure 3 was calculated using Fraunhofer's approximation where the diffracted energy can be written as:

$$I(x) = \frac{\sin^2[\pi(d/\lambda)\tan(x/y)]}{[\pi(d/\lambda)\tan(x/y)]^2} \quad (1)$$

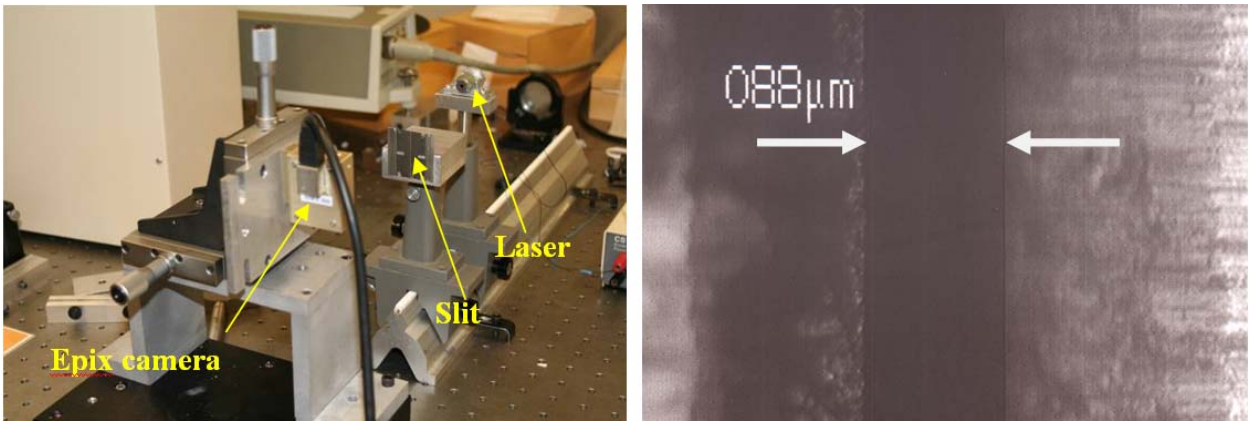

Figure 2. Camera setup to measure the diffraction from a slit and the slit gap measurement

where d is the slit width, λ is the wavelength of light, x is the distance on screen, and y is the distance from the slit to the camera which in this case was 93 mm. The comparison of the amplitude and location of the diffraction peaks provides great confidence in the camera system for measuring the features of interest.

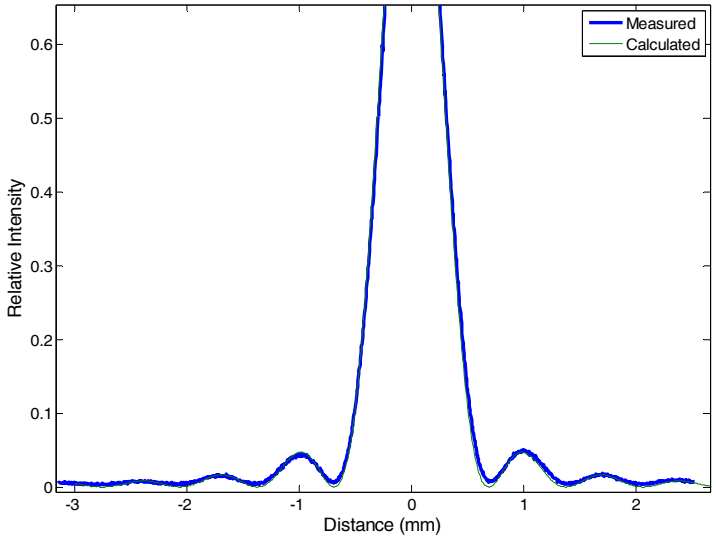

Figure 3. Comparison of the relative intensity vs. horizontal position for the laser beam through an 88 µm slit placed 93 mm from the camera array.

9.4 200 MM FOCAL LENGTH GLASS LENS

The objective of this project is to develop Fresnel focusing and scanning lenses. Before testing the lenses, experiments were conducted using a commercial glass lens to measure the quality of the spot. This would be the best case for the Fresnel lens measurements that follow. The

collimation lens on the laser was adjusted to keep the beam size constant as the laser is moved away from the camera. After adjustment, the beam diameter changed only 30 µm for a 10 cm change in beam to camera distance.

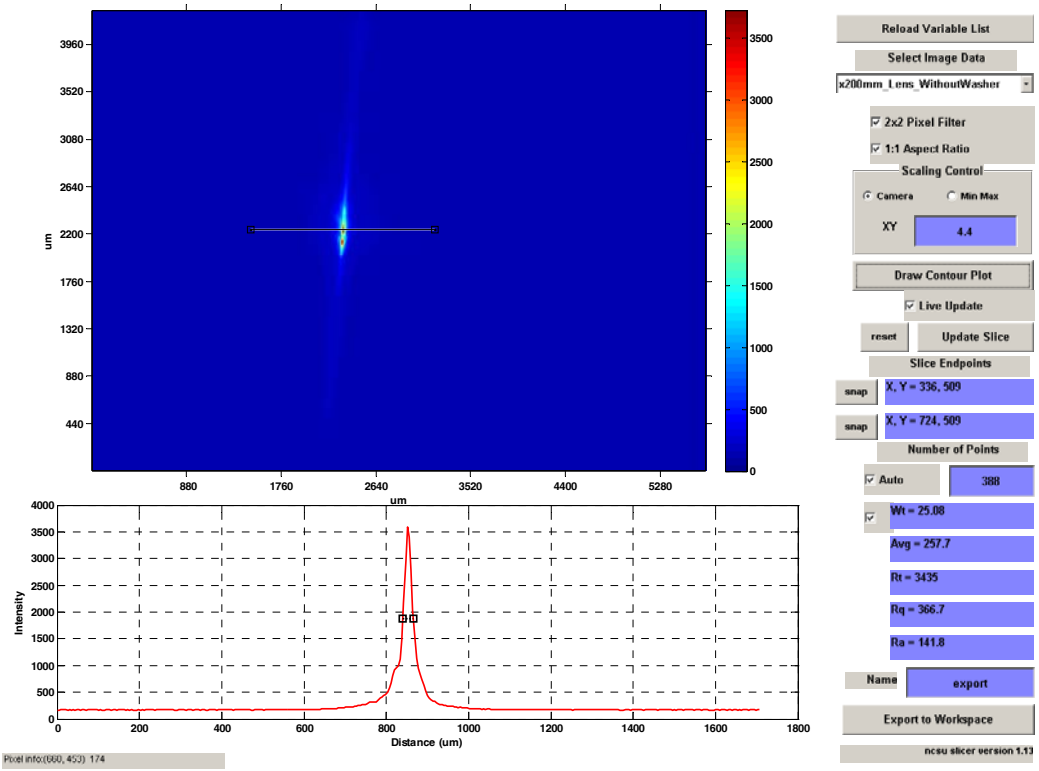

Figure 4. 200mm Glass Lens (FWHM=25.08µm)

The spot size of the glass lens is shown in Figure 4. Clearly it is not a circular spot and the reason is not clear. The lack of symmetry is not due to the lens because rotating it kept the spot size as shown. One possibility may be a lack of collimation in the incoming beam. The spot is characterized as two peaks with wings that move away from these peaks. The spot size in the lower part of this figure is measured through one of the peaks and perpendicular to the line between peaks; that is, through the cursor line in the image. The spot size (Full Width Half Maximum) is 25 µm.

9.5 CONICAL FRESNEL LENS

The next optical surface measured was a commercial conical Fresnel lens obtained from Edmond Optics. The lens is 264 mm in diameter with a 203 mm focal length. It has uniform groove spacing of 127 µm or 200 grooves per inch.

Surface Features of Fresnel Lens The surface profile of the commercial conical Fresnel lens

was measured using the Zygo NewView white light interferometer. The image taken near the center of the aperture (left image in Figure 5) shows the overall shape but also indicates a number of imperfections across the surface. The features near the center have a height of about 1.7 µm. At the right in Figure 5, the features near the outer edge of the lens are shown. Here the amplitude of the features is about 3 µm but the imperfections seem smaller at this increased vertical range.

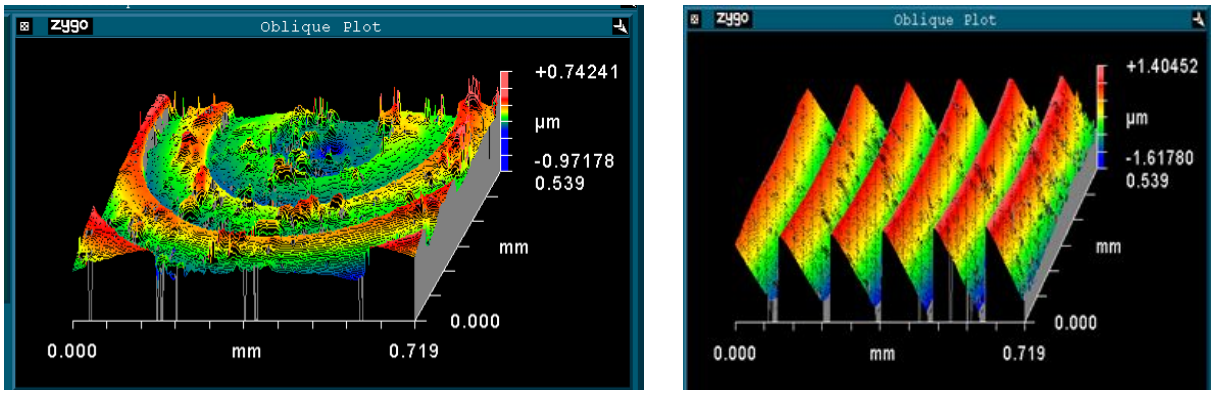

Figure 5. Optical profilometer measurement of center (left) and outside edge of a commercial conical-groove Fresnel lens. Note the poor surface quality near the center.

Spot Size Measurements The camera is centered on the laser beam (Figure 6) and the lens is placed between the camera and laser at a distance from the camera near the 200 mm focal length. The grooves are facing the camera so the light is incident on the flat back of the plastic and refracts/diffracts off the faceted front surface. The lens moves with the camera but the laser is stationary so the effect of illuminating the lens away from the center can be measured.

A spot was measured at intervals on- and off-axis as shown in Figure 6. The exposure was kept constant throughout the measurements. Figure 6 shows the shape of each spot but the location was arbitrarily shifted to the right to reduce overlap and make the shape clear. The FWHM of the spots are shown next to the off axis location. At the center, the spot size is 110 µm but it increases significantly once an off-axis beam is applied. For an input beam applied 12.7 mm off-axis, the spot size grows to 765 µm or about 10x larger. As the beam is applied farther off-axis, the spot size continues to grow but not as large as the on-axis, off-axis change. The experiments were performed with the exposure set to make the intensity at the center near the maximum (4096) and this exposure was kept constant for all of the off-axis measurements. As is clear from Figure 6, the peak intensity drops rapidly with off-axis position and the width of the spot grows. The number of illuminated facets on the lens using the 4 mm laser width is about 30 for each of these measurements. For further discussion and comparison of the results of the spot size measurements, see Section 9.8 in this report.

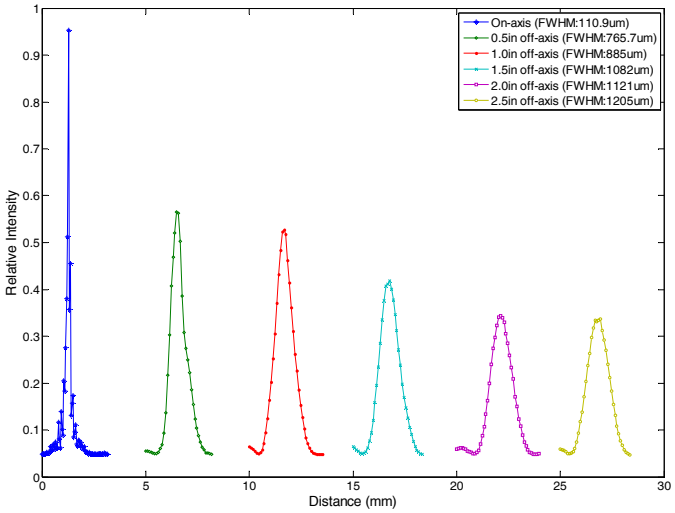

Figure 6. Measurement setup for the Fresnel focusing lenses and spot measurements for commercial Fresnel lens with 203 mm focal length both on and off axis. Distance off axis and corresponding spot sizes are shown in upper right.

9.6 ASPHERIC FRESNEL LENS

The spot pattern of the aspheric Fresnel lens was measured in the same way as the conical groove lens in the last section. The grooves face away from the camera with a 4 mm diameter solid state laser beam on-axis and at several off-axis positions.

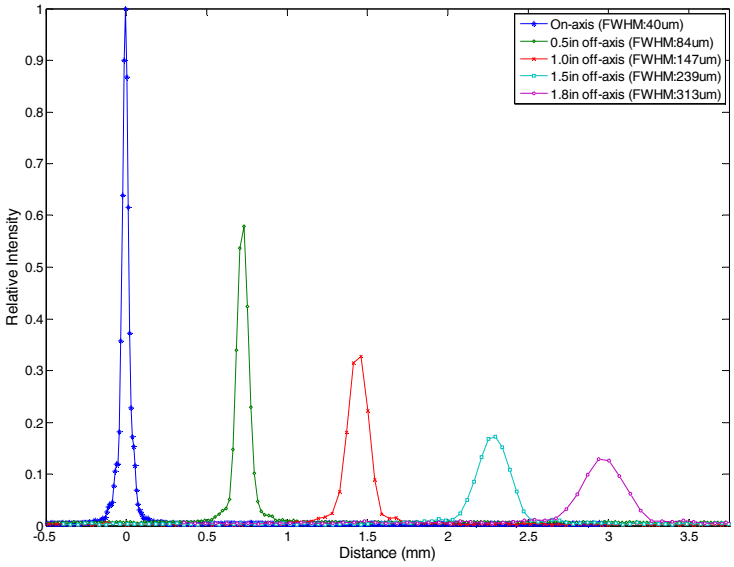

Figure 7. On axis and off axis spot sizes (data in upper left) for aspheric Fresnel lens.

Figure 7 shows the spot sizes measured for the different off-axis positions. The spot sizes for the aspheric lens are much smaller than the conical Fresnel lens ranging from 40 µm on-axis to 313 µm for a 46 mm (1.8 in) off-axis beam. Because of the increased width of the facets, fewer were

illuminated for the 4 mm diameter laser beam; varying from 1 at the center to 7 for the 45 mm off-axis beam. For further discussion and comparison of the results of the spot size measurements, see Section 9.8 in this report.

9.7 KINOFORM LENS

The spacing and angle of the facets on the Kinoform lens determine the location of the refractive and diffractive beams. For a phase match order of M = 1, the groove spacing must be very small at larger apertures and the lens becomes difficult to fabricate; for example, 6 µm spacing for a 200 mm f/l. lens at r = 11.5 mm. Even when the phase match order is increased to M = 5, the groove spacing is still very small. The lens cannot be contoured with a radius tool as was done for the aspheric lens but rather must be machined as a series of plunge cuts. The side of the dead sharp tool forms the flat refractive portion of the lens and must be rotated at each plunge to change the angle as the groove radius is changed.

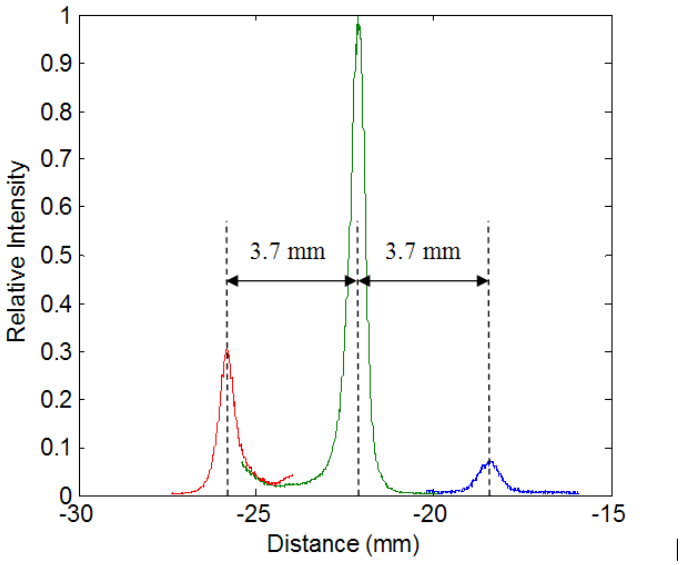

Figure 8. Kinoform Relative Intensity Plot, 190mm Focal Length. FWHM spot size at the central peak is 480 µm.

Spot Size Measurements The machined segment of a kinoform lens was used to measure the spot size in the same way as the conical and aspheric lenses. The collimated laser beam was directed into the kinoform lens (grooves away from source) and the camera was located near the designed 200 mm focal length. The spot consisted of a bright spot surrounded by a circle of lower intensity (~20%) with a radius of 3.7mm. The FWHM size of the central spot was 480 µm. The measurement shown in Figure 8 was created by moving the camera to make 3 images with the same exposure. Stitching them together provides a wider field of view than possible with the 4.5 mm focal array width. The image of the center was made and then the camera was

translated left and right to add segments outside the field of view. The variation of the magnitude of the secondary peaks is probably caused by the alignment of the lens and camera.

The size of the spot from the kinoform was disappointingly large – nearly 0.5 mm. Since only an annular ring was machined, only one off axis segment (approximately 25 mm off-axis) could be measured. While a large spot, it is significantly better (half the size) than the commercial conical Fresnel lens (885 µm), but it is larger than the aspherical Fresnel lens (147 µm) machined at the PEC. Additional work related to the fabrication technique (ball bearing stage is potentially a problem) and lens design sensitivity studies will provide reasons for the measured performance.

9.8 DISCUSSION OF SPOT SIZE MEASUREMENTS

The size of the spots measured for the aspheric Fresnel lens was shown in Figure 7. The spot for the 38 mm (1.5 in) off-axis beam is reproduced in Figure 10. This has all the hallmarks of a diffraction pattern from a single slit. The experimental shape matches the shape from a 510 µm wide slit which is 203 mm from the camera. The shape of the aspheric lens at 38 mm from the axis is shown in Figure 9. If the assumption is made that the curved region of the Fresnel lens created by the tool radius does not play a role in the diffraction, the resulting width of the facets is 510 µm which agrees with the diffraction pattern that matches the data in Figure 10. This result was not expected but has some relevance to diffraction theory.

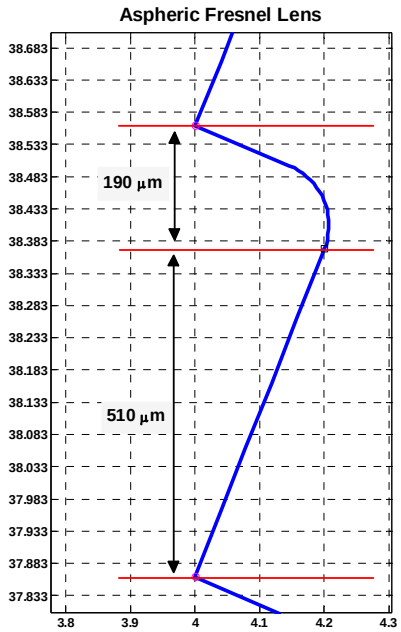

Figure 9. Section of two grooves of the aspheric Fresnel lens 38 mm off-axis. Note the 0.15 mm obscured region formed by the 0.1 mm radius tool and the relief angle.

Based on the result for the 38 mm off-axis beam, the data from Figures 6 (conical Fresnel) and 7 (aspheric Fresnel) are compared in Figure 11. The data for the FWHM intensity from the spot measurement are shown as the markers and compare the results from the conic and aspheric lenses. While both lenses have small FWHM spots on-axis, each grows as the beam is moved off-axis. However, the aspheric lens is superior throughout the range. The steep increase in spot size for the conic Fresnel lens as the beam moves off-axis is dramatic.

The intensity of the diffracted light from a single linear slit can be estimated from Equation 1. This diffraction equation is written in a different form in Equation 2 with the variable $\beta = (\pi d \sin\theta)/\lambda$ where d is the width of the slit, λ is the wavelength (650 nm) and θ is the

angle between the center of the slit and the location of interest at the camera.

$$I = I_0\left(\frac{\sin\beta}{\beta}\right)^2 \qquad (2) \qquad FWHM = \frac{2.783\lambda y}{\pi d} \qquad (3)$$

In this form, the first zero for the function exists at $\beta = \pi$. It can also be used to find the value of I at the 0.5 or the half-maximum point. The 0.5 intensity occurs at β = 1.39155. By using this value in the definition of β, an expression for the FWHM spot size for different slit (or facet) widths, d, can be written in Equation 3 where $y = \sqrt{\text{distance(off-axis)}^2 + \text{focal-length}^2}$; that is, the distance between the facet of interest and the focus of the lens.

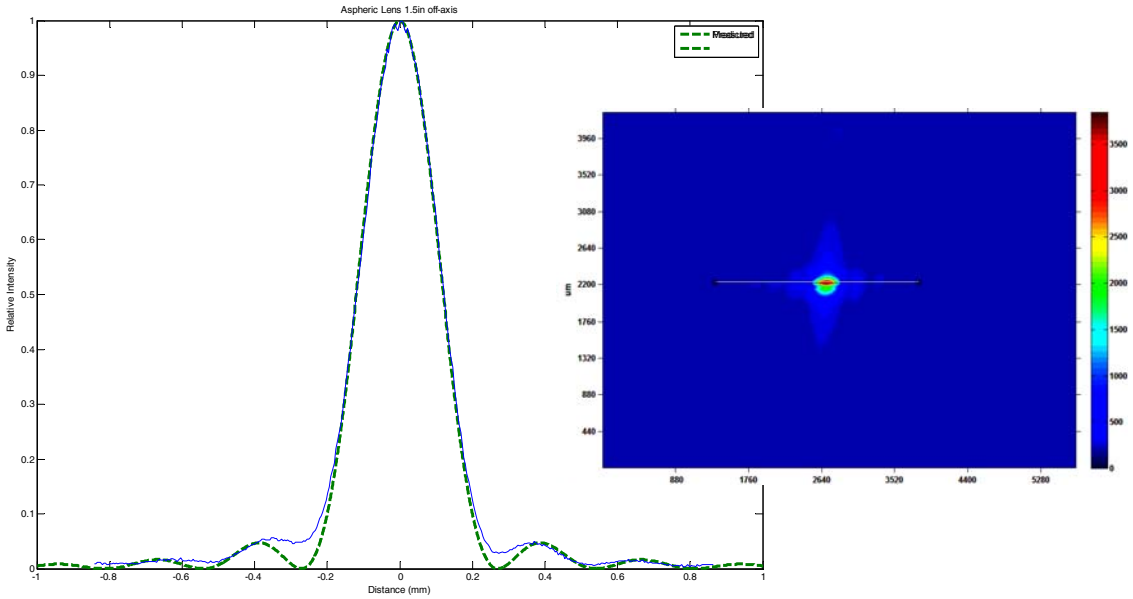

Figure 10. Spot size from 4 mm diameter laser beam 38 mm off-axis on the aspheric Fresnel lens. The diffraction pattern from a 510 μm wide slit 203 mm from the camera is also shown. Inset shows the 2D view of the spot and the line of the measurement.

The data in Figure 11 shows the FWHM values predicted for the conical and aspheric Fresnel lenses along with the measured values. The solid line is the predicted spot sizes for the aspheric lens based on the size of the facets less the width of the curved region caused by the tool nose radius shown in Figure 11. The results are surprisingly good and smoothly translate from on-axis values to the 45 mm off-axis values. The conclusion could be that the aspheric shape turns the light from each facet toward the focus but the diffraction from the boundaries increases the spot size as the size of the facets decreases.

The diffraction hypothesis that fit the aspheric lens data does not fit the spot sizes measured with the conical Fresnel data in Figure 11. For the conical Fresnel, the width of the facets is constant (127 µm) and the FWHM spot size prediction is nearly constant with off-axis distance. The prediction changes only because of the increase in distance from the off-axis point to the focus. There may be blocking of the facets as the off-axis distance increases that would reduce the "apparent" width of the slit and thus the spot size. This was not considered in the results shown in Figure 11 and no calculation was made to include the effect of blocked facets nor the effect of coherent superposition from the larger number of facets illuminated by the laser for the conical lens (31) compared to the aspheric lens (7 at the largest off-axis position).

The kinoform lens behaved much different than either the aspheric or conical lens. The kinoform is a conical lens but attempts to get all of the diffractive energy at (or near) the refractive peak. It has extremely small facet sizes (on the order of 33µm or 25% of the conical Fresnel) which will lead to large spot sizes from the diffraction model in Equation 3. The number of facets illuminated by the laser beam is much larger than the other lenses - on the order of 120. The predicted size of the spot at 25 mm would be 3.5 mm from the Equation 3 but the actual size was about 0.5 mm. This spot size is not as good as the aspheric lens but significantly better than the conical lens. The measurement of the lens facets pointed to variations in location on the order of a micrometer which is the order of the wavelength of the laser light. The sensitivity of this design to manufacturing tolerances is an important issue that should be addressed.

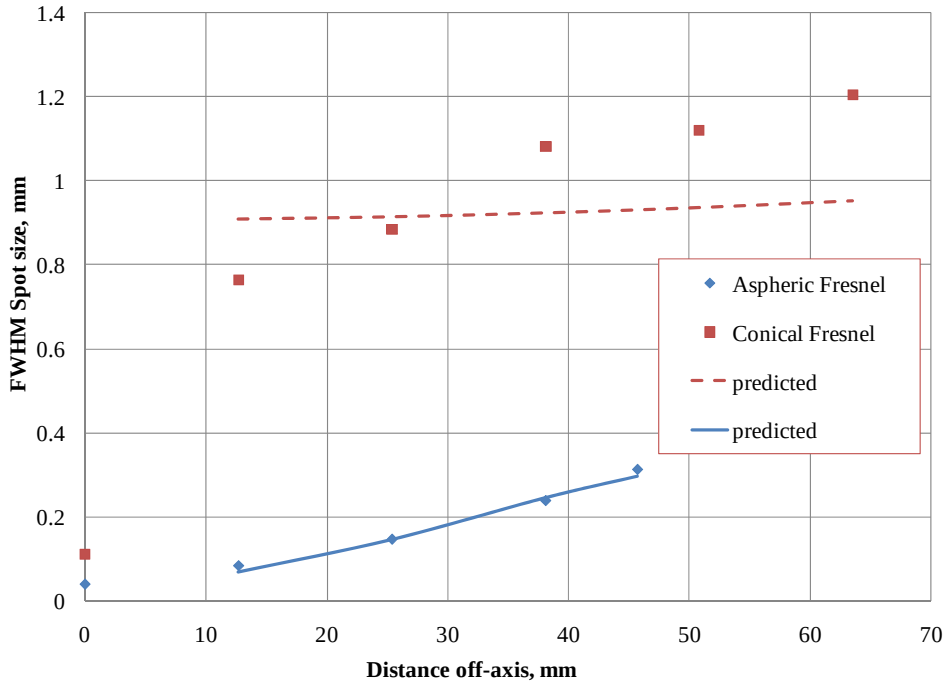

Figure 11. Full Width Half Maximum (FWHM) spot size vs. off-axis illumination distance. Data shown for aspheric Fresnel (lower) and conic Fresnel (upper).

9.9 CONCLUSIONS AND FUTURE WORK

An iterative aspheric zone Fresnel lens design code has been developed. The code includes toolpath generation and ray tracing through a simulated as-machined surface. A numerical diffraction analysis code for an arbitrary lens shape has been implemented. The code is general purpose in that aperture size, focal length and wavelength are not constrained. Extension of the routine to implement both refraction and diffraction through multiple surfaces is being implemented. A kinoform design code that matches the phase from adjacent Fresnel zones by varying the zone width as a function of optical path length and wavelength has been written. The resulting lens directs both the diffracted and refracted light to the same locations, the focus. However the kinoform lens is very sensitive to wavelength changes and presumably manufacturing tolerances.

The testing of Fresnel lenses at the PEC has progressed from photographs made with a commercial SLR digital camera to a high-resolution, specialized monochrome array. While acquiring an understanding of the operation of digital cameras, both color and monochrome, a powerful tool for image analysis is now available for subsequent experiments and development. These techniques have been used to analyze the performance of slits, prisms, conical lenses, aspheric lenses and kinoform lenses. The results show great potential for using Fresnel lenses to focus sub-millimeter-size beams.

The measured and predicted spots for several commercial and custom fabricated lenses are discussed. The best performance came from an aspheric Fresnel lens fabricated at the PEC. Spots sizes measured ranged from 40 μm on-axis to 313 μm for a beam 45 mm off-axis beam. The spot size increase has been compared to the diffraction pattern for a slit equal to the facet size of the lens with impressive accuracy. The commercial conical and kinoform lenses did not show the same performance with spot sizes that were twice as large.

The lenses designed and fabricated thus far have been focusing Fresnel lens and the next logical step could be to design a scanning lens based on the lessons learned. A foundation has been created for understanding the operation of Fresnel lenses including refraction and diffraction. The discontinuous nature of the Fresnel-type surfaces presents unique design and fabrication challenges. This activity will add to the understanding of Fresnel design and how this type of lens might fit into a lens designer’s tool box.

10 POLARIS 3D OPERATION AND CONTROL

Kenneth Garrard
Precision Engineering Center Staff
Amir Pirzadeh
Tifsoon Ulterior Systems, Cary NC

An instrument for the metrology of high-aspect ratio surfaces has been constructed. By mounting a linear axis and a probe on top of a rotary table and rotating a surface on an orthogonal spindle a hemispheric measuring volume is obtained. An additional linear axis allows a variety of convex and concave surfaces to be measured while keeping the probe nearly normal to the surface as it sweeps out a spiral path from the equator to the pole. Challenges in the construction of this instrument include the alignment of the axes, measurement of their error motions, development of an appropriate compensation strategy for those errors and building a control system that is both user friendly and fast enough to measure a part in less than two minutes. This report describes the control system and the operation of the Polaris 3D spherical measuring machine.

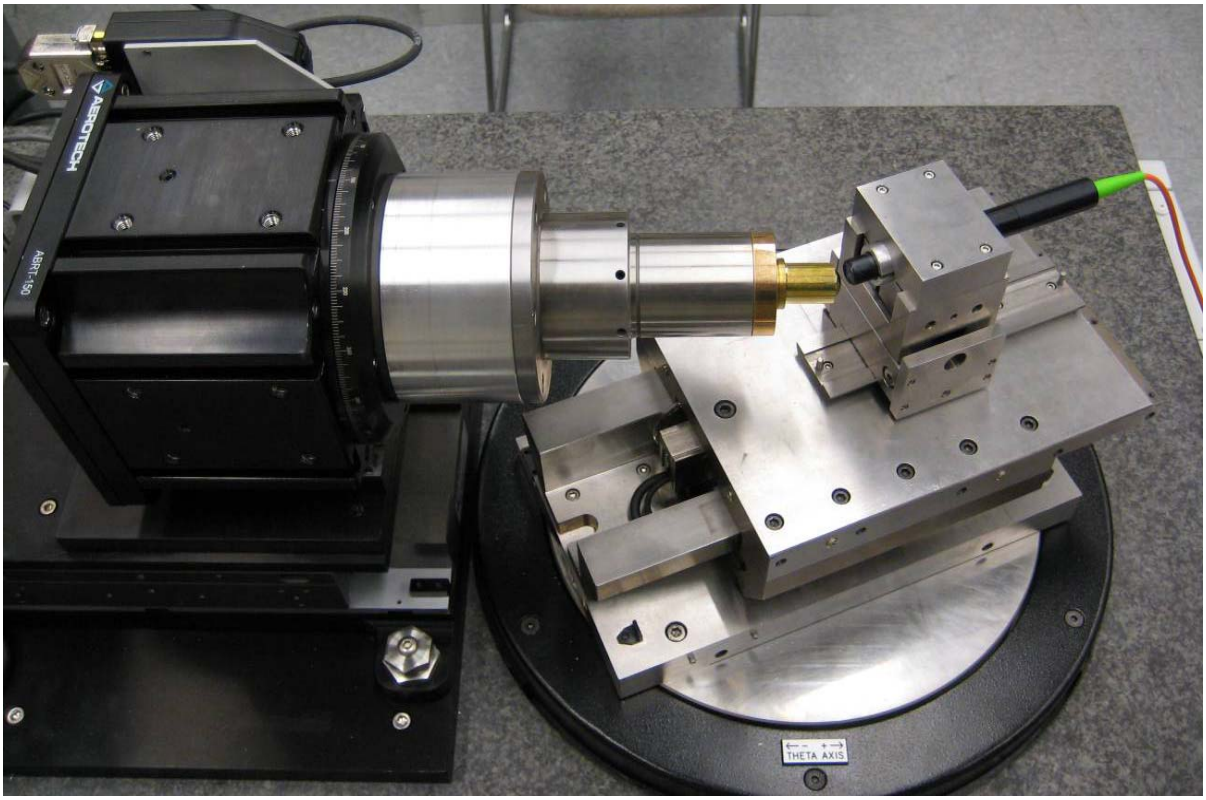

10.1 INTRODUCTION

The polar geometry measuring machine developed in by the PEC in 2000 [1-5] has been upgraded with an additional rotary axis and linear axis to create a 3D spherical coordinate measuring instrument. The 2D Polaris machine used an air bearing LVDT as a probe. The new instrument uses an optical probe to rapidly measure a surface without damage. Shown in Figure 1 are two opposing sets of stacked axes; linear on top of rotary with a vertical axis of rotation (R and θ) and rotary on top of linear with a horizontal axis of rotation (Z and φ). The measuring probe is mounted on the linear R axis. As a part is rotated in a vertical plane by the second set of axes, arcuate motion of the probe in an orthogonal horizontal plane allows a spiral set of data to be collected and assembled into a 3D surface profile.

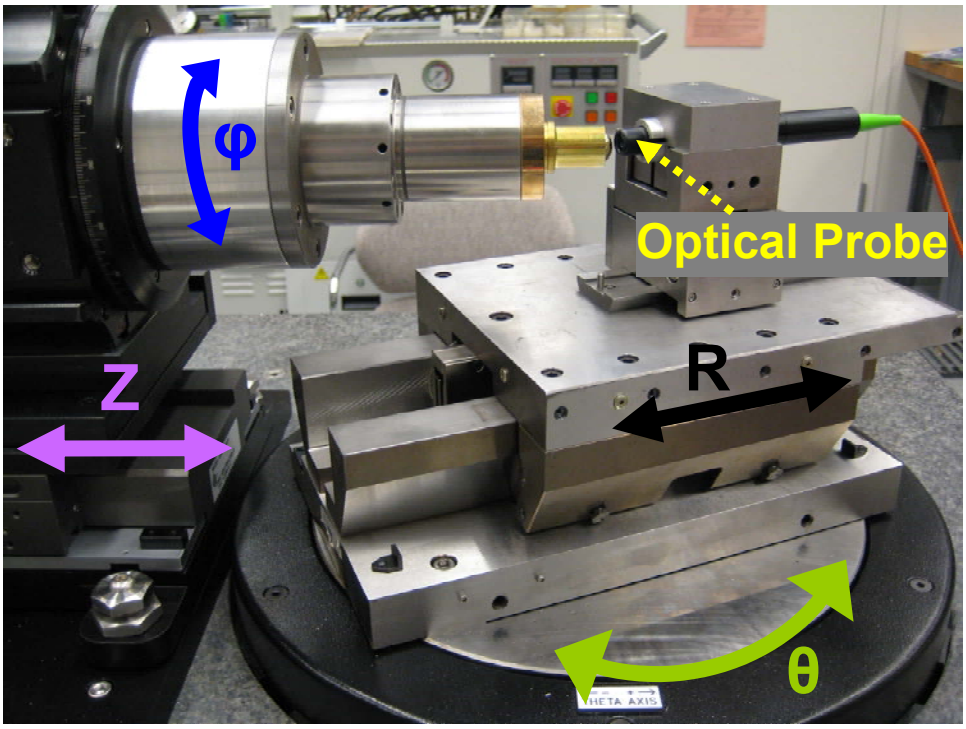

Figure 1. Polaris 3D.

10.2 STIL CHR 150 OPTICAL PROBE

Non-contract metrology for Polaris 3D is desirable to avoid damage to finished optical surfaces. A STIL CHR 150 optical probe is available for this project. In this probe a lens with an axially chromatic aberration and a double spatial filter is used to produce a confocal imaging system for distance measurement. For any probe lens to object distance, light of a specific wavelength (i.e., color) will be in focus. The CHR 150 has a spot size of 8 µm and a maximum measurement range of 300 µm at a working distance of 5 mm. Its axial accuracy is 90 nm and lateral

resolution is 4 µm. The steepest slope that can be measured from a specular surface is 25°, although this value is highly dependent on material and surface characteristics. The output of the probe controller is a unipolar 10 volt analog signal linearly scaled into the adjustable measurement range. A second analog output (also 0 to +10 volts) is proportional to the intensity of the measurement signal. The probe bandwidth is 1 kHz. The probe pen can be see in Figure 1 mounted on the R axis. The electronics enclosure for the probe is shown in Figure 2.

Figure 2. STIL CHR 150 optical gage.

The measurement signal voltage increases as the distance from the probe to the surface increases. The intensity signal represents the "quality" of the reflected light and decreases as the probe is moved closer to the sample or as the slope is increased. A highly specular surface may saturate the detector or there may not be enough returned light from a diffuse or rough surface. Both the intensity and displacement output voltages are zero when the probe is too close or too far from a reflective surface or if there is too much reflected light or not enough reflected light. Changes in specularity, scratches and sharp slope changes may all result in the loss of a signal from the probe.

It is desirable to use the probe not only as a measurement device, but for the machine controller to use the probe as a secondary feedback source such that the machine axes "follow" the probe. This will enable the measurement of complex surfaces without programming the machine axes to move in a trajectory that follows the shape of each part.

10.3 UMAC CONTROLLER

The Delta Tau UMAC controller embedded in the prototype Polaris 2D machine (see Figure 3) has been upgraded for Polaris 3D. A faster processor and more on-board memory were added to facilitate data acquisition during a measurement. A PC/104 single board computer has also been

added to the UMAC card cage, eliminating the need for a separate PC host. This should also speed up data transfer between the UMAC and the user interface software by utilizing bus communications instead of USB or RS-232 serial. Additionally a high resolution sine/cosine interpolator board has been added to the UMAC to process analog encoder feedback signals from the new rotary (φ) and linear (Z) axes.

Figure 3. UMAC controller and Polaris 3D electronics.

10.3.1 SERVO CONTROL AND PLCS

The UMAC is responsible for motion control of all axes (R, θ, Z and φ) and data acquisition during part setup, calibration and measurement. Software PLCs are used to home the axes and to detect faults and respond appropriately (e.g., stop motion if an axis is moved beyond its range). The UMAC is not programmed as a general purpose computer to control the machine axes. Rather the servo code (PID plus acceleration and velocity feedforward) and motion program interpreter are embedded in firmware and the user/OEM specifies operating modes, a mapping of the machine geometry to a coordinate system, controller gains and the I/O configuration. The firmware performs trajectory generation along a specified path through Cartesian space and servo control for the motors as a high priority real time task. Background processing (i.e., while waiting for the next real time interrupt) includes responding to commands from a host computer, reporting motor positions, machine fault detection and other housekeeping tasks. These later functions are implemented as software PLCs (programmable logic controllers). Table 1 lists the Polaris 3D PLCs and their function.

Table 1. Polaris 3D Software PLCs.

PLC	Function
estop	Initializes the controller, establishes communication with the user interface and starts other PLCs. Monitors machine state for errors and stops axis motion if there is a fault.
axpos	Reads axes positions and reports to the user interface. Monitors the overtravel status of all axes and implements a probe filter to quantify signal integrity.
psetup	Implements the probe setup procedure and data analysis.
trigger	Moves one of the linear axes until the probe is in range.
spin	Starts and stops the part spindle
probetrack	Continuously tracks probe position and commands the R axis servo filter to follow the probe. Records measurement data in a circular queue for the user interface. This high priority PLC executes once per servo update cycle.
jog, jogzero	Commands axes to move in response to user input via axis and speed selector switches and the handwheel.
homeall, homeR, homeTheta, homeZ, homePhi	Move axes to their home position and initializes the machine coordinate system.

Probe signal integrity

The STIL probe measures the change in distance between the probe pen and a reflective surface. If the probe-sample distance is not within the working range (5000±300 μm) both output voltages (distance and intensity) will be zero and the probe is out-of-range. However, it has been observed that when the probe sample distance dithers near either edge of the measurement range any signal voltage is possible. Filtering can reduce, but not eliminate, the likelihood of incorrectly deducing overtravel from the time history of probe signals. These signals can be zero for a variety of reasons not related to displacement and the probe can be crashed into a sample while still generating valid measurement data. For these reasons the probe signals are not used for overtravel detection. Instead the integrity of the probe data is monitored by the position reporting PLC, axpos, which will halt measurement if too much data is lost. The threshold for halting a measurement will be determined by the nominal part geometry, initial intensity

recorded during part setup, angular range of the measurement and a user specified tolerance for missing data.

R axis control with optical probe feedback

The R axis has two operating modes. It can be commanded to move independently of the other machine axes either from the user interface or with the manual handwheel controls. Alternatively the servo control loop for R can consider the optical probe measurement signal as an error that should be driven to zero since the probe moves with the R axis. This type of feedback loop is easily implemented on the UMAC controller using a real time software PLC, "`probetrack`," to filter and integrate the probe signal and send it into the R axis servo loop. The control action for this follower servo loop is intentionally weak so that the R axis is stable. This algorithm is depicted in Figure 4 and the PLC code is listed in Appendix A. The PLC also has a rate limiter to prevent axis oscillation in response to analog noise and it ceases to update the input to the integrator if the probe signal is not "good". Thus the R axis will complete the accumulated command and simply stop moving if the probe signal is lost. In the worst case of a rapidly changing probe signal that moves through its full range in one servo cycle the R axis will move no more than 150 µm trying to respond to the probe. In practice, the R axis position lags a rapidly changing probe signal by about 20 µm and never moves more than twice that amount when probe signal is lost. This isn't an issue for a measuring instrument since the surface displacement is a combination of the Z, R and probe displacement signals as a function of the θ and φ positions. Thus less than 20% of the probe range will be used during a measurement.

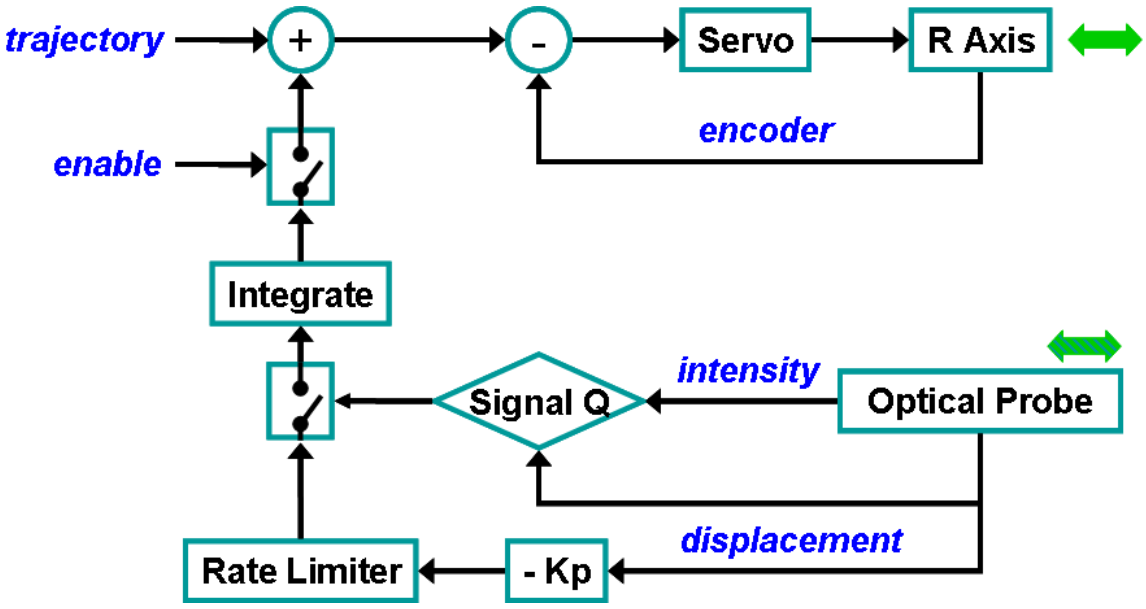

Figure 4. Probe tracking algorithm.

10.3.2 USER INTERFACE

A consultant, Tisfoon Ulterior Systems, has been contracted to assist with controller integration and prototype user interface programming. Development of a full user interface is not part of the current project, however a host PC interface is needed to operate the machine and store measurement data. The tools provided by Delta Tau, PEWIN and PMACPLOT, are sufficient, but cumbersome to use and error prone. Tisfoon Systems has developed a highly flexible application that provides similar functionality in an easier to use format. Figure 5 shows the basic screen layout of this interface. Customization of buttons, dialogs, data entry, display and data acquisition functions will be performed as the system requirements evolve.

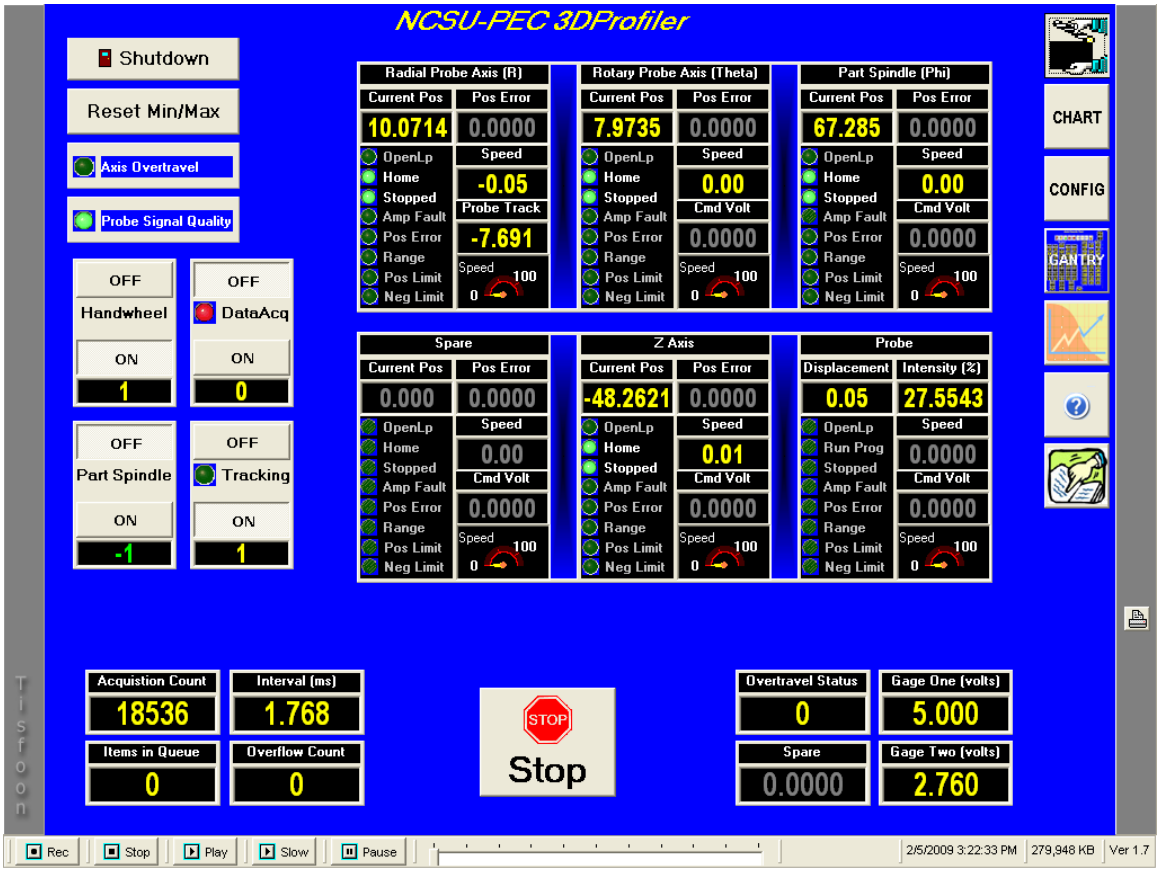

Figure 5. Prototype Polaris 3D user interface

10.3.3 DATA ACQUISITION

Synchronized, real time data acquisition of probe and axis position data during a measurement is critical to the success of the project. To rapidly measure a nominally spherical part in a few minutes with dense point spacing on the surface, the full probe bandwidth must be used and data

collected at 1 kHz. The UMAC does not have enough memory to store a full measurement data set so a region of memory has been reserved to implement a circular queue with a real time UMAC task filling the queue at one "end" while the TDProfiler application on the host PC/104 reads data from the other "end" of the queue and saves it to the disk drive. In this way the rates at which data is stored and data is retrieved do not have to match as long as the long term average rate of the reader is as fast as the writer. A larger queue allows for greater variance in the rate. However the amount of shared memory (e.g., accessible to both the controller and the host) is very limited. The new controller card with the greatest memory space offered by Delta Tau allows for an overflow buffer that can hold almost 50 seconds of measurement data collected at 1 kHz. After the measurement is complete the overflow buffer contents are transferred to the host through the circular queue. This necessarily creates a data file that is out of order, but by including a time stamp (i.e., a simple counter) with each sample the correct ordering is easily recovered. The amount of data transferred is greatly reduced by saving the difference between successive values in the queue and performing a cumulative summing operation to reconstruct the original data vectors. This is most effective for fast collection of slowly changing large values such as encoder feedback from a slowly rotating axis acquired at 1 kHz.

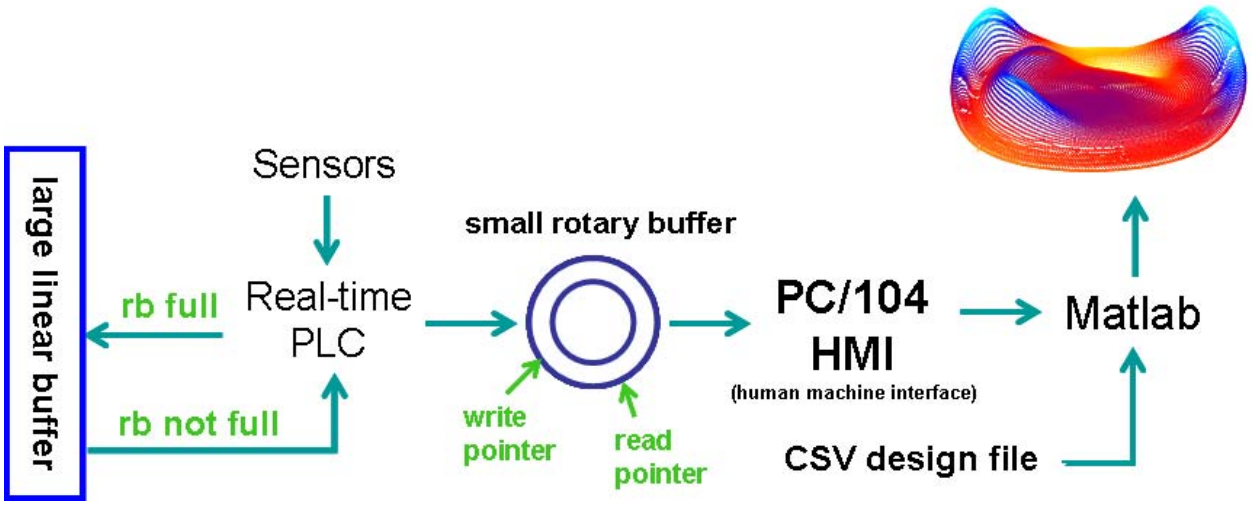

Figure 6. Polaris Data Acquisition

The flow of data from the feedback sensors and probe to an error surface plot is shown in Figure 6. The current prototype user interface is sufficient for axes calibration, part setup, initiating and stopping the measurement process and saving the raw data into a file on the host PC hard drive. For the prototype instrument, a separate application will be developed using Matlab for presentation of the results. The first version of this application was developed to aid in data collection for the evaluation of machine error motions and calibration. Figure 7 shows the GUI window for this application, Lodestar. The only link between it and the controller user interface

is a saved data file. Lodestar need not be run on the same computer provided that the Polaris hard drive is on a LAN. Lodestar will be enhanced in stages to provide 3D plots of a measurement result, compensation for repeatable machine errors, subtraction of a part design represented by a CSV file and export of measured data to CSV, Matlab and MetroPro formats.

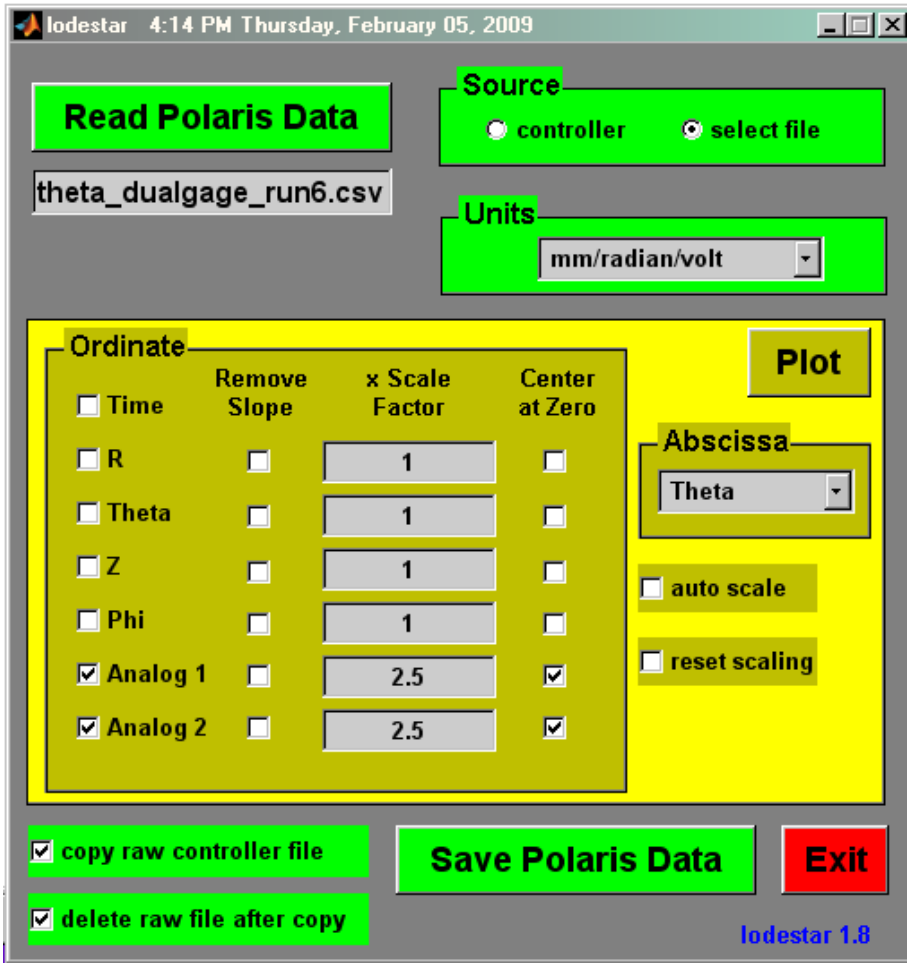

Figure 7: Matlab application for processing raw Polaris data.

10.4 INITIAL MEASUREMENTS

The prototype machine was fitted with a temporary part spindle (φ) while awaiting delivery of the Aerotech spindle and linear axis (Z). Without final alignment these axes were used to measure several parts to evaluate the performance of the optical probe.

10.4.1 PROBE SETUP WITH A FLAT

Setup of the probe on the R axis requires knowledge of its alignment with the motion of that axis and the rotary table that supports it (θ). As outlined in [1] part of this process is establishing the origin of the linear translating axis pair (R and the probe) with respect to the rotary table (θ). The goal is to find a point in the travel of the R axis such that as the table rotates the focused beam from the optical probe is stationary. This point in space can be considered the origin of the R–θ polar coordinate system and is the origin of the R–θ–φ spherical coordinate system as well if the θ and φ axes intersect at this same point. Equation 1 describes the displacement measured by the probe as a function of rotary axis position (θ), linear offset in the measurement direction (ρ_0) and linear offset tangential to the measurement direction (τ_0) if a flat surface is positioned in the measurement range of the probe and is perpendicular to the R axis motion at θ = 0°

$$\rho = \rho_0\left(\frac{1}{\cos\theta} - 1\right) + \tau_0 \tan\theta \tag{1}$$

The two unknown offsets, ρ_0 and τ_0 are zero then the probe is perfectly aligned. These offsets can be found by making two measurements at opposite angles of the flat surface, R1 and R2. Since the error due to ρ_0 is an even function it will not change in magnitude or sign. The error due to τ_0 will have the same magnitude but opposite sign. Thus the two offsets can be calculated from two measurements, R1 at θ and R2 at -θ, using Equations 2 and 3.

$$R1 + R2 = 2\rho_0\left(\frac{1}{\cos\theta} - 1\right) \tag{2}$$

$$R1 - R2 = 2\tau_0 \tan\theta \tag{3}$$

Figure 8 shows the results of measuring a nominally centered flat in both Cartesian and polar coordinates. The plots show the combined value of R plus the probe distance signal while θ was rotated 20°. The green trace is the uncorrected data and shows that there is a τ direction offset. The ρ offset is zero. The value of τ_0 can be found from Equation 3 using any two data points at opposite angles (e.g., ±9.9°). Alternatively the parameter could be found by performing a least squares fit of the tangent function to the data points or an average value could be used. The plot shows the corrected data (red trace) using a value of -7.4 μm for τ_0.

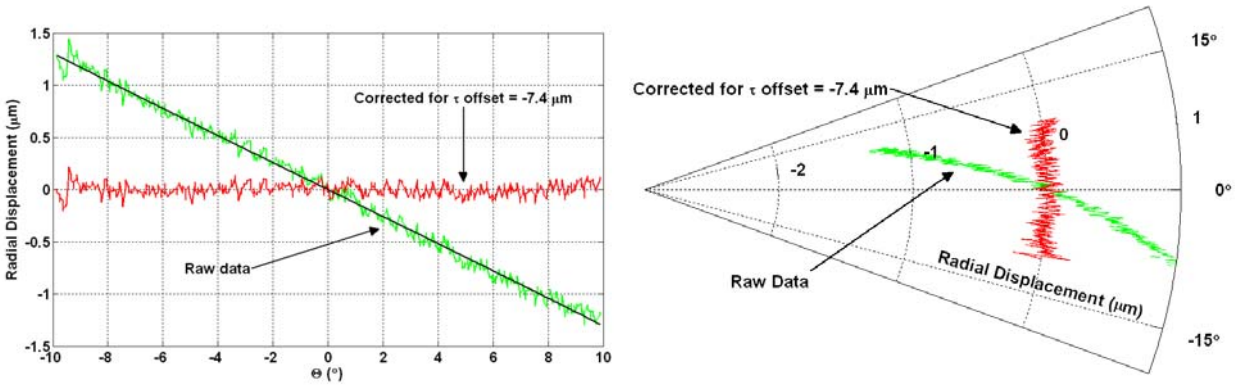

(a) rectangular coordinates (b) polar coordinates

Figure 8. Polaris measurement of a flat shows the tangential direction probe offset.

10.4.2 ASPHERE MEASUREMENT

A cross-section of an aspheric surface has also been measured with the prototype 3D machine using the coordinate origin and offsets found from the flat part measurement discussed above. Figure 10 shows the probe and part during the measurement. The table was rotated 90° while the R axis probe following was used to keep the probe distance signal near the center of its range. Data was collected at about 100 Hz. The intensity signal from the probe is shown in Figure 9a. There was a significant surface slope near the extreme edges of the part but in the central ±30° region the incident beam of the probe was nearly normal. Data points with intensity values below 8% were eliminated before further processing.

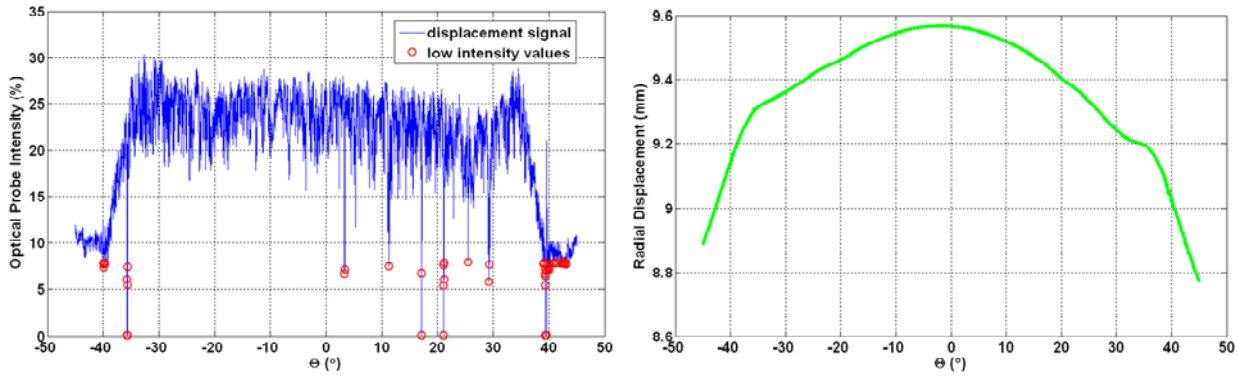

(a) Intensity signal (b) Surface cross-section

Figure 9. Asphere measurement data.

The assembled measurement is shown in Figure 9b. The R axis position and the corrected probe readings have been summed to obtain the trace in the plot. Figure 11 shows the same data set in Cartesian (11a) and polar coordinates (11b) along with two least squares circles; one with the

center constrained to the origin of the coordinate system (which is coincident with the rotational axis of θ) and the other with no constraints.

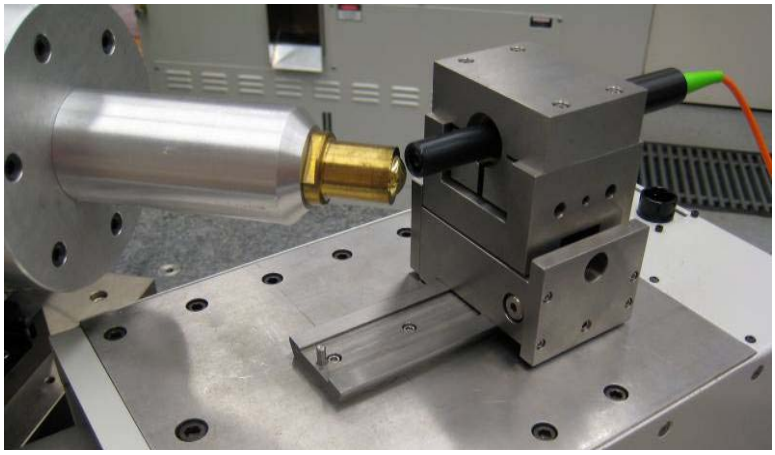

Figure 10. Measuring an asphere with the temporary part spindle.

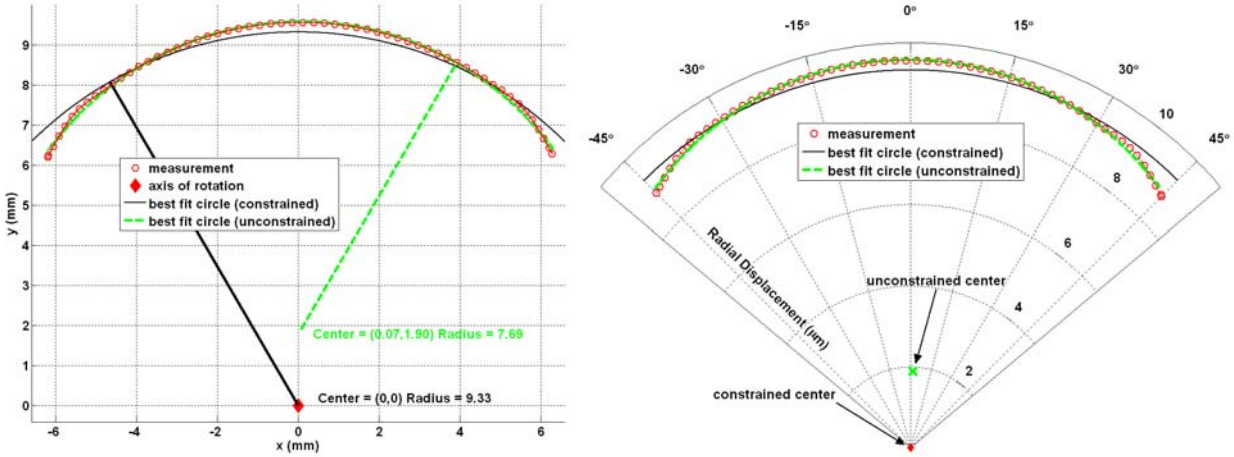

(a) Cartesian coordinates (b) polar coordinates

Figure 11. Asphere cross-sections and least squares circles.

The residual radial errors from the two curve fits shown in Figure 11 are plotted in Figure 12. The fit to the unconstrained circle shows that the central region of the part is nearly spherical. The outermost region also appears to be spherical but with a much smaller radius.

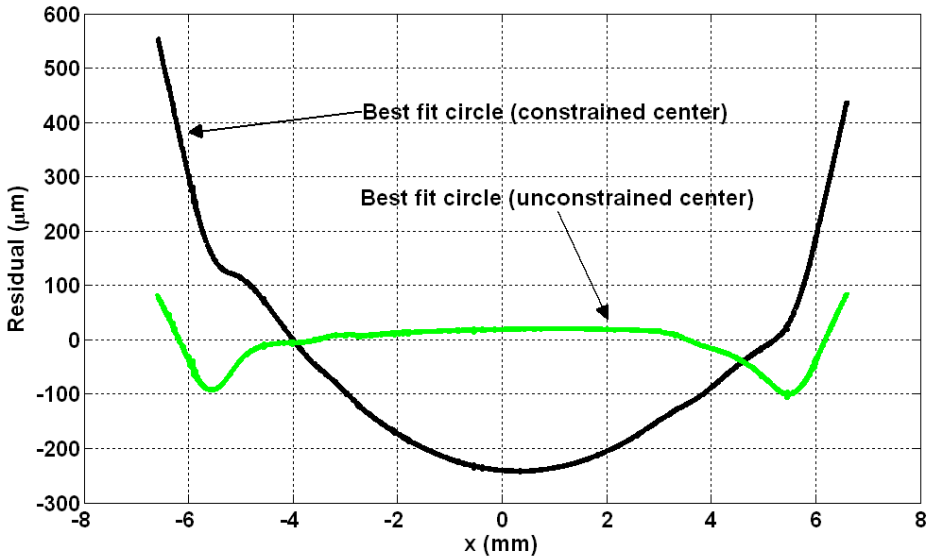

Figure 12. Asphere residual after least squares fit.

10.5 CONCLUSIONS AND FUTURE WORK

The polar geometry measuring machine, Polaris 2D, has been reconfigured as a spherical coordinate measuring machine. The control system has been upgraded and algorithms developed for basic machine operation and servo control. The STIL optical probe has been interfaced to the controller and a general probe following servo algorithm has been implemented. Data acquisition to the host PC hard drive can be sustained at the 1 kHz bandwidth of the optical probe. A user interface has been built that will serve as a test bed for further development of operating procedures.

REFERENCES

1. Sohn, A. and K. Garrard. The Polar Profilometer *Polaris*. Precision Engineering Center Annual Report, 19, 1-16, North Carolina State University (2001).
2. Sohn, A., K. Garrard, T. Dow. The Polar Profilometer "Polaris." Proceedings of the Sixteenth Annual Meeting of the ASPE, 25, 28-31 (2001).
3. Sohn, A., K. Garrard, T. Dow. Ultraform 2D. Precision Engineering Center Annual Report, 21, 45-60 (2003).
4. A. Sohn and K.P. Garrard. Tip Waviness Compensation in a Polar Profilometer. Proceedings of the Eighteenth Annual Meeting of the ASPE, 30, 355-358, (2003).
5. United States Patent 6,895,682. Polar coordinate-based profilometer and methods, May 24, 2005. Alexander Sohn, Kenneth P. Garrard and Thomas A. Dow.

Appendix A: Probe Tracking and Data Acquisition PLC

```
// Probe Tracking and Data Acquisition PLCC 0
//
// The probe input voltage is treated as an error in the position
// of the R axis.  A simple proportional filter is used to add a
// master position to the R axis servo so that this error is driven
// to zero.  The control action is intentionally weak so that noise
// from the probe and the A/D channel are damped.
//
// m98 points to an unassigned memory register and is used to couple
// the follower loop running as PLCC 0 to the R axis servo via ix05
// and ix06.
//
// p93   probe amplitude (+- in um, peak-to-valley is 2*p93)
//
// m98   free memory location used to couple servo loops
// m8012 encoder table entry for signed probe voltage
//
// p800  enable/disable probe following (==0 disable)
//       must disable to move R axis if probe is in range
// p801  delta correction
// p802  accumulated correction, sent to R axis servo
// p803  probe following limit, % of full scale position  (0..100)
//       disables probe following while out of range
// p804  probe following limit, % of full scale intensity (0..100)
//       disables probe following while out of range
// p805  rate limiter, controls velocity of R motion
// p806  gain, should be < 0
//       direction sense of probe and R are reversed
//       includes scaling for correct units of R motion
// p807  p803 converted to ADC counts
// p808  p804 converted to ADC counts
//
// A circular queue of Pvars is used for real time data acquisition.
// P900 and P901 control access to the circular queue and define its
// state. Initially P900=P901 and the queue is empty. One queue slot
// is unused to distinguish the empty and full states.
//
// p880  data acquisition state  (0=idle, 1=running)
// p881  internal state variable (0=off,  1=starting, 2=acq, 3=upload)
// p882  host trigger variable   (0->1 enable, 1->0 disable)
// p883  previous value of p882
//
// p900  read  index (ranges from 0 to P907-p904)
// p901  write index (ranges from 0 to P907-p904)
// p902  queue start (=2000)
// p903  queue end   (=8191)
// p904  items per sample (max=10, see local buffers)
// p905  error count      (incremented when data lost)
// p906  acquisition interval, servo cycles
// p907  size of queue == (p903-p902+1)
//       must be evenly divisible by P904
// p908  number of unread samples in the queue
// p909  base address for queue writing
// p910  temp copy of write index (p901)
// p911  acquisition count
// p912  pseudo-clock
// p913  overflow sample count   (* p904 = items in overflow stack)
// p914  size of overflow stack (samples)
//
// Two local buffers are used for storage of current and previous
// samples.  The difference is saved in the circular queue.  P916
// is used to toggle the base address between buffer 1 and buffer
// 2 and P917 is used to toggle the difference direction (ie sign)
// between -1 and +1.  When the enable trigger is set the the local
// buffers are cleared so that the first sample saved contains item
```

```
// values not differences.
//
// p915       local buffer base address    (920 or 930)
// p916       local buffer address toggle  (  0 or   1)
// p917       local buffer difference sign ( -1 or  +1)
// p920..929  local buffer 1
// p930..939  local buffer 2


// Required Mvar and Ivar Setups
m98->X:$10FF,0,24,S        // Loop coupling address

open plcc 0
clear

i8   = 0                   // Real time interrupt rate
i107 = 96                  // Master   scale factor (same as i108)
i108 = 96                  // Position scale factor (same as i107)
i134 = 0                   // Integration mode for R axis (0=always)
i106 = 0                   // Disable following on startup
i105 = $10FF               // Master position for R axis

// Initialize probe following Pvars
p800 = 0                   // Disable following
p801 = 0                   // Clear delta
p802 = 0                   // Clear accumulator
p803 = 96                  // 96% position  voltage threshold
p804 = 92                  // 92% intensity voltage threshold
p805 = 2500                // Rate limiter, counts
p806 = -0.01               // Loop gain for +-150 um probe range

// Initialize data acquisition Pvars
p902 = 2000                // Start of queue
p903 = 8191                // End   of queue
p904 = 8                   // Items per sample
p905 = 0                   // Error count
p906 = 4                   // Acquisition interval (2262 = 1 second)
p907 = (p903-p902+1)       // Size of queue
p908 = 0                   // Queue is empty
p909 = 0                   // Clear base address pointer
p910 = 0                   // Clear temp queue rear
p911 = 0                   // Reset acquisition count
p912 = 0                   // Initialize pseudo-clock
p913 = 0                   // Initialize overflow count

p914 = int(p940/p904*2)    // Size of overflow stack, samples
                           // "define ubuffer <p940>" required !!

// Initialize local buffer control variables
p915 = 920                 // Local buffer address pointer
p916 =   1                 // Local buffer control (index toggle)
p917 =  -1                 // Local buffer control (sign  toggle)

// Clear local sample buffers
p920=0 p921=0 p922=0 p923=0 p924=0 p925=0 p926=0 p927=0 p928=0 p929=0
p930=0 p931=0 p932=0 p933=0 p934=0 p935=0 p936=0 p937=0 p938=0 p939=0


// Initial queue is empty, read pointer = write pointer
p900 = 0                   // Read  pointer
p901 = 0                   // Write pointer

// Initial acquisition state variables
p880 = 0                   // Acquisition state   = idle
p881 = 0                   // Internal    state   = off
p882 = 0                   // Acquisition trigger = 0
p883 = 0                   // Previous    trigger = 0


// Perform probe tracking and data acquisition check on every servo clock
```

```
while (1=1)

   // ---------------------------------------
   // Probe Tracking with the R axis (Motor 1)

   // Check for mode change
   if (p800 = 1)              // Turn on following ?
      if (i106 = 0)           // Already on ? Yes, done
         cmd "PMATCH"         // No, Match axes positions to motors
         p802 = 0             //     Clear accumulated correction
         i106 = 1             //     Enable following
      endif
   else                       // Turn off following ?
      if (i106 = 1)           // Already off ? Yes, done
         cmd "PMATCH"         // No, Match axes positions to motors
         p802 = 0             //     Clear accumulated correction
         i106 = 0             //     Disable following
      endif
      p800 = 0                // Force p800 to be boolean (0 or 1)
   endif

   p807 = p803/100 * 1048576  // Position threshold for following
                              // p803/100 is decimal percentage of "in-range" voltage
                              // 1048576 = 65536*32/2 (+- full scale in counts)

   p808 = p804/100 * 1048576  // Intensity threshold for following
                              // p804/100 is decimal percentage of "in-range" voltage
                              // 1048576 = 65536*32/2 (+- full scale in counts)

   // Check for in range position and intensity
   if  (m8010 > -p807)        // Position  above lower threshold ?
   and (m8010 <  p807)        // Position  below upper threshold ?
   and (m8011 > -p808)        // Intensity above lower threshold ?
   and (m8011 <  p808)        // Intensity below upper threshold ?

      // Calculate distance to move R
      // p806 is the gain, p93/150 is gain scaling factor when not using full range
      // and m8010 is the input voltage from the probe, ie the error in R position
      p801 = p806 * p93/150 * m8010

                              // Rate limiter
      if (p801 > p805)        //   Too big ?
         p801 = p805          //   Yes, saturate at +limit
      endif
      if (p801 < -p805)       //   Too small ?
         p801 = -p805         //   Yes, saturate at -limit
      endif

      p802 = p802 + p801      // Accumulate command value for R axis

   endif

   m98 = p802 * p800          // Send command to master position register
                              //   = zero if disabled (p800=0)


   // ---------------------------------------------------------------------
   // Data acquisition into a circular queue with overflow into user memory


   // ---- Trigger variable state change ?
   if (p882^p883 = 1)
      if (p882=1) and (p881=0)            // 0->1 transition and acquisition is off
         p881=1 p880=1                    // Enable data acquisition, initialize pointers
      endif
      if (p882=0) and (p881=2)            // 1->0 transition and acquisition is on
         p881=3                           // Disable data acquisition, xfer overflow stack
      endif
   endif
   p883 = p882                            // Previous trigger value
```

```
p908 = ((p901-p900)%p907)/p904         // Number of items in the queue

// ---- Initialize data acquistion pointers and queue space
if (p881 = 1)                          // First sample ?
   p911 =  0                           // Yes, reset acquisition count
   p905 =  0                           //      reset error       count
   p913 =  0                           //      reset overflow    count
   p912 =  0                           //      reset pseudo-clock
   p900 =  0                           //      reset read  pointer
   p901 =  0                           //      reset write pointer
   p916 =  1                           //        set buffer index toggle
   p917 = -1                           //        set difference operator sign
   m51  = I4908                        //      reset overflow stack pointer lo
   m52  = I4908                        //      reset overflow stack pointer hi
   p881 = 2                            //      start acquisition into circular queue

   p920=0 p921=0 p922=0 p923=0         //      save 1st sample in p930, clear p920
   p924=0 p925=0 p926=0 p927=0         //        (p920-p920) is full sample record
   p928=0 p929=0                       //        p917=-1     makes the sign correct
endif


// ---- Data acquisition into circular queue or overflow stack
if (p881 = 2)
   p912 = p912+1                       // Increment pseudo-clock

   if (p912 % p906 = 0)                // Interval check
      p910 = (p901+p904)%p907          // Index of next slot to write
      p915 = p916*10 + 920             // Buffer base address (920 or 930)

      // Save current sample in p920.. or p930.. buffer
      p(p915)   = int((m162+m164)/(i108))    // R
      p(p915+1) = int((m262+m264)/(i208))    // Theta
      p(p915+2) = int((m362+m364)/(i308))    // Z
      p(p915+3) = int((m462+m464)/(i408))    // Phi
      p(p915+4) = int(m8008/32)              // Probe
      p(p915+5) = int(m8009/32)              // Intensity
      p(p915+6) = p1100                      // Overtravel

      if (p910 != p900)                      // Space in circular queue ?
         p909      = p902 + p901             // Yes, base address for this record
         p(p909)   = p917 * (p920-p930)      //      d(R)
         p(p909+1) = p917 * (p921-p931)      //      d(Theta)
         p(p909+2) = p917 * (p922-p932)      //      d(Z)
         p(p909+3) = p917 * (p923-p933)      //      d(Phi)
         p(p909+4) = p917 * (p924-p934)      //      d(Probe)
         p(p909+5) = p917 * (p925-p935)      //      d(Intensity)
         p(p909+6) = p917 * (p926-p936)      //      d(Overtravel)
         p(p909+7) = p912                    //      pseudo-clock

         p901 = p910                         //      update write pointer
         p911 = p911+1                       //      increment acquisition count
         p916 = p916^1                       //      toggle buffer index    ( 0, 1)
         p917 = -p917                        //      toggle difference sign (-1,+1)

      else if (p913 < p914)                  // Space in overflow stack ?
         m41 = p917*(p920-p930) m51 = m51+1  // Yes, d(R),          update lo pointer
         m42 = p917*(p921-p931) m52 = m52+1  //      d(Theta),      update hi pointer
         m41 = p917*(p922-p932) m51 = m51+1  //      d(Z),          update lo pointer
         m42 = p917*(p923-p933) m52 = m52+1  //      d(Phi),        update hi pointer
         m41 = p917*(p924-p934) m51 = m51+1  //      d(Probe),      update lo pointer
         m42 = p917*(p925-p935) m52 = m52+1  //      d(Intensity),  update hi pointer
         m41 = p917*(p926-p936) m51 = m51+1  //      d(Overtravel), update lo pointer
         m42 = p912             m52 = m52+1  //      pseudo-clock,  update hi pointer

         p913 = p913+1                       //      increment overflow    count
         p911 = p911+1                       //      increment acquisition count
         p916 = p916^1                       //      toggle buffer index    ( 0, 1)
         p917 = -p917                        //      toggle difference sign (-1,+1)
      else
```

```
            p905 = p905 + 1                    // No space, increment error count
         endif
         endif
      endif


   // ---- Transfer overflow stack through circular queue
   else if (p881 = 3)
      if (p913 !> 0)                           // overflow stack empty?
         p881 = 0                              // Yes, data upload finished
         p880 = 0                              //      acquisition state complete

      else                                     // Transfer data into circular queue
         p910 = (p901+p904)%p907               // Index of next slot to write

         if (p910 != p900)                     // Space in circular queue ?
            p909 = p902 + p901                 // Yes, base address for this record
            m52  = m52-1 p(p909+7) = m42       //      pseudo-clock
            m51  = m51-1 p(p909+6) = m41       //      d(Overtravel)
            m52  = m52-1 p(p909+5) = m42       //      d(Intensity)
            m51  = m51-1 p(p909+4) = m41       //      d(Probe)
            m52  = m52-1 p(p909+3) = m42       //      d(Phi)
            m51  = m51-1 p(p909+2) = m41       //      d(Z)
            m52  = m52-1 p(p909+1) = m42       //      d(Theta)
            m51  = m51-1 p(p909)   = m41       //      d(R)
            p901 = p910                        //      update write pointer
            p913 = p913-1                      //      decrement overflow count
         endif
      endif
   endif
   endif

endwhile
close
```

11 AUTOMATED HANDLING TECHNOLOGY FOR PRECISION TWO-SIDED PARTS

Stephen J. Furst
Graduate Student
Thomas Dow
Dean F. Duncan Distinguished Professor in Mechanical Engineering
Department of Mechanical and Aerospace Engineering

A complete part transfer and realignment system has been developed and demonstrated. The variation in radial separation between a part and a chuck can be maintained to less than 3 µm, and the axial position of the part with respect to the chuck can be controlled to within 5 µm. During the transfer demonstration, radial run-out was observed as expected and a part centering procedure was developed. A voice coil driven tapping actuator was developed and calibrated—the displacements caused by impacts of several impulse magnitudes are recorded. Run-out was measured by touching several points on the hemispherical surface of the part with a touch probe and calculating a best fit circle. The center of this circle represents the part location, and the difference between the part location and the spindle centerline is the run-out. An algorithm to calculate the number of impacts required at a given impulse magnitude to center the part was developed and run on a dSpace controller. This adaptive calibration scheme succeeded in aligning a part to within 5 µm of the spindle centerline in less than 7 steps every time tested. In each of these tests, the part was manually placed on the OC Chuck and an initial run-out of 1-2 mm was corrected.

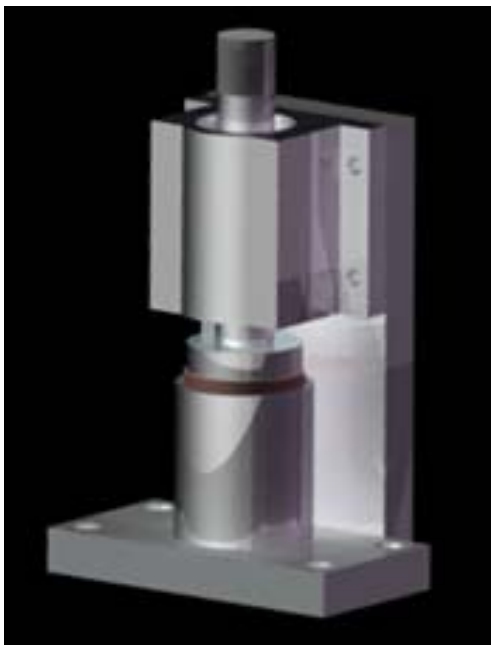

11.1 INTRODUCTION

The challenge of aligning a part on a lathe is relevant to many turning operations, including the fabrication of two-sided parts on a precision machining station. When machining a two-sided part such as a hemishell, one side is machined first. Then the part must be taken off the first holding fixture (typically a vacuum chuck), rotated, and replaced on another fixture that is suited for machining side two. During this transfer, the part becomes misaligned, and features on side two will not be properly related to features on side one.

The goal of this project is to automate both the part transfer and alignment steps required for fabrication of a hemishell. Parts are typically transferred by hand, and realignment involves an operator measuring the part run-out with a displacement gage and manually tapping the high side of the part until it is centered. The goal was to develop an actuation method capable of correcting radial run-out of up to 2.5 mm to within 5 μm.

11.2 PART MEASUREMENT AND TRANSFER

To automate part transfer, it is necessary to locate the part and the receiving chuck in the same coordinate system. A touch probe is located with respect to the IC Chuck, which is used to hold the part while its inner contour is machined, as shown in Figure 1.

The touch probe then touches the part at three different points, which are used to determine the radius and center point of the hemisphere. The probe is referenced to radial and axial fiducial surfaces on the OC (outer contour) Chuck. The measurement will tell an operating computer whether the part is appropriately sized for the receiving chuck. It will also determine the distance the part needs to be moved for vacuum chuck transfer.

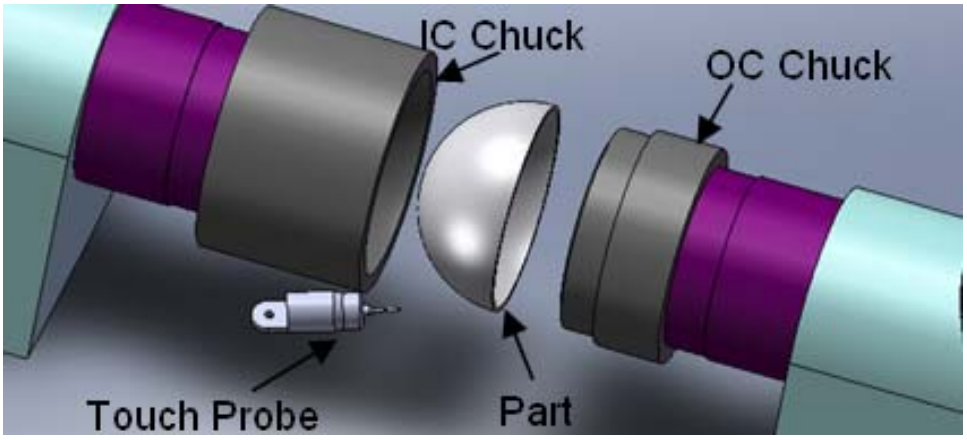

Figure 1: Exploded View of Hemishell Transfer

11.2.1 TRANSFER ERRORS

The probed points used to locate and measure the part are accompanied by uncertainty. A calibration sphere was used to determine the trigger repeatability of a Renishaw TP6 touch probe. The trigger repeatability of 0.28 μm represents that the best possible accuracy of a calibrated probe measurement. Each point touched by the probe carries this error, which results in 1.35 μm radius and 1.60 μm center-point uncertainties. Figure 2 shows how a 0.28 μm error at each of three touch points results in radius and center-point errors.

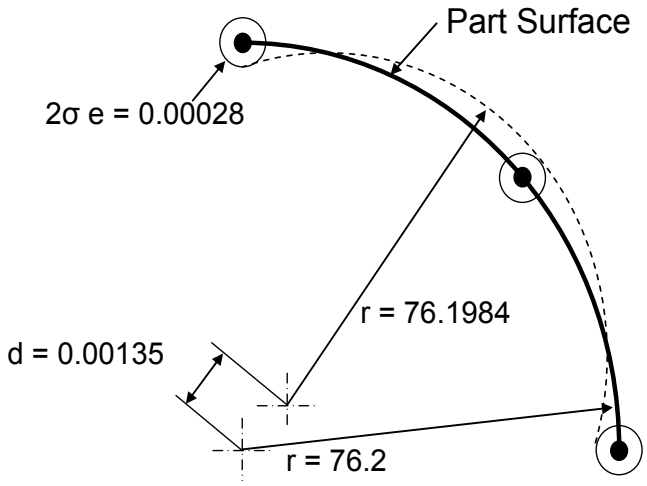

Figure 2: Measurement Errors Resulting From the Three-Point Method (mm)

11.2.2 TRANSFER DEMONSTRATION

A transfer was demonstrated on the PEC's ASG 2500 DTM. The part was effectively measured as described above. Variation in radial separation between the part and IC Chuck was less than 3 μm at transfer. Also, the part was located within 5 μm of the receiving chuck in the axial direction. Since the receiving chuck was cut 50 μm bigger than the part, these location errors are insignificant. However, radial run-out of ~50 μm resulted from the transfer.

11.3 REALIGNMENT WITH FRICTION

The radial run-out that occurs at the moment of transfer must be corrected so that the features on either side of the part will be aligned. For a part on a vacuum chuck this entails actuating the part against the force of friction.

Substantial work has been done to characterize the highly non-linear phenomenon of friction [1]. In the simplest models, friction force is computed as the product of a friction coefficient, μ, and normal force, N, as in Equation (1).

$$F_f = \mu N \tag{1}$$

In reality, friction force is much more complicated than this simple relation because the friction coefficient is not constant. For example, static friction is typically higher than dynamic or Coulomb friction. On small scales the transition between static and dynamic friction is of interest.

11.3.1 STRIBECK, COULOMB, AND VISCOUS FRICTION

Stribeck friction attempts to describe the behavior of the friction force as a function of velocity, particularly in the transition between static and dynamic friction. Figure 3 shows the different types of friction forcing phenomenon.

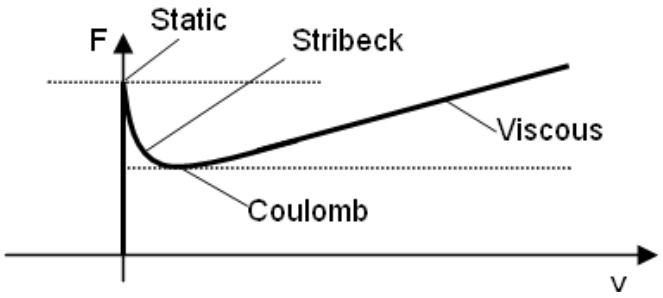

Figure 3: Combined Model of Friction Force as a Function of Velocity

For the purpose of precision part alignment, the relative velocity between the two sliding surfaces—the part and the vacuum chuck face—is small (~10 mm/s). As a result, the effects of viscous friction can be ignored.

11.3.2 STICK-SLIP BEHAVIOR

Stick-slip behavior results when a part is pushed across a friction interface by an actuator with some compliance, as diagramed in Figure 4.

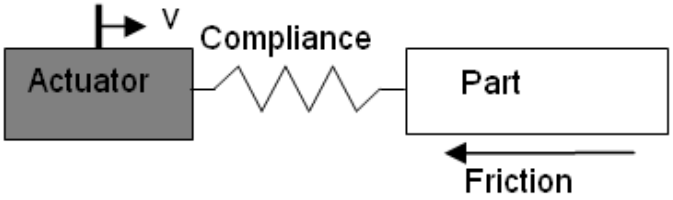

Figure 4: Stick-Slip Model Diagram

As the actuator moves towards the part at a constant velocity, the spring compresses and the force the actuator exerts increases linearly. As long as this force is less than the static friction limit, the friction force increases to exactly counter the spring force. Once the static friction limit is reached, the part begins to move. Then the friction force decreases rapidly, as described by Stribeck friction, and Equation (2).

$$F(v) = N\left(\frac{A}{\exp(bv)} + B\right) \tag{2}$$

Where A is the difference between the static and dynamic friction coefficients, B is the dynamic friction coefficient, and b is a chosen constant representing the rate of decay of the Stribeck friction curve.

The built up spring force propels the part ahead until eventually friction can slow and stop the part completely. The resulting behavior is described as stick-slip.

11.3.3 FRICTION INTERFACE MEASUREMENTS

The effects of Stribeck and Coulomb friction were measured. An aluminum puck was placed on a vacuum chuck and pushed with a load cell mounted to a DTM machining axis. The positions of the DTM axis and test puck were measured with electronic gages. These positions as well as the measured actuation force are plotted in Figure 5. It is clear from Figure 3 that the friction force drops when the test puck starts slipping. This effect results in "stick-slip" behavior, which is an impediment for precision control and must be considered in designing the positioning actuator.

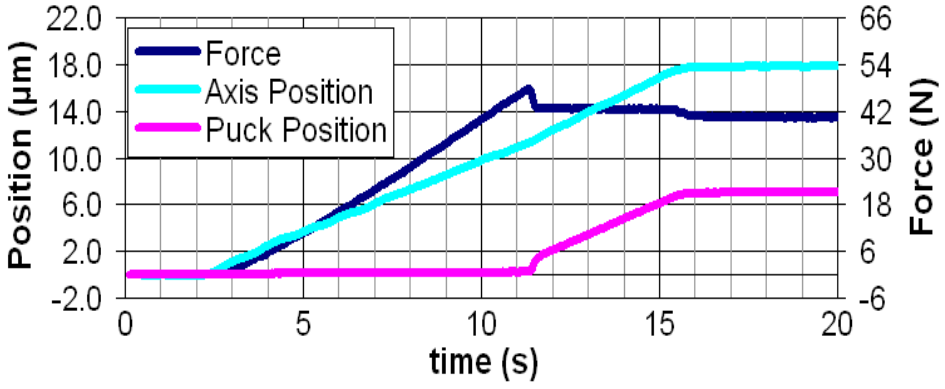

Figure 5: Measured Behavior of the Friction Interface

11.4 ACTUATION METHOD

A number of methods were considered to overcome the friction force holding a part on a vacuum chuck. The chosen method should be the one that satisfies the following criteria:

- Best position control
- Most repeatable
- Lowest risk of part damage
- Fastest realignment
- Easiest to implement

The methods considered included pushing the part with one of the machine axes, tapping the part to mimic the process currently used by skilled operators, vibrating the chuck in an attempt to reduce the friction coefficient and pulsing the vacuum to reduce the normal force.

11.4.1 TAPPING AS AN ACTUATION METHOD

For any actuation method, moving the part will require applying a force that is greater than static friction. However, once the part starts to slip and the friction force decreases, the part will accelerate rapidly under the same applied actuation force. Therefore, the best positioning control will likely come from force that exceeds the static friction limit for a short period of time before being removed. This forcing behavior is best realized with a tap, which has a force profile similar to Figure 6.

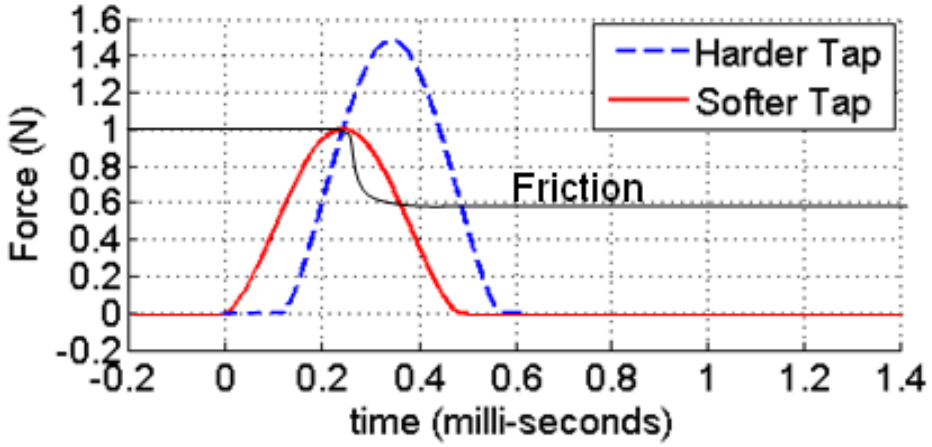

Figure 6: Force Profiles of Hammer Taps and Friction

Once a tap force exceeds the static friction limit, the friction force will drop and the difference between the input tap force and the retarding friction force will accelerate the part. The area between the tap force profile and the friction force profile is proportional to the momentum imparted on the part. Even when the peak of the tap force barely exceeds the static friction limit,

as in the case of the solid line in Figure 6, there is a non-zero amount of work done on the part. This suggests that there is a minimum distance a part can be moved against the non-linear friction force.

11.4.2 TAPPER DESIGN AND IMPACT MODELING

An actuator has been designed to apply a peak force of 250 N to a part without damaging it. An aluminum part has been assumed in the analysis. The tapper is designed based on the impact dynamics, which result from the Hertzian deflection of the plunger head and the part.

Hertzian Deflection

The Hertzian deflection of the tapper head and the aluminum part surface causes a tap to produce a force profile similar to those in Figure 6. The deflection of the impacting bodies allows the collision to take place over a finite, non-zero time, thus preventing damaging force spikes. The behavior of two impacting spheres during a tap can be related by equations for elastic deformation [2].

As a Hertzian impact progresses, the centers of the two impacting spheres approach each other and the force between them builds according to Equation (3).

$$P = \left(\frac{y}{1.040}\right)^{\frac{3}{2}} \left(\frac{K_D}{C_E{}^2}\right)^{\frac{1}{2}} \tag{3}$$

where C_E and K_D relate to the material properties and diameters of the two impacting bodies via:

$$C_E = \frac{1-\nu_1{}^2}{E_1} + \frac{1-\nu_2{}^2}{E_2} \text{ and } K_D = \frac{D_1 D_2}{D_1 + D_2} \tag{4}$$

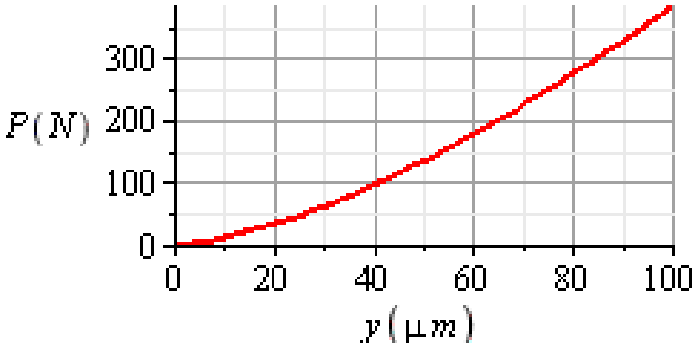

Figure 7: Variation of Impact Stroke with Applied Force

Figure 7 shows that an impact stroke of about 75 µm will develop a peak force of 250 N. At the moment the impact starts, the approach of the center-points of the two impacting bodies, y, is zero. As the impact progresses the force that the actuator is exerting on the part increases. The initial kinetic energy of the actuator's moving element required to generate an impact stroke of 75 µm and peak force of 250 N can be found via Equation (5):

$$E_0 = \int_{y=0}^{y=75} P(y)dy \tag{5}$$

Equation (5) represents the area under the curve in Figure 7. The integral is solved below:

$$E_0 = \int_{y_0}^{y_f} \left(\frac{y}{1.040}\right)^{\frac{3}{2}} * \left(\frac{K_D}{C_E{}^2}\right)^{\frac{1}{2}} dy \Rightarrow \frac{2}{5*1.040} * \left(\frac{K_D}{C_E{}^2}\right)^{\frac{1}{2}} y^{\frac{5}{2}} \Bigg|_{y_0}^{y_f} \tag{6}$$

Solving with y_0 equal to zero and substituting in Equation (3) for y, Equation (5) can be solved for the initial kinetic energy required to produce a peak impact force, P.

$$E_0 = \frac{2*1.040^{\frac{3}{2}}}{5} \frac{C_E{}^{\frac{2}{3}}}{K_D{}^{\frac{1}{3}}} P^{\frac{5}{3}} \tag{7}$$

Equation (7) is plotted in Figure 8.

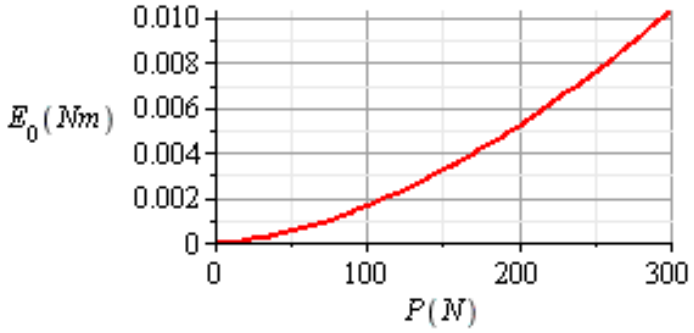

Figure 8: Initial Kinetic Energy, E_0, Required to Produce Peak Force, P

An initial kinetic energy of 0.00763 Nm is required to produce a peak force of 250 N.

11.4.3 ACTUATION SIMULATION

A friction model is combined with the impact model to simulate the response of a part on a vacuum chuck to a controlled tap. The simulations below show the displacement of an aluminum hemishell part with an outer radius of 76.2 mm and inner radius of 69.9 mm. The simulations are run with an initial energy of 0.009 Nm. The static friction coefficient is taken as 0.25, the dynamic friction coefficient as 0.15, and the normal force from vacuum is 1000 N.

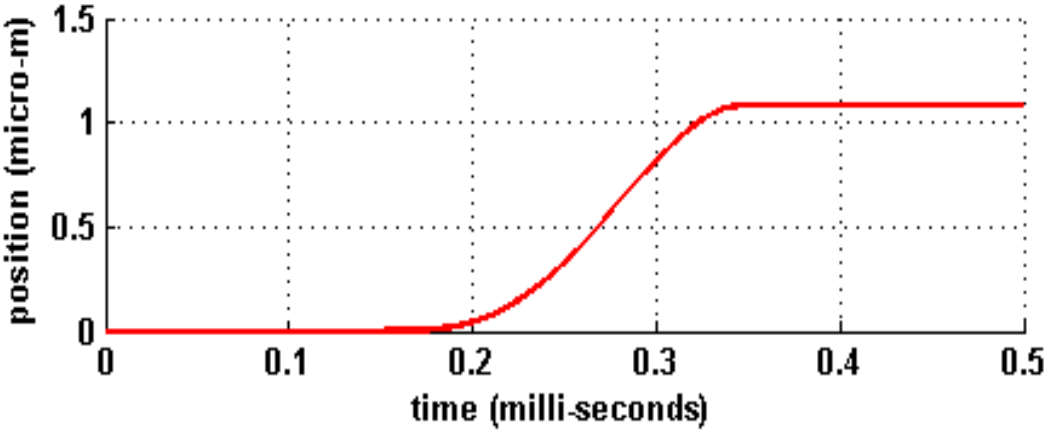

Figure 9: Part Displacement Due to Impact

Figure 9 shows that the part begins to accelerate at 0.15 ms, immediately after the impact force exceeds the friction force.

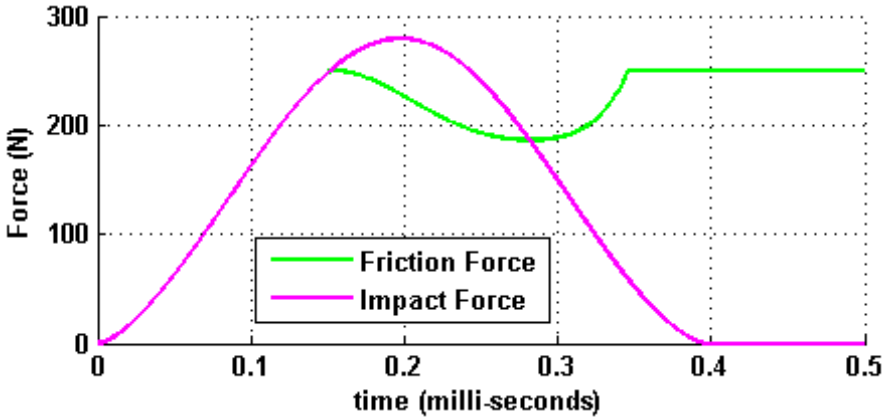

Figure 10: Simulated Actuation Forces

Figure 10 shows how the motion of the part reduces the friction force. The area between the friction force and impact force lines in Figure 10 is equal to the momentum transferred to the part. This model predicts the permanent slip motion of a part due to an applied impact.

11.4.4 ACTUATOR DESIGN

An actuator with a voice coil motor (VCM) has been designed to accelerate a translating core to the desired impact velocity then hold the core at that velocity until it impacts the part and produces the desired actuation force profile. The core travels on a linear ball bushing, as shown in Figure 11.

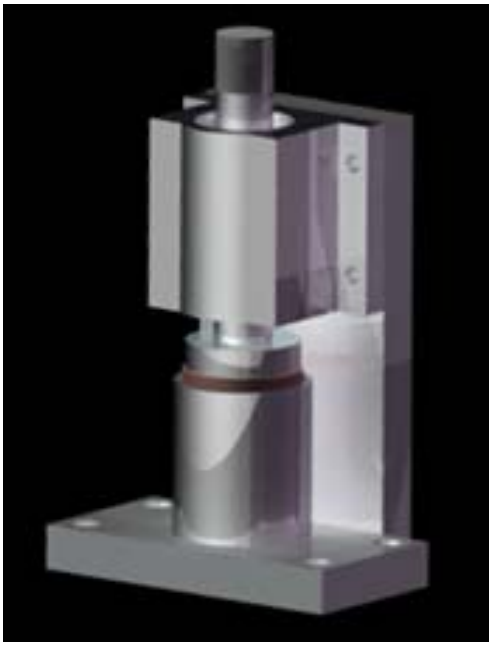

Figure 11: Model of Tapping Actuator

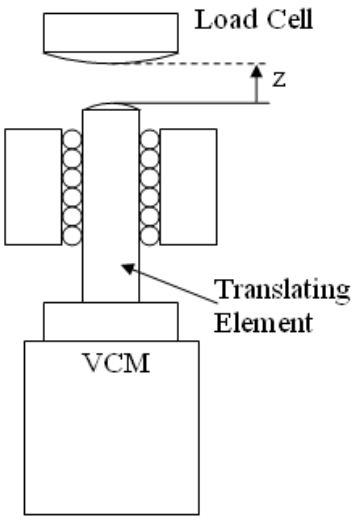

Figure 12: Test Setup for Voice Coil Motor Actuator

11.4.5 ACTUATOR PERFORMANCE

The realignment actuator was fabricated and tested in the setup shown in Figure 12. A load cell was used to measure the peak impact force.

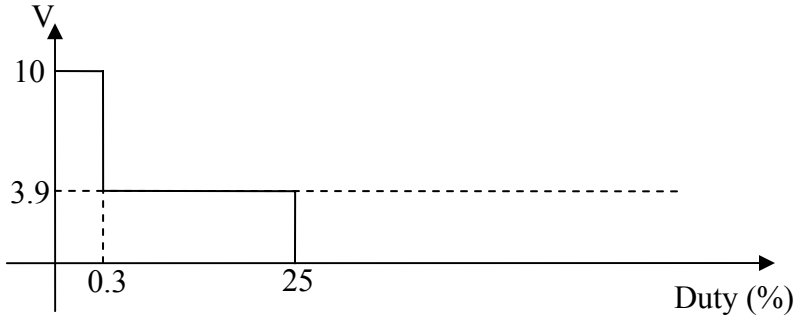

Figure 13: Voltage Input for VCM Actuator at 1 Hz

The impact was generated by the collision between the translating element of the VCM actuator and a stationary load cell. The VCM is driven with the waveform in Figure 13. The high voltage step is used to accelerate the sliding element, while the low voltage step is used hold the element at a constant velocity against gravity and viscous friction within the ball bushing. This input is multiplied by a gain to control peak force. If frequency is increased, the duty cycle is also increased proportionately.

The load cell was tapped while located at 6 different offsets using 6 different frequencies. At each position and frequency, the cell was tapped 10 times, and the average value plotted in Figure 14 and Figure 15. The repeatability is quantified by the standard deviation—the largest standard deviation in peak impact force for all of the data points taken was less than 1 N.

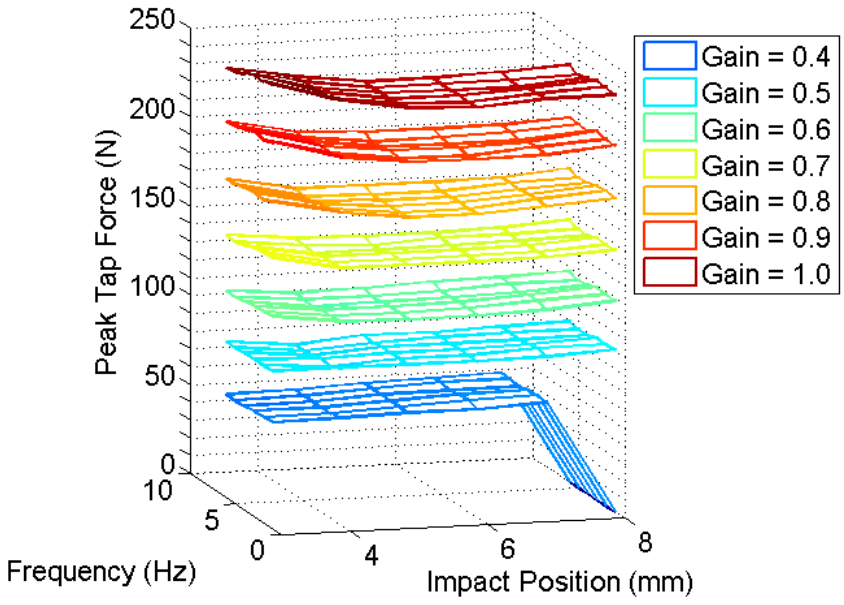

Figure 14: Peak Impact Force Variation with Operating Conditions

Tests on the VCM-based tapping actuator show that there is a range of 3 mm of stroke where the peak force variation is less than 7 N. Also, variation in operating frequency between 1 and 6 Hz does not greatly affect performance. Since the uncertainty (2σ) of each tap is less than 2 N the VCM actuator can produce a peak force with ±5.5 N uncertainty over a range of 3 mm. This will allow the actuator to realign a part with 3 mm of run-out. In future work, the effect of this impact force variation on the incremental displacement of a part will be explored.

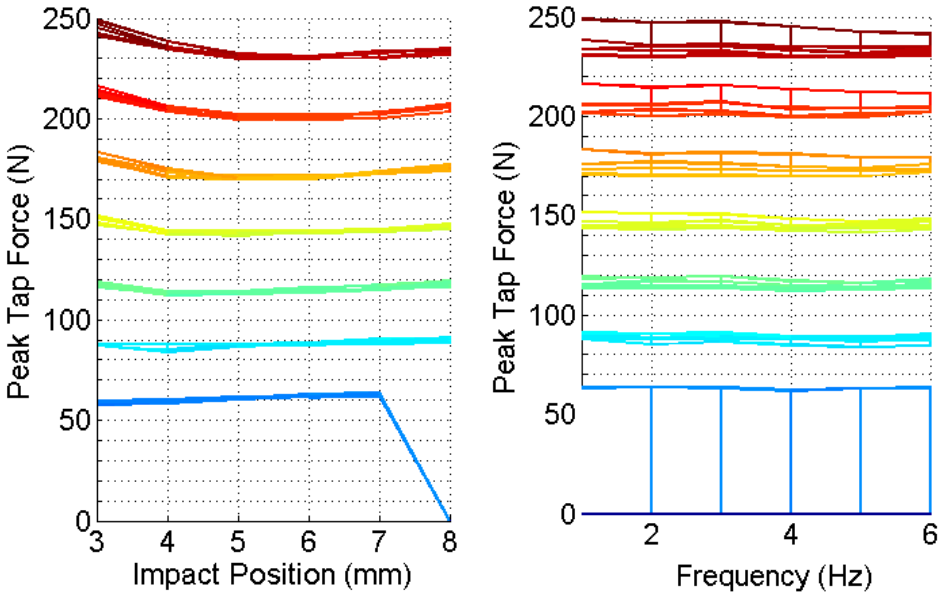

Figure 15: Peak Impact Force Variation

11.5 REALIGNMENT PROCEDURE

The procedure below describes the method for centering a part on a vacuum chuck. The steps described are specific to the ASG 2500. This is a single-spindle machining center with a single tool/probe slide. On the PEC setup the spindle position and velocity and the realignment actuator are controlled with a dSPACE controller.

11.5.1 SPINDLE CONTROL AND THE USER INTERFACE

Because a touch probe is used to measure runout, it was necessary to control the position and velocity of the DTM spindle using feedback from the spindle encoder. The control system was a dSPACE platform and is based on a Simulink model. The position and velocity controllers use PID and PI feedback, respectively. ControlDesk is used to generate a User Interface (UI), shown in Figure 16. The UI can be operated in velocity or position mode. The velocity or position can be controlled with the slider bars shown. The operator can also set the realignment actuator impulse magnitude and apply impacts from the ControlDesk UI.

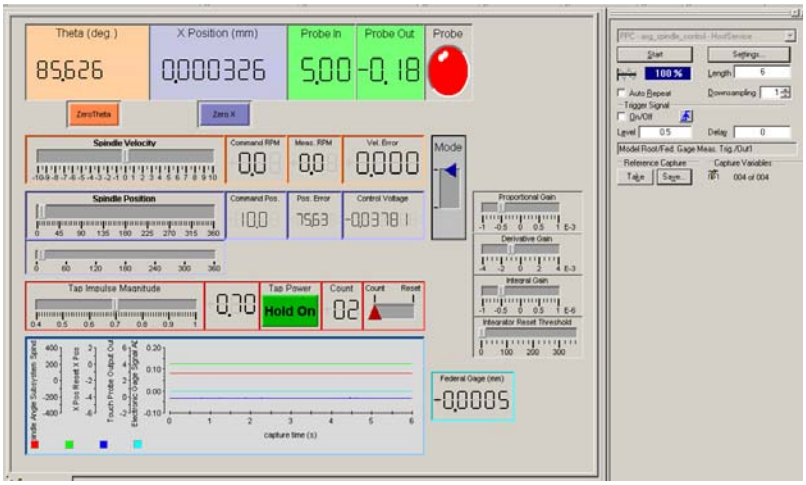

Figure 16: ControlDesk User Interface

11.5.2 SETUP

The OC Chuck, Touch Probe, and Realignment Actuator, as well as an optional electronic gage, are set up on the DTM as shown in Figure 17. The procedure for properly referencing and aligning the particular components used for this experiment is listed below. Note that these steps do not need to be repeated each time a new part is aligned.

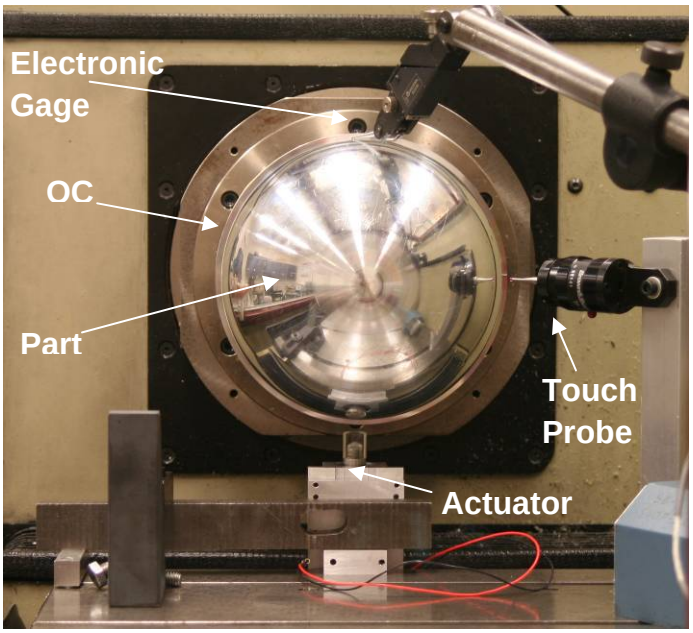

Figure 17: Realignment System Setup

1) Center the OC chuck on the spindle.
2) Mount the touch probe to the x slide to the right of the OC chuck, as shown in Figure 17.
3) Touch the OC Chuck x and z fiducials with the touch probe and set the machine relative coordinates to x = 0, z = 0. Reset the dSPACE x coordinate to zero.
4) Move the machine axes to x = 1.5, z = 6.
5) Secure the realignment actuator to the x slide so it is aligned with the spindle centerline.

11.5.3 REALIGNMENT STEPS

The basic realignment procedure is:

1) Place the part on the OC Chuck.
2) Calibrate the realignment actuator.
3) Measure the run-out to determine the run-out magnitude and the impact direction.
4) Determine the number of impacts, n, and impulse magnitude, G, needed for realignment.
5) Set the 'Tap Impulse Magnitude' on the UI to G and tap the part n times.
6) Repeat the runout measurement.
7) If the run-out magnitude is greater than 5 μm, repeat steps 3-6.

11.5.4 REALIGNMENT ACTUATOR CALIBRATION

A front view of the part, actuator, and probe setup is shown in Figure 18.

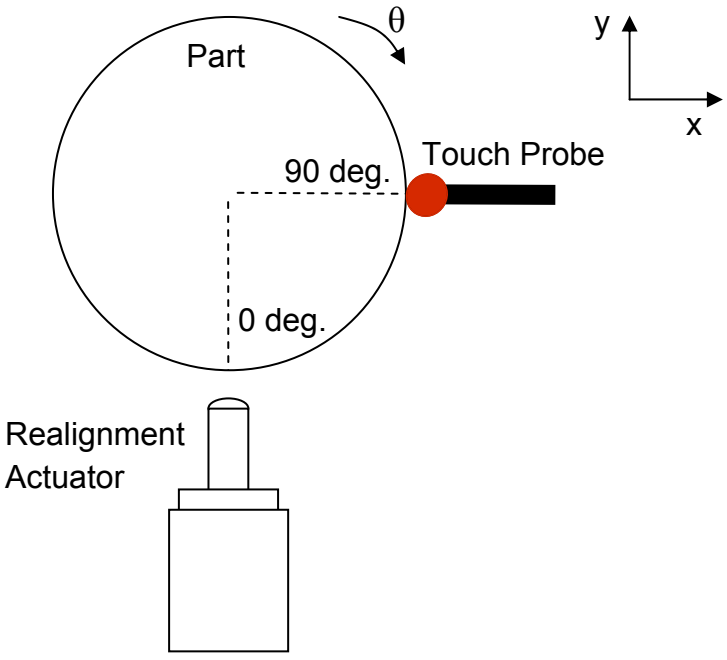

Figure 18: Front View of Part, Actuator, and Touch Probe Setup

1) Place the part on the OC chuck with θ = 90 deg. adjacent to the touch probe as shown in Figure 18 and set the vacuum pressure to 10 in. Hg.
2) Set the Impulse Magnitude gain, G, to 0.7 and tap the part 5 times.
3) Rotate so θ = 0 deg. is adjacent to the touch probe and touch the part with the touch probe by moving the x slide in, then back out. Record the x value at trigger, R0.
4) Rotate to θ = 90 deg., set G to 0.6, and tap the part 5 times.
5) Rotate to θ = 0 deg. touch the part with the touch probe and record R1.
6) Repeat steps 4 and 5 for G = 0.7, 0.8, 0.9, and 1.0. Fill in Table 1.

Table 1: Actuator Calibration

Gain	R (mm)	δ (μm)
-	R0 =	
0.60	R1 =	200*(R1-R0) =
0.70	R2 =	200*(R2-R1) =
0.80	R3 =	200*(R3-R2) =
0.90	R4 =	200*(R4-R3) =
1.00	R5 =	200*(R5-R4) =

11.5.5 RUN-OUT MEASUREMENT USING TOUCH PROBE

1) Rotate the part to θ = 0 deg.
2) Set capture time to ~150 s and start data capture by clicking "Start" on the Control Desk.
3) Within 10-15 seconds of starting data capture, execute program runout.mm n times, where n is greater than 3. Each time the probe trigger light turns from red to green, rotate the spindle 360/n degrees using the ControlDesk UI. Use command (b) to execute part program (a) n times.
    a. runout.mm:
       units metric
       move 1.5 6 250
       move 4.5 6 20
       move 1.5 6 80
    b. run rstep runout.mm n
4) After the part program is finished, stop capturing data by clicking "Stop" on the UI.
5) Save the captured data as data1.mat in the appropriate folder.
6) In the MATLAB GUI shown in Figure 19, set the pull-down menu to "Touch Probe" and click "Calculate" to determine the run-out magnitude and direction as well as the number of impacts and impulse magnitude needed for realignment [1].

[1] - The algorithm for calculating the number of impacts and impulse magnitude is shown below.

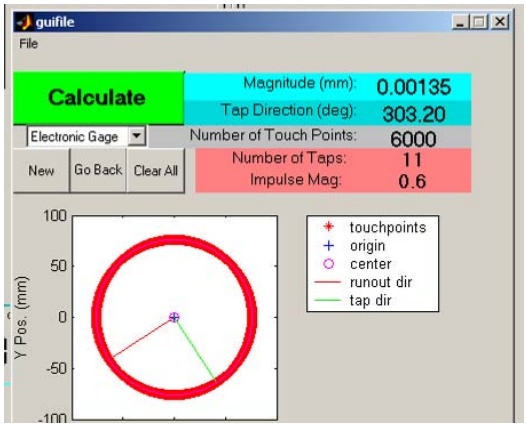

Figure 19: MATLAB GUI for Calculating Run-out

11.5.6 RUN-OUT MEASUREMENT USING ELECTRONIC GAGE

The run-out of the part can also be measured using an analog signal from an electronic gage set up as shown in Figure 17.

1) Rotate the spindle at 10 RPM (6 seconds per revolution).
2) Set capture time to 6 s and start data capture and clicking "Start" on the UI. With the sample rate at 1 kHz, the ControlDesk will record 6000 data points during the one rotation.
3) Save the captured data.
4) In the MATLAB GUI shown in Figure 19, set the pull-down menu to "Electronic Gage" and click "Calculate" to determine the run-out magnitude and direction as well as the number of impacts and impulse magnitude needed for realignment.

11.5.7 CALCULATING IMPACTS AND THEIR MAGNITUDE

The run-out measurement and data from the calibration table are used to determine the number of impacts and impulse magnitude needed to center the part. Note that since the measuring probe is aligned 90 degrees from the actuator, as shown in Figure 18, the part must be rotated to the calculated run-out direction minus 90 degrees before the actuation impacts are applied.

1) Divide run-out magnitude, Rmag, by 10.
2) Using the calibration Table 1, select δ_G as the largest δ value that is less than Rmag/10. Record the associated input gain, G.
3) Round Rmag/ δ_G down to the next lowest integer, n. n and G are the number of impacts and impulse magnitude needed.

4) If more than 50 taps are prescribed, the algorithm will attempt to pick a higher gain and allow fewer than 10 impacts.

11.6 REALIGNMENT DEMONSTRATION

The procedure above is used to center a part that has either been manually placed on the OC chuck or automatically transferred from the IC chuck to the OC chuck. Before an adaptive calibration scheme was implemented, trials showed that a poor initial calibration could prevent the part from converging to within 5 μm of the spindle centerline. For example, assume that the initial calibration predicted that the part would move 20 μm under a given impact energy. If the run-out was measured to be 500 μm at 0 deg., the non-adaptive algorithm would tell the operator to apply 25 impacts from 0 degrees. However, if the calibration value was incorrect and the part actually moved 40 μm with each impact, the part would overshoot the spindle center and end up at 500 μm at 180 deg. The algorithm would then determine that the user should apply the same impacts in the opposite direction, once again resulting in overshoot. In this case, where the calibration factor underestimates the displacement of the part by a factor of 2, the part will never converge on the spindle centerline.

Multiple tests showed that a larger error in the initial calibration would cause the realignment to take more steps to converge. Although friction force does not change greatly while a part is on the chuck, the interface can change when one part is replaced with another, thus corrupting the calibration factor.

To overcome this impediment to convergence, an adaptive calibration scheme is used to update the calibration values in Table 1 after each move. In the example above, the computer would recognize that 25 impacts produced a 1000 μm total displacement and would update the calibration value to 40 μm/impact. On the second step, the part would converge to the spindle centerline. Once this adaptive calibration scheme was applied, a part could be manually placed on the OC chuck with run-out ~1 mm and automatically realigned; in all of the tests done with the adaptive calibration scheme, the run-out never failed to converge. Since the adaptive calibration scheme needs to see the result of a tap at a given impulse magnitude to update the calibration value for that impulse, a poor set of initial calibration data can still result in realignment taking as many as 10 iterations.

Figure 20 shows the location of the part on the spindle after each iteration for several tests using the adaptive algorithm. All of the tests shown converge in less than 7 steps. It may be beneficial to reduce the number of available impulse magnitude gains so that there is only a "coarse adjustment impact" and a "fine adjustment impact." Then the adaptive calibration

scheme would only have to update calibration values for 2 impulse magnitudes, thus reducing the number of iteration steps required. Note that the radial scale is logarithmic.

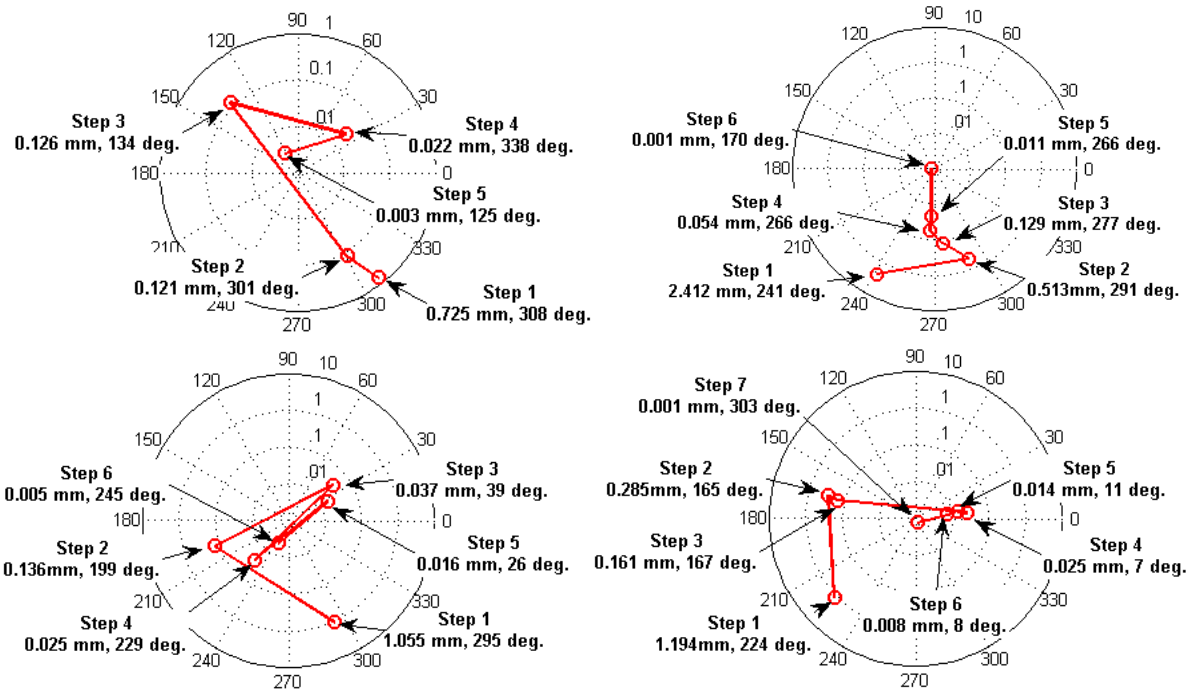

Figure 20: Path of Part during Various Centering Operations. The radial scale is logarithmic and exaggerates the size of the final corrections.

11.7 SUMMARY AND FUTURE WORK

A complete part transfer has been developed and demonstrated. The variation in radial separation between a the part and IC Chuck can be maintained to less than 3 µm, and the axial position of the part with respect to the chuck can be controlled to within 5 µm. During the transfer demonstration, radial run-out was observed as expected.

A part centering procedure was developed. First the actuator is calibrated—the displacements caused by impacts of several impulse magnitudes are recorded. Then the run-out is measured by touching several points on the hemispherical surface of the part and calculating a best fit circle. The center of this circle represents the part location, and the difference between the part location and the spindle centerline is the run-out. The number of impacts required at a given impulse magnitude to center the part is then calculated. Initially, previous calibration values are used in this algorithm. However, since poor initial calibration values can result in non-convergence, it is necessary to update the calibration values based on the previous actuation steps. This adaptive

calibration scheme succeeded in aligning a part to within 5 μm of the spindle centerline in less than 7 steps every time tested. In each of these tests, the part was manually placed on the OC Chuck and an initial run-out of 1-2 mm was corrected.

The realignment system can be improved substantially with additional work. If a long-range analog gage can be used to measure the position of the part at all times during alignment, the number of steps and time required for a centering operation could potentially be reduced from 5-10 minutes to less than 1 minute. With an analog gage constantly measuring the displacement of the part, the impacts can be repeated until the analog gage returns the desired position measurement. This would essentially close the loop on the positioning process, and eliminate the need to calibrate the realignment actuator and calculate the number and impulse magnitude required for centering. Since an analog gage can only measure displacement in one direction, errors may still result if the part does not move exactly along the measurement direction of the gage during actuation. However, during realignment tests these errors were typically observed to be second order. Convergence will still take multiple iteration steps.

REFERENCES

1. Olsson, H. et. al. "Friction Models and Friction Compensation." European Journal of Control (1998) 4: 176-195.
2. Roark, R., Young, C. K., "Formulas for Stress and Strain." McCraw Hill, 1975.

FACULTY

THOMAS A. DOW

Director, Precision Engineering Center
Dean F. Duncan Distinguished University Professor in Mechanical Engineering
Professor, Department of Mechanical and Aerospace Engineering

BS, Mechanical Engineering, Virginia Polytechnical Institute, 1966
MS, Engineering Design, Case Institute of Technology, 1968
PhD, Mechanical Engineering, Northwestern University, 1972

After receiving his PhD degree from Northwestern University in 1972, Dr. Dow joined the Tribology Section of Battelle Columbus Laboratories and worked there for ten years. His research interests were in the areas of friction and wear and included studies on a wide variety of topics from lubrication of cold-rolling mills using oil-in-water emulsions to wet braking effectiveness of bicycle brakes to elastohydrodynamic lubricant film generation in ball and roller bearings. He developed experimental apparatuses, established analytical models, and corroborated those analyses with experimental measurements. Dr. Dow joined the faculty at North Carolina State University in 1982 and was instrumental in developing the academic and research program in precision engineering. His current research interests include the design of precision machining systems, real-time control, and metrology. He was one of the founders of the American Society for Precision Engineering and currently acts as the Executive Director.

JEFFREY W. EISCHEN

Associate Professor
Department of Mechanical and Aerospace Engineering

BS, Mechanical Engineering, UCLA, 1978
MS, Mechanical Engineering, Stanford University, 1981
PhD, Mechanical Engineering, Stanford University, 1986

Dr. Eischen has been with North Carolina State University since 1986 and his research areas of interest include: linear and nonlinear finite element analysis, multi-body kinematics/dynamics/control, fabric mechanics, and stress analysis in microelectronic devices. He teaches undergraduate courses in strength of mechanical components and mechanical design. His graduate courses include fracture mechanics and advanced machine design. He has collaborated with colleagues in the Precision Engineering Center for several years on computer simulation related projects dealing with precision shape control of disk drive read/write heads, stress and deformation analysis of high energy physics equipment, and contact lens mechanics.

RONALD O. SCATTERGOOD

Professor
Materials Science and Engineering Department

BS, Metallurgical Engineering, Lehigh University, 1961
MS, Metallurgy, Massachusetts Institute of Technology, 1963
PhD, Metallurgy, Massachusetts Institute of Technology, 1968

R.O. Scattergood is a Professor in the Department of Materials Science and Engineering. He received BS degrees in Mining Engineering and Metallurgical Engineering from Lehigh University. His MS and PhD degrees were obtained in Metallurgy from M.I.T. In 1968 he became a member of the basic research staff in the Materials Science Division at the Argonne National Laboratory. In 1981, he joined the faculty as a Professor of Materials Engineering at North Carolina State University.

Professor Scattergood's major research interests have been focused on the mechanical behavior of solids. He has worked in the areas of strengthening mechanisms in solids, mechanical testing, fracture, tribology, nanocrystaline materials and precision machining processes. He has expertise in He has published over 200 technical papers, books and reports.

STAFF

KENNETH P. GARRARD

Senior Research Associate
Precision Engineering Center

BS, Computer Science, North Carolina State University, 1979
MS, Computer Studies, North Carolina State University, 1983

As a full-time staff researcher at the Precision Engineering Center, Mr. Garrard's interests and duties have included the development of high performance control systems for ultra-precision machines and software development for custom, multiprocessor computer systems. He participated in the development of the original PEC fast tool servo as well as three other fast tool servo systems that have been delivered to commercial and government sponsors. One of these systems was built specifically for the on-axis turning of off-axis segments of conic surfaces of revolution and another is being used for the fabrication of inertial confinement fusion target mandrels. He has performed numerous prototype fabrication projects that required unique machine configurations and controller software. Mr. Garrard also has a long standing interest in the analysis of scientific data, programming language structures, sorting and searching algorithms, multiprocessor computer architecture and the design and implementation of hard real-time systems.

ALEXANDER SOHN

Research Assistant/Lecturer
Precision Engineering Center

B.S., Physics, University of Texas at Arlington, 1992
M.S., Physics, University of Texas at Arlington, 1994

Mr. Sohn joined the Precision Engineering Center in August, 1997 as a member of the technical staff. His current research interests range from machine design and metrology to the design and fabrication of nonimaging optics. Mr. Sohn's varied research activities began in microwave optics and atomic physics as a student at the University of Texas at Arlington and later progressed to precision machine design, design and fabrication of plastic optics as well as automation and machine vision at Fresnel Technologies, Inc. in Fort Worth, Texas.

PAULA J. KELLEY

Administrative Assistant
Precision Engineering Center

BA, Liberal Arts / Criminal Justice/ University of New Hampshire 1990

Ms. Kelley became a member of the PEC Staff in September 2007. Previously, Ms. Kelley has worked as the book-keeper for Lead Mine Elementary School in Raleigh; office manager for a private non-profit school in New Hampshire; supervisor for a school serving behaviorally challenged teens in Massachusetts and coordinator for a G.E.D. and job training program serving at risk teens. Ms. Kelley provides the overall administrative support for the Center.

CONSULTANTS

KARL FALTER

Consulting Engineer

BS, Mechanical Engineering, North Carolina State University, 1987
MS, Mechanical Engineering, North Carolina State University, 1989
PhD, Mechanical Engineering, North Carolina State University, 1992

Prior to working as an independent consultant, Dr. Falter was a senior development engineer with Eastman Kodak from 1997 to 2003. He designed and developed electrical and control systems for custom precision machine tools. Dr. Falter also worked for Rank Pneumo from 1994 to 1997.

DAVID YOUDEN

Senior Engineer, Olympic Precision, Inc.
Adjunct Lecturer, Department of Mechanical and Aerospace Engineering

ASME, Central New England College, Worcester, MA, 1965

Prior to joining Olympic Precision's Precision Valley Institute for Advanced Manufacturing in 2006, Mr. Youden was an Applied Research Engineer at Eastman Kodak Company's Manufacturing Systems Technology Division. Between 1984 and 1997 he was Research and Development Manager at Rank Pneumo, a division of Rank Taylor Hobson Inc. Before that, he was Director of Engineering at the Cone Blanchard Machine Company. He has also worked at Ocean Systems, Inc. of Reston, Virginia and the Heald Machine Company, a division of Cincinnati Milacron. During his professional career, Mr. Youden has been granted numerous patents in the field of machine tools, and he has published and presented technical papers on the design and testing of ultra-precision machine tools in the US, Japan, and Germany. In 2006, Mr. Youden received The American Society for Precision Engineering's Lifetime Achievement Award for his contributions to the field of precision engineering.

GRADUATE STUDENTS DURING 2008

DAVID BREHL's extensive industrial career includes a range of design, development, and project engineering roles with AERCO International, BOC Gases, and Babcock & Wilcox. A deepening interest in design of integrated electromechanical systems, along with a desire to focus his career on technology development, led him to pursue a PhD in Mechanical Engineering at NCSU; this follows a recent Master's in ME program at Stevens Institute of Technology (Hoboken, NJ). He joined the PEC in August 2004 and is currently employed at Terrera North America in Charlotte, NC.

QUNYI CHEN first entered NCSU in 1997. He obtained a MSME in 1998 and a MSEE in 1999. After graduation, Qunyi worked at GE Healthcare to design and develop electro-mechanical subsystems for medical diagnostic X-ray equipment. His passion for technology development in precision electro-mechanical engineering led him to return to NCSU in 2005, where he was able to find an ideal match on the PEC's Fast Long Range Actuator project in June 2006. Qunyi was born and raised in Jiangsu, China. There, he received a BSME in 1993 and a MSME in 1996 before coming to the United States.

STEPHEN FURST is a native of Goshen, NY, came to NC State in 2003 to undertake a degree in Aerospace Engineering and run on the NCSU track and cross country teams. Stephen spent the summers after his junior and senior year at NASA studying Space Science and its applications. The PEC offered Stephen the opportunity to expand his skill set and gain valuable experience working on real-world engineering problems. After finishing a MSME, he hopes to continue to learn a systematic approach to technology development through PhD work.

TIM KENNEDY was born and raised in Chapel Hill, NC. Tim received his BS from NCSU in May 2004. Before working at the PEC, he worked at the Analytical Instrumentation Facility for two years as an undergraduate research assistant. He started working with the PEC August 2004 and currently works for the US Patent and Trademark Office in Washington, DC.

BRANDON LANE joined the PEC in the June, 2008 after graduating with a B.S. in Mechanical Engineering from University of Nevada, Reno. In Reno, he gained engineering experience working as an intern for the Robotics R&D division of Hamilton Company, designing components and technical drawings for automated fluid handling workstations. He also worked as an undergraduate researcher for the UNR Nanocomposites lab where he researched fabrication techniques for carbon nanofiber and nanotube composites. These experiences in R&D sparked his interest in a career that continues higher levels of engineering learning and

understanding. His schedule as a graduate student is supplemented by distance running, fishing, and mountain hiking in his free time.

MEIRONG SHI is a graduate student of Department of Material Science and Engineering. She received her MS degree in Microelectronics from East China Normal University in 2007 and joined the PEC in August 2008. The research project Meirong is involved in now is Material Effects and Tool Wear in Vibration-Assisted Machining.

ERIK ZDANOWICZ was raised in Hendersonville, NC. After receiving his BS in mechanical engineering from NCSU in May of 2007, Erik began his MSME degree and worked as a teaching assistant for Statics and Dynamics. Erik joined the PEC in January of 2008 as a research assistant for the redesign of the first generation Fast Long Range Actuator. Upon completion of his MS degree in 2009, Erik hopes to utilize the valuable experience gained at the PEC when he takes his position with Harris Corporation in Melbourne, FL.

GRADUATES OF THE PRECISION ENGINEERING CENTER

Student	Degree	Date	Company/Location
Jeffrey Abler	PhD	December 1994	ETEC Systems, Inc. Tucson, AZ
William Allen	PhD	December 1994	North Carolina State Univ. Raleigh, NC
Kelly Allred	MS	June 1988	
Christopher Arcona	PhD	May 1993	Norton Worcester, MA
Bradford Austin	MS	June 2000	IBM Corporation Fishkill, NY
Markus Bauer	PhD	December 2001	SCYNEXIS Chemistry & Automation, Inc. Research Triangle Park, NC
Tom Bifano	PhD	June 1988	Phillips Automation Pittsburgh, PA
Scott Blackley	MS	May 1990	Motorola Austin, TX
Peter Blake	PhD	December 1988	NASA Goddard Greenbelt, MD
Dave Brehl	PhD	December 2008	Tessera North America Charlotte, NC
Brett Brocato	MS	June 2005	Tessera North America Charlotte, NC
Nathan Buescher	MS	May 2005	Consolidated Diesel Rocky Mount, NC
Mark Cagle	MS	June 1986	NASA-Langley Norfolk, VA
John Carroll	PhD	January 1986	Cummins Engine Co. Columbus, IN

Matthew Cerniway	MS	October 2001	Naval Surface Warfare Ctr West Bethesda, MD
Damon Christenbury	MS	June 1985	Michelin Tire Co. Spartanburg, SC
Stuart Clayton	MS	May 2003	Naval Depot Cherry Point
James Cuttino	PhD	December 1994	UNC – Charlotte Charlotte, NC
Bob Day	PhD	July 1998	Los Alamos National Lab Los Alamos, NM
Joseph Drescher	PhD	May 1992	Pratt & Whitney East Hartford, CT
William Enloe	MS	December 1988	ITT Roanoke, VA
Karl Falter	MS	December 1989	Eastman Kodak Company Raleigh, NC
Peter Falter	PhD	May 1990	Lockheed-Martin Orlando, Florida
John Fasick	MS	May 1998	Kodak Rochester, NY
Steven Fawcett	PhD	June 1991	MicroE Natick, MA
Karalyn Folkert	MS	May 2005	Consolidated Diesel Rocky Mount, NC
Andre Fredette	PhD	May 1993	IBM Research Triangle Park, NC
Karl Freitag	MS	August 2004	Northrop Grumman Baltimore, MD
Stephen Furst	MS	December 2008	NCSU Raleigh, NC

David Gill	PhD	August 2002	Sandia National Laboratories Albuquerque, NM
Jim Gleeson	MS	June 1986	Battelle Columbus Labs Columbus, OH
Mary Smith Golding	MS	May 1990	Harris Corporation Melbourne, FL
David Grigg	PhD	August 1992	Zygo Corporation Middlefield, CT
Hector Gutierrez	PhD	October 1997	Florida Inst. Of Tech. Melbourne, FL.
Christian Haeuber	MS	December 1996	Harris Corporation Melbourne, FL
Simon Halbur	MS	December 2004	
Matias Heinrich	MS	July 2001	Vistakon Jacksonville, FL
Gary Hiatt	PhD	May 1992	Caterpillar Zebulon, NC
David Hood	MS	May 2003	
Peter Hubbel	MS	December 1991	Delco Electronics Kokomo, IN
Konrad Jarausch	PhD	December 1999	Intel Corporation San Jose, CA
Bradley Jared	PhD	December 1999	Sandia National Laboratories Albuquerque, NM
David Kametz	MS	August 2002	Naval Air Warfare Center Aircraft Division Patuxent River, MD
Jerry Kannel	PhD	June 1986	Battelle Columbus Labs Columbus, OH

Tim Kennedy	PhD	May 2008	US Patent and Trademark Office Washington, DC
Byron Knight	MS	May 1990	US Air Force Washington, DC
Lucas Lamonds	MS	July 2008	Micron Technology Boise, ID
Mark Landy	MS	June 1986	Battelle Columbus Labs Columbus, OH
Mike Loewenthal	MS	December 1988	SVG Norwalk, CT
Michael Long	PhD	June 2000	Eastman Kodak Rochester, NY
Bryan Love	MS	May 2001	Virginia Tech
Michael Hung-Tai Luh	MS	June 1989	Proctor and Gamble Cincinnati, OH
Dan Luttrell	MS	1987	Luttrell, Inc. New Boston, NH
Edward Marino	MS	September 1999	Pratt Whitney Hartford, CT
Edward Miller	MS	December 2000	General Electric Greenville, SC
Michele Miller	PhD	December 1994	Michigan Tech. University Houghton, MI
Paul Minor	MS	September 1998	Hartford, CT
Gary Mitchum	MS	June 1987	Harris Corporation Melbourne, FL
Charles Mooney	MS	December 1994	AIF – NC State University Raleigh, NC
Patrick Morrissey	MS	May 2003	

Larry Mosley	PhD	June 1987	Intel Corporation Chandler, AZ
Patrick Moyer	PhD	May 1993	UNC-Charlotte Charlotte, NC
Nobuhiko Negishi	MS	August 2003	
Ayodele Oyewole	MS	October 1997	Barnes Aircraft East Hartford, CT
Hakan Ozisik	PhD	December 1989	
Witoon Panusittikorn	PhD	December 2004	Fabrinet Kookot, Lumlookka Thailand
John Pellerin	MS	May 1990	Sematech Austin, TX
Travis Randall	MS	August 2004	MBA student NCSU
Ganesh Rao	MS	December 1994	Oak Ridge National Lab Oak Ridge, TN
John Richards	MS	September 1997	Intel Corporation San Jose, CA
Walter Rosenberger	MS	May 1993	The East Group Kinston, NC
Alex Ruxton	MS	December 1996	Pratt &Whitney Palm Beach, Florida
Anthony Santavy	MS	August 1996	Ford Dearborn, MI
Keith Sharp	PhD	May 1998	Morgan Crucible Dunn, NC
Gordon Shedd	PhD	March 1991	
Wonbo Shim	PhD	May 2000	Seagate Inc. Oklahoma City, OK

Robert Skolnick	MS	September 1997	San Diego, CA
Denise Skroch	MS	May 1989	IBM Corporation Raleigh, NC
Elizabeth Smith	MS	April 1989	
Stanley Smith	PhD	May 1993	
Ronald Sparks	PhD	May 1991	Alcoa Corporation Pittsburg, PA
Brent Stancil	MS	December 1996	Harris Corporation Melbourne, FL
Gene Storz	MS	May 1994	
Anand Tanikella	PhD	August 1996	Norton Industrial Ceramics Northboro, MA
Donna Thaus	MS	May 1996	Northern Telecom Research Triangle Park, NC
John Thornton	MS	December 1993	Digital Instruments Santa Barbara, CA
Michael Tidwell	MS	December 1991	
John Tyner	MS	June 1995	Naval Depot Cherry Point
Nadim Wanna	MS	December 2006	ExxonMobil Corporation Houston, TX
Robert Woodside	MS	December 2006	Harris Corporation Melbourne, FL
Tao Wu	PhD	December 2003	
Yanbo Yin	PhD	October 2007	

ACADEMIC PROGRAM

Problems and limitations associated with precision manufacturing can originate in the machine, the process, or the material. In fact, most problems will probably be caused by a combination of these factors. Therefore, improvement of current processes and development of new manufacturing methods will require knowledge of a multi-disciplinary array of subjects. The educational goal of the Precision Engineering Center is to develop an academic program which will educate scientists and engineers in metrology, control, materials, and the manufacturing methods of precision engineering.

The graduate students involved in the Precision Engineering Center have an annual stipend as research assistants. They can take up to 3 classes each semester while spending about 20 hours per week on their research projects. These students also work in the Center full-time during the summer months.

The Precision Engineering Center began in 1982 with an emphasis on the mechanical engineering problems associated with precision engineering. As a result, the original academic program proposed was biased toward courses related to mechanical design and analysis. However, as the research program has developed, the need for complementary research in sensors, materials, and computers has become obvious. A graduate student capable of making valuable contributions in the computer area, for example, will require a significantly different academic program than in mechanical engineering. For this reason, the Center faculty has set a core curriculum and each student in the program is required to take at least 3 of these core courses. The remainder of the courses for the MS or the PhD degree are determined by the university or department requirements and the faculty committee of the student.

The required courses are:

- MAE 545 Metrology in Precision Manufacturing
- PY 516 Physical Optics
- MAT 700 Modern Concepts in Materials Science
- CSC (ECE) 714 Real Time Computer Systems

PhD DEGREE PROGRAM

The PhD program in Precision Engineering has been set up as a multi-disciplinary program, drawing upon courses throughout the University to provide background and expertise for the students. It should contain required courses to insure solid grounding in the fundamentals plus electives to prepare the student in his area of specialization. Because Precision Engineering is concerned with an integrated manufacturing process, students interested in computer control, materials, machine structure, and measurement and actuation systems are involved in the program. Student research projects include the wide variety of topics addressed in this report. Each student's thesis should have an experimental component because Precision Engineering is basically a hands-on technology.

MS DEGREE PROGRAM

The Master of Science degree will have a higher percentage of application courses than the PhD degree. The emphasis will be to develop the foundation for involvement in precision engineering research and development. A total of 30 credits, including 6 credits for the MS thesis, are required. The thesis, while less comprehensive than the PhD dissertation, will be directed at important problems in Precision Engineering. Typically, the MS program will take four semesters plus one summer.

UNDERGRADUATE PROGRAM

The undergraduate degree broadly prepares an engineering student for industrial activities ranging from product design and engineering sales to production implementation. Because a large share of engineers only have the BS degree, these will be the people who must implement the new technology developed in research programs like the Precision Engineering Center. Therefore, a way must be found to acquaint engineers at the BS level with the techniques, problems, and potential of precision manufacturing.

In most undergraduate degree programs only limited time is available for technical electives. However, these electives offer the student the opportunity to expand his knowledge in many different directions. Beginning graduate courses (such as metrology) can be used as undergraduate electives.

Undergraduate projects and summer employment have also been utilized to include undergraduate students into the research program of the Center. During the 1998-1999 academic year, four undergraduate students in Mechanical Engineering were involved various projects at the PEC.

STUDY PLANS

Study plans for several example students are given below both for the MS and the PhD degree. Because of the breadth of the field and the wide range of thesis topics, few if any study plans will be exactly the same. The plan will depend upon the student's background, his interests, his thesis topic, the department, and the chairman and members of his committee.

PhD PROGRAM IN MECHANICAL ENGINEERING

Major Courses:

- MAE 740 Advanced Machine Design I
- MAE 741 Advanced Machine Design II
- MAE 706 Heat Transfer Theory & Applications
- MAE 713 Principles of Structural Vibration
- MAE 760 Computational Fluid Mechanics and Heat Transfer
- MAE 545 Metrology in Precision Manufacturing
- MAE 715 Nonlinear Vibrations
- MAE 716 Random Vibration
- MAE 714 Analytical Methods in Structural Vibration
- MAE 742 Mechanical Design for Automated Assembly
- MAE 895 Doctoral Dissertation Research

Minor Courses:

- MA 511 Advanced Calculus I
- MA 775 Mathematical Methods in the Physical Sciences I
- CSC 780 Numerical Analysis II
- PY 516 Physical Optics
- ECE 716 System Control Engineering
- MAT 700 Modern Concepts in Materials Science
- ECE 726 Advanced Feedback Control
- ECE 764 Digital Image Processing

PhD PROGRAM IN MATERIALS ENGINEERING

Major Courses:

- MAT 710 Elements of Crystallography and Diffraction
- MAT 700 Modern Concepts in Materials Science
- MAT 556 Composite Materials
- MAT 715 Transmission Electron Microscopy
- MAT 795 Defect Analysis/Advanced Materials Experiments
- MAT 753 Advanced Mechanical Properties of Materials
- MAT 712 Scanning Electron Microscopy
- MAT 895 Doctoral Dissertation Research

Minor Courses:

- PY 414 Electromagnetism I
- ST 502 Experimental Statistics for Engineers I
- MAE 740 Advanced Machine Design I
- MAE 741 Advanced Machine Design II
- MAE 545 Metrology in Precision Manufacturing
- PY 516 Physical Optics
- MA 401 Applied Differential Equations II

PhD PROGRAM IN ME (FOR STUDENT WITH MS DEGREE)

- ECE 716 System Control Engineering
- ECE 791 Gate Array Design
- MAT 700 Modern Concepts in Materials Science
- PY 516 Physical Optics
- MA 502 Advanced Mathematics for Engineers and Scientists II
- MA 775 Mathematical Methods in the Physical Sciences I
- MA 780 Numerical Analysis II
- MAE 732 Fundamentals of Metal Machining Theory
- MAE 740 Advanced Machine Design I
- MAE 741 Advanced Machine Design II

- MAE 545 Metrology in Precision Manufacturing
- MAE 716 Random Vibration

MS PROGRAM FOR ME STUDENT

- MAE 713 Principles of Structural Vibration
- MAE 740 Advanced Machine Design I
- MAE 545 Metrology in Precision Manufacturing
- MAT 700 Modern Concepts in Materials Science
- PY 516 Physical Optics
- MA 501 Advanced Math for Engineers and Scientists I
- MA 502 Advanced Math for Engineers and Scientists II
- MAE 695 Master's Thesis Research

MS PROGRAM FOR COMPUTER SCIENCE STUDENT

- CSC 501 Operating Systems Principles
- CSC 506 Architecture of Parallel Computers
- CSC 512 Compiler Construction
- ECE 521 Computer Design and Technology
- CSC 715 Concurrent Software Systems
- MAE 545 Metrology for Precision Manufacturing
- MAE 789 Digital Control Systems
- ECE 764 Digital Image Processing

MS PROGRAM FOR MATERIALS SCIENCE STUDENT

- MAT 700 Modern Concepts in Material Science
- MAT 710 Elements of Crystallography and Diffraction
- MAT 715 Transmission Electron Microscopy
- MAT 712 Scanning Electron Microscopy
- MAT 722 Advanced Scanning Electron Microscopy and Surface Analysis
- MAE 545 Metrology for Precision Manufacturing
- PY 516 Physical Optics
- ECE 738 IC Technology and Fabrication
- MAT 695 Master's Thesis Research

MS PROGRAM FOR PHYSICS STUDENT

- PY 516 Physical Optics
- PY 552 Introduction to Structure of Solids I
- PY 753 Introduction to Structure of Solids II
- PY 781 Quantum Mechanics I
- PY 782 Quantum Mechanics II
- PY 783 Advanced Classical Mechanics
- PY 785 Advanced Electricity and Magnetism I
- PY 786 Advanced Electricity and Magnetism II
- MAT 700 Modern Concepts in Material Science
- MAE 545 Metrology for Precision Manufacturing
- PY 695 Master's Thesis Research

SHORT COURSES AND TV COURSES

Six graduate level courses: Scanning Electron Microscopy (MAT 712), Advanced SEM Surface Analysis (MAT 722), Modern Concepts in Material Science (MAT 700), Mechanical Properties of Materials (MAT 705), and Metrology (MAE 545) have been offered as video courses nationwide via National Technological University. In a typical year, approximately 120 students from industry and national laboratories participate in these courses. .

TECHNICAL REPORTS

Volume 1 - 1983	December 1983	136 pages
Volume 2 - 1984	January 1985	168 pages
Volume 3 - 1985	January 1986	294 pages
Volume 4 - 1986	January 1987	255 pages
Volume 5 - 1987	December 1987	336 pages
Volume 6 - 1988	December 1988	362 pages
Volume 7 - 1989	March 1990	357 pages
Volume 8 - 1990	March 1991	385 pages
Volume 9 - 1991	March 1992	382 pages
Volume 10 - 1992	March 1993	289 pages
Volume 11 - 1993	March 1994	316 pages
Volume 12 - 1994	March 1995	268 pages
Volume 13 - 1995	January 1996	251 pages
Volume 14 - 1996	January 1997	232 pages

Volume 15 - 1997	January 1998	298 pages
Volume 16 – 1998	January 1999	258 pages
Volume 17 – 1999	January 2000	232 pages
Volume 18 – 2000	January 2001	274 pages
Volume 19 – 2001	January 2002	201 pages
Volume 20 – 2002	January 2003	328 pages
Volume 21 - 2003	January 2004	208 pages
Volume 22 – 2004	February 2005	207 pages
Volume 23 – 2005	February 2006	264 pages
Volume 24 – 2006	March 2007	274 pages
Volume 25 – 2007	March 2008	192 pages
Volume 26 – 2008	March 2009	209 pages

PUBLICATIONS

PAPERS PUBLISHED

1. Q. Chen, T. Dow and K. Garrard, A. Sohn *Fast Long Range Actuator (FLORA)*. Proceedings of the ASPE, Vol. 42, pp.287-290 (2007).
2. D. Brehl and T. Dow, *Review of Vibration-Assisted Machining,* Precision Engineering, Vol.32, No 3 , pg 153-163, July 2008.
3. D. Brehl, T. Dow, K. Garrard and A. Sohn, *Millimeter-Scale Reflecting Optics Fabricated Using Elliptical Vibration-Assisted Machining (EVAM),* Proceedings of the ASPE, Vol. 42, pp.363-367 (2007).
4. D. Brehl and T. Dow, *3-D Microstructure Fabrication Using Elliptical Vibration-Assisted Machining,* Proceedings of the ASPE, Vol. 40, pp. 21-25 (2007).
5. D. Brehl, MA. Cerniway, T. Dow and N. Negishi, *Machining Forces for Elliptical Vibration-Assisted Machining,* Proceedings of the ASPE, Vol. 40, pp. 71-75 (2007).
6. Q. Chen, T. Dow, Garrard, K, Sohn, A, Richardson, D., *Control of a fast long range Actuator (FLORA),* Proceedings of the ASPE, Vol. 44, pp. 100-103 (2008).
7. E. Zdanowicz, J. Eischen, T. Dow, *Design of a Long Range Actuator (FLORA II),* Proceedings of the ASPE, Vol. 44, pp. 164-167 (2008).
8. K. Garrard, A. Sohn, T Dow, *Design, Fabrication and Testing of Kinoform Lenses,* Proceedings of the ASPE, Vol. 44, pp. 558-561 (2008).
9. S. Furst, T. Dow, K. Garrard, and A. Sohn; Automated Part Centering through Impulse Actuation, Proceedings of the ASPE, Vol. 44, pp. 566-567 (2008).
10. R. Brent Dixon, Jack R. Edwards, Alex Sohn, Thomas A. Dow and David C. Muddiman, "Can the Diagnostic and Prognostic Value of Prostate Specific Antigen Be Improved by Harnessing the Specificity of Mass Spectrometry?" Poster Session, Engineering Fundamentals in Life Science, AIChE Annual Meeting, Nov 16-21, 2008

REPORTS PUBLISHED

1. S. Furst, T. Dow, K. Garrard, A. Sohn, Final Report to Babcock and Wilcox Technical Services Y12, LLC, *Automatic Handling Technology For Hemispherical Artifacts,* Precision Engineering Center (2008).
2. T. Dow, A. Sohn and B. Lane, Final Report to Panasonic, *Micromachining Optical Feature with the Ultramill,* Precision Engineering Center (2008).